Radiolabelling and biodistribution of IgE antibodies

Koers, Alexander Magnus Maria

Awarding institution:
King's College London

King's College

Radiolabelling and biodistribution of IgE antibodies

by Alexander Koers

A thesis submitted in partial fullfillment for the
degree of Doctor of Philosophy in the

Department of Imaging Science
School of Medicine

London, September 2014

Declaration of Authorship

I, Alexander Koers, declare that the thesis entitled 'Radiolabelling and biodistribution of IgE antibodies' and the work presented in the thesis are both my own, and have been generated by me as the result of my own original research. I confirm that:

- This work was done wholly or mainly while in candidature for a research degree at this University
- Where any part of this thesis has previously been submitted for a degree or any other qualification at this University or any other institution, this has been clearly stated
- Where I have consulted the published work of others, this is always clearly attributed
- Where I have quoted from the work of others, the source is always given. With the exception of such quotations, this thesis is entirely my own work
- I have acknowledged all main sources of help
- Where the thesis is based on work done by myself jointly with others, I have made clear exactly what was done by others and what I have contributed myself
- None of this work has been published before submission

Signed: .....

Date: .....

Abstract

Antibodies used for cancer treatment and immune therapy have, to date, been of the IgG class. Efficacy might be improved by using the IgE class of antibodies as these have higher affinity for their Fc-receptors. IgE has a greater tissue penetration and longer half-life in tissue and IgE bound to IgE-receptor-expressing effector cells is thought to actively infiltrate tumours. IgE has not been subject of *in vivo* imaging studies to date.

Objectives: The aim was to radiolabel both anti-CSPG4-IgE and MOV18-IgE, and their IgG counterparts targeted to the same antigen, while maintaining the functionality of the antibodies; and subsequently, to compare IgE with IgG in *in vivo* imaging and biodistribution studies in a disease model.

Methods: IgE's and their antigen-matched IgG counterparts were engineered against two different tumour antigens. Tumour models were developed to assess targeting *in vivo* and imaging and biodistribution studies using radiolabelled IgE were carried out. Six antibodies were engineered for comparison: MOv18-IgE and -IgG antibody targeted against the folate receptor alpha (FRα) expressed on ovarian cancer cells; A MOv18-IgE and -IgG chimeric rat/mouse were engineered for evaluation in a new syngeneic immunocompetent rat model to mimic the immunotherapeutic antibody (human/mouse chimeric MOv18-IgE and -IgG) planned for a clinical study; and a second antibody, anti-CSPG4-IgE, targeted against the chondroitin sulfate proteoglycan 4 (CSPG4), expressed in melanoma cancer was compared to its IgG counterpart. The antibodies were analysed in a NOD/SCID xenograft mouse model with splenic engraftment of human peripheral blood lymphocytes. All antibodies were labelled with ^{111}In using the same bifunctional chelator and labelling conditions (p-SCN-CHX-A"-DTPA) and radiolabelled with ^{111}In at room temperature. Functional assays using FACS were carried out to assure binding to the target and high- and low-affinity Fc-binding to FcεR expressing immune effector cells. NanoSPECT/CT imaging and biodistribution studies were used to determine targeting and clearance of IgE *in vivo*.

Results: ^{111}In-CHX-A"-DTPA-IgE and -IgG antibodies were labelled with high efficiency (>98%). Binding of the conjugated antibody to the target antigen and FcεR expressing immune effector cells was identical to that of the native antibody. IgE showed a higher liver uptake in biodistribution (up to 75% ID IgE vs 5% ID IgG 8 h post injection) compared with the IgG counterpart as well as more than 10 times faster blood clearance where as IgG showed prolonged

half-life (2.5 days) in blood. Tumour-to-blood and tumour-to-muscle ratios of IgE and IgG showed significant (tbr: $P<0.05$; tmr: $P<0.0005$) differences. Conclusion: Similar conjugation and radiolabelling of all antibodies as well as the *in vivo* assessment allowed the evaluation of targeting, biodistribution and clearance of IgE compared with its IgG counterpart. Observed characteristics of IgE like the rapid blood clearance and the higher liver uptake were found to be fundamentally different compared to its IgG counterpart and suggest a different and mostly unknown mode of action.

To my parents Edeltraud and Friedrich
and to my sister Victoria

Acknowledgements

Writing this part of my thesis starts with an emotional journey through the time of my PhD and all the people that accompanied me. I was very lucky to be part of such a wonderful group and project and to work along so many amazing people. Completing the PhD and writing this thesis was a unique journey that would not have been possible without the support and encouragement of the many outstanding people at the King's College London and the friends and family around me.

My greatest appreciation and gratitude goes to my advisors Phil Blower and James Spicer for their trust, support and patience. I would like to thank both of you for supporting and advising me during all phases of my PhD, but also for giving me the freedom to find my own way during this time. The environment Phil and James created at the Imaging Sciences & Biomedical Engineering institute and the project group is probably the best a PhD student could ever hope for. Professor Philip Blower and Dr James Spicer, it was a pleasure and a great honour to work for you.

My gratitude and appreciation extends to all the people I was privileged to work along within the IgE project. Special thanks to Sophia Karagiannis, Hannah Gould, Frank Nestle, Andrew Beavil for leading this project to success. Very special thanks to all the other PhD students and colleagues in this project for all your help and your friendship. Panos, Debra, Amy and Tihomir it was a pleasure to work with you.

I am especially grateful to Maggie Cooper and Florian Kampmeier, who not only are precious friends to me, but also dedicated their support and help to the problem of moments and shared their time, experience and vast knowledge in discussions and in the lab. Thank you very much for guiding me through this PhD. It is a privilege to call you my friends.

During my PhD at the IMIG lab I had the pleasure of working with a number of great colleagues and students some of which became close friends and it would have been impossible to finish the thesis without. I thank every one of you for a great time in- and outside the lab during sometimes long hours and for all the fun we had. Richard Tavare, Ehsan Sharif-Paghaleh, Kavitha Sunassee, Rafael Torres, James Ballinger, Greg Mullen, Julia Blower, Pete Williamson, Ricky Southworth, Katsumi Chia, Jen Williams, Seckou Diocou, Putt Charoenphun, Gareth Smith, Maite Jauregui-Osoro, Istvan Szanda and Levente Meszaros.

I want to thank our lab manager and my good friend David Thakor. Without your support executing such a multidisciplinary project in a world of restrictions, SOP's and risk assessments

would not have been possible. Thank your for always finding a way to give me access to all labs, even when I installed illegal beer fridges and nuts drawer, and for your friendship.

I'm very grateful for the close friendship and support during all the years to Adam, Alex, Sabine and Max. I couldn't have made it without your toilette rap songs, nervous confessions of undercover affairs and relaxed hours around good food.

To Flo, Sana and Mieke I want to say how wonderful it is to be a friend of yours and how much pleasure it is to be around you. Thank you for being there for me whenever I needed your company and help.

I would like to thank Eileen, Jürgen and Greta for their support and love and for well needed time outs on the Isle of Wight, the sailing yacht or in Kronach.

David, I could write pages about the good times we had but nothing says better how much your friendship means to me than: Nananana..nanana..eheheheh..1.3!

I dedicated this thesis and my PhD to my family for all the love and support only a family can give you. In all the times, no matter if good or bad, you all were by my side. Thank you for everything you've done for me. I also want to include all of my family, uncles, aunts and all my cousins. Thank you to all of you.

Finally, I want to say thank you to the most important person in my life, Hanna. You are the most amazing, bright, intelligent and beautiful being I've ever seen and I'm madly in love with you. Thank you for all the love and help you've given me.

Contents

List of Figures

List of Tables

List of abbreviations

Ab	Antibody
ADCC	Antibody dependent cellular cytotoxicity
ADCP	Antibody dependent cellular phagocytosis
APC	Antigen presenting cell
BCR	B-cell receptor
BFC	Bi-functional chelator
CDC	Complement-dependent cytotoxicity
CDR	Complementarity determining regions
CSPG4	Chondroitin sulfate proteoglycan 4
CT	Computed Tomography
FACS	Fluorescence-activated cell sorting
Fc	Fragment crystallizable
FDA	Food and Drug Administration
FRα	Folate receptor alpha
Fv	Variable fragment
GC	Germinal centre
GMP	Good manufacturing practices
GPI	Glycophosphatidylinositol
HPLC	High-performance liquid chromatography
ID	Injected dose
IL	Interleukin
iTLC-SA	Instant thin layer chromatography on paper with salicylic acid
NCBI	National center for biotechnology information
mAb	Monoclonal antibody
MHC	Major histocompatibility complex
MTD	Maximum tolerated dose
NSG	NOD SCID gamma
PBMC	Peripheral blood mononucleated cell
PET	Positron emission tomography
RAID	Radioimmunodetection
RAIT	Radioimmunotherapy
SCID	Severe combined immunodeficiency
SEC	Size exclusion chromatography
SPECT	Single photon emission computed tomography
TLC	Thin-layer chromatography
UV	Ultra-violet
WAG	Wistar albino glaxo

1 Introduction

1.1 Immune system and structure and function of antibodies

1.1.1 Adaptive immune system

The human immune system is a complicated set of pathways that allows a network of cells, tissues, and organs to work together to respond to antigens. Antigens are any of the various substances that when recognised as non-self by the immune system trigger an immune response. The human immune system has innate and adaptive components, and is divided into two main parts: humoral immunity, which deals with infectious agents in the blood and tissues, and cell-mediated immunity, which deals with cells that have been infected, e.g. with a virus. The adaptive immune system consists of different types of cells, each of which have a specific task assigned to them in the defence of the body. It uses the principles of selection and selective agents as it prepares its response to various foreign invasions.

1.1.2 Cellular immune system

In general, the cell-mediated immune response involves the activation of phagocytes, antigen-specific cytotoxic T-lymphocytes, and the release of various cytokines in response to an antigen. The T-lymphocytes have an important role in managing the cell-mediated system. Cells that have been infected by a pathogen (e.g. virus), present fragments of antigens on specialised receptors on the cell surface. The display of such foreign peptides by major histocompatibility complex (MHC) proteins makes the infected cell recognisable for T-lymphocytes, which in response are activated and destroy the infected cell. Cytotoxic T-lymphocytes recognise these displays and respond by releasing their cytotoxic granules (e.g. granzymes and perforins) or otherwise destroying the infected cell.

1.1.3 Humoral immune response

The extracellular spaces are protected by the humoral immune response, in which antibodies produced by B cells cause the destruction of extracellular microorganisms and prevent the spread of intracellular infections. The activation of B cells and their differentiation into antibody-secreting plasma cells is triggered by antigen and usually requires helper T cells.

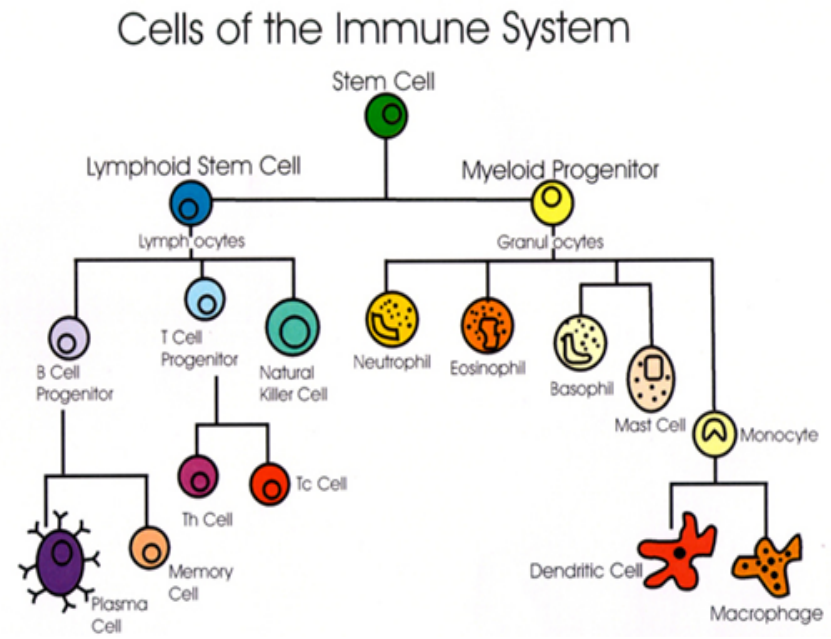

Figure 1.1: Origin and differentiation of cells of the immune system [1].

Humoral immunity is based on the production and secretion of pathogen-specific antibody molecules by B-lymphocytes. The first step of defence in the humoral pathway is phagocytosis of foreign matter by specialised antigen presenting cells (APCs). These cells digest the infectious agent and subsequently display some of its components on their surfaces. Cells called helper-T cells recognise this presentation of antigen fragments and activate an immune response. In the following immune response helper-T cells and B-cells communicate. This communication leads among other immune activities to the maturation of B-cell progenitors to plasma cells. The matured and proliferated plasma cells begin to produce large quantities of antibodies.

1.1.4 B-cells clonal selection

B-cells can make antibodies against almost any pathogen invading the body and the underlying concept is called clonal selection and expansion. During immune responses, B lymphocytes clonally expand and undergo secondary diversification of their immunoglobulin genes in germinal centres (GCs). Large receptor diversity is achieved by gene re-arrangement in the binding region of the antibody. During this process B-cells undergo a rearrangement of genes at the antibody loci, through different stages from early pro-B cell to mature B-cell. This random recombination of various gene loci for every segment of the antigen binding part of the antibody produces a huge quantity of B-cell receptors with a wide range of specificities. The clonal selection hypothesis postulates four important principles; the first one is that each lymphocyte has a single type of receptor with a unique specificity. Second, the interaction between an antigen and the unique specific lymphocyte receptor that can bind the antigen with high affinity leads to the activation of this lymphocyte. Further, the differentiated effector cells derived from this activated lymphocyte will express receptors with the identical specificity. The fourth principle is that lymphocytes expressing receptors

specific for ubiquitous self-molecules are deleted at an early stage of development and are not part of the mature lymphocyte population. After binding to the specific antigen the B-cell becomes activated if a second signal is mediated by a helper T-cell and the process of maturation is initiated. Once activated as described above, it differentiates into a plasma cell secreting large amounts of a specific antibody. The production of antibodies is the main function of the humoral immune system.

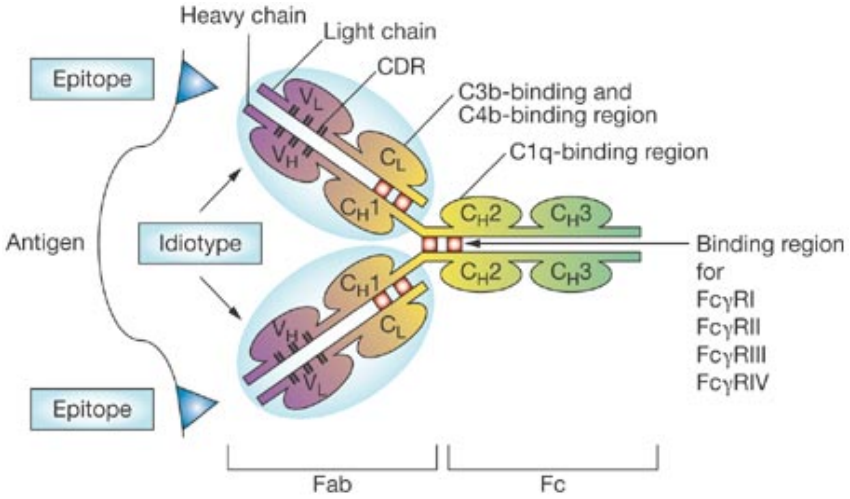

Figure 1.2: The structure of IgG. The site of interactions between IgG and an antigen (epitope) is shown, as are the binding sites for the complement components C1q and activated C3b and C4b, and the sites of interaction between heavy chains of IgG and FcγR. CDR, complementarity-determining regions; CH, constant heavy domain; CL, constant light domain; Fab, fragment antigen binding; Fc, fragment crystallisable; FcγR, Fcγ receptors; VH, variable heavy domain; VL, variable light domain [2]

1.1.5 Antibodies

Antibodies (Ab), part of the immunoglobulin superfamily (Ig), are one of three classes of specific antigen-recognition molecules in the immune system, the others being the T-cell receptor and the major histocompatibility complex (MHC) with its class I and II molecules. Antibodies are large proteins of a Y-shape produced by B-cells. Immunoglobulins are either bound to the membrane and are then referred to as B-cell receptor (BCR) or secreted by terminally differentiated B-cells (called plasma cells). Soluble antibodies are released into blood and tissue fluids and help immune cells to identify and neutralise foreign objects such as bacteria and viruses. Antibodies are bifunctional molecules. They specifically bind to an epitope on an antigen and at the same time can elicit responses of the host immune system that can lead to removal or destruction of the bound antigen. The effector functions and the nature of the recruited host response are determined by the constant region, also historically called Fc region (Fragment crystallisable) of the antibody (Figure 1.2). Each distinct type of constant region defines an antibody isotype with different biological functions depending on which receptors they bind to and the cellular distribution of

those receptors.

1.1.6 Antibody specificity

Antibodies bind their antigen targets with high specificity and consist of two identical light chains and two identical heavy chains, interconnected by disulfide bonds as depicted in figure 1.2. Depending on the isotype, the heavy chain consists of 4-5 immunoglobulin domains of ∼110 amino acids each. The light chain consists of 2 domains. The domains are organised in two opposing β-pleated sheets stabilised by a disulfide bond. (This structure is also called a β barrel). The N-terminal domains of the heavy and light chain are highly variable in their amino acid sequence and are referred to as variable regions VL+VH or Fv (fragment variable), respectively. Within these variable regions three short hypervariable loops, also known as complementarity determining regions (CDR) are enclosed by less variable framework regions (FR). The unique three-dimensional structure of the CDRs in concert with the framework regions determines the specificity and affinity of the antibody for a given antigen. The combination of the CDRs of the light and heavy chain forms the antigen binding site or paratope. The antigen binding site is highly specific for the three-dimensional conformation of the epitope. The principles of clonal selection ensure that antibodies are produced against an extremely high diversity of epitopes. To reach such variability antibody genes undergo a complex rearrangement of small gene segments called VDJ-recombination. This results in a unique combination of gene segments across the heavy and light chain variable region in a given B-cell. Further diversity is introduced upon joining the segments and after B-cell activation by an antigen in a process called directed somatic hypermutation.

1.1.7 Antibody isotypes

Antibodies come in different isotypes (the class switch occurs during the course of an immune response). Five classes of antibody molecules, namely, IgG, IgA, IgM, IgD and IgE are known in humans, including four subclasses of IgG (IgG1, IgG2, IgG3, IgG4) and two subclasses of IgA (IgA1, IgA2). Each class (or subclass) differs in size and number of immunoglobulin domains, amino acid (aa) sequence, isoelectric charge, carbohydrate side chains and most importantly its effector function. The class, subclass and isotype are determined by the heavy chain constant region (CH). Each antibody has a characteristic type of heavy chain (IgG: γ chains; IgM: μ chains; IgA: α chains; IgD: δ chains; IgE: ε chains). The C-terminal regions of the CH form the constant region and determine the effector functions mediated by binding to different cellular receptors for antibody.

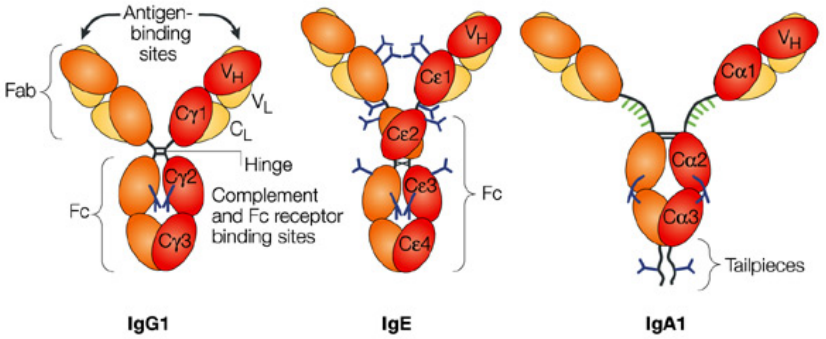

Figure 1.3: Immunoglobulins are composed of two identical heavy chains and two identical light chains, linked by disulfide bridges. The class of antibody is determined by its heavy chain, with all classes sharing the same light chains. Light chains fold into a variable domain (VL) and a constant domain (CL), whereas heavy chains are composed of one variable domain (VH) and either three (in IgG and IgA) or four (in IgE) constant domains. The antigen-binding sites at the tip of the Fab regions are formed from the variable domains of both the heavy and light chains. The Fc region mediates interaction with effector molecules, such as complement and Fc receptors. In IgG and IgA, the Fab and Fc regions are separated by a flexible hinge region, which varies in length and sequence between different immmunoglobulin classes and subclasses. In IgE, the classical hinge is replaced by an extra pair of constant domains. For each antibody, one heavy chain is shown in red, the other in orange, with light chains in yellow. N-linked oligosaccharides are shown in blue and O-linked oligosaccharides on the IgA1 hinge region in green [3].

1.1.8 Fc-receptor

The function of the antibody is determined by its Fc-region. Each subclass has different functions and characteristics transmitted through the Fc-region (Table 1.1). Fc-receptors are found on a variety of immune cells. Depending on cell type or isotype of the antibody, the binding of an antibody to an Fc-receptor can trigger different effector functions within the cell. In order to elicit specific host responses, antibodies need to bind to isotype specific Fc-receptors displayed on the cell surface of a variety of immune effector cells. The interaction of antibodies and Fc-receptors on immune effector cells presents a link between the humoral and the cell mediated immunity. Studies have shown the role of Fc-receptors in triggering effector responses such as phagocytosis, natural killer cell (NK cell) driven ADCC, neutrophil activation, or the inhibition of B cell activation [4]. Generally, effector cells are activated by cross-linking with and aggregation of two or more Fc-receptors by specific antibody-antigen immune complexes [5]. Each isotype may have more than one isotype specific Fc-receptors expressed by effector cells. For IgE antibodies, for example, two receptors can be found, FcεRI and FcεRII. The pathway of immune response depends on the specific Fc-receptor.

Table 1.1: Overview of FcR, binding antibodies and effector functions.

FcR	Antibody ligand	Immune effector cells	Effect elicited by binding of antibody to effector cell via FcR
FcγRI (CD64)	IgG1 & IgG3	Macrophages, Neutrophils, Eosinophils, Dendritic cells	Phagocytosis, Cell activation, Activation of respiratory burst, Induction of microbe killing
FcγRIIA (CD32)	IgG	Macrophages, Neutrophils, Eosinophils, Platelets, Langerhans cells	Phagocytosis, Cell killing (Degranulation)
FcγRIIB1 (CD32)	IgG	B Cells, Mast cells	Inhibition of phagocytosis, Inhibition of cell activity
FcγRIIB2 (CD32)	IgG	Macrophages, Neutrophils, Eosinophils	Phagocytosis, Inhibition of cell activity
FcγRIIIA (CD16a)	IgG	NK cells, Macrophages	Antibody-dependent cell-mediated cytotoxicity (ADCC), Cytokine release by macrophages
FcγRIIIB (CD16b)	IgG	Eosinophils, Macrophages, Neutrophils, Mast cells, Follicular dendritic cells	Induction of microbe killing
FcεRI	IgE	Mast cells, Monocytes, Eosinophils, Basophils, Langerhans cells	Antibody-dependent cell-mediated cytotoxicity (ADCC), Antibody-dependent cell-mediated phagocytosis (ADCP)
FcεRII (CD23)	IgE	B cells, Eosinophils, Langerhans cells	IgE transport across human intestinal epithelium, Positive-feedback mechanism to enhance allergic sensitization (B cells), Possible adhesion molecule
FcαRI (CD89)	IgA	Monocytes, Macrophages, Neutrophils, Eosinophils	Phagocytosis, Induction of microbe killing
Fcα/μR	IgA and IgM	B cells, Mesangial cells, Macrophages	Endocytosis, Induction of microbe killing
FcRn	IgG	Monocytes, Macrophages, Dendritic cells, Epithelial cells, Endothelial cells, Hepatocytes	Transfer of IgG from mother to foetus via placenta, Transfer of IgG from mother to infant in milk, Protection of IgG from degradation

1.1.9 IgE and Fc-receptor

FcεRI is expressed as an $\alpha\beta\gamma_2$ tetramer on human mast cells and basophils, and as an $\alpha\gamma_2$ trimer on human antigen-presenting cells (APCs), monocytes, eosinophils, platelets and smooth-muscle cells. The low-affinity receptor CD23 is also known as FcεRII. CD23 is distinguished structurally from almost all other immunoglobulin receptors as it belongs to the C-type (calcium dependent) lectin superfamily. Both membrane bound as well as soluble CD23 can be found as well as two different size versions CD23a and CD23b. CD23 is also expressed by different cells: CD23a is expressed by antigen-activated B cells before differentiation into antibody-secreting plasma cells, whereas CD23b expression is induced by interleukin-4 (IL-4) on a variety of inflammatory cells, B cells and epithelial cells.

1.1.10 IgE-Fc crosslinking and IgE functions

IgE can crosslink with both its high affinity receptor FcεRI and its low affinity receptor FcεRII or CD23. The crosslink of IgE in the mucosal tissues leads to recruitment of mast-cell and APC's and IgE production in the mucosal tissues. This is a central function of IgE, and occurs within the first hour of crosslinking complexes of IgE with FcεRI at the surface of mast cells or basophils by allergens. Mast-cell precursors are generated in the bone marrow and migrate to mucosal tissue before expressing FcεRI ($\sim$500,000 copies per cell) [6, 7].

IgE binds to FcεRI on the surface of Langerhans cells and to epithelial dendritic cells (APCs). Antigen-presenting cells (APCs) can internalise and process antigen, and then display antigenic peptide fragments on their surface, together with molecules required to activate the cognate lymphocytes. Langerhans cells are professional antigen presenting dendritic cells localised in the skin epidermis. Following the capture of allergens they either migrate to local lymph nodes or remain in the tissues where they present the processed allergens to helper T cells [8]. Helper T (TH) cells are critical to coordinating the activity of the immune response. The chemical messages they secrete (cytokines) stimulate the non-specific immune response to continue, and strengthen and boost specific responses. Allergen-IgE complexes can also crosslink in the mucosa to CD23 that is expressed by activated B cells. They then can facilitate antigen presentation to the T cells [9]. The process of antigen presentation by way of CD23 is termed facilitated antigen presentation (FAP). The interaction between CD23 and HLA-DR in the cell membrane is involved in the trafficking of allergen-IgE-CD23 complexes to endosomes, where the allergen-derived peptides are loaded onto the HLA-DR molecules for presentation at the B-cell surface [10]. HLA-DR plays a central role in the immune system by presenting peptides derived from extracellular proteins. Class II molecules are expressed in antigen presenting cells (APC: B lymphocytes, dendritic cells, macrophages). Antigen presentation through the membrane bound B-cell receptor (BCR) involves the interaction of B cells that are bound to a specific antigen with TH cells.

An antigen activated B cell expressing CD23 can in effect behave as a 'professional' APC such as a dendritic cell. This can simultaneously process unrelated antigens through FcγRs and cause epitope spreading to other antigens, a process by which an antibody response to one epitope on an antigen leads to the production of antibodies specific for other epitopes on the same antigen or for epitopes on entirely unrelated antigens. Research showed that CD23-mediated FAP is as efficient as FcγR-mediated antigen presentation by dendritic cells [11]. Monocytes and eosinophils are also bound by IgE. Crosslinking of these cells with IgE upregulates the expression of FcεRI, or in combination with IL-4 and IL-13 stimulates the expression of CD23 by these cells. Monocytes and eosinophils are recruited by these interactions for different functions, such as the clearance of antigen-IgE complexes, and killing and phagocytosis of pathogens [12] and tumour cells that bear 'foreign' antigens [13]. The ability of FcεRI and CD23 to mediate IgE-dependent monocyte- and eosinophil-mediated lysis of target cells and phagocytosis of the resulting cell fragments was shown by experiments with an IgE antibody against tumour cells [13]. The upregulation of CD23 was also observed to release soluble fragments that interacted in IgE-independent monocyte-mediated cytotoxicity. In addition to IgE, CD23 binds a second ligand in a carbohydrate-dependent manner called CD21. CD21 is expressed by B cells, follicular dendritic cells (FDCs), activated T cells and basophils. Crosslinking between these two molecules shows the ability of CD23 to bind both IgE and CD21 and links the IgE antibody and complement systems. The complement system is a heat-labile component of normal plasma that entails many proteins acting together to augment opsonisation of targets by antibodies and promote antibody-mediated target destruction by forming membrane-attack complexes that form pores in target cell membranes, and also leads to clearance of immune complexes.

1.1.11 Antibody-dependent cellular cytotoxicity and phagocytosis

Antibody-dependent cellular (e.g. monocyte-mediated) cytotoxicity or phagocytosis described above (ADCC and ADCP) is one of the central functions of antibodies. ADCC and ADCP, while important in antitumour activity, may also have an important role in antibody dependent antitumour mechanism of tumour-antigen specific antibodies, but evidence supporting its relevance to efficacy of antibody-based immunotherapy is scarce [14]. Antibody-dependent cellular cytotoxicity might directly induce a variable degree of immediate tumour destruction. This leads to an antigen presentation of the lysed cell debris and the induction of cross-primed tumour-antigen-specific T-cell responses [15].

Tumour cells are ineffective at initiating host-protective immunity, and the activation of tumour specific cytotoxic T-cells depends on uptake of tumour antigens by dendritic cells and their subsequent presentation to both helper and cytotoxic T cells [16]. Cytotoxic T cells kill their targets by programming them to undergo apoptosis. Specific recognition of MHC class I

complexes on a target cell by a cytotoxic T cell (CTL) leads to the death of the target cell by apoptosis. Killing requires a series of steps, including receptor binding and directed release of cytotoxic proteins stored in lytic granules [17, 15]. The membrane-bound MHC I protein displays the antigen for recognition by special immune cells known as cytotoxic T cell lymphocytes. MHC I proteins work to present the types of proteins being synthesised within a cell, which can then be monitored by killer T cells as part of a surveillance system that identifies and destroys any cell with over-abundant or unfamiliar peptide antigens, such as malignant cells or those harbouring viruses.

If not cited otherwise all information about the immune system development and the structure and function of antibodies originates from Chapter 3 of Immunology by David Male et al., 8th Edition and Chapter 9 of Janeway's Immunobiology by Janeway et al., 7th Edition [18].

1.1.12 Monoclonal and recombinant antibodies

The development of hybridoma technology by Köhler and Milstein in 1975 (continuous cultures of fused cells secreting antibody of predefined specificity [19]) has led to sophisticated methods for the generation and production of antibody molecules with predefined specificity and against any protein of interest [19]. The first generation of recombinant antibodies was polyclonal and generated from various species. These antibodies predated the hybridoma technology, which marked the second generation. Hybridoma technology enabled the production of murine monoclonal antibodies, and the new generation of antibodies showed first promising clinical results, although, these were outweighed by disappointing outcomes. The third and current generation of antibodies is characterised by the development, testing and use of antibodies with essentially human properties and broad clinical applicability [20]. The current generation of clinically effective unconjugated antibodies emerged from fundamental advances in antibody engineering. Advances like the replacement or avoidance of rodent immunoglobulin sequences permitted the development of antibodies with human properties. The replacement of rodent sequences improved the pharmacology and reduced the immunogenicity of antibodies, thus allowing repeated therapy for prolonged periods of time [21]. Chimeric monoclonal antibodies contain human constant domains and rodent variable domains [22, 23]. Humanised antibodies, such as trastuzumab and alemtuzumab, represented a further evolution of antibody engineering technology, with human sequences replacing all rodent sequences except for the complementarity determining regions (CDRs) that are responsible for antibody specificity [24].

1.1.13 Antibodies in targeted therapy

Various definitions of targeted therapy can be found in literature. Hait and Hambley [25] defined targeted therapy as 'drugs developed against a specific target based on its important biological

function in cancer. In contrast, non-targeted therapies are drugs identified by phenotypic screening of natural products or chemical libraries against established cancer cell lines or preclinical animal models without a priori knowledge of the target. Targeted therapies are designed to selectively inhibit a target that is abnormal in malignant compared with normal tissues. While therapeutic antibodies have changed and expanded the therapeutic landscape, most have limited efficacy in cancer when used alone and, therefore, they are most often combined with more conventional chemotherapeutic agents [26].

Much of the progress in targeted therapy came from the identification of cell surface antigens that are central to the tumour cell signal transduction pathways. These pathways control proliferation and differentiation of cells and the mutations in these pathways often lead to the development of tumours. Antibodies targeting and disrupting these pathways result in the death of the tumour cells. Small molecules, such as imatinib and antibodies, such as trastuzumab, are early examples of successful targeted therapy [26].

Cell surface antigens that are expressed by human cancers and are suitable targets are overexpressed, mutated or selectively expressed compared with normal tissues [28]. One of the key challenges in targeted antibody therapy has been, and still is today, to identify antigens that are suitable for antibody-based therapeutics. Ideally, the target antigen should be abundant and accessible with a homogeneous expression, consistently and exclusively on the surface of cancer cells. Antigen secretion and shedding should be minimal because secreted antigens can bind the antibody in the circulation and could prevent sufficient antibody from binding to the tumour. If the desired mechanism of action is ADCC or complement-dependent cytotoxicity (CDC), then the antigen-antibody complex should not be rapidly internalised to maximise the availability of the Fc region to immune effector cells and complement proteins, respectively. However, rapid internalisation is desirable for antibodies that deliver drugs or toxins to the tumour cell and for antibodies targeting the downregulation of cell surface receptors [27]. Aside from targeting antigens that are involved in cancer cell proliferation and survival, antibodies can also function to either activate or induce apoptotic-signalling events, by binding and subsequently blocking growth factors (e.g., VEGF), thereby depriving tumour cells of the necessary components to survive [26].

Antibody therapeutics can also function through various pathways. For example, antibodies can mediate modifications of the antigen or can activate the immune system and recruit immune responses or deliver a specific drug or toxin conjugated to an antibody with a specific target [29–31]. Antibody therapeutics might also have a role in the generation of de novo immune responses to the antigen targeted by the antibody through promoting antigen presentation to Fc receptor-bearing cells [32], thus allowing the effects of therapeutic antibodies to persist after the treatment is completed. While this ability of antibodies to promote anti-tumour effects through tumour-antigen-specific immune responses has been almost ignored [15] in recent years researchers are now more and more trying to engineer antibodies to improve these functions. Antigen-specific

Table 1.2: FDA approved antibody-based therapeutics. ADCC, antibody-dependent cellular cytotoxicity; CDC, complement-dependent cytotoxicity; CLL, chronic lymphocytic leukaemia; CTLA4, cytotoxic T lymphocyte-associated antigen 4; EGFR, epidermal growth factor receptor; FDA, US Food and Drug Administration; IgG, immunoglobulin G; NHL, non-Hodgkin's lymphoma; NSCLC, non-small-cell lung cancer; SCCHN, squamous cell carcinoma of the head and neck; VEGF, vascular endothelial growth factor.

Antibody	Target	Indication	Mechanisms of action
Naked antibodies for solid malignancies			
Trastuzumab (Herceptin; Genentech): humanized IgG1	ERBB2	ERBB2-positive breast cancer & ERBB2-positive gastric or gastro-oesophageal junction carcinoma	Inhibition of ERBB2 signalling and ADCC
Bevacizumab (Avastin; Genentech/Roche):humanized IgG1	VEGF	Metastatic colon cancer; Advanced NSCLC; Glioblastoma; Metastatic kidney cancer	Inhibition of VEGF signalling
Cetuximab (Erbitux; Bristol-Myers Squibb):chimeric human–murine IgG1	EGFR	SCCHN; Metastatic EGFR-positive colorectal cancer	Inhibition of EGFR signalling and ADCC
Panitumumab (Vectibix;Amgen): human IgG2	EGFR	EGFR-expressing metastatic colorectal carcinoma	Inhibition of EGFR signalling
Ipilimumab (Yervoy;Bristol-Myers Squibb): IgG1	CTLA4	Metastatic melanoma	Inhibition of CTLA4 signalling
Naked antibodies: haematological malignancies			
Rituximab (Mabthera;Roche): chimeric human–murine IgG1	CD20	CD20-positive B cell NHL and CLL; Follicular CD20-positive NHL	ADCC, direct induction of apoptosis and CDC
Alemtuzumab (Campath;Genzyme): humanized IgG1	CD52	B cell chronic lymphocytic leukaemia	Direct induction of apoptosis and CDC
Ofatumumab (Arzerra;Genmab): human IgG1	CD20	CLL refractory to fludarabine and alemtuzumab	ADCC and CDC
Conjugated antibodies: haematological malignancies			
Gemtuzumab ozogamicin (Mylotarg; Wyeth):humanized IgG4	CD33	CD33-positive acute myeloid leukaemia; Withdrawn from use in June 2010	Delivery of toxic payload, calicheamicin toxin
Brentuximab vedotin (Adcetris; Seattle Genetics):chimeric IgG1	CD30	Relapsed or refractory Hodgkin's lymphoma and systemic anaplastic lymphoma	Delivery of toxic payload, auristatin toxin
^{90}Y-labelled ibritumomab tiuxetan (Zevalin; IDEC Pharmaceuticals): murine IgG1	CD20	Follicular B cell NHL	Delivery of the radioisotope ^{90}Y
^{131}I-labelled tositumomab (Bexxar; GlaxoSmithKline):murine IgG2	CD20	CD20 antigen-expressing relapsed or refractory, low-grade, follicular or transformed NHL	Delivery of the radioisotope ^{131}I, ADCC and direct induction of apoptosis

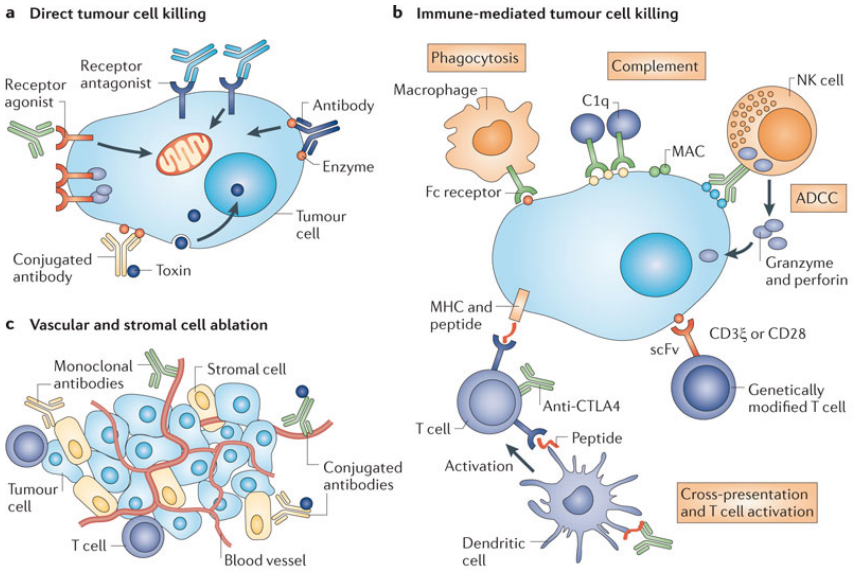

Figure 1.4: Mechanisms of tumour cell killing by antibodies. a) Direct tumour cell killing can be elicited by receptor agonist activity, such as an antibody binding to a tumour cell surface receptor and activating it, leading to apoptosis (represented by the mitochondrion). It can also be mediated by receptor antagonist activity, such as an antibody binding to a cell surface receptor and blocking dimerization, kinase activation and downstream signalling, leading to reduced proliferation and apoptosis. An antibody binding to an enzyme can lead to neutralisation, signalling abrogation and cell death, and conjugated antibodies can be used to deliver a payload (such as a drug, toxin, small interfering RNA or radioisotope) to a tumour cell. b) Immune-mediated tumour cell killing can be carried out by the induction of phagocytosis; complement activation; antibody-dependent cellular cytotoxicity (ADCC); genetically modified T cells being targeted to the tumour by single-chain variable fragment (scFv); T cells being activated by antibody-mediated cross-presentation of antigen to dendritic cells; and inhibition of T cell inhibitory receptors, such as cytotoxic T lymphocyte-associated antigen 4 (CTLA4). c) Vascular and stromal cell ablation can be induced by vasculature receptor antagonism or ligand trapping (not shown); stromal cell inhibition; delivery of a toxin to stromal cells; and delivery of a toxin to the vasculature. MAC, membrane attack complex; MHC, major histocompatibility complex; NK, natural killer. Figure original from Nature Cancer Reviews [27]

immune responses are the result of a complex interaction between antigen-presenting cells (APC), T lymphocytes and tumour cells. A large proportion, as much as 50%, of tumour lesions are made up of infiltrating immune cells that are also found in higher concentrations around the tumours [33, 4, 34]. Some of these infiltrates are known powerful FcεR- and FcγR-expressing effector cells such as monocytes/macrophages, mast cells, dendritic cells and eosinophils [35–37].

The mechanism triggered and the quality of its reaction depends on specificity and isotype of the antibody and its ability to interact with the FcR. ADCC has been demonstrated to have a major role in antibody efficacy, and there is evidence that in IgG class antibodies FcγRIIa-131H polymorphisms have a favourable effect on response rates for cetuximab in colorectal cancer,

trastuzumab in breast cancer and rituximab in follicular lymphoma [38–40].

To address the difficulties in engineering new antibody-based therapies molecular techniques that can alter antibody pharmacokinetics, effector function, size and immunogenicity have emerged as key elements in the development. In general, changes to the Fc domain structure can affect antibody clearance and the interaction of Fc domains with cellular FcR of effector cells. Activation of FcR helps the recruitment of adaptor proteins that mostly function as molecular mediators and interact with signal transduction pathways. They regulate cell signalling and can amplify a receptor-mediated signal to facilitate coupling of the signal to different signal transduction pathways for the activation of immune effector cells. Strategies to improve ADCC activity, such as fucosylation modification (a process in which fucose sugar residues are added to a antibody to increase its affinity to the FcR), have become introduced into the clinic. However, FcγR genotypes are not completely predictive of response, indicating that other factors are also highly relevant to tumour response to antibody therapy. Different strategies have emerged, like the use of targeted IgE antibodies to exploit the naturally high affinity to its FcεRI [41, 42, 13]. Furthermore, the ability of antibodies to generate T cell responses to tumour antigens may be affected by a broad range of factors, including cross-presentation of antigen by dendritic cells, the efficiency of antigen processing and immune escape through regulatory T cells [43].

1.1.14 The role of antibodies of the IgE isotype and their potential use in targeted therapy

IgE has unique properties that could overcome some of the limitations of antibody treatment. IgE is commonly known as a powerful trigger of immune responses in allergic reactions. These strong reactions are based on strong interaction of the allergy antigen-IgE complex with the high affinity IgE Fc-receptor and its ability to recruit and bind effector cells efficiently. Another factor might be the ability of IgE to reside in tissue for extended periods of time.

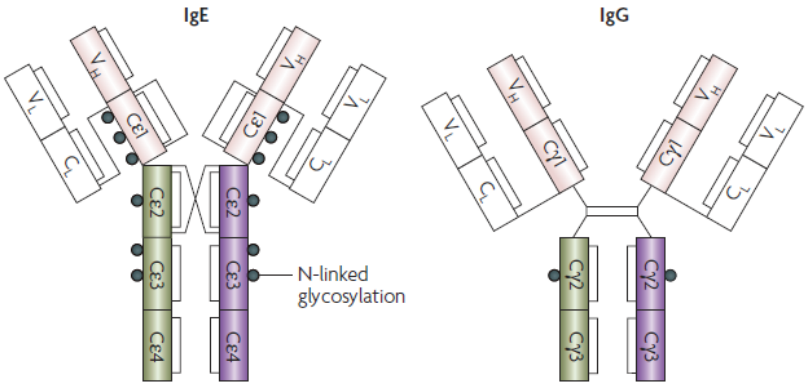

Figure 1.5: Domain structures of IgE and IgG. Schematic representations of the polypeptide and domain structures of human IgE and IgG1, showing the intra- and inter-domain disulfide bridges and the sites of N-linked glycosylation [44].

While very few data are available on the elimination pathways of therapeutic IgG and IgE type monoclonal antibodies, there are some data on IgE serum and tissue half-life in general. The half-life of IgE in human serum is found in literature with variations ranging from 1.5 to 3 days and everything in between. Most publications seem to publish a compromise of 2 or 2.5 days as IgE serum half-life for humans [45–47, 42, 48, 49]. The half-life of IgE in tissue or cell-bound was found in literature with 14 days or weeks. This data was based on measurement of IgE in skin of rats [48] and based on the affinity calculations for the interactions of the FcεRI with its corresponding receptors [45, 49]. For comparison, the IgG half-life in serum is ∼20 days and ∼2-3 days in tissues. The neonatal Fc receptor (FcRn) expressed on endothelial cells might provide an explanation for the extended half-life of IgG in serum and the regulations of IgG levels in rodents and in humans [50]. An FcRN knock-out study has been shown to reduce the plasma half-life of IgG in mice from 9 days to 1.4 days [47]. Thus, indicating that the main reason for the difference in half-life between IgG and IgE is this stabilising interaction between IgG and FcRn. The FcRn receptor possesses two main functions: the transport of IgG known as transcytosis and the control of IgG catabolism [51, 50]. The IgG in excess (not bound to the saturable FcRn) undergoes degradation in lysosomes [52, 50]. The behaviour of monoclonal antibodies bound to target cells is unknown. Kennedy et al. [53] suggested that circulating B lymphoma cells bound to rituximab via the CD20 antigen could be sequestered by phagocytic cells where the complex antigen/antibody is removed [54]. However, the FcRn receptor binding domain is not present in IgE antibodies. But the factors influencing the half-life of IgG can give further evidence to support that the turnover of IgE may be much faster than that of IgG and a substantially higher amount of IgE may be produced than is reflected in its plasma levels. Further, it has to be considered that the majority of IgE is bound to high-affinity FcεRI on the surface of basophils and mast cells or the low affinity receptor FcεRII on B-cells [44, 55, 35]. This is in marked contrast to IgG that instead is primarily found in free circulating form. The IgE-FcεRI interaction has a potentially stabilising effect on IgE half-life [47]. The half-life of receptor bound IgE has been estimated to approximately 14 days, which indicates that the majority of IgE may have a half-life similar to IgG, despite its much lower plasma half-life, once bound to FcεRI immune effector cells [47, 56].

With a serum half-life of 21-24 days, compared to a half-life of 2-3 days in tissues, IgG antibodies may be the most effective antibody class to target blood-resident tumours and circulating tumour cells, while their ability to exert tumour surveillance in tissues may be less potent [47, 42, 35, 4].

In vivo research performed by Kershaw et al., showed a syngeneic animal model used to examine the anti-cancer effects of a rat/human chimeric IgE specific for murine Ly-2 [57].

Syngeneic mouse models have also been used to evaluate the ability of murine IgE to act as an adjuvant for cancer immunotherapy [58]. Reali et al,. postulated that IgE on the surface of tumour cells would affect tumour immunogenicity by the activation of innate immunity within

the tumour microenvironment and that these changes might affect tumour growth. The study showed that the treatment of tumour bearing mice with IgE significantly reduced tumour growth and prolonged survival compared to IgG treatment. These studies were later confirmed in a more immunogenic tumour model using the syngeneic murine lymphoma RMA-Thy1.1 cell line under comparable conditions [58]. Karagiannis and colleagues demonstrated the potency of IgE to mount superior immune responses against tumours in disease-relevant models [35].

FcεRI-receptor expressing effector cells, such as monocytes-/macrophages and eosinophils, were found to kill tumour cells by activation by tumour specific IgE antibodies. They describe the engineering of a humanised IgE counterpart of commercially available trastuzumab IgG, an antibody against HER2/neu. Remarkably, the IgE retained all proliferation restricting functions in HER2/neu-expressing tumour cells but also showed activation of effector cells and tumour killing by different mechanisms like ADCC and ADCP [42].

The receptors for IgE expressed on immune effector cells are the high-affinity receptor, FcεRI, and the low-affinity receptor, FcεRII (CD23), which they bind to with affinities of 10^{-9} - 10^{-11} and 10^{-6} - 10^{-8} M^{-1}, respectively [44, 45]. The structures of these receptors differ hugely: The high affinity receptor is a critical component of IgE-mediated allergic reactions. It is expressed as a tetramer, with subunits ac_2, on eosinophils and monocytes. FcεRI exists also as a tetramer, with subunits abc_2, on mast cells and basophils, A trimeric form is expressed on antigen presenting cells where it acts to facilitate antigen presentation via IgE.

Both the expression and the signalling capacity of the trimer are lower than those of the tetramer and in both of these receptors the IgE binding domain is on the extracellular α-chain [59–61].IgE binding to FcεRI and FcεRII receptor has a significantly different signalling response in each case. IgE bound to the high affinity receptor FcεRI and cross-linking with a specific antigen will result in aggregation and downstream signalling through a Syk-dependent pathway. The spleen tyrosine kinase (Syk) is associated with Fcγ receptors (FcγRs) and transmits activation signals through FcγRs in myeloid cells. The consequences are the degranulation of mast cells and release of inflammatory mediators like histamine, leukotriene and proteases as well as cytokines attracting T cells, monocytes, basophils, eosinophils and APCs to the site of inflammation [44, 45, 62]. *In vivo* experiments showed IgE mediated anti-tumour efficacy in immunosupressed rodents to utilise human T cell receptors expressed on murine T cells and human tumour cells [63]. The same mediators also activate infiltrating cells *in situ* to induce ADCC through release of pro-inflammatory cytokines, enzymes and other cytotoxic mediators (e.g., TNF-α, lysozyme, nitric oxide (NO), H_2O_2 and other reactive oxygen species) [64–66].

IgE that is bound via the low affinity receptor FcεRII to CD23 leads to an ADCP immune response through activation of macrophages/monocytes. In a Th2 introduced immune response and particularly through IL-4 and IL-13 CD23 is tremendously up regulated [67–72]. So, it can be seen that differential methods of cell killing are promoted by the binding of IgE to the receptors

FcεRI and CD23: degranulation with release of pro-inflammatory mediators and cytokines by mast cells and basophils, ADCC, mediated by the release of mediators such as NO, enzymes and cytokines resulting in target cell lysis, and ADCP, mediated by the activation of macrophages and monocytes.

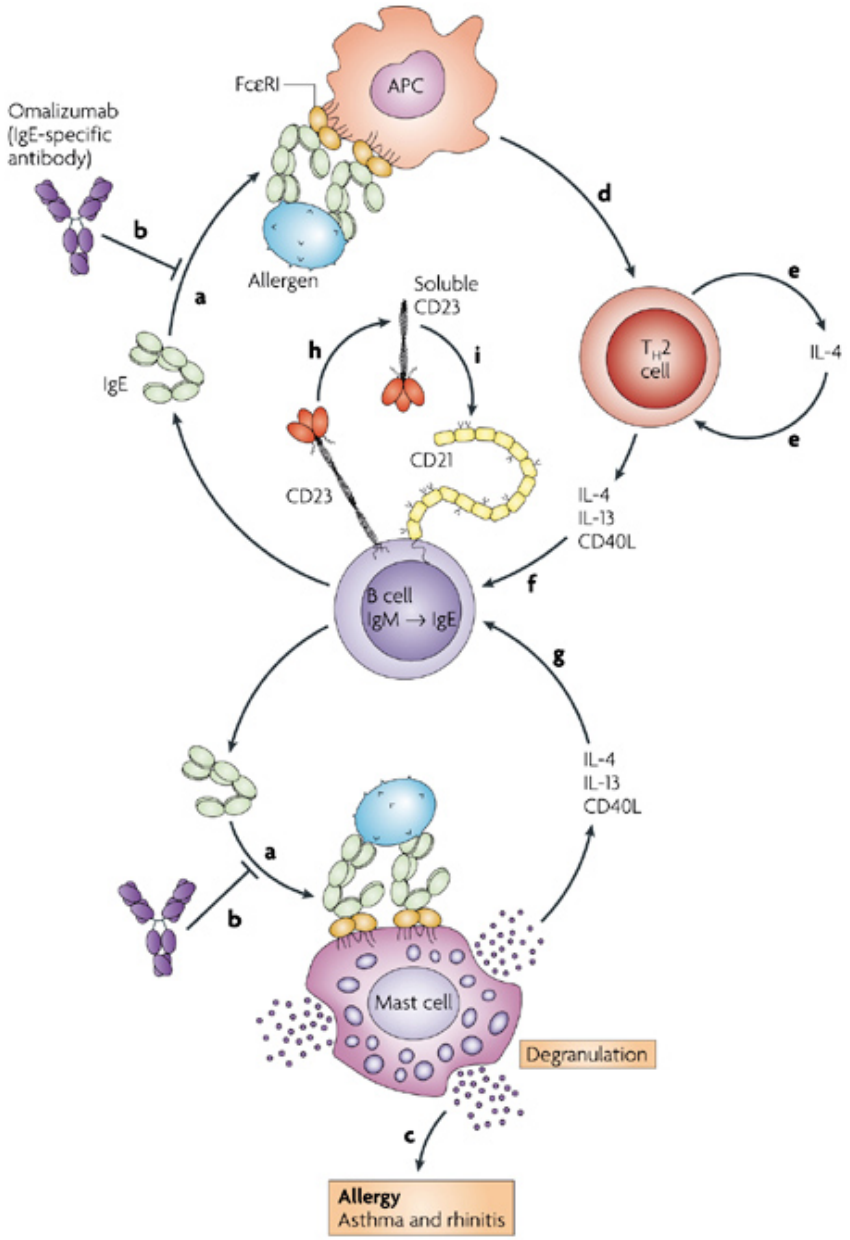

Figure 1.6: IgE is synthesized and secreted by B cells that have undergone heavy-chain class switching from IgM to IgE. The IgE binds to FcεRI on mast cells and antigen-presenting cells (APCs) (a) and sensitizes these cells to the antigen. Omalizumab inhibits the binding of IgE to FcεRI on mast cells and APCs (b). Allergen binding to IgE triggers mast-cell degranulation to elicit an ADCC/ADCP response(c). Antigen binding to the APC leads to the presentation of antigen peptides to T helper 2 (TH2) cells (d). The allergen-activated TH2 cells secrete interleukin-4 (IL-4) (e) to maintain the TH2-cell lineage and recruit more TH cells into this lineage (e). The TH2 cells also secrete IL-13, which together with IL-4 stimulates heavy-chain class switching to IgE (f). The allergen-activated mast cells contribute to the production of IL-4 and IL-13 [44].

1.1.15 Human chondroitin sulfate proteoglycan 4 (CSPG4) and folate receptor (FRα) as target receptors for antibody therapy

Human chondroitin sulfate proteoglycan 4 (CSPG4)

The CSPG4 receptor is also known as 'Human high molecular weight-melanoma-associated antigen' (HMW-MAA) [73] or melanoma chondroitin sulfate proteoglycan (MCSP) [74]. It consists of an N-linked glycoprotein of 280 kDa and a proteoglycan component of about 450 kDa [75] and plays an important role in melanoma cell proliferation, migration, and metastasis [76]. CSPG4 has a restricted expression in normal tissues, although it is expressed at high levels on both activated pericytes and pericytes in tumour angiogenic vasculature, which are associated with neovascularization *in vivo* [77–80]. CSPG4 is overexpressed on over 90% of the surgically removed benign nevi and melanoma lesions [73]. It has also been found to be overexpressed on triple negative breast cancer cells and expressed by basal cell carcinoma, tumours of neural crest origin (astrocytomas, gliomas, neuroblastomas and sarcomas); some forms of childhood leukemias and lobular breast carcinoma lesions. *In vitro* experimental data have shown that CSPG4 is involved in the adhesion, spreading and migration of melanoma cells and may play a role in cell invasion and metastasis [81, 73, 76]. CSPG4-specific mAbs have been shown to disrupt melanoma cell adhesion to collagen type I (CI), CVI, and fibronectin [82, 83].

Folate receptor alpha

Folate receptor (FRα), also known as the high affinity membrane folate-binding protein, is a glycosylphosphatidylinositol (GPI)-linked glycoprotein with an apparent molecular weight of 38-40 kDa [84, 85]. FR appears in two known membrane-bound isoforms in humans, designated α and β. FRs bind folic acid with high affinity. Folic acid is needed by all eukaryotic cells for DNA synthesis and one-carbon metabolism and an essential dietary vitamin [86, 85].

FR driven molecule uptake follows the endocytosis mechanism by which cells transport essential molecules, such as vitamins and hormones, across the cell membrane and into the cell interior [87–90]. This process is dependent on a specific binding of a ligand to a membrane-bound receptor, with subsequent formation and release of an intracellular vesicle termed an endosome. Inside the cell the endosome can experience different fates depending on the uptake pathway, including ligand release into the cytoplasm [91, 92]. The role of FR in cellular folate transport is not well understood, although a 'potocytosis' model has been proposed [87]. The recycling rate for the folate receptor is relatively slow. FRα recycling reportedly occurs in the range of 0.5 to 5 hours [93–95]. Folate receptor expression can be very high in cultured KB human oral carcinoma cells (up to $30\text{x}10^6$ receptors/cell), with moderately high expression in IGROV-I ovarian carcinoma cells ($1\text{x}10^6$ receptors/cell) [96].

Elevated expression levels of FR have also been evaluated in various types of cancers. [97–

101]. Additionally, FRs were found to be clustered in non-coated membrane regions called caveolae [85]. The receptor has been found on epithelial originated tumors such as ovarian carcinomas. Studies show that over 90% of ovarian carcinomas overexpress the FR [102, 103]. High frequencies of receptor overexpression were found in many types of tumors, including ovarian, endometrial, colorectal, breast, lung, renal cell, brain metastases derived from epithelial cancers, and neuroendocrine carcinomas [102, 85].

The overexpression in tumour cells makes FR a potential molecular target for tumour-selective drug delivery, including radiolabelled conjugates for diagnostic imaging. Tumour overexpression of the folate receptor has been exploited *in vitro* as a marker to localise and visualise tumour cells [104, 105, 93, 106, 100], with FRα ultimately being recognised to be the antigen target of many tumour-specific monoclonal antibodies (e.g., MOv18, MOv19) [107, 102, 108, 106, 99, 100]. The folate receptor has been targeted for tumour imaging using radiolabelled antibodies to the folate receptor [109–113]. However, the kinetics of tracer uptake in tumour tend to be unsatisfactory and limited presumably by the rate of antibody extravasation, resulting in relatively poor target-to-background tissue contrast at short times after administration [86].

1.2 Imaging

SPECT and PET are radionuclide molecular imaging techniques that enable evaluation of biochemical changes and levels of molecular targets within a living subject. Both techniques have deep penetration and enable whole body imaging of molecular targets and processes with high sensitivity [114]. To image a certain molecular target using SPECT a target has to be identified and a radiolabelled imaging agent that is specific and selective for the target of interest has to be available. A suitable radionuclide in terms of half-life has to be chemically bound to the imaging vector and finally, a nanomolar amount of the chosen radiolabelled agent is administered to the patient/subject, typically via an intravenous injection. The radioactivity is then traced through the body and its distribution determined from scans obtained with a SPECT camera [115, 116, 114].

1.2.1 Basic principles of SPECT

The basic principles and instrumentation of SPECT, assume an accumulation of the radiopharmaceutical at a targeted specific area (e.g. tumour) [117]. SPECT uses nuclides such as ^{99m}Tc ($t_{1/2}$=6 h), ^{123}I ($t_{1/2}$=13.3 h), and ^{111}In ($t_{1/2}$=2.8 days), which decay via the emission of single gamma rays with differing energies (Table 1.3). During the decay of the radionuclides γ-rays are emitted in all directions and some of the γ-rays are attenuated and scattered in the body due to the photoelectric interaction and the Compton scattering. The photoelectric effect is described as emitted electrons from solids, liquids or gases after the absorption of energy from electromagnetic radiation and the Compton scattering is the decrease of energy of an X-ray or γ-ray photon, when

it interacts with matter.

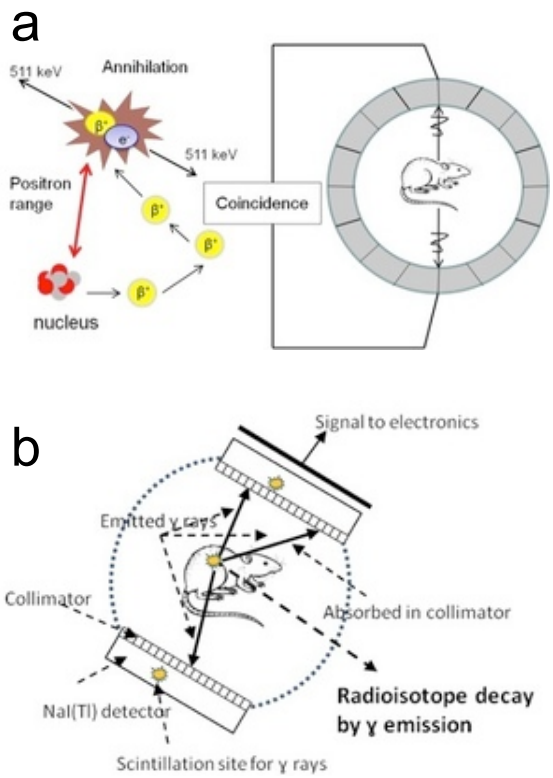

Figure 1.7: a) PET scans are acquired following administration of a radiotracer. The radiotracer accumulates in the target of interest, and its radionuclide decays by emission of a positron. A positron will collide with an electron, simultaneously releasing two gamma rays with energy of 511 keV into opposite directions. These two photons are detected by the PET camera and simultaneously localised within a fixed period of time by a series of opposing detectors, which correspond to multiple rings of scintillation crystals. By collecting a statistically significant number of radioactive events, mathematical algorithms reconstruct a three-dimensional image that shows the distribution of the positron-emitting molecules in the brain. b) Gamma-ray photons emitted from the internal distributed radiopharmaceutical penetrate through the animals or patient's body and are detected by a single or a set of collimated radiation detectors. Most of the detectors used in current SPECT systems are based on a single or multiple NaI(TI) scintillation detectors. In SPECT, projection data are acquired from different views around the animal/patient.

SPECT employs the use of a gamma camera that rotates around the subject to capture data on the emitting γ-rays from numerous positions to obtain a tomographic reconstruction. However, the position detection of the photons in SPECT does not deliver specific information about its origin or the direction it was travelling (Figure 1.7b).

The direction of the travelling photon is determined by adding a lead collimator that acts as a γ-ray lens between the source and the detector. This collimator rejects most of the photons not travelling along certain directions. As a result the direction can be determined but typical sensitivity of SPECT is several orders of magnitude lower than for PET systems described below [118, 114] depending on the collimator diameter. The collimator selects only those γ-rays that

Table 1.3: Common gamma-emitting radionuclides for SPECT imaging

Common gamma-emitting radionuclides for SPECT studies		
Radionuclide	Physical half-life	Energy (keV)
^{99m}Tc	6.02 h	140
^{111}In	2.8 days	171; 245
^{131}I	8.02 days	364
^{123}I	13.2 h	159
^{67}Ga	78.2 h	93

have an angle of 90°$\pm\alpha$ to the detector plane, the cone angle α being defined by diameter and length of the collimator. γ-rays with other angles are blocked; typically 1 out of 10000 emitted γ-rays is transmitted through the collimator. By modifying α, the resolution and sharpness can be increased or decreased. If the collimator is built of a narrow diameter it rejects most rays and if built with a larger diameter the origin of the γ-rays can only be determined imprecisely. New systems use up to nine distinguishing pinholes with different α and reconstruct an image resulting in increased signal and resolution.

Two-dimensional distribution of the activity is measured, where the intensity in each pixel represents the total number of emitted γ-rays that have passed the collimator stage. Three-dimensional imaging is performed, by rotating the γ-ray detector/camera around the body. The γ-rays that pass through the collimator are converted into a detectable signal using a photomultiplier. When the γ-ray hits the scintillation crystal, it loses energy through photoelectric and Compton interactions with the crystal. This photoelectric interactions result in the emission of light, the intensity of which is proportional to the energy of the γ-rays [119, 115]. The camera acquires several planar images from different view angles in a stop-and-go mode. Up to 120 pictures are acquired and a filtered back-projection algorithm is then applied to reconstruct a three-dimensional image of activity distribution within the body. Modern SPECT systems have an integrated X-ray CT, which provides anatomical information. The basic design of a γ-camera was described by [120] and there are three components: the collimator, the scintillation crystal and several photomultiplier tubes.

1.2.2 Basic principles of PET

Noninvasive positron emission tomography (PET) is another important nuclear imaging technique that is very similar in some aspects, but uses positron-emitting isotopes instead of single photon emitters. To image a certain molecular target using PET the radioactivity is traced through the body and its distribution determined from scans obtained with a PET camera. Radionuclides frequently used in PET include ^{18}F ($t_{1/2}$= 109.8 min), ^{64}Cu ($t_{1/2}$= 12.7 h), or ultra-short-lived

radionuclides such as ^{11}C ($t_{1/2}$= 20.3 min) [121, 122]. These radioactive isotopes decay via positron emission, otherwise known as beta-plus decay. Nuclei that decay in this manner have an excess of protons, making them unstable. This instability is rectified by transforming a proton into a neutron, a positron, and a neutrino. PET measures the coordinates of the annihilation of positrons emitted from the radioisotope injected into the body. Due to the conservation laws of energy and momentum, the combined mass of the positron and electron is converted into two photons, each with energy of 511 keV, travelling at opposite directions to one another, 180°apart [114, 123, 124]. The positron range effect poses a lower limit to the spatial resolution with PET, achievable without the use of sophisticated mathematical models [118, 125]. The average distance that a positron travels from its origin is small (∼0.5 mm or more depending on its energy) and has bi-exponential shape (Figure 1.7a) [126, 127].

PET detectors take the form of a closed ring, or set of rings, surrounding the subject to be imaged. These rings are designed to detect annihilation events (gamma-rays) and convert the resulting electrical signals into sinograms that are ultimately reconstructed into tomographic images, following dead time correction, detector normalisation, subtraction of random coincidences, attenuation correction, and scatter correction [128, 129]. The detector signals are processed by specialised coincidence circuitry and, if the difference in the time of arrival of these photons is smaller than a pre-determined value, then the two detectors define a line of response. This is the geometric region between the two detectors in which the annihilation photons were detected [118, 130, 114].

1.2.3 Alternative imaging modalities

Like SPECT, PET imaging instrumentation was originally developed for clinical applications and translated into small animal SPECT/CT and PET/CT, specifically designed for imaging small animals [118, 130–132].

Since biochemical changes generally occur before anatomical changes in disease, PET and SPECT have a clear diagnostic advantage over anatomical techniques such as classical CT and MRI. The initial lack of an anatomical reference frame in PET and SPECT was addressed by combining the systems with a CT (X-ray computed tomography) or recently introduced with MRI (Magnetic resonance imaging) [133, 134].

Pre-clinical MRI is generally performed using high-field systems, due to the signal-to-noise gains that can be achieved with larger magnetic fields. Such imaging systems are able to characterise both anatomical and functional information across the whole body. MRI is a highly versatile imaging modality [135] that uses a powerful magnet and radiofrequency (RF) energy to visualize the internal structure and soft tissue morphology of the body. The underlying principles of MRI allow imaging of atomic nuclei within the body. Nuclear particles (protons and neutrons) are in

constant motion and spin about their axes, which gives rise to angular momentum. Atoms with an equal number of protons and neutrons have a net angular momentum of zero, whereas atoms with an unequal number possess a specific spin angular momentum. Along with angular momentum, certain nuclei can also produce a small magnetic field (due to the mass, spin, and charge of protons). This magnetic field is termed magnetic moment and, like angular momentum, is a vector quantity. The ratio of angular momentum to magnetic moment is known as the gyromagnetic ratio and is unique for each magnetically active nucleus [136]. In general, an MRI scanner is comprised of a set of embedded coils: one coil that generates the main relatively homogeneous magnetic field; gradient coils that produce variations in the magnetic field in the X, Y, and Z directions that are used to localize the source of the MR signal; and finally RF coils that generate an RF pulse responsible for altering the alignment of the magnetic dipoles. After every RF pulse, the magnetic dipoles in the subject are tipped away from equilibrium and subsequently undergo two forms of relaxation back towards equilibrium. The contrast between different tissues in MR images is generated due to the different relaxation times of each tissue [longitudinal (T1) and transverse (T2) relaxation times]. For instance, proton nuclei in fat and hydrocarbon-rich environments have relatively short relaxation times compared with those in aqueous environments [137]. MRI has a number of important advantages compared with other imaging modalities including no need for ionizing radiation; unlimited depth of penetration; high spatial resolution (clinical: 1 mm compared with 5-7 mm for PET, preclinical: micrometers, as opposed to millimeter resolution achievable via optical and radionuclide imaging; unparalleled soft tissue contrast, superior to that attainable with CT; concurrent collection of physiological or metabolic data with high-resolution anatomical images, and even molecular information when used in conjunction with targeted MRI-compatible imaging agents. A major limitation of MRI is its extremely poor sensitivity compared with other molecular imaging modalities. This low sensitivity can lead to relatively long acquisition times, and in the case of physiological/molecular MRI, is the reason why large amounts of imaging agents are often required to obtain an adequate signal. These large amounts of imaging agents (i.e., many log orders higher compared with that needed for PET or SPECT) can be problematic due to the likelihood of altering the biological system of interest through pharmacological effects (generally proportional to the mass of agent administered). Toxicity issues associated with administrating large doses of MR imaging agents are also an important consideration. For this reason, MRI molecular imaging is sometimes thought to be more suited for targets within the vasculature, as then the imaging agent does not have to reach an extravascular target which would require a greater injected mass of imaging agent [138].

Clinical diagnostic ultrasound (US) scanners typically use sound frequencies between 1 and 20 MHz [139]. During a US study, a transducer (also called a probe) sends and receives sound waves. In simple terms, the transducer converts electrical signals to US waves, the US waves enter the body, and some sound waves are reflected back to the transducer where they are detected and

converted into electrical signals. These signals are then processed by a computer and displayed as an image. Resolution of US improves significantly with higher frequencies, but at the cost of depth of penetration. This decrease in depth of penetration is due to the fact that high- frequency sound waves possess shorter wavelengths, meaning they are more likely to interact with matter and slow down, thus reducing their travelling distance. Depending on the subject and on the required data, the imager needs to consider resolution versus depth. The main strengths of US include its relative cost effectiveness, wide availability, good temporal resolution, good safety profile (no ionizing radiation), and excellent sensitivity (picogram level) when microbubbles are used. On the other hand, US is limited by its difficulty in imaging structures that contain bone or air, due to the tendency of air and bone not to transmit sound waves and also by its limited depth of penetration.

Optical fluorescence and bioluminescence (BLI) imaging. The required infrastructure for optical fluorescence and bioluminescence imaging, namely, a charge-coupled device (CCD) camera and a source of filtered light, is relatively inexpensive and easy to setup. Imaging sensitivities achievable with these techniques are typically very good and since they involve the detection of low-energy photons, as opposed to high-energy gamma rays detected by PET and SPECT, they are considered relatively safe. However, the use of low-energy photons means that the depth of penetration is limited to only a few centimeters, which makes it virtually impossible to study deep tissues in large animals or human subjects, unless one uses endoscopes or their equivalent to get closer to the tissue(s) of interest. This limitation cannot be overcome by using a higher intensity laser due to the risk of overheating the tissue/system being studied [140]. Depth of penetration is not so much of a problem in mice and small animals (no bigger than a rabbit) due to their size. In fact, many of the commonly used fluorescent and bioluminescent imaging agents can be visualized in internal organ structures of small animals [140], making these optical imaging techniques suitable for preclinical research. BLI is one of the most extensively used technologies for assessing biological function in preclinical models of disease. The underlying mechanism of BLI is the enzymatic conversion of luciferins, in the presence of ATP and oxygen, resulting in the emission of light. The introduction of luciferase genes into non-expressing cells allows various biological functions to be assessed by the administration of a luciferin substrate. Different luciferase enzymes can be introduced into a biological system as a molecular reporting device. These enzymes are usually introduced into cells via transfection with the gene that encodes them. Unlike fluorescence imaging, bioluminescence does not need an external light source. Due to this, and because tissues do not exhibit endogenous bioluminescence, greater sensitivities and higher signal to background ratios can be achieved compared with fluorescence techniques. One of the main advantages of bioluminescence imaging compared with fluorescence imaging is its higher sensitivity due to enzymatic amplification of signal and low background signal due to the lack of natural bioluminescence from tissues (however, it should be noted that substrates themselves also lead to background signals). Although bioluminescence imaging has limited depth of penetration like fluorescence imaging, its

primary limitation is getting light out of the subject, whereas fluorescence imaging is limited by both the ability to pass light into and out of a subject. Its multiplexing capabilities, by combining different luciferases/substrates, make it a flexible and highly useful modality. The substrate requirements of bioluminescence may limit its clinical translatability [138].

1.2.4 Advantages and limitations of SPECT and PET

The combination of two or more different imaging modalities is called 'multimodality imaging' to compensate for weaknesses of each imaging system whilst exploiting their individual strengths [114]. Another limitation of radionuclide imaging techniques is the exposure of radiation workers and patients to ionising radiation. Consequently, there is a limit to how many scans a subject can have per year which needs to be considered when planning clinical and pre-clinical studies.

The key strengths of SPECT and PET include its excellent sensitivity (10^{-10} to 10^{-11} M for SPECT and 10^{-11} to 10^{-12} M for PET), good depth of penetration, and quantitation capabilities. Although, the spatial resolution is limited compared with MRI, it is extremely flexible in terms of the types of imaging agents that can be used to bind specific molecular targets. SPECT has, additionally, some multiplexing capabilities due to different nuclides giving rise to gamma rays with differing energies. While SPECT is less expensive and more widely available than PET, it is generally less sensitive and has a lower spatial resolution (8-10 mm, compared with 5-7 mm seen with clinical PET) [141]. PET has up to a 10-fold advantage over SPECT in terms of sensitivity [142, 143], SPECT on the other hand has the advantage of being capable of imaging two or more radionuclides of different energies simultaneously and has a wider range of radionuclides and linking chemistry available. In small animal models, SPECT has greater resolution [144, 145].

Unlike MRI and optical imaging techniques, both PET and SPECT only require small mass amounts of imaging agent (nanogram to milligram range). They are, therefore, used in tracer studies. A tracer study is performed using a sub-therapeutic amount of the proposed therapeutic biological attached with radiopharmaceutical, with subsequent serial imaging assessing uptake in tumour and critical normal organs such as liver, kidneys, bone marrow, and lung [146].

Overall, PET and SPECT are extremely valuable imaging modalities for investigating molecular processes in living intact subjects/patients [141, 114, 123].

1.2.5 Imaging in therapy and diagnosis of cancer

Imaging occupies a central position in the development and application of targeted cancer therapy. Very early on in the history of antibody-targeted therapy radioimmunoconjugates were field-tested. Starting in the 1950's radioiodinated polyclonal antibodies were used. However, it was not before the 1970's that scientists were able to locate human tumour with the help of radiolabelled antibodies used a in process called external scintigraphy or radioimmundetection (RAID). In the 1980's the

therapeutic activity of ^{131}I-labelled polyclonal anti-CEA IgG against human tumour xenografts was another milestone marking the introduction of radioimmunotherapy (RAIT) [26]. Since then a variety of antibody-based formats have been explored based around the IgG antibody and including different proteins based on single-chain variable fragment (scFV), the minimal component required for antigen binding. Today, imaging is used for a variety of tasks from patient selection, dosimetry and assessment response to imaging distribution of antibody targeted therapeutics.

When a targeting moiety delivers a therapeutic payload, imaging can potentially be used to identify deposits of tumour, decide on the most appropriate treatment strategy, confirm delivery of the therapeutic, measure the dose and function of the therapeutic delivered and to assess tumour response. In clinical drug development the advantage of imaging as a tool in drug development and first-in-man studies is the injection of a sub-therapeutic dose into patients. This dose is too small to have any effect, good or bad in the patient, but enables the researcher to validate targeting and initial therapeutic dosing.

The antibodies initially developed for imaging and therapy were intact IgG molecules with a molecular weight of 150 kDa. Mach et al. showed that in some cases only 0.0001-0.01% of the injected dose of full size antibody localises to a gram of tumour [142].

Dancey and colleagues suggested in their paper from 2009 that the standard approach in drug development until now was to establish a new capable mechanism of action with evidence of efficacy and lack of toxicity in a pre-clinical model [142, 147]. The starting dose for a clinical trial was then calculated or estimated taking the toxicity data into account at a 'no observed adverse effects level' (NOAEL) [148] with the addition of a safety factor. This procedure has been proven reasonably safe for small molecule 'off target' drugs. With the newer biological agents especially antibodies the toxicity comes from an 'on target' effect as was tragically illustrated by the TGN1412 trial of an agonist antibody to CD28 T-cell antigen [149, 150]. The message was that there is a need to study mechanism of action more thoroughly in animal model systems and in phase 0 clinical trials. Imaging studies are likely to play a crucial part in this process.

1.2.6 Imaging in pre-clinical drug development

Imaging in a pre-clinical setting has become a valuable tool in diagnostic and therapeutic drug development. In particular, the development and validation of biomarkers has the potential to accelerate research and transfer it into clinical exploitation in the future. Where imaging in first-in-man or phase 0 studies gives crucial information it comes short in biodistribution data because the injected quantity is usually in trace amounts. Information to predict efficacy and pharmacokinetics and biodistribution can be acquired in pre-clinical *in vivo* imaging studies using appropriate animal models. *In vivo* testing is a critical part of preclinical development because it offers the first evidence that the new agent has a superior anti-tumour effect in a whole animal, thus accounting for other

mechanisms impacting on cancer growth such as the stromal environment. It provides valuable animal pharmacokinetic and pharmacodynamics information that can be used to plan the starting dose and schedule of subsequent phase I studies [147].

Animal models have been an integral part of biomedical research in the study of drug development and disease processes [151]. In pre-clinical nuclear imaging radioactive tracers that rely on the application of a conjugated target specific molecule in very small concentrations were traditionally used, in combination with organ dissection and tissue counting, which still are a crucial part of pre-clinical evaluation [152]. Alternatively, whole-body cryosection followed by digital autoradiography [153] can provide anatomic images with good spatial resolution ($\sim$50 μm) correlated with quantitative measures of the tracer concentration. The disadvantage of these *ex vivo* methodologies is that only a single time point per animal can be sampled during an investigation. The lack of a method to study repeatedly the same animal model before, during, and after an intervention has been a significant limitation of these traditional investigative methods. Small animal PET and SPECT imaging instrumentation can achieve exactly these desired types of studies and results in one animal. Furthermore, pre-clinical PET and SPECT are able to give an answer to questions at a very early stage in regards to biological drug development in suitable projects with validation of biomarkers and quantification of response to therapy and proof of principle studies. It can also help to predict the clinical outcome or predict the efficacy ahead of time. For example, Dancey et al. reported a study in 2009 in which the maximum tolerated dose (MTD) was determined on the basis of imaging data [142]. While the ultimate goal is the clinical application, the advantage of pre-clinical animal experiments that include *in vivo* imaging techniques is aiding validation and the reduction of animals used in research [154].

1.2.7 Molecular imaging and imaging probes

Radionuclides used for imaging need to fulfil certain properties and are selected for every target and target environment individually to match appropriate therapeutic or diagnostic assignments. While some radionuclides such as iodine-131 emit both β and γ radiation and are therefore suitable for both imaging and therapy, others are more suited to imaging or therapy alone. For example, based on similar chemistry and distribution pre-clinical imaging for iodine-131 and yttrium-90, with half-lives of 8.02 days and 2.67 days respectively, can be performed with iodine-123 (half-life, 13.3 h) and indium-111 (half-life, 2.8 days). Other combinations include imaging with ^{99m}Tc and therapy with rhenium-186 [142]. Radiometals like indium-111 or technetium-99m are coupled with antibodies through a chelating agent. There are various chelating agents at hand with often differing affinities for various metals. This results in a vast possible combination of chelators and radiometals, in which the *in vivo* stability of one radiometal bound to a particular antibody-chelate conjugate might not be the same as another radiometal bound to the same conjugate. A

number of techniques have been developed for radiolabelling biomolecules, including antibodies, peptides and non-peptide receptor ligands. They are often classified into three main categories: direct labelling approach [155, 156], pre-labelling or preformed chelate approach, and post-labelling approach [157, 158]. Every labelling procedure has to be critically assessed to determine how much impact of the procedure and the isotope is made on the biological activity and functionality.

In direct labelling of an antibody, a radiometal is attached to a disulfide bond or a functional group of the antibody, such as tyrosine, lysine without any use of intervening spacer.

Radioiodination was one of the first methods to label antibodies with iodine-131 and iodine-125 [159, 160]. Iodine anions in aqueous solutions undergo an equilibrium reaction process in the presence of an oxidising agent to form reactive H_2OI^+ species that is capable of modifying the tyrosine side chains and imidazole groups of histidine. This reacts with chemically reactivated iodine [161, 155, 156].

The pre-labelling or pre-formed chelate approach involves as a first step the formation of a radio isotope-chelate complex, before in a second step this complex is conjugated to the biomolecule [162, 163]. Advantages are the better defined chemistry and the protection of the biomolecule from often harsh chemistry conditions.

In the indirect labelling approach, a bifunctional chelator (BFC) is attached to the biomolecule (BM) [158, 157]. In the second step the BFC-BM conjugate is prepared and a radio isotope can be attached by direct reduction in the presence of a sufficient amount of BFC-BM or by exchange with an intermediates. This approach combines the advantages of direct labelling with the defined chemistry of the pre-labelling approach. The latter approach is widely recommended in literature for kit formulation and product development, which is aimed for in this project.

1.3 Hypothesis and project overview

Previous studies have reported significant experimental support of the anti-tumour efficacy of IgE type antibodies. IgE may be comparable or even superior to its IgG counterpart [44, 58]. However, the mode of action of IgE in immunotherapy is still not well understood. This thesis and the overall project were based on the hypothesis that unique properties of IgE can trigger powerful immune responses focused on the ability to efficiently recruit immune effector cells with its high affinity receptor FcεRI and the low affinity receptor FcεRII. There is strong evidence that IgE class antibodies could be employed for passive immunotherapy of solid tumours [164, 165, 13]. Different studies form a part of a growing body of evidence suggesting that IgE antibodies may have a role in cancer therapy [41, 58, 165, 13, 42, 166, 35, 167, 168].

The overall project that consisted of 5 specific co-ordinated PhD projects was funded with the aim of translating IgE antibodies to a first in man (MOv18) IgE study and to develop a clinical concept for IgE treatment in cancer. The studies involved both the anti-folate, MOv18 antibody

and an anti-CSPG4 antibody, although only the MOv18 was initially to be taken through to clinical trial.

The results of this PhD thesis aim to contribute to the overall project and give a better understanding of the role of IgE and its immunological mechanism in cancer medicine.

The specific aim of this PhD thesis was to develop a method for radiolabelling IgE antibodies and to investigate the biodistribution, targeting and clearance of these novel diagnostic and therapeutic antibodies in pre-clinical imaging studies compared to their counterpart IgG antibodies.

It was important that, during the radiolabelling, full functionality of the antibodies was maintained. It was also important that the labelling method was readily translatable to the clinic in order to later be able to prepare labelled antibody to GMP standards for planned clinical studies using the MOv18 IgE antibody. This is, to our knowledge, the first time the biodistribution of a therapeutic IgE antibody was studied using preclinical imaging in a clinically relevant *in vivo* model.

2 Antibody conjugates: synthesis, *in vitro* radiolabelling, serum stability, antigen binding and functional assay

2.1 Introduction

This chapter describes the development of a radiolabelling method for IgE that is straightforward, easy to use and will therefore allow an easy translation into the clinical environment and would enable assessment of the IgE, in comparison with IgG, without the loss of affinity or functionality. This contributes to the overall aim for this thesis which is to compare the targeting, biodistribution and clearance of IgE in comparison to its IgG counterpart in animal models. In addition, the aim was to deliver important biodistribution and pharmacokinetic data to allow IgE class antibodies to be translated into a clinical setting for applications in humans as a potential anti-cancer therapeutic. Six different antibodies were used and are mentioned in this chapter. To avoid confusion and give more overview the six antibodies are summarised below together with a brief description and are defined by using a simple numbering system (1E/G-3E/G). All antibodies are referred to by their number throughout this chapter.

MOv18-IgG - Antibody number 1G: This antibody is a human/mouse chimeric IgG class antibody that targets the folate alpha receptor overexpressed on ovarian cancer cells among others. MOv18-IgG was available at the start of the thesis in large quantities and was primarily used to investigate different bifunctional chelates and other experiments where larger quantities of antibody had to be used.

MOv18-IgE - Antibody number 1E: This antibody is the IgE counterpart to MOv18-IgG. MOv18-IgE is also a human/mouse chimeric antibody and was engineered with the same variable region (Fv) as the MOv18-IgG against the FRα. This antibody was available in smaller quantities and used, for example, as an isotype control.

Rat MOv18-IgG - Antibody number 2G: This antibody was engineered as rat/mouse chimeric antibody. Like all MOv18 antibodies it has the same variable (Fv) mouse region against the FRα.

Rat MOv18-IgE - Antibody number 2E: This antibody was also engineered as rat/mouse chimeric antibody and is the IgE class counterpart to the rat MOv18-IgG. Both antibodies were only available in very small amounts and after radiolabelling used for biodistribution experiments.

Anti-CSPG4-IgG - Antibody number 3G: A human/mouse chimeric IgG class antibody against the chondroitin sulfate proteoglycan (encoded in humans by the CSPG4 gene).

Anti-CSPG4-IgE - Antibody number 3E: A human/mouse chimeric IgE class antibody against the chondroitin sulfate proteoglycan overexpressed on A375 melanoma cancer cells. Both antibodies anti-CSPG4-IgE and -IgG were engineered with only the constant (Fc) region different as the class-determining part. Both antibodies were available and used for radiolabelling, stability and functional tests before being used in *in vivo* studies.

To successfully use the radiolabelled IgG and IgE antibodies in NanoSPECT/CT and biodistribution studies a suitable radiolabelling method had to be found. Antibodies, after production and purification, can undergo degradation while stored and often lose their affinity partially or even completely if exposed to harsh conditions of temperature or pH. The process of conjugating a bifunctional chelator, whatever the method chosen, exposes the antibody to chemical and/or thermal treatment of some kind. The physical handling, for example centrifugation and/or filtering of protein and the storage, can also have direct or indirect negative impact on the structure and, therefore, on the affinity and functionality of the antibody. All antibodies, IgE and IgG, were conjugated to a bifunctional chelator and radiolabelled for later use in biodistribution and *in vivo* imaging studies and therefore had to be tested for a potential loss of affinity to the target receptor and contamination prior to and after conjugation with bifunctional chelators and subsequent radiolabelling. Furthermore, in the constant region of all IgG and IgE class antibodies receptor binding areas were located. It was important to preserve the affinity and functionality of the FcR binding region located within the Fc-region.

In this chapter the data are presented and discussed to show that the approach taken to conjugate and radiolabel the antibodies preserves full affinity and functional potency. Several conditions had to be fulfilled to make a later translation process as smooth as possible.

- The imaging chemistry must not interfere with the immunological properties of the antibodies.
- The antibody conjugate must be radiolabelled with high specific activity.
- The labelling method must be usable on site of the clinic without cost-intensive training or equipment.

2.1.1 IgE and IgG antibodies

This presents the opportunity to compare IgG and IgE class of antibodies *in vivo*, for the first time.

To compare antibody 3E to its IgG counterpart 3G, both antibody class types were constructed from the same Fv-region and therefore had the same affinity and specificity for the target CSPG4. The existing antibody 3G targeted against the melanoma-specific antigen (the chondroitin sulfate proteoglycan 4) was converted into IgE (antibody 3E) by cloning the existing antibody 3G variable (Fv) region into the vector for antibody 3E. For the antibody 3E, the heavy chains, as the antibody class-determining region, of antibody 3G was exchanged for IgE heavy chain as the heavy chain determines the antibody class. The cDNA for the IgE (antibody 3E) was derived from the protein sequences of the heavy and light chains variable regions from the existing V genes from antibody 3G (CSPG4-IgG) (Vector: pSGH-CSPG4 and pSGK-CSPG4). The heavy chain cDNA was synthesised based on the published protein sequence of antibody 1E (MOv18-IgE) in a pVITRO1 vector, containing the epsilon heavy chain of IgE (humighae2, accession no: L00022) and kappa light chain constant region cDNA (IGKC, accession no: BC110394). The antibody 1E (MOv18-IgE) stock used as an isotype control throughout the experiments was produced on an older pUC8 expression vector based cloning process [41]. Vector systems were based on two vectors, one for the mouse light chains and one for the human heavy chains. Vector, promoter and induction options were chosen with the main aim of a high production output. Disadvantages of these systems were higher production costs caused by two batches for each antibody and due to the slight overproduction of the light chain potential purification issues. For this project the genetic engineering of antibody vectors was performed by Tihomir Dodev at the laboratory and under supervision of Dr Andrew Beavil and Prof Hannah Gould in order to produce IgG class antibodies and IgE class antibodies. Antibody 3G (anti-CSPG4-IgG) was produced and purified by Tihomir Dodev and Andrew Beavil. Antibody 3E (anti-CSPG4-IgE) productions and purification was performed in collaboration with Tihomir Dodev and Panos Karagiannis. Antibodies 3G and 3E were produced, purified and supplied mainly by Panagiotis Karagiannis and Tihomir Dodev and on several occasions by myself at the laboratories and under supervision of Hanna Gould, Andrew Beavil, Frank Nestle and Sophia Karagiannis.

2.1.2 Radionuclide

To match the requirements for *in vivo* imaging and biodistribution of both IgG and IgE it was important to choose a suitable radionuclide. While IgG class antibodies have been the subject of numerous imaging and biodistribution studies in the past and suitable radionuclides are well-established [114, 169], the requirements for these studies involving IgE class antibodies were relatively unknown. It was understood that IgE has a much longer half-life in tissues than IgG, and

a much shorter half-life in serum, but the factors influencing the biodistribution and the way IgE would accumulate at the target site or its clearance were unknown at the outset of this project [47, 170].

Technetium-99m (^{99m}Tc) remains the most widely used radioisotope in nuclear medicine due to its optimal nuclear properties and easy availability at low cost. ^{99m}Tc has a half-life of 6.01 hours. The half-life gives enough time for most medical procedures while keeping the radiation exposure low for patients. ^{99m}Tc emits gamma rays at 140 keV in a single peak energy window that coincides with optimal imaging properties for detection in SPECT. In comparison to most other SPECT isotopes technetium-99m based imaging will result in a high contrast and image quality. However, for antibodies with long half-life (IgG in serum ∼20 days and IgE in tissue 14 days) the window for imaging provided by the half-life of ^{99m}Tc was considered too short. Gallium-68 is clinically used in form of gallium-68 citrate injection and more recently has had increased use in the somatostatin receptor imaging agent ^{68}Ga-DOTATATE [171–174]. It is used in PET/CT which was an imaging modality available for this project. The advantages of ^{68}Ga over other PET-based radionuclides are its availability from an in-house generator independent of an onsite cyclotron. The half-life of ^{68}Ga is 68 minutes. Eighty-nine percent of Ga-68 decays by emitting positron of 1.92 MeV and the rest 11% by electron capture. Several suitable bifunctional chelators have been developed, and coupled with biomolecules for gallium-68 labelling. DOTA, NODAGA and NOTA are commonly used bifunctional chelators. Many peptides/biomolecules like receptor peptides and antibodies have now been successfully modified by these chelating agents without compromising their functional properties which further widened the role of gallium-68 PET/CT imaging. These peptides/biomolecules show very fast target localisation and fast blood clearance thus, making the short half-life ideal for smaller biomolecules in clinical studies. In the last decade ^{68}Ga-DOTA-octreotides replaced ^{99m}Tc/^{111}In-DTPA-octroescan used for neuroendocrine tumour (NET) imaging [175]. However, the short half-life was seen as a disadvantage for imaging an IgE class antibody with an expected long half-life in tissue. Other radioisotopes that were considered because of at least partially fulfilling the requirements were, for example, zzirconium-89, copper-64 or iodine-131.

^{89}Zr has a half-life of 78.5 h with a beta emission (897 keV, 23%) and EC (77%). Due to its long half-life, it is an attractive isotope for radiolabelling of biomolecules over a prolonged period of time. It was at the time of the start of the project not available and was not considered. However, it is now available in the laboratory and would be considered because of its well-described bifunctional chelator chemistry and the for IgE antibody imaging attractive half-life.

^{64}Cu is another attractive isotope. The half-life (12.7 h) and decay properties (beta(+), 0.653 MeV, 17.8%; beta(-), 0.579 MeV, 38.4%; the remainder is electron capture) of ^{64}Cu make it a good choice as radioisotope for PET imaging and radiotherapy. The well-established coordination chemistry of copper allows for its reaction with a wide variety of chelator systems that can potentially

Table 2.1: Commonly used and for this thesis considered radioisotopes.

Isotope	t1/2 (h)	Production methods	Decay mode	E_γ (keV)	E_{β^-} (keV)
^{64}Cu	12.7	Accelerator , ^{67}Zn(n,p)	β- (38.4%) β+ (17.5%)	91, 93, 185	577, 484, 395
^{68}Ga	1.13	Cyclotron	EC+ β+ (100%)	91, 93, 185, 296, 388	
^{111}In	67.3	Cyclotron, ^{111}Cd(p,n)^{111}In	EC (100%)	245, 172	
^{99m}Tc	6.01	^{99m}Tc generator	Iγ (100%)	141	
^{89}Zr	78.41	^{89}Y(p,n)^{89}Zr or ^{89}Y(d,2n)^{89}Zr	β+ (23%), EC(77%)	897	
^{131}I	192.96	^{124}Te(p,2n)	β- (81%)	364	

be linked to antibodies, proteins, peptides, and other biologically relevant molecules. New chelators with greater *in vivo* stability, such as tetraazamacrocyclic 1,4,8,11-tetraazacyclotetradecane-1,4,8,11-tetraacetic acid (TETA), are now available and extensively covered in literature [176]. However, during the course of this project, copper-64 production was disrupted and availability was limited and at times unpredictable in quantities. Also, it seemed very difficult to obtain very high specific activity caused by the instability of the production process. Another reason for not considering copper-64 was the short half-life (12.7 h) compared to other available isotopes.

Iodine-131 has a half-life of 8.02 days. The half-life would have extended the imaging time and allowed biodistribution studies of antibodies over a much longer period than with other radioisotopes. However, ^{131}I emits both β and γ radiation and would have, similar to ^{64}Cu, made it difficult to distinguish between the potential imaging of a local therapeutic effect of IgE and β decay. In general, direct iodination of proteins occurs on tyrosyl or to lesser extent histidyl residues within a protein following electrophilic attack by a positive iodine species. The point of attachment is at the most electron-dense part of the ring i.e. at the ortho position in the tyrosine ring [177]. This method could have potentially ended in a greater loss of activity of the antibodies and more importantly loss of radiolabel *in vivo*.

^{111}In was eventually chosen as the radioisotope with the best compromise between available labelling methods, accessible chelators, half-life and imaging quality with regards to its energy windows and its availability. It is a cyclotron-produced isotope and has a half-life of 67.9 h (2.83 days). ^{111}In decays by electron capture with two γ-photon emissions at 173 and 247 keV (89% and 95% abundance, respectively), and has been widely used in gamma scintigraphy to investigate

antibody biodistribution. The half-life resulted in an imaging time frame of at least 5 days. indium-111 has a long history in the use of medical applications and made it reasonable choice for the development of an imaging-guided first in man study of IgE based anti-cancer therapy. Methods for labelling monoclonal antibodies using bifunctional chelators that can then be labelled with indium-111 have been developed [178–180] and tested in animal models [178, 181]. The advantages of ^{111}In-labelled antibodies include: (a) favourable energy for imaging; (b) a 2.8 day half-life allowing extended periods for imaging studies; (c) suitability for kit formulation; and (d) the stability of radiolabelled antibodies [181]. Several clinical trials with ^{111}In-labelled antibodies have shown excellent imaging results [182, 183].

2.1.3 Bifunctional chelator

To connect the radioisotope to the antibody a bifunctional chelating agent (BFC), which consists of a chelator to complex the radiometal and a functional group for attachment to the biomolecule, had to be chosen. Functional groups that form amide, thiourea, urea, Schiff base, or thioether linkages with amine or thiol groups on proteins and peptides have been described in literature [184–186]. There were two requirements for using in In(III) complexes: indium-111 had to be bound with high kinetic stability in biological conditions and the conjugation and radiolabelling process had to be straightforward, reproducible, high-yielding and robust. Indium is in group IIIB of the periodic table. Like gallium, under physiological conditions, the only stable aqueous indium oxidation state is +3, and this is the oxidation state relevant to radiopharmaceutical chemistry. ^{111}In has coordination numbers of 6, 7, and 8 depending on the ligand, and it also readily forms 9-coordinate complexes. The tripodal NS3 chelators, EDTA, DTPA, and DOTA all complex In(III) securely, as well as with high denticity. Differences in fundamental coordination preferences have significant consequences in their biological behaviour [187]. Popular acyclic chelators like EDTA and DTPA form very thermodynamically stable complexes with indium. The seven-coordinate ^{111}In-EDTA structure features a hexadentate chelator and approximates a pentagonal bi-pyramidal geometry with single water at an equatorial position. ^{111}In-DTPA structures feature both seven- and full eight-coordination by the chelator in distorted pentagonal-bi-pyramidal and square-anti-prismatic geometries, respectively. Well known mAb agents approved for clinical use that use DTPA to complex ^{111}In are for example ^{111}In-DTPA-B72.3 (OncoScint) and ^{111}In-DTPA-7E11.C5.3 (ProstaScint) [184–186]. A DTPA derivative with a trans-1,2-diaminocyclohexane backbone, p-SCN-CHX-A"-DTPA, was conjugated to a targeting peptide and antibodies, and found to be a viable ligand for ^{68}Ga, ^{86}Y, and ^{111}In radiometals for melanoma imaging (Wei et al., 2009). The versatile octadentate macrocyclic chelator DOTA has also been shown to form a robust complex with In(III) [188, 189].

The bifunctional chelator p-SCN-CHX-A"-DTPA was chosen over its non-backbone substi-

tuted DTPA derivative for the experiments because it features a preorganised DTPA analogue, CHX-A" (trans cyclohexyldiethylenetriaminepenta-acetic acid). Due in part to its overall acyclic structure, CHX-A" is even more capable of achieving rapid complex formation with a variety of radiometals at room temperature than DTPA without CHX-A" thus offering a distinct advantage over the macrocyclic chelator, DOTA, described below. In addition, p-SCN-CHX-A"-DTPA was developed to allow CHX-A" preorganised DTPA an optimised complexation of In(III), Lu(III), or Y(III). At the time of the experiments other backbone substituted DTPA derivatives, like MX-DTPA, were used in clinical setups but not commercially available. CHX-A"-DTPA was commercially available from Macrocyclics (USA).

Initially, DOTA-NHS ester was used as BFC because of its availability in large amounts for no cost in conjunction with other experiments in our laboratory not related to this project. The advantage of using DOTA-NHS ester as BFCs is the kinetic inertness of its radiometal chelates. However, the radiolabelling rate of DOTA-NHS ester is normally very slow, and more dependent on radiolabelling conditions, including DOTA-antibody (DOTA-Ab) concentration, pH, reaction temperature and heating time, buffering agent and buffer concentration, and presence of other metal ions, such as Fe(III). At room temperature, the radiolabelling yield of the DOTA-Ab conjugate is very low and heating at the elevated temperatures (>50°C) is needed for successful radiolabelling. The high temperature radiolabelling often causes a significant loss of immunoreactivity of radiolabelled antibodies.

2.1.4 Aims

The specific aim of this chapter was to produce and evaluate indium-111 radiolabelled antibodies within a set of constraints. It was aimed to develop a robust, reproducible and straight forward method of conjugation and radiolabelling anti-CSPG4-IgE and -IgG antibodies for the application of *in vivo* imaging and biodistribution studies. Importantly, the radiolabelling method had to be the same for anti-CSPG4-IgE and -IgG to successfully compare both antibodies *in vivo*. The conjugation and radiolabelling method had to be carried out in a way to preserve full affinity of IgE FcεR receptors and affinity of IgE and IgG to the target receptor FRα. This chapter describes the preparation and characterisation of the labelled antibodies using indium-111 as the radiolabel and p-SCN-CHX-A"-DTPA as the bifunctional chelator.

2.2 Materials and Methods

2.2.1 Stable expression of antibody 3G and 3E (anti-CSPG4-IgG and -IgE)

After exchange of variable- or constant-region domains within the dual antibody expression cassette in pVITRO1, stable cell lines were generated to support large-scale antibody production for

subsequent use in animal model studies. The mammalian cell line, FreeStyle™ 293-F cells (Life Technologies), a suspension culture cell line adapted to grow in serum-free conditions, was used for upscale antibody production. The FreeStyle™ 293-F cells were transfected and selected for 2 weeks with Hygromycin. Cells expressing anti-CSPG4 specific IgE or IgG were expanded into a 1 L shaker flask (Sigma), 1 L spinner bottle (Sigma) or 5 L WAVE bioreactor (GE Healthcare), producing 10 mg/L, 15 mg/L and 25 mg/L of respective antibody at 30 days post-transfection.

2.2.2 Purification of antibody 3G and 3E (anti-CSPG4-IgG and -IgE)

The anti-CSPG4 specific IgE isotype was purified by affinity chromatography using IgG4-Fc-(sFcεRIα)2 fusion protein. The anti-CSPG4-IgG isotype was purified by affinity chromatography with a 5mLHiTrap Protein-G HP column (GE Healthcare) using an ÄKTA Prime system (Amersham, Uppsala Sweden).

2.2.3 Expression of antibody 2G and 2E (rat MOv18-IgG and -IgE)

The rat MOv18 IgE and IgG2b were engineered as chimeric antibodies with rat constant domains and mouse variable domains specific for the human FRα. The rat IgG2b subclass was selected due to its reported equivalence to mouse IgG2a/b [190], which are the murine equivalent of human IgG1 in terms of their ability to efficiently activate the complement cascade, and to mediate ADCC [191].The antibody variable DNA sequence of MOv18 IgE specific for the epitope on the human FRα (determined and kindly provided by Dr H. Harries, Division of Asthma, Allergy and Lung Biology, King's College London) was combined with the rat immunoglobulin constant (Cε, Cγ2b and CK) DNA sequences for rat IgE and IgG2b. cDNA encoding the light and heavy chains of the rat MOv18 IgE and IgG2b antibodies were synthesised (GeneArt®). The heavy and light chains of each rat MOv18 antibody were then cloned into a single mammalian expression vector containing a hygromycin resistance gene (pVITRO1) generating pVITRO-Rat MOv18 IgE and pVITRO-Rat MOv18 IgG2b expression vectors (all cloning was performed by Mr. T Dodev, Division of Allergy, Asthma and Lung Biology, King's College London; all production was performed by Dr Debra Josephs, Cutaneous Medicine and Immunotherapy Unit, St John's Institute of Dermatology, Division of Genetics & Molecular Medicine, King's College London). Suspension FreeStyle™ 293-F cells were selected for the transfection of the pVITRO-Rat MOv18 IgE and pVITRO-Rat MOv18 Ig2b expression vectors. The cells were cultured under continuous selective pressure using hygromycin B in FreeStyle™ 293 Expression Medium. After 7 days in culture, antibiotic selection at 50 μg/mL hygromycin B killed the untransfected cells. To produce sufficient quantities of the surrogate rat antibodies for the subsequent extensive *in vivo* studies, vectors from selected cell lines were purified ans used to transfect new cell lines which could be frozen and stored and were stable in expression of the antibodies 2G and 2E. Therefore, the FreeStyle™ 293-F cells transfected with the pVIT-

RORat MOv18 IgE and IgG2b expression vectors were frozen in 10% DMSO at -80°C. After 1 month the cells were thawed, expanded under hygromycin B selection and incubated for antibody production. ELISA analysis of harvested supernatants 5 days after transfection with pVITRO-Rat MOv18 IgE and 5 days after thawing from frozen showed similar antibody expression levels.

2.2.4 Purification of antibody 2E (rat MOv18-IgE)

MEP HyperCel™ is a high capacity, high selectivity sorbent specifically designed for the purification of mAbs. MEP HyperCel™ principally operates by Hydrophobic Charge Induction Chromatography (HCIC). The functional ligand, 4-mercaptoethylpyridine (MEP) is Ig-selective and can bind a broad range of Ig isotypes and subclasses [192]. Binding to Ig is achieved principally through hydrophobic interactions at neutral pH, at which both the Ig and the pyridine group of the ligand are uncharged. As the pH is lowered, both the ligand and the Ig acquire positive charges, resulting in electrostatic repulsion and elution of the Ig [193]. The MEP HyperCel™ resin was packed into an XK26/20 column (GE Healthcare, 56 mL packed column volume) and equilibrated at a flow rate of 5 mL/min with PBS pH 7.0. A total volume of 2 L of culture supernatant (rat IgE concentration of approximately 10 mg/L) was loaded onto the column at a rate of 5 mL/min. After washing the column with sufficient quantities of PBS pH 7.0 to detect only baseline levels of UV 247 absorbance, elution of antibody with 25% isopropanol elution buffer was commenced, and a large elution peak with an elution proportion of 1.7% was detected. Subsequent analysis of the eluted fractions on SDS-PAGE revealed a strong band at the expected MW for rat IgE of 200 kDa. The total protein content of the eluted fractions, estimated by using a UV spectrophotometer at 280nm with percent solution extinction coefficient (A0.1%/280nm) for IgE of 1.62 [194], was approximately 15 mg, thereby indicating an antibody yield of 75%. HPLC-SEC was subsequently used to purify the eluting fraction using a Superdex™ 200 gel filtration column. Fractionation was performed as a final polishing step to isolate pure monomeric antibody from remaining contaminant proteins, antibody degradation products or aggregates according to size.

2.2.5 Purification of antibody 2G (rat MOv18-IgG)

Purification of rat MOv18 IgG2b from culture supernatants was performed using protein G affinity chromatography as previously described, with elution using 0.2 M glycine, pH 2.3 followed by immediate neutralisation with 1 M Tris pH 8.6 [195]. After neutralisation the antibody was dialysed against PBS pH 7.4.

2.2.6 Tissue culture and cell lines

All cells were maintained in a 5% CO_2 humidified incubator at 37°C.

HEK293E - Human Embryonic Kidney (HEK) 293, expressing the Epstein-Barr Virus nuclear

antigen-1 (EBNA-1) [196], were cultured in Dulbecco's Modified Eagles Media (DMEM), 10% FBS, 1% Penicillin-Streptomycin-Glutamine and 250 μg/mL G418 to maintain selection of transfected EBNA-1 plasmid, and kept between 1 - 9 x 10^5 cells/mL. 293-F Human Embryonic Kidney (HEK) 293-F Suspension FreeStyle™ cells (Life Technologies) were cultured in FreeStyle™ 293 Expression Medium.

U-937 - This non-adherent human monocyte-like cell line was kindly provided by Professor J.P. Kinet (Harvard University, Boston, MA, USA). Cells were maintained in RPMI 1640 media with standard additives at densities between 2x10^5 to 2x10^6 cells/mL. Where U937 cells were cultured in IL-4, this involved supplementation of the standard culture media with 320 U/mL recombinant human IL-4, four days prior to experiments. For ADCP/ADCC experiments CD23 was upregulated with 320 U/mLrecombinant IL-4 over 2 days. This protocol was established by Dr. Sophia Karagiannis.

A375 - Human Melanoma cell line, naturally expressing the chondroitin sulfate proteoglycan 4 (CSPG4) (CRL-1619, ATCC, Manassas, VA) was grown in DMEM supplemented with 10% FCS, 2 mM L-glutamine, penicillin (5000 U/mL) and streptomycin (100 μg/mL).

Passaging Adherent Cells: When cells were ∼80-90% confluent, the medium was removed from the flask and the cells washed once with 10mLPBS to remove excess medium and serum. A minimal amount of TrypLE™ Trypsin (Invitrogen) was used to coat the flask surface and incubated for 5 minutes at 37°C. The cells were observed under a microscope to confirm cell detachment. 10mLof fresh medium was added to stop trypsinisation. The solution was pipetted up and down to break up clumps of cells and 1mL(to split them at 1/10) was transferred to a new 75 cm^3 flask and 14mLfresh medium was added (with selection agent where required). Cells were incubated in a humidified, 37°C, 5% CO_2 incubator until 80-90% confluent and then passaged again. All tissue culture was performed under sterile conditions in a laminar flow hood. Cells were grown in a humidified atmosphere at 37°C in 5% CO_2. Culture media was specifically supplemented with FCS and 1% Penicillin/Streptomycin/Glutamin for every cell line. For storage aliquots of 7x10^6 cells in 1mL freezing medium (90% FCS, 10%DMSO) were prepared and kept in liquid nitrogen.

2.2.7 SDS-PAGE analysis of antibodies 1G and 1E (MOv18 IgG and IgE)

Antibodies were provided in PBS and the same buffer was used for further dilutions to a stock antibody solution of 1 mg/mL. 1 μL of stock solution was mixed with the NuPAGE lithium dodecyl sulfate (LDS) sample buffer (Invitrogen, Carlsbad, CA). It was then heated to 70°C for 10 min to denature the protein. For sample reduction, 3 μL of the NuPAGE reducing agent (0.5 M DTT in stabilised liquid form) was added prior to heating for 10 min at 37°C and loading the sample. For non-reducing conditions, the NuPAGE reducing agent was not included. The

acrylamide/bis-acrylamide 4-12% Bis-Tris gels (1.0 mm thickness) were purchased from Invitrogen and were pre-casted in 8x8 cm format. The NuPAGE MES SDS running buffer (Invitrogen) was used, which contains 2-(N-morpholino) ethane sulfonic acid. The voltage was 200 V (constant) and 120 A, with a total run time of approximately 35-45 min. Gels were then stained with SimplyBlue Safe Stain (Invitrogen, Paisley, UK) for 45 minutes followed by 3 washes with deionised water.

2.2.8 Conjugation and radiolabelling

Conjugation of antibody 1G (MOv18-IgG) with Bi-functional chelator DOTA-NHS ester

Metal ion free conditions were used to protect the bifunctional chelator (DOTA-NHS) from binding free metal ions. To achieve this, buffers were prepared using TraceSELECT® chemicals (Sigma Aldrich) and water for irrigation (Baxter). All buffers were pH adjusted using 2 M NaOH solution or 1 M HCl solution. The usual amount of antibody 1G used for conjugation with DOTA-NHS ester was 2 mg in 1mL(2 mg/mLstock solution). The antibody was supplied in PBS, pH 7.4. For the conjugation the calculated amount for a 1:20 antibody to chelate ratio of DOTA-NHS ester was mixed with DMSO at RT. The DOTA-NHS ester in DMSO was added instantly to the antibody 1G in PBS buffer. The conjugation reaction was transferred to a dialysis cassette (Thermo Scientific™ Slide-A-Lyzer™ Dialysis Cassettes, 20K MWCO) and dialysed over night at 4°C against phosphate buffer Na_2HPO_4 0.05M, pH 6.8. The next day the conjugation reaction mixture was transferred into a glass vial for radiolabelling.

Radiolabelling of DOTA conjugated antibody 1G with indium-111

A glass vial containing the DOTA-NHS conjugated MOv18-IgG (2mg/mL) was transferred into a heating block and set to a temperature of 40°C. 50 μL (3-8 MBq) of ^{111}In chloride solution (Covidien, UK) added to the radiolabelling reaction (the activity being higher or lower dependent on the reference date of the ^{111}In chloride solution). The reaction mixture was incubated for 1 hour at 40°C. After incubation, the reaction mixture was transferred into a Vivaspin™ ultracentrifugation tube and 1 mLof Na_2HPO_4 0.05M, pH 6.8 was added and centrifuged at 1,000-1,700g for 10-15 min so that the protein solution volume was reduced by a factor of 2-3. This step was repeated 2-3 times to wash excess indium-111 off. The radiolabelled antibody was transferred into a vial and samples were analysed by TLC and SEC HPLC for radiolabelling efficiency (TLC and HPLC methods described below).

Conjugation with Bi-functional chelator p-SCN-CHX-A"-DTPA

In general, free metal ions and especially free iron ions have always been a major source of contamination in conjugation and radiolabelling methods. Free iron ions can bind to freshly

conjugated chelators and block them during later radiolabelling with metal radionuclides. The conjugation method was based on the method described by Maggie S Cooper et al. in the Nature protocol publication 2006 [197].

For HEPES, the pH was adjusted with 1M NaOH and for ammonium acetate buffers, the pH was adjusted with acetic acid. All other buffers were pH adjusted using 2 M NaOH solution or 1 M HCl solution.

The minimum amount of protein used for conjugation with a bifunctional chelator was 2.5 mg (and up to 12 mg) in 1 to 6 mL. The solution was pipetted into the a Vivaspin™ centrifugal concentrator (Hydrosart membrane, 30,000 MWCO) and 50 μL of 50 mM EDTA in 0.1 M ammonium acetate was added for every 10 mg of protein to chelate free metal ions. The solution was left at room temperature for 30 min and then diluted 15 mLwith 0.1 M HEPES buffer, pH 8.5. The tube was subsequently centrifuged at 1,000-1,700g for 30-40 min so that the protein solution volume was reduced by a factor of 2-3. In the next step the ultrafiltrate (flow through <50kDa passing the membrane) was discarded and the above described steps were repeated for two or three times. Finally, the tube was spun until the volume fell to a level that corresponded to a protein concentration of about 10 mg/mLand pH was checked to be pH 8.5. The contents of the ultrafiltration tube were transferred to a metal-free plastic test tube (Nalgene, USA). Protein concentration was measured on a Nanodrop 2000c UV-spectrometer (Thermo Scientific, USA). The total molar amount of protein was calculated and the amount of p-SCN-CHX-A"-DTPA (Macrocyclics, USA) calculated to give a 20-fold molar excess over the protein. Initially, molar ratios added were between 5- and 40-fold excess of the antibody and it was found, in a series of experiments that quantified the chelator-to-antibody ratio and compared different chelate-to-antibody ratios in functional and FACS binding experiments, that a 20-fold excess gave optimal conjugation. A sufficient quantity of the chelator was dissolved in 100% dimethyl sulfoxide (DMSO) at a concentration of 50 mg/mL, such that the volume of DMSO was not more than 10% of the total protein solution volume, and added to the antibody solution. The solution was mixed immediately and incubated at 4°C overnight. The next day the reaction mixture was pipetted into a Vivaspin™ centrifugal concentrator and diluted to 15 mL with 0.1 M sodium phosphate buffer, pH 7.4. The tube was then spun in the centrifuge at 1,000-1,700g for 30-40 min. The centrifugation was repeated and after every centrifugation the absorbance in the ultrafiltrate was measured with the Nanodrop until measurement at 280 nm was zero (meaning that no more free chelating agent was being eliminated from the solution). After free chelating agent was cleared the ultrafiltrate was concentrated to a protein concentration of ∼2-5 mg/mL. The antibody conjugate was test labelled with ^{111}In chloride to ensure that all the excess ligand had been removed and that the radiolabelling was satisfactory. This is described below. If the radiolabelling efficiency was below 95% (as assessed by thin layer chromatography) then further wash steps, as outlined above, were carried out and the test radiolabelling repeated. If the labelling efficiency was satisfactory (>95%), the reaction

mixture was filtered with a 0.22 μm spin filter (Fisher Scientific).

Radiolabelling with indium-111

Typically, to 20 μL of CHX-A"-DTPA-mAb (2-5 mg/mL) was added 10 μL (3.7-7.4 MBq) of ^{111}In chloride solution (Covidien, UK). The reaction mixture was incubated at room temperature (RT) for at least 30 min and then labelling efficiency was assessed by thin layer chromatography (TLC) and high-performance liquid chromatography (HPLC). Adjustment of pH was not necessary for further analyses or *in vivo*/*in vitro* experiments. In preparation for *in vivo* injection, the radiolabelled antibody was diluted with 0.1 M sodium phosphate buffer, pH 7.4 to 150 μL total volume (total volume of injection per animal).

ITLC-SA: To determine the efficiency at which indium-111 associated with the protein in sample, 1 μL of radiolabelled sample was spotted at 10mm on a thin layer chromatography (ITLC) (10mm x 90 mm, ITLC-SA, Varian, UK). The mobile phase comprised of 0.1 M sodium citrate, pH 5 with 5 mM ethylenediaminetetraacetic acid (EDTA). The solvent front was allowed to run to 80 mm, and plates were analysed with a gamma-ray TLC scanner (Lablogic and Laura software). Radiolabelling efficiency was expressed as the radioactivity associated with radiolabelled protein peak integral (Rf=0) as a percentage of the total radioactivity on the strip. In this system, unincorporated indium-111 runs to the solvent front (Rf=1.0).

TLC on Silica 60F with aluminium back: At a time during the experiments the supply of Varian iTLC-SA paper ran out because of production stop. During this time iTLC-SA was replaced by a TLC utilising Silica 60F coated aluminium with a mobile phase of 0.2 M citric acid, pH 2. The labelling efficiency can be calculated in the same way as outlined above and is expressed as the radioactivity at the origin as a percentage of the total radioactivity on the strip.

High-performance liquid chromatography (HPLC): Binding of radioactivity to protein was also confirmed with analysis using an analytical size exclusion chromatography column on HPLC (Series 1200, Agilent, UK) equipped with an in-line gamma detector (Lablogic, UK) and according to manufacturer's instructions. For SEC-HPLC a 20 μL sample of the radiolabelling reaction mix was loaded onto a BioSep s3000 gel filtration column (BioSep 5 μm SEC-S 3000 LC Column 300 x 7.8 mm, Phenomenex, UK), which had been equilibrated with size exclusion buffer (PBS pH 7.4 and 2 mM EDTA). Size exclusion buffer was then passed at 1 mL/min and signals were detected in-line by a variable wavelength detector (Variable Wavelength Detector G1314B, Agilent Series 1200, Agilent, UK) and gamma detector. For reverse-phase HPLC a 5 μL sample of the radiolabelled conjugate was loaded onto a C18 column (Extend-C18 5um, 4.6 x 250mm, Agilent, UK) which had been equilibrated with reverse-phase buffer (5% methanol and 0.1% formic acid). Reverse-phase buffer was then

passed gradually at 0.5 mL/min with 5% methanol in water as the initial solvent, and 100% methanol as the final solvent. To both buffer ingredients, water and methanol, 0.1% formic acid was added. Signals were detected in-line by a variable wavelength detector (Variable Wavelength Detector G1314B, Agilent Series 1200, Agilent, UK) and gamma detector. Data were analysed using the software Laura (Laura, version 4.0.2.75, Lablogic, UK).

Phosphorimaging: Radiolabelled antibodies were analysed by reduced and non-reduced SDS PAGE (200 V, 120 A, 50 min). Gels were then stained with SimplyBlue Safe Stain (Invitrogen, Paisley, UK) for 45 minutes followed by 3 washes with deionised water. SDS PAGE gel samples were laid in contact with the phosphor screen in the exposure cassette for a predetermined period of 10-15 min. The exposed phosphor screen was of medium size and scanned with the Cyclone Plus phosphorimager (PerkinElmer, MA, USA). The image obtained was stored as a digital file with 300 DPI and analysed by the Optiquant software (PerkinElmer).

Competitive assay to determine the quantity of chelators per antibody

For this experiment 100 μg of the antibody were taken from a 4 mg/mLantibody solution (4 mg/mL = 25μL required). A 0.25 mM stock solution of carrier added ^{111}In was made up from no carrier added ^{111}In and indium (III) acetate standard solution (Sigma Aldrich, indium (III) acetate 10,000μg/mL solution). The 25 mM trace-labelled solution was made with 1 mL indium(III) standard solution combined with 5.787 g of water for irrigation in a metal free vial. 1.7 mL of the resulting indium solution was added to the entire contents of the ^{111}In vial. A 1:100 dilution was made of this 25mM stock solution using metal free buffer solution 0.1M ammonium acetate, pH5.9 to give a 0.25mM solution.

Vials were prepared with 10:1 indium(III) to antibody ratio. Into the vials 100 μg (25 μL) of antibody solution was added and combined with 26.7 μL of indium(III) (25μL, 6.7 x 10^{-10} moles). The vials were then made up to the volume of 100 μL using 0.1M ammonium acetate, pH 5.9 buffer. The indium/antibody mixture was then gently mixed and centrifuged. The vial was then left for 1 h incubation at RT. After incubation 10 μL of 50 mM EDTA solution was added and incubated for another 5 min at RT to chelate any unbound or non-specifically bound ^{111}In. Thin layer chromatography was carried out in triplicate for each vial using iTLC-SA. Strips (10 mm x 90 mm) were cut in half and radioactivity measured in each half of the strip in the gamma counter (Wallac, 1282 Compugamma). The percentage of radioactivity in each bottom half strip was calculated as this represents the activity bound to the antibody. Since a 10 molar excess of indium was added to each antibody dilution the number of chelators was calculated as % bound antibody. This experiment was repeated for antibody conjugates, which were previously conjugated with CHX-A"-DTPA in 5, 10, 20 and 40 times molar excess of chelator to antibody, to assess the number of chelates per antibody under these different conditions in order to optimise the conjugation methodology.

Stability of ^{111}In-Antibody conjugates in serum and phosphate buffered saline

10 μL of CHX-A"-DTPA conjugated and ^{111}In labelled antibody 3G, 3E or isotype control antibody 1E (2-5 mg/mL antibody radiolabelled with 10 μL (3.7-7.4 MBq of ^{111}In) were added to 5 mL AB type human serum (Sigma) or 5 mL 0.1 M PBS (Gibco) at 1:4 v/v and incubated at 37°C for 72 h. Samples were analysed at 0, 24, 36 and 72 h by HPLC-SEC using a BioSep SEC-300 column (Phenomenex, Macclesfield, UK) with an isocratic mobile phase of 100 mM phosphate buffer, 5 mM EDTA, pH 7.0, at a flow rate of 1 mL/min. Stability was calculated as the area under the antibody peak as a percentage of the total activity.

Antigen binding assays

To assess the antibody binding to the tumour-associated antigens FRα (MOv18) and CSPG4 and to FcεR (IgE) and FcγR (IgG) receptors on receptor-expressing cells, flow cytometric assays were used. For CSPG4 experiments, 2 x 10^5 U937 cells were used and for MOv18 experiments, 2 x 10^5 IGROV1 cells were used. Cells were incubated in triplicate in 12 x 75 mm FACS tubes (Falcon, Becton Dickinson) with 0.5 μg/mL of either the non-radiolabelled antibody conjugates (10 μg/mL IgE and IgG) or the unconjugated (native) antibody version of both (IgE and IgG) for 30 min at 4°C, followed by two washes in FACS buffer (PBS, 5% normal goat serum). Cells were then incubated with anti-human IgE-FITC or antihuman IgG-FITC (10 μg/mL) for 30 min at 4°C, washed in FACS buffer and fixed in 1% paraformaldehyde-FACS buffer prior to acquisition and analysis on a dual laser FACSCalibur™ (BD Biosciences). For quantitative assessments of Fcε and Fcγ cell surface receptors, cells were stained with mouse mAbs by indirect immunofluorescence using the QIFIKIT® (Dako). For analysis, a threshold was set on forward and side scatter plot to exclude cell debris. Fluorophores bound to cells were excited at 488 nm generated by an Argon laser. CFSE+ labelled cells were detected in the FL1 channel (530/30 nm band pass filter). PE-labelled (Phycoerythrin) effector cells were detected in the FL2 channel (585/42 nm band pass filter). PI (propidium iodide) was used to identify dead cells and was detected in FL3 channel (670 nm LP band pass filter). Photomultiplier voltages were set to place the CFSE-labelled cells within the third log decade of the FL1 channel and the first log decade of the FL2 channel. Based on this setting, a series of voltage and compensation adjustments were made using control tubes. Control tubes included live unstained cells, live PE+ effectors and live unstained cells with added secondary antibody against tumour cell line (488Alexa Fluor).

Functional assay (cytotoxicity/phagocytosis assay)

A flow cytometric assay was adopted previously by Bracher et al. to quantify killing induced by antibodies against tumour cells by monocytic effector cells [198]. The assay makes it possible to detect the proportion of cells which have been phagocytosed by effector cells and the ones which

have been killed by cell-mediated cytotoxicity. To distinguish between tumour cells and effector cells they are differently labelled: tumour cells were labelled with CFSE, effector cells were labelled with PE and dead cells were labelled with propidium iodide (PI). Tumour cells (U937 for CSPG4 and IGROV1 for MOv18) were incubated with CHX-A"-DTPA-antibody conjugates against the FRα on IGROV1 (antibodies 1G and 1E) and CSPG4 (antibodies 3G and 3E) receptor. Effector cells that had phagocytosed tumour cells showed a CFSE/PE double positive staining. Tumour cells were stained with CFSE one day prior to performing the assay. Cells were trypsinised and resuspended in serum-free medium, following another wash in RPMI 1640 medium free of phenol red and FCS. Cells were then counted with trypan blue to check cell viability and warmed at 37°C. After cell counting, 0.75 μL CFSE per 1x10^6 cells were added to the tumour cells. Cells were gently mixed and incubated at 37°C for ten minutes. Staining was stopped by washing with serum-enriched medium and cells were stored overnight in cell culture flask until used in the assay. For the assay, tumour cells were trypsinised, washed in culture media and re-suspended to a number of 100,000 cells/100 μL media. Effector cells were washed and re-suspended in different concentrations according to the effector cell: target cell ratio of 3:1 in aliquots of 100 μL media. Aliquots (100 μL) of each effector and target cell suspension were added and mixed in FACS tubes. Antibodies or PBS (control), were added at a defined concentration or volume and incubated at 37°C (5% CO_2) for 2.5 hours. After incubation, cells were washed once with 2 mL of ice cold FACS buffer. After washing, 4.5 μL of anti-CD89 PE per tube was added to stain effector cells for 30 minutes at 4°C. Staining was followed by one wash in 2 mL of FACS buffer and staining with 7.5 μL of PI at 10 μg/mL for 15 minutes, 4°C. Cells were than washed in ice-cold FACS buffer and re-suspended to 350 μL in FACS buffer for acquisition analysis on a FACSCalibur®. The analysis was set up as described by Bracher et al. using CellQuest® software on a FACSCalibur® flow cytometer [198]. Two dot plots were created to follow the acquisition of the events of each tube. The different conditions were performed in triplicate. The average number of events in the region R1 of the dot plot from the control tubes containing effector and target cells but no antibodies was evaluated and was used as 'R1 total events'. From this number the number of events in R1 of the test tubes was subtracted. If the value was positive it was added to the number of events in R3, divided into the 'R1 total events' and multiplied by 100. This value represents the percentage of target cell killed by cytotoxicity. The number of target cells killed by phagocytosis is calculated as follows: number of events in R2 divided into 'R1 total events' and multiplied by 100. R1 = number of CFSE+ tumour cells; control R1 = mean number of CFSE+ tumour cells from control tubes (n=3) given no antibody; X = (control R1 ï¿½ R1); R2 = number of PE+ tumour cells; R3 = number of CFSE/PE stained tumour cells.

3-colour functional flow cytometry assay

CFSE-labelled tumour cells were detected in FL1 (530/30 nm band pass filter), PE-labelled

monocytic effector cells in FL2 (582/42 nm band pass filter) and PI+ dead cells in FL3 (670 nm LP band pass filter) channels, whilst control samples were set for compensation adjustments between fluorochromes. Two dual colour flow cytometric dot plots were generated to calculate ADCC and ADCP as previously described [198, 13, 170]. Briefly, one dot plot depicted CFSE + tumour cells and PI + cells, allowing quantitation of tumour targets killed externally by effector cells (ADCC, cytotoxicity) (CFSE +/PI + cells). The second dot plot depicted CFSE + tumour cells and CD89-PE + effector cells in order to quantitate total CFSE + tumour cells and the number of tumour cells present within PE + effector cells, depicting phagocytosis (ADCP) by effector cells (CFSE +/PE + cells). This dot plot would also indicate any non-specific uptake of CFSE fluorescence by PE + U937 effector cells.

Confocal imaging of cell contact and antibody-mediated ADCC/ADCP

U937 monocytes, which served as effector cells, were incubated on Lab-Tec II glass chamber slides (SLS Ltd, Manchester, UK) with CFSE-labelled A375 tumour cells at an original effector cells:tumour cells ratio of 2:1. Mixed cell cultures were incubated for 3 h with antibody 3E. At the end of the incubations, cells were then given anti-CD33-APC for 40 min at 4°C, to label monocytic cells (U937). Cells were then washed, fixed in 4% paraformaldehyde-FACS buffer and mounted with fluorescence preserver (Dako). Fluorescence microscopy was performed on a Zeiss Axiovert 200 confocal microscope (63x oil immersion objective). Acquisition and analysis was performed with UltraView software (PerkinElmer, Waltham, MA, USA).

2.3 Results

2.3.1 SDS-PAGE prior to radiolabelling

SDS-Page was used to assess the quality of the samples of antibody 1G and 1E. Denatured and native folded proteins were differentiated by size using electrophoresis. Degradation products or contamination with foreign proteins of different size were made visible by protein staining of the SDS-Gel. IgE and IgG antibodies were loaded onto a pre-cast gel (Invitrogen) reduced and unreduced and in two different amounts. Dominant bands were expected and observed for the reduced IgE at 80 kDa and slightly lower than 30 kDa and a lighter band is present with the higher protein amount loaded at around 60 kDa. This result (Figure 2.1) is in accordance with the expected full size of the MOv18-IgE of 215 kDa. Bands are present at 50 kDa and 25 kDa for the reduced antibody 1G according to the full size of antibody 1G of 150 kDa. Unreduced antibody 1E loaded onto the gel appears in a prominent band between 160 and 260 kDa (approx. 215 kDa) with fainter bands observed at 160 kDa and 110 kDa. Unreduced antibody 1G shows a narrow double band at 150 kDa with faint bands at 80, 50, 25 kDa.

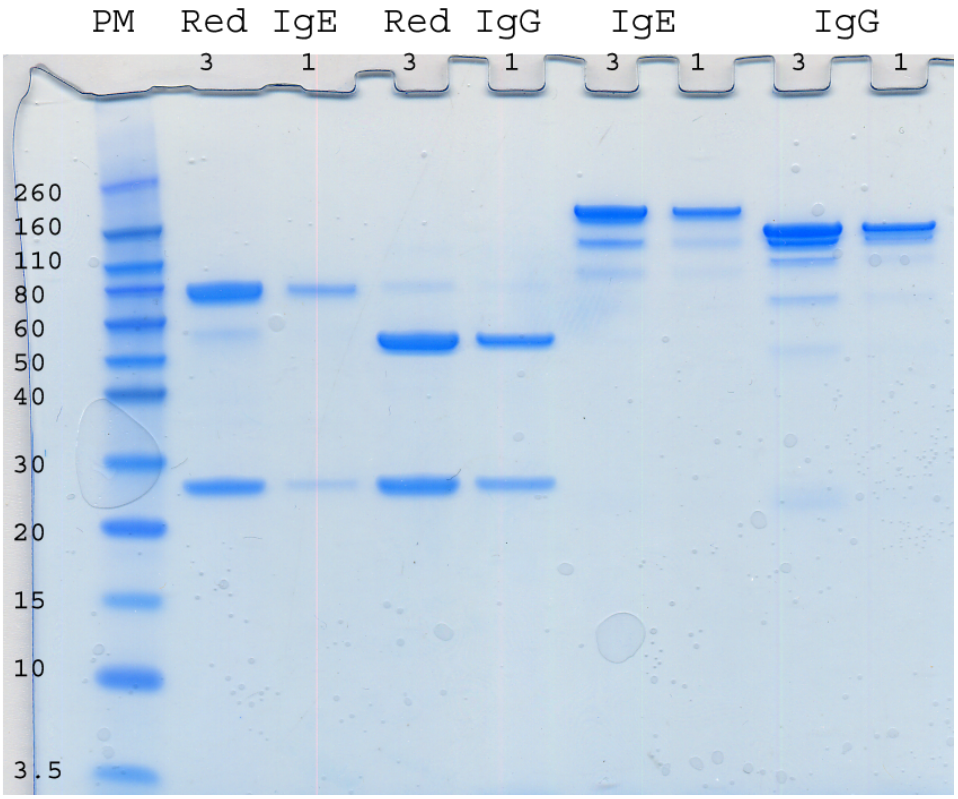

Figure 2.1: SDS-Page of antibody 1G and 1E (MOv18-IgG and -IgE) reduced (RED antibody volume per lane 3 μL and 3 μL concentration 1mg/mL) and unreduced (IgE and IgG). PM= protein marker (kDa).

2.3.2 Conjugation and radiolabelling analysis of antibody 1G with DOTA-NHS-ester

At the initial stage of the project different bifunctional chelators (BFC) were considered. First experiments were carried out with DOTA-NHS-ester chelates to assess feasibility in regards to stability and labelling efficiency. Conjugation of antibody 1G with DOTA-NHS-ester was carried out according to the methods described earlier. DOTA-NHS-ester is known to hydrolyse in aqueous solutions and hydrolysis of DOTA-NHS-ester was observed on quality control assays, ITLC and C18 column with HPLC. The results showed a high level of hydrolysis of DOTA-NHS-ester and a low labelling efficiency. DOTA-NHS-ester was assessed and final evaluation resulted in the rejection of DOTA-NHS-ester in favour of p-SCN-CHX-A"-DTPA.

Thin layer chromatography showed >96% labelling efficiency (Figure 2.2) with <4% detected DOTA:indium-111 complex. The iTLC was carried out after the BFC was mixed with the antibody at 40°C for at least 40 min.

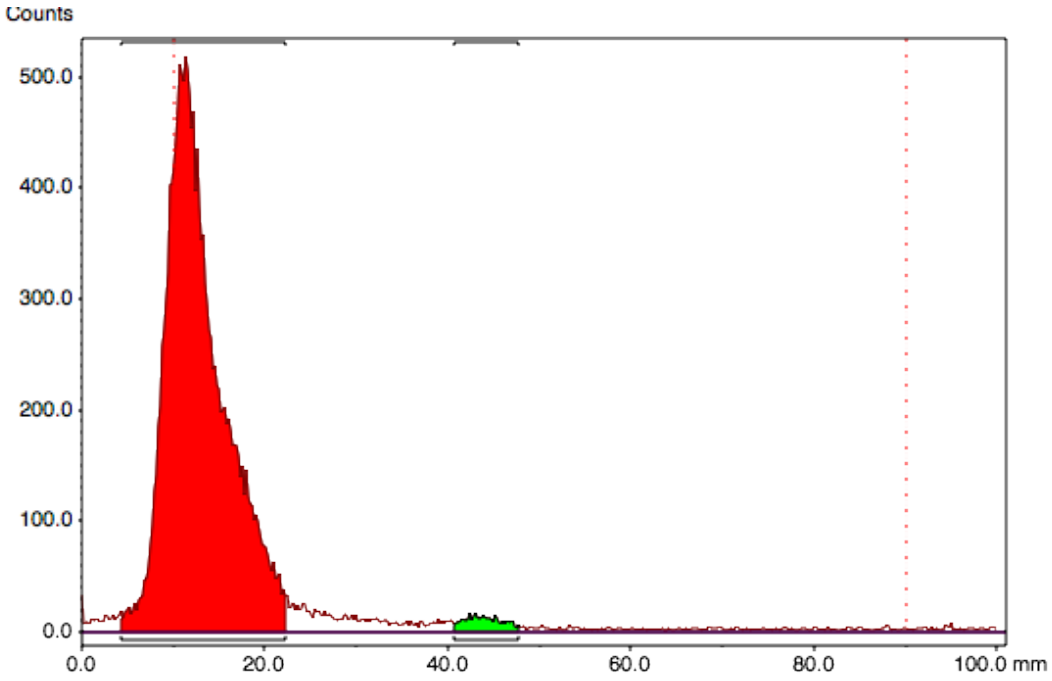

Figure 2.2: Thin layer chromatography of indium-111 labelled DOTA-antibody 1G. Red peak shows radiolabelled protein, green peak shows free indium-111:DOTA complex. Area under the peaks shows a labelling efficiency of >96%.

Reverse-phase HPLC of DOTA-NHS-ester

Further evaluation of DOTA-NHS-ester BFC in buffer was performed using a reverse-phase C18-HPLC. Products observed were DOTA (red peak, Figure 2.3) and DOTA-NHS-ester (green peak, Figure 2.3). Both products showed a distinct retention time 1:50 min and 2:20 min, respectively, on the reverse phase column on the HPLC. Figure 2.3 A and B show the degree of hydrolysis of DOTA-NHS-ester after contact with aqueous buffer solutions (UV detection). HPLC reverse phase analyses started 5 min after DOTA-NHS-ester was dissolved in DMSO and mixed

with H_2O. Measurements were carried out repeatedly throughout the 120 min. Figure 2.3 A and B show changes in hydrolysis after 120 min.

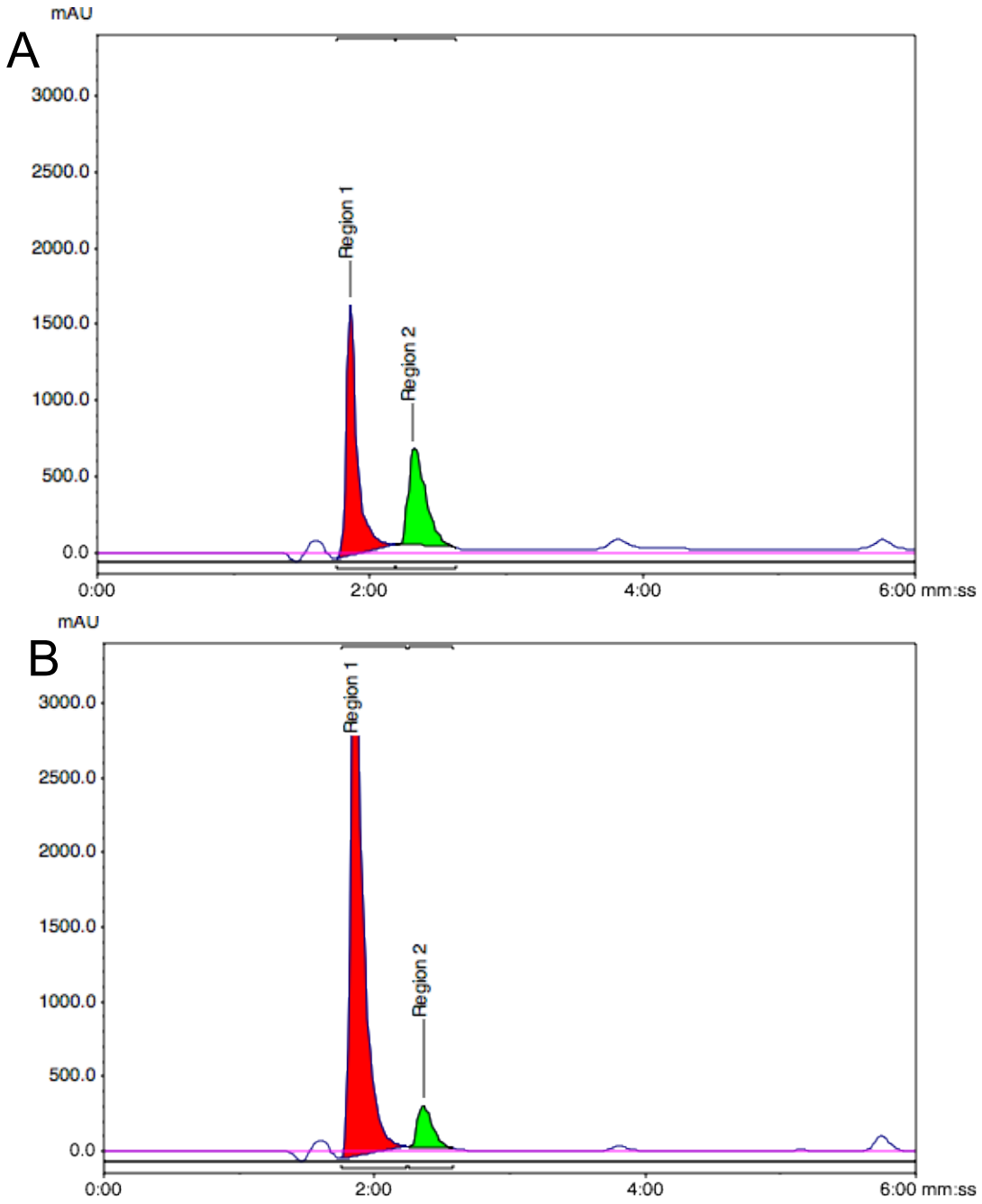

Figure 2.3: A. HPLC C18 column UV-detection profile of DOTA-NHS-ester after solution in water. DOTA-NHS-ester 5 min after solution in water. B. The second figure shows the hydrolysis process 120 min after solution in water. Retention time (RT) for DOTA=1:50 min and for DOTA-Nhs-ester=2:20 min. The region 2 (green) shows DOTA-NHS-ester region 1 (red) shows hydrolised DOTA.

The hydrolysis process progresses at a linear rate within 105 min after dissolving in aqueous solution (Figure 2.4). One example is the hydrolysis of DOTA-NHS-esters. For radiolabelling antibody 1G with ^{111}In DOTA-NHS-ester was used with a ratio of 1:20 of antibody to chelate. To analyse the conjugation of antibody 1G with DOTA-NHS ester the antibody was radiolabelled with indium-111. After radiolabelling the labelling efficiency was assessed by TLC and size exclusion

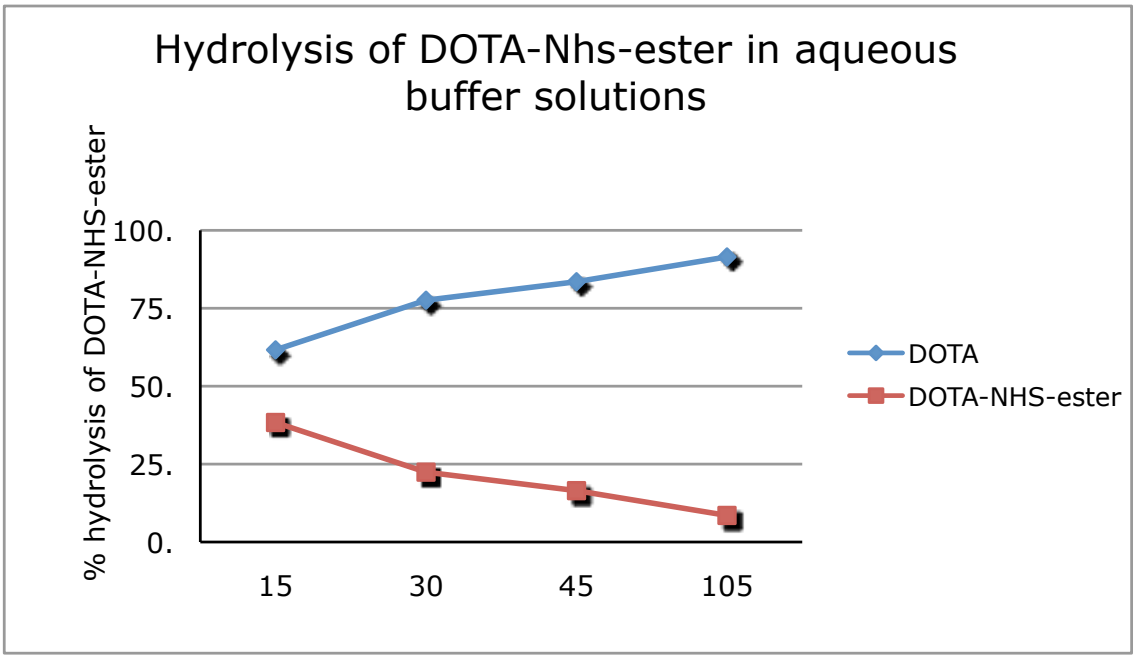

Figure 2.4: Hydrolysis of DOTA-NHS-ester in % over the time course of 105 min. After 15 min 60% of the DOTA derivatives were hydrolised, after 105 min 90% of DOTA-NHS-ester was hydrolised. HPLC measurement by γ detection of indium-111

HPLC. To remove hydrolised DOTA chelate and excess DOTA-NHS-ester, antibody 1G conjugated with DOTA-NHS-ester was purified by PD-10 desalting columns before it was radiolabelled with ^{111}In. It was then analysed with HPLC using a size exclusion column appropriate for the size of the molecule (Figure 2.5).

EDTA was added to the HPLC mobile phase to prevent potentially free ^{111}In binding to the column. The results of the HPLC show a labelling efficiency of >76% and an EDTA: indium-111 complex of <6%. In addition a peak of a small molecule, indicating a small protein fraction with high UV absorption, showed a radiolabelling of <20% (Figure 2.5). The labelling efficiency could have been improved by a purification step after the radiolabelling incubation to remove free indium-111. But it was not possible to reach a high specific activity after repeated conjugation attempts with DOTA-NHS-ester chelates.

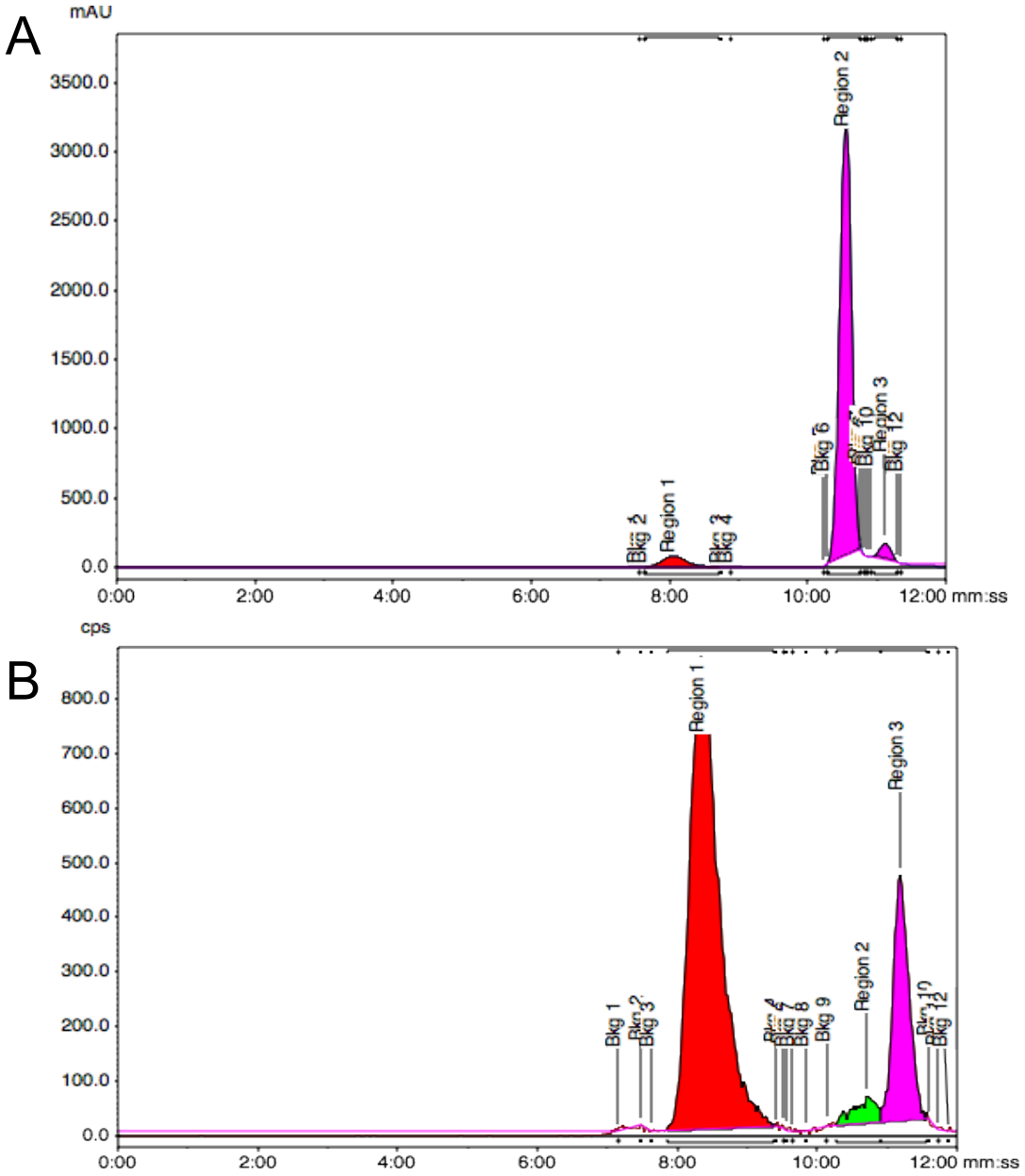

Figure 2.5: Top figure shows UV-detection of the ^{111}In labelled antibody 1G conjugated with DOTA-NHS ester in a HPLC using a BioSep 3000 size exclusion column (Phenomenex) and 0.1 M sodium phosphate buffer, pH 7.4 with 10 mM EDTA added. Antibody 1G=red peak (region 1), RT=8:15 min. Violet peak (region 2) at RT=10:50 eluted as EDTA: indium-111 complex. The pink peak (region 3) is indicating a radiolabelled protein, possibly a degradation product of antibody 1G. Bottom figure shows the parallel monitored gamma detection. Red peak (region 1) shows the detection of the radiolabelled antibody at RT= 9 min, green peak shows the detection of free EDTA: indium-111 complex at RT=10:30 min and pink peak shows a small protein fragment.

FACS of DOTA-NHS ester conjugated antibody 1G

The flow cytometric assay compares the binding to the antigen receptor FRα on IGROV1 cells of conjugated and unconjugated antibody 1G. It was done to confirm that the conjugated antibody's ability to bind to the target receptor (FRα) was not affected by the conjugation. The FACS binding assay was performed on folate receptor alpha (FRα) overexpressing IGROV-1 tumour cells. IGROV-1 cells are known to down-regulate expression levels of FRα after several cell passages. At the time IGROV-1 cells available were not selected and sorted for high expression of FRα. The heterogenic FRα expression levels resulted in broader peaks (Figure 2.6). Binding of DOTA conjugated antibody 1G and binding of unconjugated (native) antibody 1G was therefore detected only partially (Figure 2.6), blue= DOTA-NHS-ester conjugated MOv18-IgG and green line unconjugated MOv18-IgG). The fluorescent signal excited by the FACS laser and picked up by the detector originates from a secondary antibody which has a fluorophore of a specific wave length attached. Secondary antibodies were used to bind the human heavy chain of the chimeric antibody 1G.

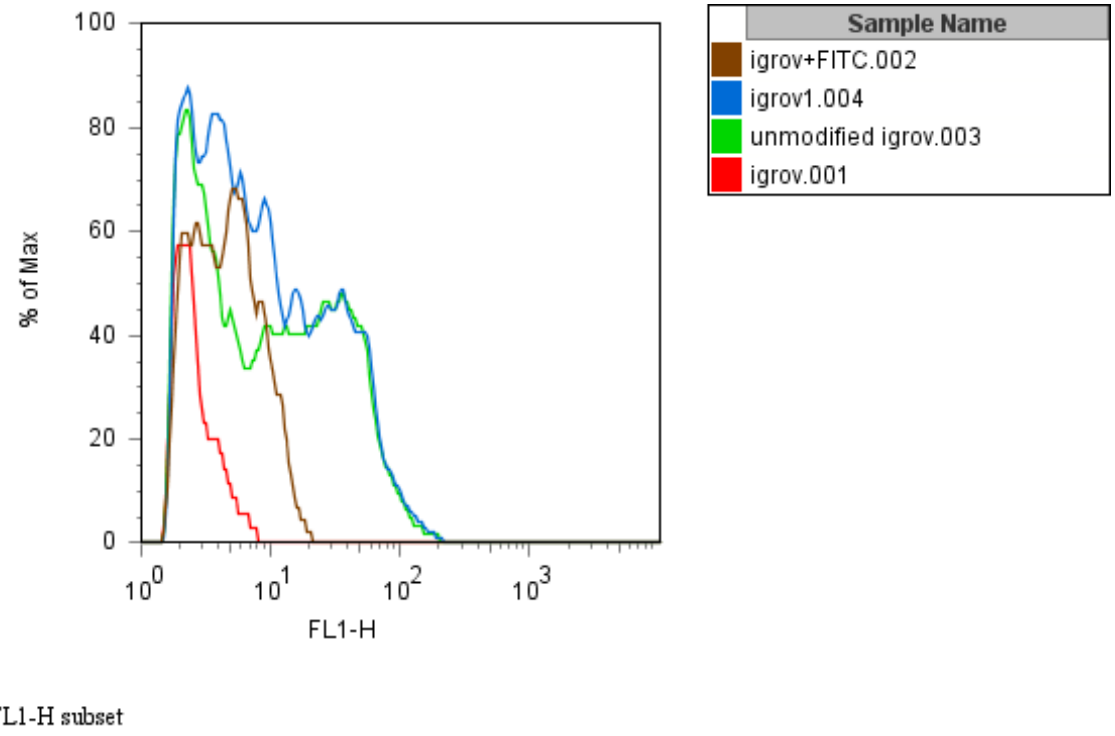

Figure 2.6: FACS binding assay on folate receptor alpha overexpressing IGROV-1 cell line. Red= IGROV1 cells; brown=control IGROV1+ secondary AB with fluorescence marker attached; green=IGROV1+MOv18-IgG unconjugated; blue=IGROV1+DOTA-NHS-ester conjugated MOv18-IgG.

2.3.3 Radiolabelling of antibodies 1G and 1E conjugated to p-SCN-CHX-A"-DTPA

SEC radioHPLC was used for quality control throughout the experiments to make sure radiolabelling efficiency was at an optimum and ensure that a purification step could be avoided. SEC radioHPLC showed three peaks with $>$ 95% of activity eluted at 8.4 min for IgG (Figure 2.9) and 8.3 min for IgE (Figure 2.7), corresponding to antibody fraction, and a proportion ($<$ 3%) eluted at 12 min of a complex of free ^{111}In with EDTA. In most analyses a small peak of up to 2% activity eluted at 7.6 min for IgG and 7.4 min for IgE corresponding to aggregated antibody (see Figure 2.3 and 2.5). In figure 2.7 free indium-111 eluted at 12 min compared to figure 2.9 with 10.5 min. The reason was that for cMOv18-IgE a guard column was used to protect the HPLC column and this changed the elution time for ^{111}In-EDTA. Figures 2.8 and 2.10 show the corresponding TLCs for antibodies 1E and 1G. The TLC control with free indium can be found in figure 2.11.

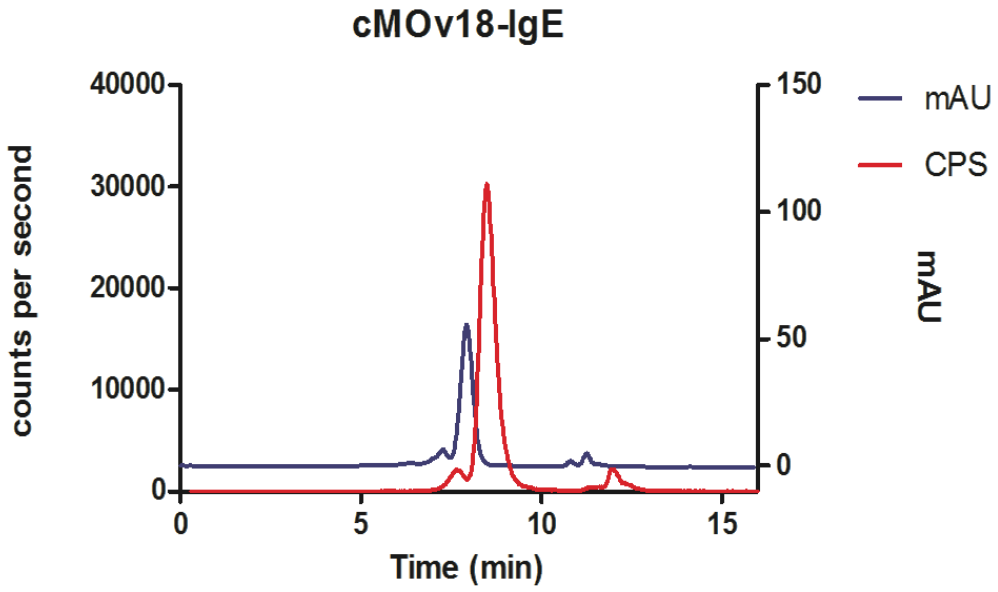

Figure 2.7: Size exclusion HPLC of radiolabelled antibody 1E following conjugation with p-SCN-CHX-A"-DTPA. Antibody 1E was radiolabelled with indium-111. Figure shows UV-detection at 280nm (blue) and gamma ray detection (red) over time course of 16 minutes. Activity is mainly eluted with the antibody (t= 8.3 min, $>$96%) with a small peak showing aggregated antibody at 7.4 min ($<$2%). Free indium-111 complex with EDTA is eluted in a small peak ($<$2%) at 12 min.

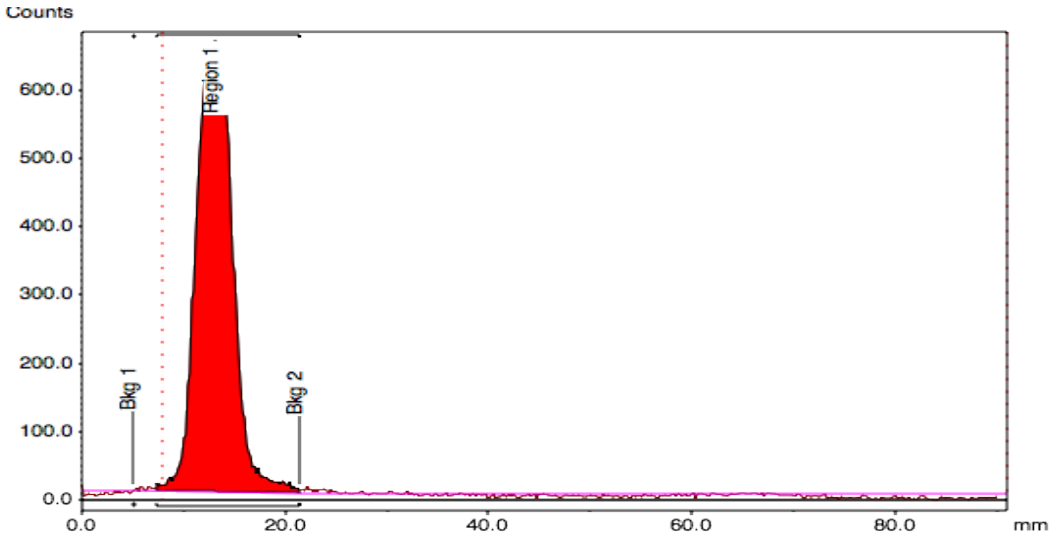

Figure 2.8: ^{111}In-CHX-A"-DTPA- MOv18-IgE; TLC on Silica 60F with aluminium back; mobile phase: 0.2 M citric acid, pH 2.

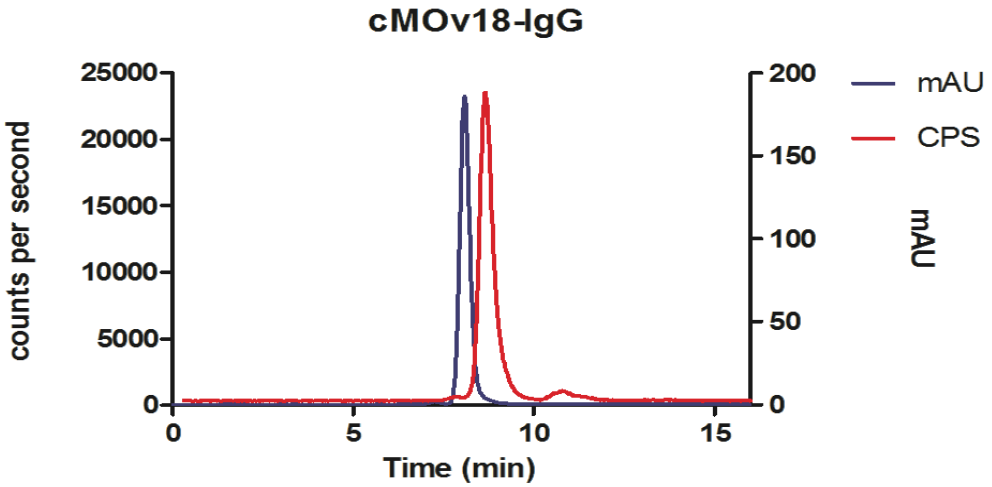

Figure 2.9: Size exclusion HPLC of radiolabelled antibody 1G. Following conjugation with p-SCN-CHX-A"-DTPA antibody 1G was radiolabelled with indium-111. Figure shows UV-detection at 280nm (blue) and gamma ray detection (red) over time course of 16 minutes. Activity is mainly eluted with the antibody (t= 8.3 min, >95%). Aggregation is below 1% (t=7.6 min) and free indium-111 is below 4% (t=10.5 min).

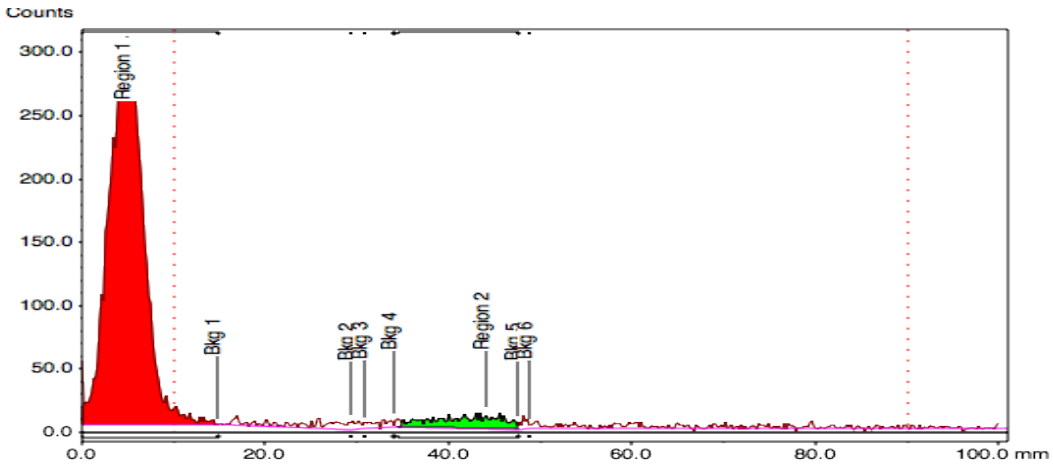

Figure 2.10: TLC of conjugated and radiolabelled antibody 1G. TLC on Silica 60F with aluminium back; mobile phase: 0.2 M citric acid, pH 2. Region 1 shows radioactivity associated with the protein. Region 2 shows free radioactivity in complex with EDTA.

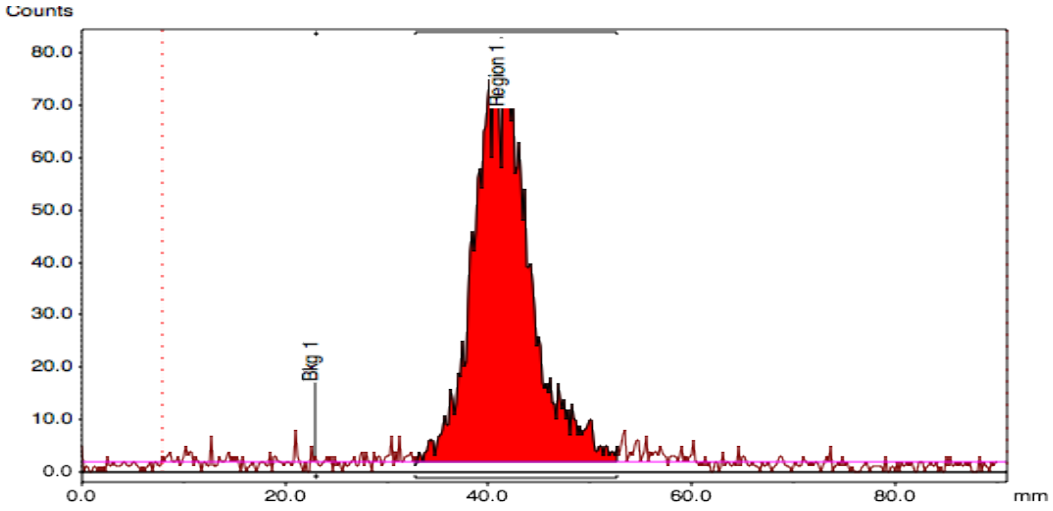

Figure 2.11: TLC control with free indium-111. Region 1(red): ^{111}In: EDTA complex, y-axis: gamma counts; x-axis distance (mm) moved with the mobile phase on TLC strip (10mmx 90mm).TLC on Silica 60F aluminium back; mobile phase: 0.2 M citric acid, pH 2 with 10mM EDTA.

2.3.4 Radiolabelling of antibodies 2G and 2E conjugated to p-SCN-CHX-A"-DTPA

Radiochemical purity and yield were assessed by SEC radioHPLC. SEC radioHPLC of antibody 2E showed two peaks at > 96% of activity eluted at 8.3 min, corresponding to antibody fraction, and a proportion (< 4%) eluted at 12 min of free indium-111 (Figure 2.12). Antibody 2G (Figure 2.13) showed a labelling efficiency of 84% with some degradation products. Radiolabelling efficiency itself was excellent with only 2% free indium-111. It was identified that a significant fraction (>9%) of antibody showed accelerated degradation in storage specific to rat antibodies and resolved with an added purification step prior to the conjugation and radiolabelling. The purification step was added for antibody 2G and 2E.

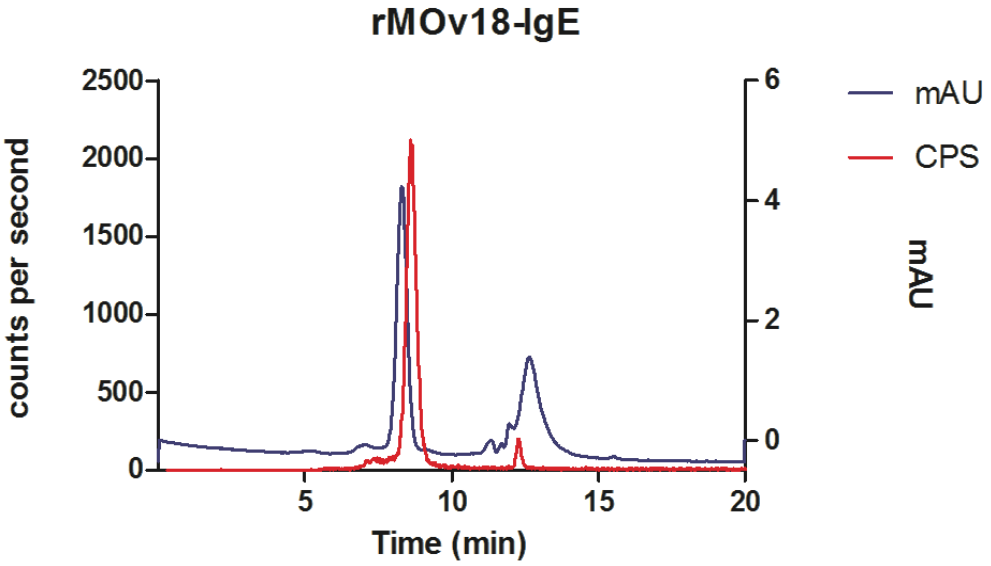

Figure 2.12: Size exclusion HPLC of radiolabelled rMOv18-IgE, mobile phase 0.2M sodium citrate, pH 7.4 with 10mM EDTA added. Following conjugation with p-SCN-CHX-A"-DTPA rMOv18-IgE was radiolabelled with indium-111. Figure shows UV-detection at 280nm (blue) and gamma ray detection (red) over time course of 16 minutes. Activity is mainly eluted with the antibody (t= 8.3 min, >96%). 2nd peak (t=12 min) is free indium-111 complexed with EDTA, <4% radioactivity.

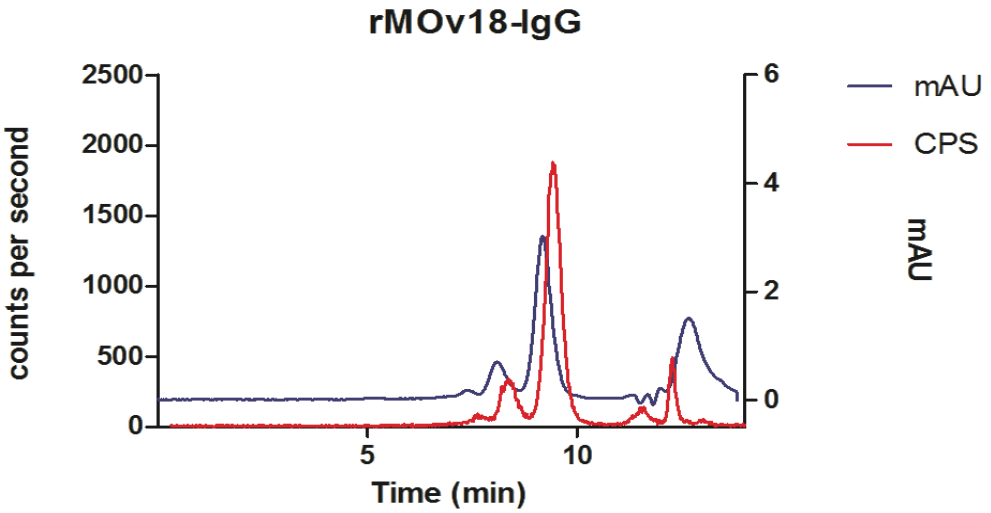

Figure 2.13: Size exclusion HPLC (mobile phase: 0.2M sodium citrate, pH 7.4 + 10mM EDTA) of radiolabelled rMOv18-IgG. Following conjugation with p-SCN-CHX-A"-DTPA rMOv18-IgG was radiolabelled with indium-111. Figure shows UV-detection at 280nm (blue) and gamma ray detection (red) over time course of 16 minutes. Activity is mainly eluted with the antibody (t= 9 min, >84%). Aggregated antibody (t=7.1 min) was observed with <9%. 3rd peak (t=12 min) was free indium-111 in complex with EDTA at <2%. Along with the free indium-111 peak a 4th peak of degraded antibody material elutes at 13 min (<5%).

Phosphor imaging on SDS-PAGE of ^{111}In labelled antibody 1E

The phosphor imaging technique was used for evaluation of the radiolabelling because of its sensitivity by relying on high energy particle decay. Phosphor imaging was able to detect radioactivity in case it was bound to contaminating products not seen on SDS-Gel-PAGE when dyed with a visual marker. For further validation of radiolabelling with indium-111, a Western blot was performed and from this blot a phosphor imager was used to show co-localisation of antibodies and ^{111}In. Thus, not only showing the association of the radionuclide to the antibody but also showing if any radioactivity was bound to a contaminant. Furthermore, in a reduced state of the antibody it was possible to determine that most of the radioactivity is associated with the heavy chain or the light chain of the antibody. IgE was loaded onto the gels in a reduced (Figure 2.14), right line reduced and left line non-reduced) and unreduced state. It shows that ^{111}In is completely associated with the antibody. The reduced antibody gel shows that most radioactivity was bound to the Fc-part of the antibody.

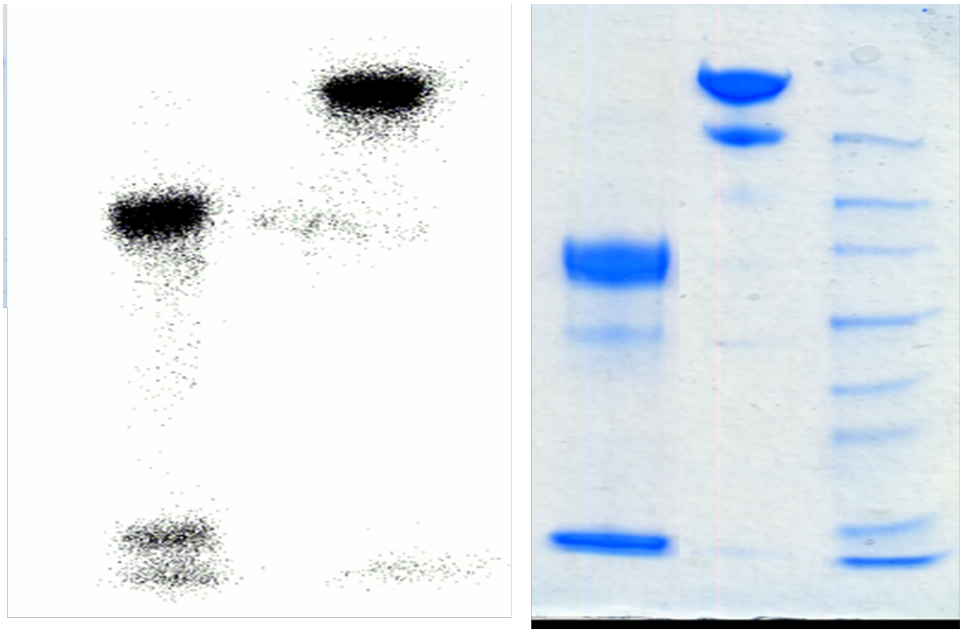

Figure 2.14: Autoradiography of gel electrophoresis of indium-111 radiolabelled MOv18-IgE. Left: Autoradiography of reduced (left lane) and non-reduced (right lane) MOv18-IgE. Right: Picture of the SDS-PAGE Gel (Precision Gel, Thermo Fisher).

2.3.5 Study to assess the best chelate-to-antibody ratio on antibody 1G

To investigate the ideal amount of chelator to use for the conjugation reaction to give a conjugate that could be labelled with high specific activity while not affecting its functionality, an experiment was performed. An increasing ratio of bifunctional chelator to antibody was added in conjugation reactions and then the ratio of chelator to antibody in the antibody conjugate was determined [199]. A further study was conducted to assess functionality using FACS. Conjugates were prepared using 5:1, 10:1, 20:1 and 40:1 ratios of chelator (p-SCN-CHX-A"-DTPA) over antibody. Each conjugate was then radiolabelled with ^{111}In-chloride to determine radiolabelling efficiency (Figure 2.15). The chelator to antibody ratio was then determined by radiolabelling with a trace amount of ^{111}In-chloride in the presence of a 10 times molar excess of 'cold' indium(III) chloride compared with antibody conjugate. All antibody conjugates showed a high labelling efficiency of >95% on average, with exception of the 1:40 ratio, with a drop down to an efficiency of >84%, showing <16% of unconjugated indium-111 impurities, most likely excess ^{111}In bound to chelator that was not removed during the purification steps in the conjugation process. The average number of chelators bound per antibody when increasing amounts of bifunctional chelator were added to the conjugation reaction are shown in table 2.2. The fall in the number of chelators per antibody when a 40 times molar excess of CHX-A"-DTPA was used probably reflects the fact that there is still chelator present in the antibody conjugate solution rather than a real drop in the number of ligands per antibody. However, this indicates that at high molar ratios of bifunctional chelator, purification becomes increasingly difficult and hence, to optimise the reaction a slightly lower molar ratio (e.g. 1:20) of chelator to antibody should be used.

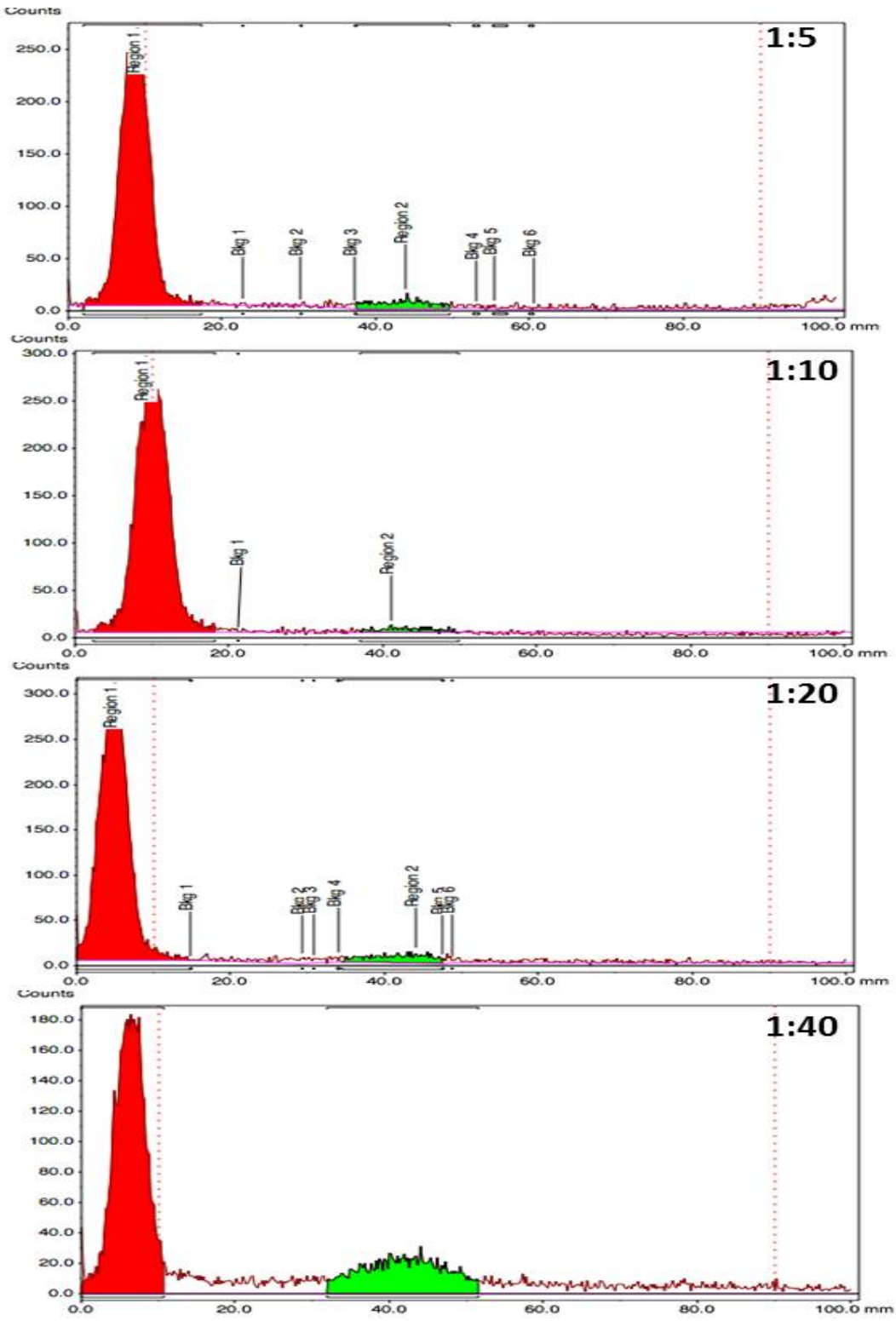

Figure 2.15: iTLC-SA of MOv18-IgG conjugated with 1:5, 1:10, 1:20 and 1:40 excess of p-SCN-CHX-A"-DTPA over antibody and radiolabelled with ^{111}In. Chromatogram shows a labelling efficiency of >97% for 1:5 excess of chelate, >99% for 1:10, >96% for 1:20 and >84% for 1:40 ratio of mAb to chelate. Red = radiolabelled antibody; green = free indium-111: EDTA complex. Mobile phase: 0.1 M sodium citrate, pH 5 with 5 mM EDTA.

Table 2.2: Different ratios investigated for optimal ratio of antibodies to chelators (1:5, 1:10, 1:20, 1:40). The specifically bound ^{111}In added with 10 fold excess of indium(III) in percent of labelling efficiency. Chelates (p-SCN-CHX-A"-DTPA) attached to the antibody on average.

Ratio chelate:mAb	Labelling efficiency	Ligands/mAb
	10x excess In(III)	
1:5	12.1	1.21
1:10	20.62	2.07
1:20	32.09	3.22
1:40	26.21	2.63

2.3.6 Stability of conjugated Antibodies in human serum

To test the stability of the antibody in similar environment as *in vivo* experiments, the antibodies were incubated with human serum and analysed by size exclusion HPLC. At certain time points a sample was taken to look for radioactivity associated with the antibody or other serum proteins and if any radioactivity has become dissociated from the antibody conjugate. This assay is one indicator of likely stability *in vivo*. Over the 120 h time course of the stability assay (Figure 2.16), there was no evidence of instability of the radiolabelled antibody conjugates. For ^{111}In-labelled antibody 3G there was a slight decrease in the amount of activity associated with the antibody conjugate after 120 h, (89% of radioactivity being associated with antibody at this time point) with the remaining activity being associated with a shoulder on the main elution peak of antibody 3G which is possibly related to indium-111 binding to serum proteins but could be an artefact of the HPLC since the levels of radioactivity were quite low for detection. The activity associated with antibody 3E (anti-CSPG4-IgE) and antibody 1E (MOv18-IgE) remained unchanged at 100% during all measurements although slight shoulders appeared to be present on the main antibody peaks possibly an artifact of the HPLC analysis since the levels of radioactivity are quite low. The amount of activity associated with the shoulder was difficult to quantify but was $<$10% of the total activity in all cases.

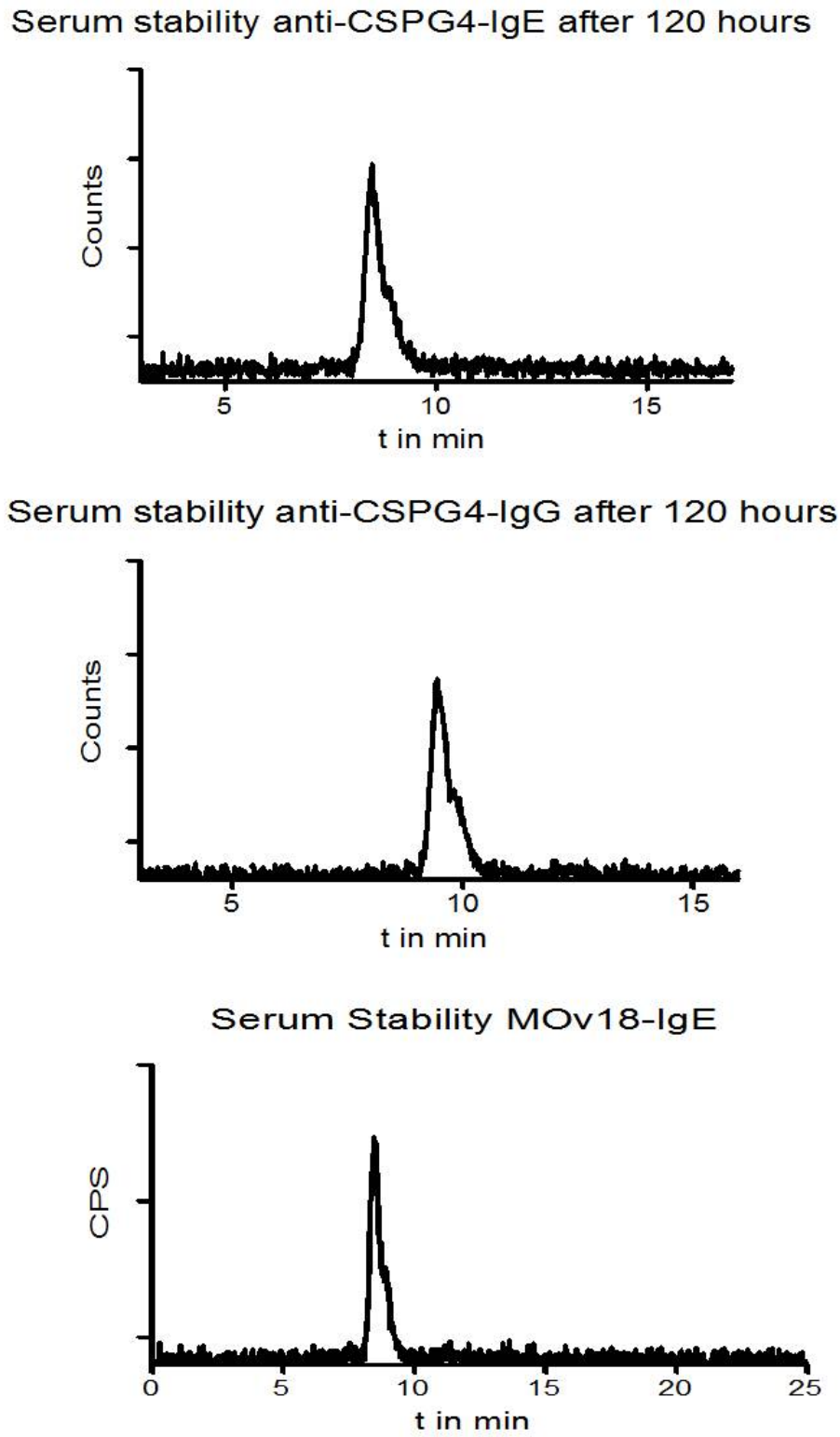

Figure 2.16: Serum stability SEC radioHPLC of ^{111}In labelled anti-CSPG4-IgE, -IgE and MOv18-IgE after 120 hours after incubation with human serum at 37^{C}.

2.3.7 FACS of CHX-A"-DTPA conjugated antibody 1G

To investigate the ideal amount of chelator to use for the conjugation reaction the above described experiments were conducted. To further investigate interference of the conjugation reaction with antibody functionality and binding to the target receptor FACS analysis were performed. To detect possible changes in the affinity, conjugated antibody 1G was compared to its unmodified equivalent, using FACS binding assays to the target receptor (FRα) overexpressing cell line IGROV1. To assess possible effects of the conjugation reaction on the functionality and FcγRI receptor binding, FACS binding studies with a monocyte cell line U937 were performed. This study was conducted to assess the optimal chelate to antibody ratio. Antibodies which were conjugated with 1:5, 1:10, 1:20 and 1:40 fold excess of chelate in the conjugation reaction and which resulted in 1.2, 2.07, 3.22 and 2.63 chelates per antibody on average (Table 2.2), respectively, were compared to unconjugated native antibody. All conjugated antibodies were used without any radiolabelling.

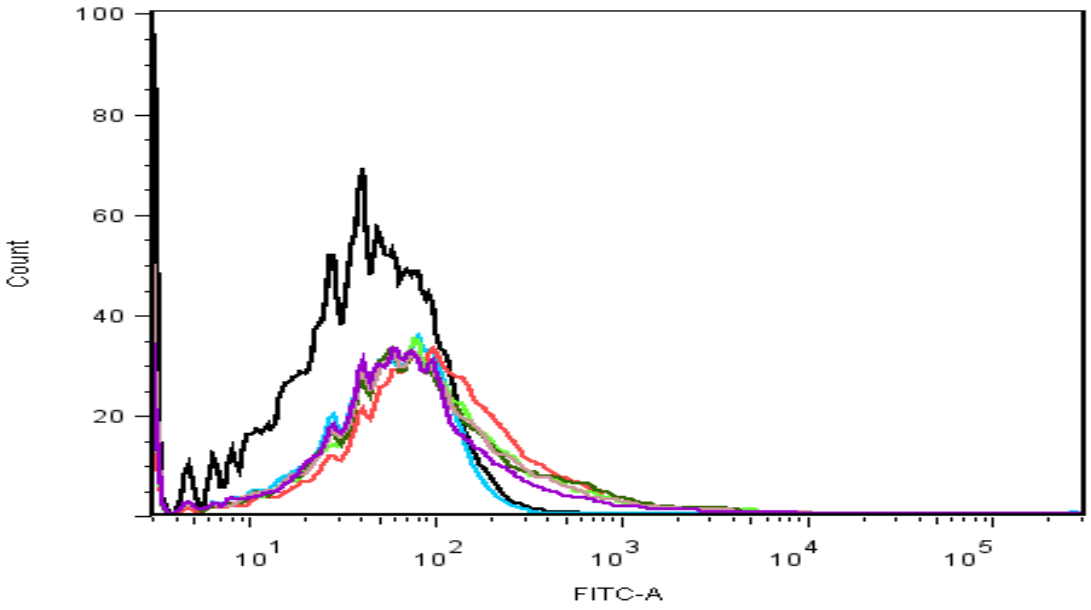

Figure 2.17: Graph shows the binding of antibody 1G to the folate binding receptor (FRα) on the surface of IGROV1 cells in different chelator-to-antibody ratios. Unconjugated and conjugated antibodies did not show any difference in the binding of the FRα. Black= IGROV1 native antibody (cell line without antibody 1G or secondary antibody added); blue= control IGROV1+Secondary antibody with attached fluorescence marker; orange= 5:1 ratio chelator-to-antibody ratio; green= 10:1; dark green= 20:1; violet= 40:1 and red= unconjugated native antibody 1G

Figure 2.17 compares the binding to the target FRα receptor, expressed on the surface of IGROV1 cells, of CHX-A"-DTPA conjugated antibody 1G to its native unconjugated antibody 1G. The antibodies were conjugated with different molar ratios of chelator in excess as shown in table 2.2. The different conjugates of antibody 1G were compared to unconjugated antibody 1G and are represented in the different coloured lines with chelate-to-antibody ratio of 5:1 (orange), 10:1(green), 20:1(dark green) and 40:1 (violet). The conjugated antibody 1G shows the same shifts

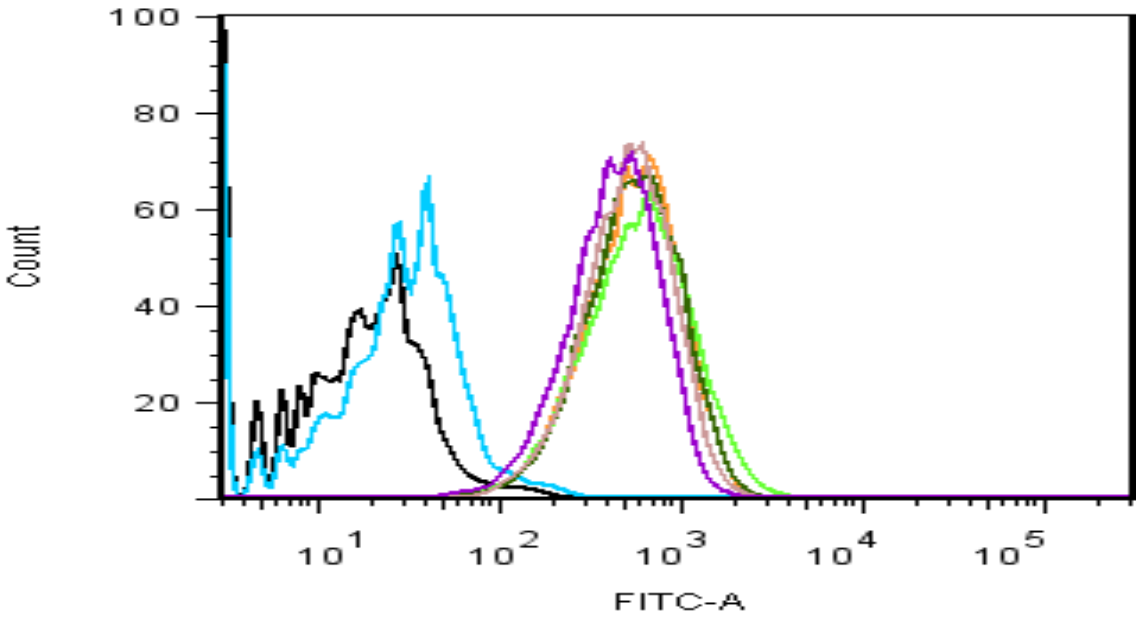

Figure 2.18: Graph shows the binding of CHX-A"-DTPA conjugated antibody 1G to the FcγRs of U937 cells (monocytes cell line) in different chelator-to-antibody ratios (molar excess of chelate used in conjugation reaction). Black= U937 (base line of U937 cells); blue= U937+Secondary Antibody with fluorescence marker; pink= 5:1 ratio chelate-to-antibody 1G; orange= 10:1; dark green= 20:1; violet= 40:1 and green= unconjugated antibody 1G.

at all ratios as the native version of antibody 1G. The shift is a result of positive excitation of the bound fluorophores when positive binding to the cell is detected. Similar shifts of unconjugated and conjugated antibody 1G derivatives show, therefore, positive and comparable binding.

In figure 2.18 the binding of the FcγRI of conjugated antibody 1G to the FcγRI-receptor on the surface of U937 cells was shown positive when compared to the control (black) and the cell line + the secondary antibody with fluorescence marker (light blue). Unconjugated and conjugated antibody 1G showed the same shift in this FACS assay. However, a slight downshift in binding for the antibody 1G with a chelate-to-antibody ratio of 40:1 was detected when compared to the unconjugated antibody 1G could be interpret that the number of chelators present is beginning to affect binding to target cells at this chelator-to-antibody ratio.

2.3.8 FACS of CHX-A"-DTPA conjugated antibody 3G and 3E

Here, the same process of binding assessment described above was followed with the antibody 3G and 3E. To detect changes in affinity and binding of the antibodies 3G and 3E after the conjugation with 20-fold molar excess of chelator used in the conjugation and which resulted in ~3.22 chelates per antibody on average (Table 2.2), a flow cytometric binding assay was carried out. The FcγRI expressing cell line U937 was used to show binding of antibody 3G, conjugated with CHX-A"-DTPA, via the Fc-receptor (Figure 2.19). Furthermore, a FACS binding study was performed with both CHX-A"-DTPA conjugated versions of the antibodies 3G and 3E on an A375 cell line

which overexpresses the chondroitin sulfate proteoglycan 4 antigen (CSPG4). Positive binding on the A375 cell line and comparison to FACS data on native unconjugated antibody 3G and 3E versions (unconjugated antibody control not shown, data from Panos Karagiannis) showed that the binding was unaffected by the conjugation reaction for both conjugated antibodies 3G and 3E (anti-CSPG4-IgG and -IgE), respectively (Figure 2.20). Conjugated antibody 3E was analysed by two different flow binding assays to show unaffected binding to the high affinity FcεRI-receptor and the low affinity FcεRII receptor on primary monocytes (Figure 2.21). CHX-A"-DTPA conjugated antibody 3G and 3E showed a clear positive binding to their specific receptors, both, via the FcR and the target receptor FRα. The conjugation of both antibodies with the bfc p-SCN-CHX-A"-DTPA using a 20 fold molar excess of chelator resulted in ~3.22 chelates per antibody on average. It was successfully shown that the binding capacities via FcR and to the antigen receptor were fully functional.

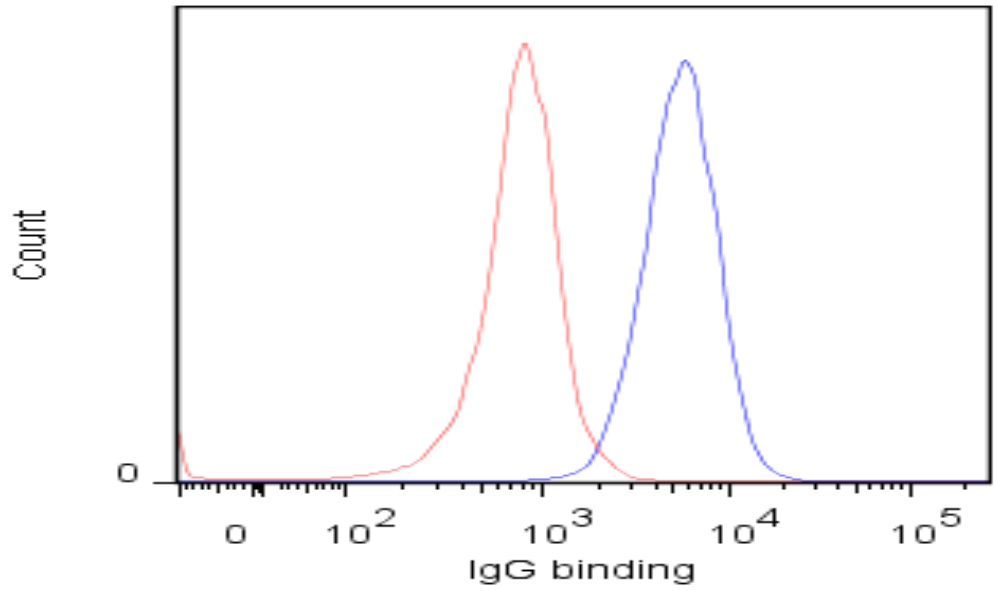

Figure 2.19: Graph shows the binding of p-SCN-CHX-A"-DTPA conjugated anti-CSPG4-IgG antibody to the FcγRI-receptor of U937 cells. Blue= CHX-A"-DTPA conjugated antibody 3G (anti-CSPG4-IgG) on U937 cells; red= U937 cells + Secondary Ab with attached fluorescence marker as control.

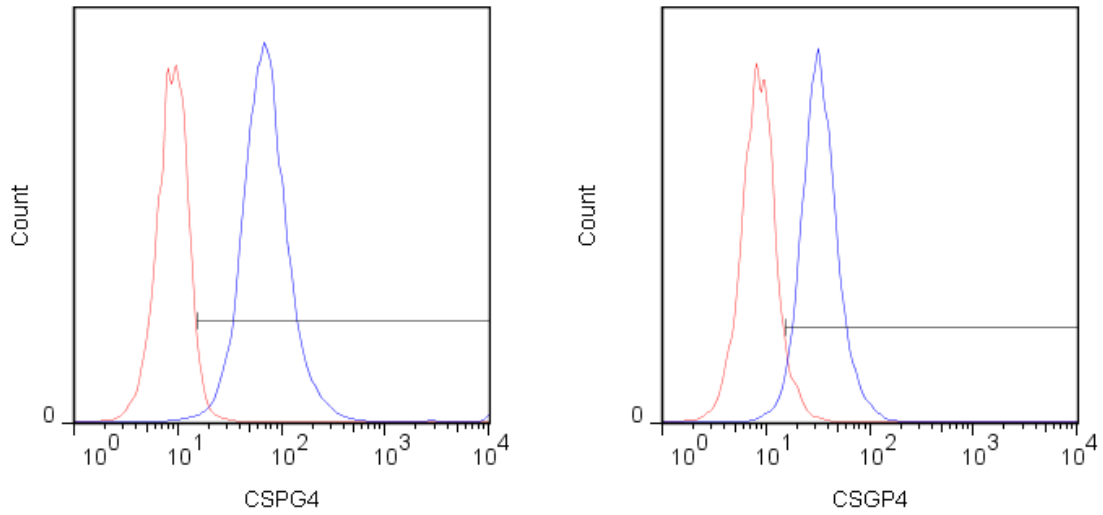

Figure 2.20: Graph shows the binding of CHX-A"-DTPA conjugated antibody 3E (anti-CSPG4-IgE) (left) and antibody 3G (right) on A375 cells overexpressing the target antigen receptor chondroitin sulfate proteoglycan 4. Red= control secondary antibody with attached fluorescence marker + A375 cells; blue= Antibody 3G or 3E conjugated with CHX-A"-DTPA.

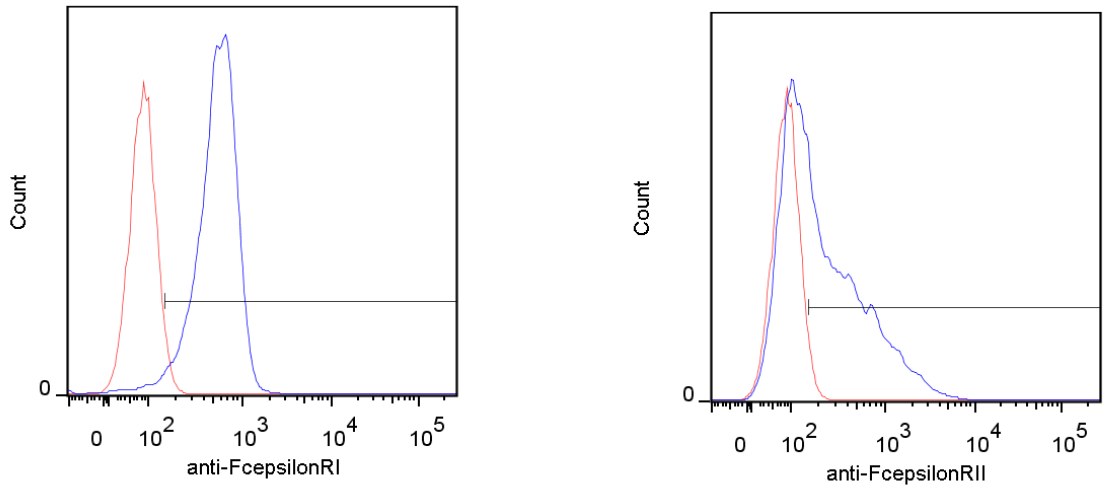

Figure 2.21: Graph shows the binding of conjugated antibody 3E to the high affinity FcεRI (left) and the low affinity FcεRII (right) on primary monocytes expressing FcεR receptors (monocytes were recovered from an anonymised patient melanoma skin sample). Red= control shows secondary antibody with fluorescence marker attached + A375 cells; blue= antibody 3E conjugated with CHX-A"-DTPA.

2.3.9 ADCP/ADCC assay

The tumour cell killing properties of the CHX-A"-DTPA conjugated antibody 3E were evaluated using the three colour flow cytometric functional assays. The assay assessed the ability to mediate tumour cell killing by human effector cells and is able to distinguish tumour cell killing by ADCC and ADCP (Figure 2.22). Antibody 3E directed monocytic cells to kill tumour cells expressing

the CSPG4 antigen by ADCC, a mechanism clearly different from ADCP typically employed by antibody 3G and monocytic cells. The antibody concentrations (0.5 μg/mL) required to achieve tumour cell killing were roughly the same for IgG (antibody 3G) and IgE (antibody 3E) in these *in vitro* assays.

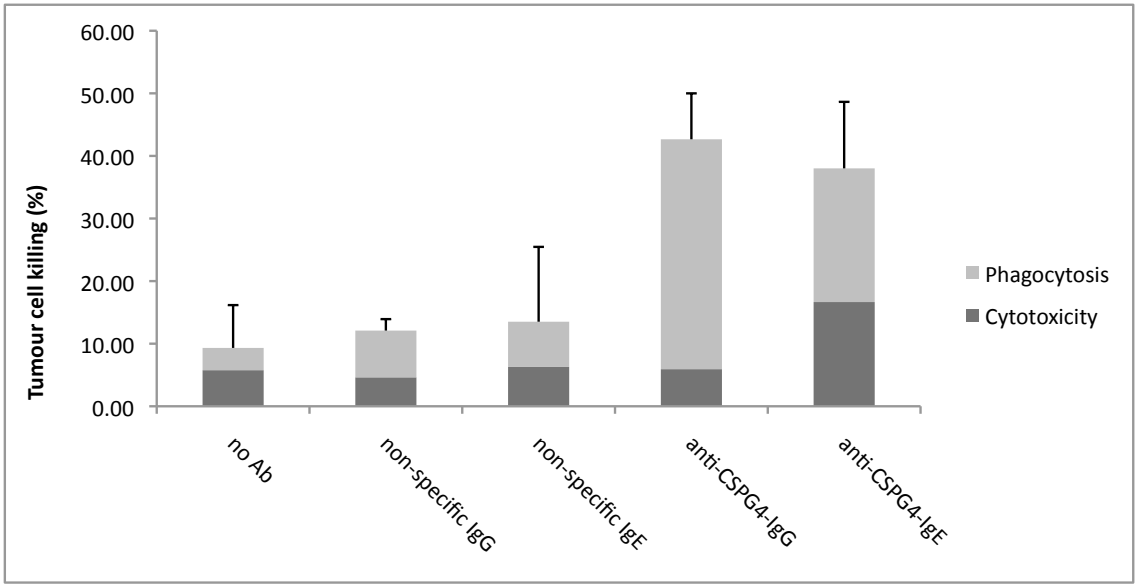

Figure 2.22: Evaluation of antibody 3E (anti-CSPG4-IgE) targeted against CSPG4 overexpressing A375 cancer cells in presence of monocytes (U937). Quantification of ADCC and ADCP using CHX-A"-DTPA conjugated versions of antibody 3G (anti-CSPG4-IgG) and antibody 3E (anti-CSPG4-IgE). Both antibodies mediated killing of CSPG4 expressing target cells by U937 monocytes after 2.5 h in the ADCC/ ADCP assay. Cytotoxicity: black bars; phagocytosis: grey bars. Results are means ± SD. Results compared to isotype control IgG and IgE antibody or no antibody control samples.

2.3.10 Confocal imaging of CHX-A"-DTPA conjugated antibody 2E

The tumour-targeting activities of CHX-A"-DTPA conjugated antibody 2E were studied by confocal microscopical imaging (Figure 2.23 B). IGROV1 cells (FRα expression) were pre-labelled with CFSE (green), incubated with U937 cells which were labelled with anti-CD33-APC (blue). Next, both cell lines were combined with either the FRα antigen specific and CHX-A"-DTPA conjugated antibody 2E or an unspecific IgE control antibodies for 3 h on glass chamber slides. In samples incubated with antibody 2E, contact between IGROV1 tumour cells and U937 monocytic cells, was clearly evident, and two or more monocytic cells were frequently observed in contact with or in close proximity to a single tumour cell. Tumour cell killing was observed and visualised by the appearance of red stained dead cells and the reduction of IGROV1 tumour cell appearance (green). In contrast to the observations with conjugated antibody 2E the unspecific control IgE did not mediate or enhance any tumour cell killing (Figure 2.23 A).

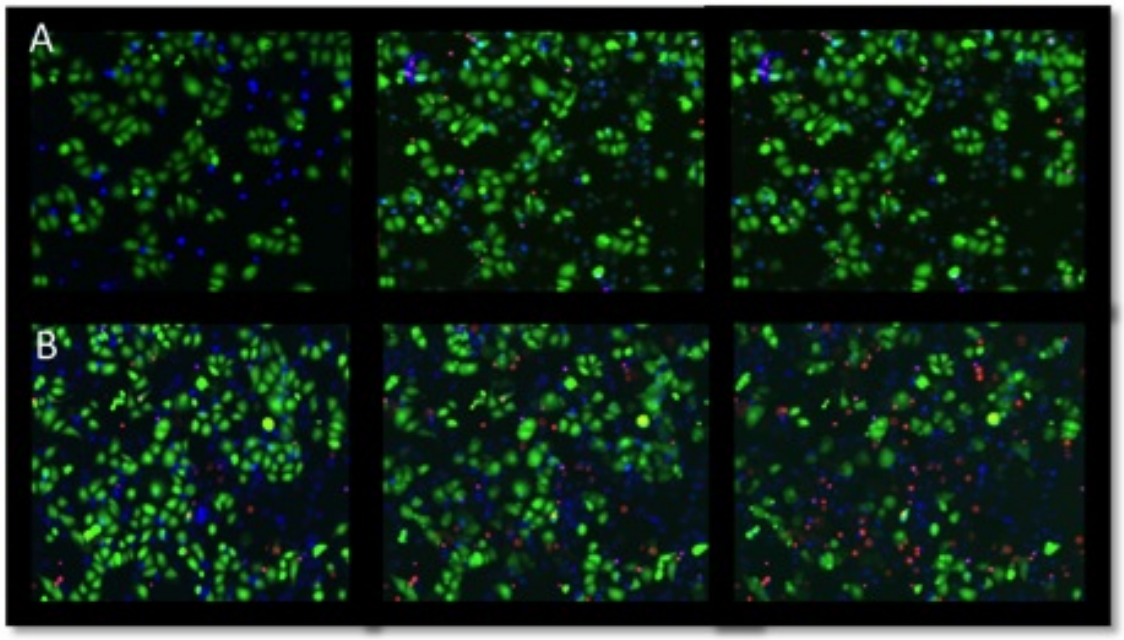

Figure 2.23: Representative confocal fluorescence images of tumour-effector cell interactions mediated by antibody 2E. CFSE-stained IGROV1 FRα expressing tumour cells (green) and CD33-APC labelled U937 cells (blue) combined at 2:1 E:T ratio after 3 h in culture. U937 cells (blue) given antibody 2E (B) showed enhanced contact with tumour cells (green) and killing of tumour cells (dead cell population in red). Neither effector-target cell contact nor phagocytosis was observed when cells were incubated with isotype controls (A). Original magnification x63 (Scale bar 15 μm).

Table 2.3: Overview of antibodies in this chapter and assays performed.

Antibody	Number	Target	Bifunctional chelate	SDS	Stability	TLC	HPLC	FACS	ADCC/ ADCP	Confocal imaging	Phosphor imaging	Bfc:mAb ratio	*in vivo*
Mov18-IgG	1	FRα	DOTA-NHS ester; p-SCN-CHX-A"-DTPA	X		X	X	X				X	
Mov18-IgE	2	FRα	p-SCN-CHX-A"-DTPA	X	X		X			X	X		X
Rat MOv18-IgG	3	FRα	p-SCN-CHX-A"-DTPA				X						X
Rat MOv18-IgE	4	FRα	p-SCN-CHX-A"-DTPA				X						X
Anti-CSPG4-IgG	5	CSPG4	p-SCN-CHX-A"-DTPA	X	X		X	X	X				X
Anti-CSPG4-IgE	6	CSPG4	p-SCN-CHX-A"-DTPA	X	X		X	X	X				X

2.4 Discussion

Both IgG and IgE classes of antibodies were conjugated to the bifunctional chelator, p-SCN-CHX-A"-DTPA, and radiolabelled with indium-111. The impact of the conjugation on antibody function and integrity was investigated. As part of this process, the method for conjugation was optimised to achieve a high enough chelator to antibody ratio in the antibody conjugates to afford high radiolabelling efficiency whilst retaining biological activity. The conjugation and radiolabelling of the IgE class of antibodies has not previously been described in the literature so it was essential to ensure that binding and functionality were retained by comparing these antibody conjugates to their unconjugated native and IgG counterparts.

Prior to conjugation, antibodies were assessed by SDS-PAGE for contamination and degradation. All antibodies used within the project corresponded to the expected size of an intact monoclonal IgG antibody (approx. 150 kDa) or IgE antibody (190 kDa). In addition, all antibodies were also loaded on the SDS-PAGE in a reduced form and results showed the characteristic bands at 25 kDa and 50 kDa corresponding to the light and heavy chain of IgG, respectively. Intact IgE showed intact bands at 190 kDa due to alternative glycosylation [200] and light contamination around 25 kDa. Alternative glycosylation in IgE is thought to play a role for the correct three-dimensional folding of the protein [201].

The reduced antibody 3E (anti CSPG4-IgE) resulted in corresponding bands at 25 kDa and 70 kDa, respectively with light contaminations around the 50-60 kDa mark. Light chain contamination was expected by the antibody supplying team and seen before in experiments and described in literature [202, 203]. The IgG and IgE antibody production for anti-CSPG4 (antibody 3G and 3E) and MOv18 (antibodies 1G/E and 2G/E) antibodies used in this project was based on a two vectors system. Vectors, one for heavy chains and one for the light chains, were introduced to a HEK293 eukaryotic cell production system. The heavy chain is synthesised more slowly than for the light chain because the light chain plays a crucial role in the intracellular folding of the heavy chain. The light chains possesses five cysteine residues, four of them are involved in two disulfide bonds that stabilise the variable (V) and constant (C) domains respectively, and a carboxyl terminal cysteine that is responsible for the intermolecular disulfide bond to the Ig heavy chain. It is, therefore, desirable to offer light chain polypeptides in a higher quantity that ensure the maximum of correctly folded antibodies can be yielded in production [203]. Since the contamination with light chain fragments was very low a re-purification was disregarded because of first the resulting additional loss of protein for each additional purification step. All radiolabelled antibodies used in later experiments were evaluated in the same way and proved to be intact, at the right size and pure.

Initial conjugations were carried out using DOTA-NHS ester. However, it was found that extensive hydrolysis of the ester during the conjugation reaction led to poor conjugation and low

radiolabelling efficiency. The pure solid form of DOTA-NHS contains a few water molecules in the crystal lattice and undergoes significant autohydrolysis at a rate depending on the storage temperature. To obtain a consistent conjugation ratio between DOTA and the antibody, the percentage of intact DOTA-NHS, which varies with batches as well as with time, must be accurately determined prior to the well-controlled conjugation. The unactivated free DOTA does not contribute to the conjugation, and has to be discounted in calculating the molar input of DOTA-NHS for the reaction. Due to DOTA-NHS's ease of hydrolysis back to DOTA, the comparison of different batches of DOTA-NHS is difficult; a straight forward and not too time consuming quality control scheme could not be used in this analysis [204]. Furthermore, once mixed with aqueous buffer solutions, DOTA-NHS hydrolysis reaction is a first-order reaction because H_2O is in large excess.

Another reason for discarding the DOTA-NHS in favour of p-SCN-CHX-A"-DTPA was that HPLC data of the DOTA-NHS conjugated antibody 1G showed another small radiolabelled protein. This indicated antibody degradation, most likely triggered by the extended incubation period at 40°C of the DOTA conjugated antibody with indium-111 chloride. Therefore, it was decided instead to adopt the conjugation protocol of Cooper et al. [197] using the isothiocyanobenzyl derivative of DTPA, p-SCN-CHX-A"-DTPA. It was important to try to achieve high radiolabelling efficiency such that the antibody could be labelled to high specific activity for *in vivo* imaging. Therefore, the conjugation method was optimised by adjusting the molar ratio of chelator to antibody added during the conjugation reaction. It was found that a 20 times molar excess of chelator over antibody gave optimum results in terms of final chelator to antibody ratio in the antibody conjugate (2.6:1) whilst retaining biological activity, as assessed in binding studies compared to the native antibody.

Higher molar ratios of chelator in the conjugation reaction led to two main problems. Firstly, it was difficult to remove the excess chelator from the antibody conjugate at the end of the conjugation reaction. Purification was carried out by using ultracentrifugation in Vivaspin centrifugal concentrator tubes. However, the excess chelator had a tendency to stick to and block the ultracentrifugation tube membrane and would leach back into the solution containing the antibody conjugate, therefore making it difficult to remove, and more extensive washing was required. Since the method would need to be translated to clinical scale production later for clinical trials, the method needed to be as straightforward as possible so extra purification steps were unwanted and would have been detrimental to translation to clinical production. The second problem was that at higher chelator to antibody ratios, it was noted that there was a decrease in the binding of the antibody with the conjugation ratio of 1:40. Conjugation is via the lysine residues in the antibody. Initially the most accessible lysine residues are used for the conjugation and, as the chelator excess is increased, the less accessible lysine residues begin to get conjugated. If these less accessible lysine residues are in the binding region of the antibody then increasing the chelator to antibody ratio can lead to a decrease in binding to the target receptors. Additionally, steric hindrance due to bulky chelator groups close to the binding region of the antibody will have a similar effect.

The average number of chelators attached to each antibody was calculated for the different conjugates prepared (where different ratios of chelator to antibody had been used in the conjugation reaction). Several methods for determining the ligand-to-antibody ratio for chelates that bind radiometals have been described in the literature including tests utilising radionuclides, matrix-assisted laser desorption/ionisation time of flight (MALDI TOF) mass spectrometry (MS), ultraviolet/visible light (UV/VIS) spectrometry, electrophoresis and terbium fluorescence (TF) [205–209]. The method used in this project was based on the published method of Langford et al. [199] which uses a ^{57}Co assay. This was adapted to use trace amounts of ^{111}In with a known excess of indium(III) over antibody rather than using cobalt.

A main limitation of the analysed chelate to antibody ratio is that the average of chelators per antibody is measured. This describes a heterogenenous population of chelators per antibody. Antibodies with more chelators attached are more likely to show loss of binding or affinity and functionality but will account for a larger amount of radioactivity. Therefore, the results can lead to a under estimation of the damage to function when function is measured using the antibody conjugate rather than the radiolabelled antibody. The here shown assays were not able to detect this 'average' effect and the consequences may be under-estimation of this effect on the functionality and binding of the antibodies.

To investigate the binding ability and antibody functions translated by the FcR binding region of anti-CSPG4-IgG and -IgE (antibody 3G and 3E) and MOv18-IgE (antibody 1E) in regards to the optimal antibody to chelate ratios, FACS binding studies and a 3-colour FACS functional assay were performed. Since the bifunctional chelator p-SCN-CHX-A"-DTPA was attached non-specically to any lysine and terminal amine within the amino sequence of the antibody, it was possible that the chelator would attach to lysine or terminal amine within the antibody's complementarity determining regions (CDRs) or FcR binding regions. This would influence the antibody's ability to bind to the antigen with the same affinity as the unconjugated FcR binding region. Therefore, binding studies and functional studies of the radiolabelled antibodies (antibodies 1G, 1E, 3G and 3E) were performed to show full binding and functionality of all employed antibodies. All binding and functional FACS studies showed positive results for conjugated anti-CSPG4-IgE and -IgG and MOv18-IgE antibodies. Only the 40 fold molar excess of chelate used in the conjugation showed slight interference with slightly off-peak results compared to unconjugated antibody counterparts.

All antibody conjugates were labelled with high efficiency as assessed by both instant thin layer chromatography (ITLC/TLC) and size exclusion high performance liquid chromatography (SEC HPLC). Results showed a minimum of 95% of the radioactivity associated with the antibody for all antibody conjugates. A 95% yield was considered as a successful radiolabelling antibody batch - suitable for clinical use. Antibody aggregation if seen at all was always less than 1% of the overall batch in terms of radioactivity, which is excellent since antibody aggregates can lead to

higher liver or kidney accumulation of the antibody compromising diagnosis and giving unnecessary radiation dose to the liver or kidney. In the SEC HPLC system, unchelated indium-111 complexes with EDTA, which was added to the mobile phase. The ^{111}In-EDTA complex is well resolved from the antibody peak and elutes somewhat later. The unchelated indium-111 never exceeded 4% of the overall radiolabelling. This excellent radiolabelling yield meant that the conjugation and radiolabelling methods employed were suitable both for *in vivo* imaging and for later translation into the clinic.

The overlaying signal from the gamma detector and UV detector showed, as expected, an association of radioactivity with the protein. The delay in signal between the two detectors (maximum of 30 seconds) results from the fact that the detectors are in-line with the UV detector before the radionuclide detector.

Throughout this project, radiolabelled antibody was not used for further experiments unless radiolabelling efficiency was above 95%. Radiolabelling efficiency below this would have required an additional purification step which was undesired. The streamlined conjugation and labelling process was one of the main aims. It was important for a future clinical translation that the production steps were kept to a minimum to enable a straight-forward production at the clinical site. It was necessary to develop a method that would allow the labelling without the use of specialised equipment and training rather than production off site associated with higher costs, time and transport limitations. For laboratory research it was important to keep antibody loss to a minimum. The antibody 3E (anti-CSPG4-IgE) and even more the antibody 1E & 2E (MOv18-IgE human/mouse and rat mouse chimeric) were only available at limited quantity due to more difficult production. Purification or wash steps were associated with a loss of about 0.5 to 1 mg of antibody unrelated to the original stock amount to begin with. The high loss of protein was mainly caused by the protein sticking to the Vivaspin 2 centrifugal concentrator membrane. Later, Hydrosart membrane by Vivaspin 2 centrifugal concentrator replaced the polyethersulfone membrane and reduced initial loss of up to 1mg per wash step to about 0.5 mg or less.

The radiolabelled antibody (anti-CSPG4 and MOv18) reaction mixture was intended for use directly for i.v. injection into the *in vivo* models (see chapter 3 and 4). The final pH of the radiolabelled antibody solutions was approximately pH 6, which was not expected to affect the *in vivo* models negatively in any way. The radiolabelled antibody formulations (buffers and radionuclide) used have previously been used for injection into patients in clinical trials and are pharmaceutically acceptable [210].

Stability in human serum of ^{111}In-anti-CSPG4-IgE and -IgG and -MOv18-IgE (antibodies 1G, 1E, 3G and 3E) was analysed using SEC HPLC. HPLC showed that labelled IgE and IgG antibodies were fully intact and radiolabel remained with the antibody throughout the 120 h time course; however after 72 h all peaks identified as antibodies developed a small shoulder. This shoulder seemed to show a slow and only partial degree of degradation described in literature by

Jones et al. and Rogers et al. [211, 212]. They concluded that about 35% of the radioactivity found in the liver originated from antibody labelled ^{111}In-DTPA in the form of the degradation product ^{111}In-DTPA-ε-lysine. In the study by Jones et al.[211] looking at metabolites of an IgG antibody conjugated with DTPA and labelled with ^{111}In, four distinct degradation products were identified:(i) greater than 400,000 Da; (ii) 150,000 Da; (iii) 15,000-50,000 Da; (iv) and less than 10,000 Da. Overall degradation seen with human serum was between 0% and ∼10% for all antibodies IgG and IgE. Degradation was difficult to quantify because elution peaks became broader or showed a small shoulder not easily defined for quantification. The size exclusion column used for HPLC does not have the ability to clearly resolve the full antibody from the degradation products. The shoulder observed associated with the main antibody peak on the HPLC traces may have been as a result of degradation products described by Rogers et al.[212], but without further analysis it would be difficult to determine if this was the case. However, it is clear that the labelled antibodies are very stable in serum for a prolonged length of time and therefore it was deemed appropriate to move forward to *in vivo* studies based on these results.

At the early stage of the project, radiolabelled samples of MOv18-IgE were run on a SDS-gel followed by autoradiography using a phosphor imager. Data showed an association of ^{111}In with the antibody. Standard SDS-PAGE with radiolabelled MOv18-IgE was followed by an autoradiography. A marker spotted with radioactivity at 190 kDa, 25 kDa, and 90 kDa was than aligned to the results and compared to the SDS-gel. This showed that nearly all radioactivity was bound to the MOv18-IgE antibody and especially within the Fc-region of the IgE where most lysine amino groups were located as described in literature [34, 213]. Lysine and terminal amines are the reactive groups for the attachment of the p-SCN-CHX-A"-DTPA bifunctional chelator. Sayers et al.[213] described not only high lysine content in the low affinity receptor area (CD23-receptor) but a complete loss of function depending on the lysine Lys-352 [213]. However, the constant domain in IgE antibodies replacing the hinge region known from IgG is folded back onto the remaining constant domains of IgE and undergoes a conformational change only when bound to a FcR. This might protect the FcεRI and FcεRII and the lysine within the receptor region so they are not accessible to reactive groups of the BFC [49, 213, 55].

2.5 Conclusion

Overall, the main aims for this part of the project were met. All antibodies were successfully conjugated, the conjugation was optimised and is robust and straightforward enough for later translation into the clinic. Radiolabelling efficiency was excellent (>95%) for all antibodies, the radiolabelled antibodies were stable in serum and all antibodies retained functionality of binding the target receptor to FcεRI and FcεRII. Therefore, it was possible to move onto the next stage of the project, *in vivo* imaging.

3 *In vivo* comparison of anti-CSPG4-IgE and -IgG in a tumour xenograft NOD/SCID mouse model

3.1 Introduction

IgE is a class of antibodies with prolonged tissue half-life and commonly associated with allergies. IgE has a very strong affinity to particular FcR receptors on effector cells, like FcεRI and FcεRII, which potentially make IgE class antibodies attractive as a cancer therapeutic. In this chapter *in vivo* imaging and biodistribution studies were used to research IgE class antibodies and to compare them to their IgG counterpart, investigating the biodistribution and *in vivo* trafficking of cancer targeted IgE.

IgE is known for its powerful immune responses from allergic reactions, which differs from IgG class antibodies used as the main antibody class in cancer therapy today. IgE and IgG are also known to have oppositional half-lives, with IgG having a long half-life in serum and IgE a long half-life in tissues. Different modes of action are based on the different Fc-receptors of IgE and IgG and the subsequent difference in recruiting an immune response.

The induction of the immune response follows an allergic-like reaction mediated through the interaction of IgE with FcεRI on the surface of effector cells. The affinity of IgE for its high affinity receptor, FcεRI (Ka =10^{11} M^{-1}), is two to five orders of magnitude higher than that of IgG for the FcγRs (FcγRI-III) [34, 214, 45]. Its affinity for the low affinity receptor, CD23 (Ka=10^{8} M^{-1}), is as high as that of IgG for FcγRI [45]. The binding of IgE with its Fc receptors has been shown to efficiently recruit mast cells and basophils and other effector cells compared to IgG class antibodies [44, 170]. As described for allergens [44], tumour cells are thought to bind IgE and crosslink the receptors leading to rapid degranulation of these effector cells, resulting in the release of multiple factors, including histamine, enzymes, and lipid mediators as seen in IgE mediated (allergic) inflammatory responses [45, 44, 170, 215, 216].

More precisely, IgE antibodies used for this project that target the chondroitin sulphate proteoglycan 4 (CSPG4) overexpressed on A375 tumour cells showed *in vitro* and *ex vivo* superior

anti-tumour efficacy compared to the IgG version in an *in vivo* mouse xenograft model (efficacy data provided by P. Karagiannis, Cutaneous Medicine and Immunotherapy Unit, St. John's Institute of Dermatology, Division of Genetics and Molecular Medicine, KCL).

The anti-CSPG4-IgE antibody and mouse tumour model used for the efficacy studies (Figure 1) was here used in NanoSPECT/CT imaging and biodistribution studies to show organ distribution, targeting and clearance and to compare them to those of its IgG counterpart.

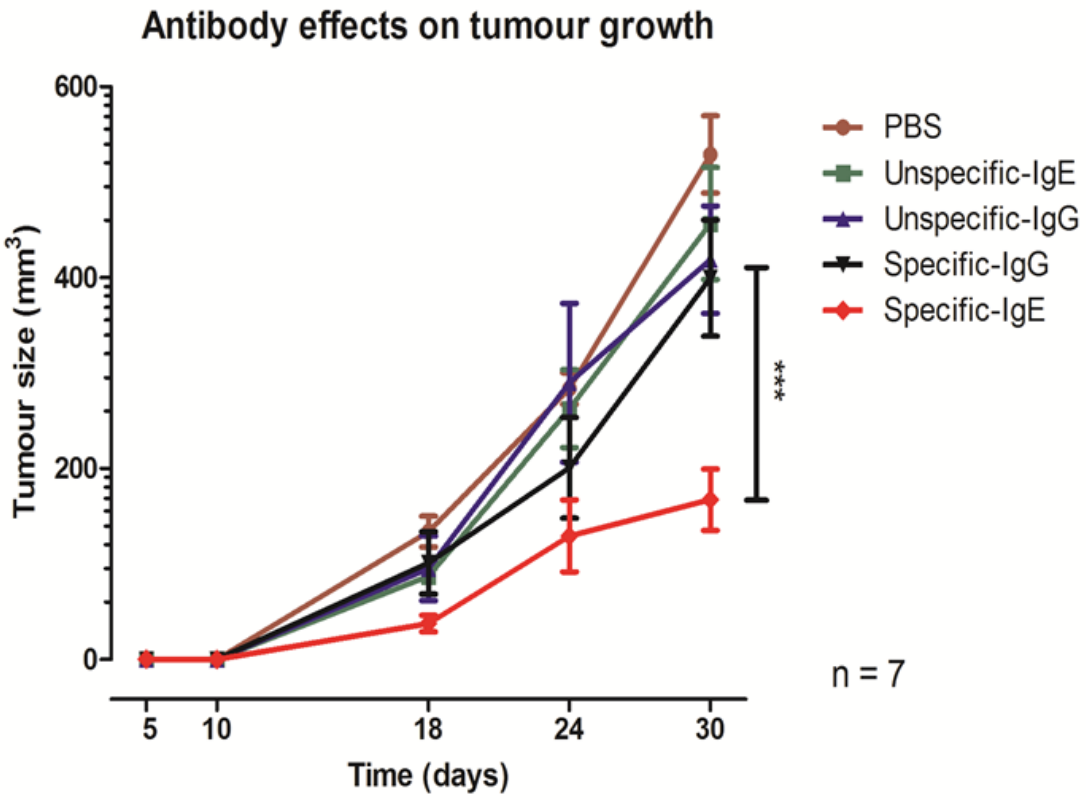

Figure 3.1: Efficacy study of CSPG4-IgE, CSPG4-IgG, unspecific chimeric IgG and IgE and PBS control in a NOD/SCID mouse model with engrafted human peripheral blood lymphocytes (hPBMCs) over time (days) comparing tumour growth inhibition. CSPG4 IgE restricts growth of an A375 human melanoma xenograft grown subcutaneously compared to CSPG4 IgG1 (***$p<0.001$) and non-specific antibody isotype controls when administered intravenously in a humanised mouse model with splenic engraftment of human immune effector cells.

3.1.1 The chondroitin sulphate proteoglycan 4 (CSPG4) target receptor

Human chondroitin sulfate proteoglycan 4 (CSPG4), originally named high molecular weight-melanoma-associated antigen (HMW-MAA) or melanoma chondroitin sulfate proteoglycan (MCSP), was first identified 30 years ago on human melanoma cells [75]. CSPG4 is a cell surface proteoglycan that consists of an N-linked 280 kDa glycoprotein and a 450 kDa chondroitin sulfate proteoglycan [81, 217, 218]. Stallcup and colleagues identified in the rat an ortholog of CSPG4 termed nerve/glial antigen 2 (NG2) (Stallcup, n.d.). CSPG4 and NG2 are highly conserved, and concepts regarding the significance and functions of CSPG4 are based on studies from both orthologs. It is

important to mention that complete structural/functional comparisons between each ortholog are still in process.

CSPG4 and NG2 are expressed in a number of normal tissues throughout development, suggesting an important role in the development and homeostasis of adult tissues [81, 219]. NG2 has also been found to play an important role in the development of vascular tissue, as it is expressed by angiogenesis-associated pericytes (both normal and pathologic) and mice lacking NG2 have defective vasculature [220, 221]. Expression of CSPG4 and Ng2 in several pluripotent progenitor cell populations also indicates a role for CSPG4 in tissue development and stem cell niche maintenance. CSPG4 is detected in stem-like cells associated with the interfollicular epidermis, where it regulates the position and motility of these progenitor cells [222, 223]. CSPG4 has a high expression in >80% of primary and metastatic melanoma lesions and limited interlesional and intralesional heterogeneity. Because of this and its restricted distribution in normal tissues, it has been successfully used as a marker to locate melanoma lesions with radiolabelled monoclonal antibodies (mAb) and as a target of immunotherapy [73, 224].

CSPG4-positive stem cells in the epidermis are important for the renewal of epithelial keratinocytes. CSPG4/NG2 is also expressed in both fetal and adult articular chondrocytes [225, 74], bone marrow mesenchymal cells [226], and smooth muscle cells [227, 228]. CSPG4 is expressed on melanocytes, although at levels lower than what is seen on most melanomas [229, 230, 81, 231]. CSPG4 is associated with the progression of various cancers other than melanoma including oligodendrocytomas, gliomas, triple-negative breast carcinomas, and squamous cell carcinoma [74, 232].CSPG4 seems essential to the growth of melanoma tumours aiding it in form of modulation of integrin function and enhanced growth factor receptor regulated pathways like activation of ERK 1,2. This activation of integrin, RTK, and ERK1,2 function by CSPG4 modulates numerous aspects of tumor progression. CSPG4 expression has further been correlated to resistance of melanoma to conventional chemotherapy [74].

3.1.2 Tumour models

There are significant limitations in the use of animal models. The most important reason is the fact that human IgE does not interact with rodent FcεRs and there is a distinct difference in cellular distribution of FcεRs in humans and rodents [164, 44]. The expression of murine FcεRI is restricted to mast cells and basophils while human FcεRI is expressed on mast cells, basophils, eosinophils, monocytes, Langerhans cells, and DC [6]. Compared with murine expression levels of FcεRI on mast cells and basophils the human cell types show higher expression levels of FcεRI [6]. Despite the limitations different rodent models have been used with success to evaluate the *in vivo* anti-cancer activity of several IgE antibodies. These models include wild-type immunocompetent animals bearing syngeneic tumours, xenograft models using immunocompromised mice bearing

human tumours and reconstituted with human effector cells, and human FcεRIα transgenic mice bearing syngeneic tumours [164, 41, 42, 13, 233, 58]. Immunocompetent syngeneic *in vivo* rodent models using tumour cells from the same genetic background are commonly found in literature to evaluate antibody-targeted therapy.

Xenograft models are an alternative approach to the described syngeneic studies in *in vivo* models. This type of model is based on the use of human cancer cells in order to assess the anti-cancer efficacy. These types of models are the preferred option when studying the efficacy of species specific monoclonal antibodies. Animals used in these xenograft studies are commonly immunocompromised. Severe combined immunodeficiency (SCID) in nude mice that have impaired cellular and humoral immune responses is one of the best known and most commonly used *in vivo* models with immunosupressive gene defect. Although xenograft models allow the transfer of human tumour grafts to an animal model, these models cannot be used to evaluate the adaptive immune response elicited by immunotherapies, including therapeutic antibodies. Moreover, these models cannot be used to examine the anti-cancer activity triggered by human IgE effector functions because of their lack of interaction with murine FcεRs [164].

Despite the limitations, previously published results have highlighted the applicability of this type of animal model in some respects, showing at the same time anti-cancer effects of a tumour-specific IgE [234].

3.1.3 NOD/SCID/Il2rg$^{-/-}$ mouse model employed for the experiments in this study

To investigate and compare the anti-tumour efficacy of anti-CSPG4-IgE and -IgG and to overcome some of the limitation of commonly used *in vivo* model described earlier an immunocompromised (NOD/SCID) mouse model with genetic deficiency of regulatory T cells (NOD/SCID/Il2rg$^{-/-}$) was used. Commonly referred to as NSG mice, they lack mature T cells, B cells, and natural killer (NK) cells. NSG mice are also deficient in multiple cytokine signalling pathways, and they have many defects in innate immunity [235–237]. NSG mice were injected with human peripheral blood mononuclear cells (PBMC) to provide the mice with a human immune effector cell function that was known to show splenic engraftment [238]. This NOD/SCID mouse model was used for all *in vivo* experiments in this chapter, including the efficacy study (Figure 3.1), biodistribution and imaging studies. The animals were tested for splenic engraftment to make sure only animals with successful engraftment of PBMC and steady proliferation and supply of human immune effector cells were used in the experiments.

3.1.4 Biodistribution & Imaging

To help to identify the role of IgE in a tumour disease process that showed antibody efficacy *in vivo* and to understand more of the IgE interactions or modes of actions *in vivo*, imaging and biodistribution studies were performed. The mechanisms that lead to IgE mediated anti-tumour activity *in vivo* are not well understood. Biodistribution of IgE used as an immunotherapeutic agent has not been investigated. Careful assessment of IgE biodistribution in a relevant (therapeutic) tumour model and direct comparison to the corresponding IgG are likely to provide further insight into the mode of action. Radionuclide imaging and *ex vivo* biodistribution studies with radiolabelled antibodies might represent a critical bridge between discoveries at the molecular level and implementation of clinically relevant diagnostics or therapeutics [26]. Based on differences on the FcRs, size and metabolism of IgE and IgG, the kinetics of biodistribution and clearance for IgG and IgE were expected to show different biodistribution [239–242].

The main aim of the overall project was to develop and translate IgE based therapeutics into a clinical application. *In vivo* imaging and biodistribution tests are a critical part of this preclinical development as they offer important insight on how IgE provides anti-tumour effects *in vivo*. Additionally, they can provide valuable animal pharmacokinetic and pharmacodynamic information that can be used to plan the starting dose and schedule of subsequent first-in-man studies. Animal pharmacokinetic data including absorption, distribution, metabolism and organ distribution were thought to help to predict and avoid adverse drug interactions [147, 169].

3.1.5 Factors governing the biodistribution of IgE antibodies

While very few data are available on the elimination pathways of therapeutic IgG and IgE type monoclonal antibodies, there can be some data found on IgE serum and tissue half-life in general. The half-life of IgE in human serum is found in literature with variations ranging from 1.5 to 3 days and everything in between. Most publications seem to suggest a compromise of 2 or 2.5 days as IgE serum half-life for humans [45–47, 42, 48, 49]. The half-life of IgE in tissue or cell-bound was found in literature to be 14 days based on measurement of IgE in skin of rats [48] and based on the affinity calculations for the interactions of the FcεRI with its corresponding receptors [45, 49]. For rodents, however, less data are available on the serum half-life of IgE antibodies. IgE half-life in rodents is reported as 5-12 hours. Haba et al. into the clearance of IgE in mice [46] found a half-life of 1-2 hours initially after injection. A longer half-life of 5-8 hours and a slower clearance were later (5 hours post injection) measured. In agreement with its function in humoral immunity IgG has a long serum half-life of $\sim$20 days and $\sim$2-3 days in tissues. This is to a large extent mediated by interaction with the neonatal Fc receptor. The receptor is expressed on endothelial cells where bound IgG gets internalised, is released in the acidic environment of the endosomes and is then recycled back to the cell surface. In a similar way, FcRn is also responsible for the

transfer of IgG through the placenta and into the foetus. [50]. The significance of this mechanism with regard to IgG serum half-life has been shown in FcRn-knock out studies were the the plasma half-life of IgG in mice was reduced from 9 days to 1.4 days [47]. Thus, indicating that the main reason for the difference in half-life between IgG and IgE is this stabilising interaction between IgG and FcRn. The FcRn receptor possesses two main functions: the transport of IgG known as transcytosis and the control of IgG catabolism [51, 50]. The IgG in excess (not bound to the saturable FcRn) undergoes degradation in lysosomes [52, 50]. Antibodies of the IgE isotype do not bind to FcRn. But the factors influencing the half-life of IgG can give further evidence to support the conclusion that the turnover of IgE may be much faster than that of IgG and a substantially higher amount of IgE may be produced than what is reflected in its plasma levels. As a result of the high affinity interaction of IgE with the FcεRI, the vast majority of IgE molecules at any time are bound to basophils and mast cells or the low affinity receptor FcεRII on B-cells [44, 55, 35].

This is in marked contrast to IgG that instead is primarily found in free circulating form. The IgE-FcεRI interaction has a potentially stabilising effect on IgE half-life [47]. The half-life of receptor bound IgE has been estimated to be approximately 14 days, which indicates that IgE may have a half-life similar to IgG, despite its much lower plasma half-life, once bound to FcεRI immune effector cells [47, 56].

3.1.6 Free indium-111

Free indium-111 and ^{111}In-DTPA are known to accumulate in the liver. Degraded ^{111}In-DTPA or transferrin bound radionuclide could account for *in vivo* liver binding and excretion of radioactive signal. Several studies performed with ^{111}In-labelled IgG type antibodies showed accumulation of significant signal in the liver. In all cases it appeared that the DTPA-amino acid linkage remained intact even after degradation. The main radiolabelled excretion product recovered was a low molecular weight metabolite of ^{111}In-DTPA-ε-lysine. Free ^{111}In-DTPA was trapped and remained in the liver when injected *in vivo* but was not found as a metabolic product in liver of ^{111}In-DTPA labelled *in vivo* models. The studies suggested that the sequestration of ^{111}In after the injection of ^{111}In-DTPA-labelled antibody was the result of a normal hepatic cellular mechanism which was largely dependent on the presence of the Fc portion of the molecule and not affected by radiolabelling [211, 212]. In addition, Jones et al., [211] showed that when ^{111}In-DTPA was injected into rats, ^{111}In was not transferred to ferritin in liver but remained as ^{111}In -DTPA.

3.1.7 Hypothesis and chapter outline

This project was based on the hypothesis that the high affinity (FcεRI) and low affinity (FcεRII) receptor of IgE can trigger powerful immune responses via recruitment of immune effector cells and therefore IgE could be employed for passive immunotherapy of solid tumours such as ovarian

and breast carcinomas [35]. IgE properties may translate to longer retention of the administered antibodies in tissues and longer anti-tumour immune surveillance [35]. The purpose of the work described in this Chapter was to analyse IgE tissue biodistribution, targeting properties and systemic clearance using an indium-111 labelled CSPG4 specific chimeric (mouse/human) IgE in the human PBMC engrafted mouse tumour model described above. A preliminary therapeutic study with the same *in vivo* model by Panagiotis Karagiannis to evaluate and compare efficacy and efficiency of anti-CSPG4-IgE compared to its counterpart anti-CSPG4-IgG showed superior tumour growth inhibition with anti-CSPG4-IgE. The CSPG4 specific IgE, injected into this 'humanised' mouse model resulted in a significantly higher anti-tumour activity compared to CSPG4-IgG, a PBS control or unspecific antibody treatment (Figure 3.1). In this chapter NanoSPECT/CT and biodistribution studies were used to analyse targeting, distribution, clearance and common pharmacological markers like tumour-to-blood ratio. Results were compared to its IgG counterpart and an unspecific IgE isotype control.

3.2 Materials and Methods

3.2.1 Human cell isolation and *ex vivo* stimulation assays

Peripheral blood B cells from patients with melanoma and healthy volunteers were isolated using the B cell enrichment cocktail (Stemcell Technologies) and cultured at a density of 500 cells per well (in 96-well plates). PBMC were activated and cultured in combination with (3,010 cGy) irradiated autologous PBMCs, Epstein-Barr virus, and the TLR9 agonist CpG 2006, as previously described [243]. Single cell suspensions were derived from patient tissues (lymph nodes or melanoma skin lesions) using a Gentle MACs Tissue Dissociator (Miltenyi) and filtered through a 100 μm strainer. In *ex vivo* stimulation experiments, human peripheral blood B cells were co-cultured for 5 days together with irradiated PBMCs and tumour cells at 1:5:10 ratios in RPMI 1640 medium, 10% FCS, 2 mM l-glutamine, penicillin (5,000 U/mL), and streptomycin (100 μg/mL) (all Life Technologies) [244]. Primary human monocytes from patients with melanoma were obtained using the monocyte enrichment cocktail (Stemcell Technologies) according to the manufacturer's instructions [13].

3.2.2 Subcutaneous human melanoma xenograft model

Male and female NOD/SCID/Il2rg$^{-/-}$ mice (NOD.cg-Prkdc SCID Il2rg tm1Wjl/SzJ [NSG]; The Jackson Laboratory) were used at between 6 and 10 weeks of age. Mice were maintained under specific pathogen-free conditions and handled in accordance with the Institutional Committees on Animal Welfare of the UK Home Office (The Home Office Animals Scientific Procedures Act, 1986). NSG mice were injected on day 0 subcutaneously with 5 x10^5 A375 melanoma cells in 150 μL PBS into the lower left side above the leg. On day 5, mice received an intravenous injections of 10 x10^6

human PBLs (derived from whole human blood by lysis of red blood cells). Tumour growth was monitored and measured using callipers. Tumour size (mm^3) was calculated using the following formula: $mm^3 = d^2$ x (D/2), where d stands for the small diameter of tumour and D stands for the large diameter of the tumour. Animals were used for imaging and biodistribution studies once the first animal was measured with a subcutaneous tumour size no greater than 750 mm^3. Spleen engraftment of 40%-70% human CD45+ cells (against mouse cells, human CD45-) was confirmed by flow cytometry for all experiments. In case of the assessment of tumour inhibitory effects of IgE compared to IgG a dose of 10 mg/kg of antibody was injected on day 12. Subsequent injections of antibody treatments were given 2 times on days 18 and 25 at doses of 10 mg/kg each in 150 μL PBS. A control group was treated with 10 x 10^6 human PBLs on day 12 and injected with 150 μL of PBS on days 18 and 25.

3.2.3 NanoSPECT/CT imaging of anti-CSPG4 antibody *in vivo*.

Anti-CSPG4 IgE or IgG (5-7 mg) were conjugated with the bifunctional chelator CHX-A"-DTPA prior to experiments (chapter 2), and on the day of imaging (∼25-28 days after tumour injection), the antibodies were radiolabelled with 20 MBq of indium-111 (St. Thomas' and Guy's Trust, KCL, London, Radiopharmacy) (described in chapter 2) and administered intravenously at ∼10 mg/kg. Images were captured under isoflurane anaesthesia after 4 h, 12 h, 24 h, 48 h, 72 h and 120 h using a NanoSPECT/CT preclinical imager (Bioscan) equipped with a multipinhole (9 pinholes; aperture 1.0 mm) collimator. After an initial low resolution CT image for spatial orientation the scanning parameters were set (general parameters: tube voltage - 45 kVp, exposure Time - 500ms, topogram direction - side view, mouse position - prone and feet-first). Subsequently, a CT of the chosen range was acquired (parameters: acquisition field; number of projections - 180, pitch - 1, number of scans - 1, frames field; frame resolution - standard, tube voltage - 45kVp, exposure time - 500ms). Finally, SPECT imaging was carried out using 1mm multi (9) pinhole mouse apertures and pyramid collimators in helical scanning mode (parameters: detected energy range - 126-143 keV, number of projections - variable, time per projection - ∼60 seconds). Scan times were approximately 5 min for topogram, 6 min for CT, and variable from a minimum of 25 min to up to 60 min for SPECT acquisition. The scan time was adjusted depending on injected dose and calculation of decay of indium-111. Images were reconstructed using InVivoScope (IVS) software (Bioscan).

3.2.4 Biodistribution Studies

Mice for biodistribution studies were prepared in the way described in the methods earlier. NSG mice showed splenic PBMC engraftment and were confirmed of bearing a A375 tumour xenografts. Tumour-bearing mice were injected through the tail vein with ^{111}In labelled anti-CSPG4-IgE or

-IgG antibodies conjugated with CHX-A"-DTPA that had been prepared using the methods outlined in chapter 2. A group of male and female NOD/ SCID/Il2rg$^{-/-}$ mice bearing A375 tumours were injected with either anti-CSPG4-IgE or anti-CSPG4-IgG (70 μg, ~5 MBq). If a group were of mixed gender mice, mice were held in different cages with only male or female mice. Mice (three per group) were culled at 4 h, 12 h, 24 h, 48 h, 72 h or 120 h post injection of the radiolabelled antibody. Blood, tumour, and various organs were collected immediately, weighed and the radioactivity was measured by gamma counting after the last collection at 120 h together with standards prepared from the injected material. The percentage of the injected dose/g (% ID/g) for each organ was determined, and tumour-to-tissue ratios were calculated.

3.2.5 Excretion of indium-111

To gain the data necessary to calculate the excretion of indium-111, all radioactive signals measured for each specific time point and found in organs, tissues and carcass were added and then deducted from the overall injected radioactive dose. This was done for each time point of biodistribution and all values were decay corrected. All radioactivity measured was assumed to be attached to a fully functional anti-CSPG4-IgE or a degradation product of this antibody. Excretion was defined here as radioactivity outside of the body of the NSG mouse. To calculate the excretion rates a single 3-parameter exponential equation was applied. The calculations are shown below where f is in the percent of indium-111, x is time in hours, a is an amplitude change (i.e., the change in value of the data on the y-axis) b is the first-order rate constant and y0 is an end-point value for y-axis data.

Exponential Decay, Single, 3 Parameter:

$$f = y0 + a * exp(-b * x) \tag{3.1}$$

Using the loss of IgE from the mouse it was defined as analogous to an irreversible first order reaction like radioactive decay or excretion (i.e. once indium-111 comes out of the animal it can't go back in) to simplify the mathematics. The means of the construct of the equation as below where d[IgE]/dt is the rate of change of IgE at a particular time, k is fundamental underlying rate constant for the process (i.e. the RATE changes with time as the absolute amount of IgE lost per a fixed unit of time changes but the RATE CONSTANT for the physical process that is rate-limiting for loss of IgE does not change). So the relevant numbers quoted are the rate constants for the process NOT the rates.

$$\frac{d[IgE]}{dt} = k[\text{IgE at start}] \tag{3.2}$$

The half-life ($t_{1/2}$) was calculated as below where k is the fitted first order rate constant.

$$t_{1/2} = \frac{ln2}{k} \tag{3.3}$$

3.2.6 N-Deglycosylation of anti-CSPG4-IgE

To remove the high mannose sugar residues from the anti-CSPG4-IgE the enzyme peptide-N-glycosidase F (PNGase F) was used. PNGase F is a widely used enzyme for the deglycosylation of glycoproteins. The enzyme releases asparagine-linked (N-linked) oligosaccharides from glycoproteins and glycopeptides. A tripeptide with the glycan-linked asparagine as the central residue is the minimum substrate for PNGase F. PNGase F is commonly used for deglycosylation of glycoproteins with high-mannose residues, hybrid or complex type. Deglycosylation was performed under native conditions without the addition of detergents. PNGase F works at a pH range of 6-8 and is used under native conditions with PBS buffer. Prior to the deglycosylation the anti-CSPG4-IgE antibody was conjugated with p-SCN-CHX-A"-DTPA and subsequently radiolabelled with 4 MBq of indium-111 as described in chapter 2, sections 'conjugation' and 'radiolabelling'. PNGase F (8 μL) was added to indium-111 labelled anti-CSPG4-IgE (70 μg) in a volume of 0.5 mL of PBS buffer, pH 7. The reaction mixture was incubated over 24 h at 37°C. The mixture of PNGase F, deglycosylation products and radiolabelled anti-CSPG4-IgE was then injected into one NSG mouse as described here in chapter 4 under biodistribution studies. The mouse was culled for *ex vivo* biodistribution after 48 h.

3.3 Results

3.3.1 NanoSPECT/CT and biodistribution of anti-CSPG4-IgE and-IgG

NanoSPECT/CT was used to determine the biodistribution and tumour accumulation of the indium-111 labelled anti-CSPG4-IgE and -IgG antibodies over time (120h). A non-specific IgE isotype control (human/mouse chimeric MOv18-IgE) was used to assess the contribution of Fc-receptor interaction on biodistribution. The isotype control was used in the imaging study as well as in the *ex vivo* biodistribution studies. In all of the NanoSPECT/CT studies, one mouse was injected with ~70μg (~20MBq) of ^{111}In labelled anti-CSPG4-antibody or ^{111}In labelled isotype control and imaged. The mouse was culled and dissected for biodistribution studies. For biodistribution studies, each time point three mice were injected with ~70μg of ^{111}In labelled anti-CSPG4-antibody or isotype control. Lower activity (3-5MBq/70μg) was used to enable gamma counting.

NanoSPECT/CT images of anti-CSPG4-IgE

Whole body imaging (Figure 3.2) showed rapid and strong accumulation of ^{111}In-anti-CSPG4-IgE in the liver and spleen, with a rapid drop in blood pool activity. Imaging also revealed ^{111}In signal in the gastrointestinal tract. Visible accumulation of radiolabelled antibody in the tumour was not observed. This was also true when overlaying stronger signal of liver, spleen and intestines were removed by software processing post imaging and underlying weaker signal was boosted to better visualise weaker signals. Residual activity from the *i.v.* injection in the tail was detected.

Blood clearance appeared to be fast and no signal was found in organs with high blood perfusion like the heart or lungs even in the first images acquired at 4h p.i.

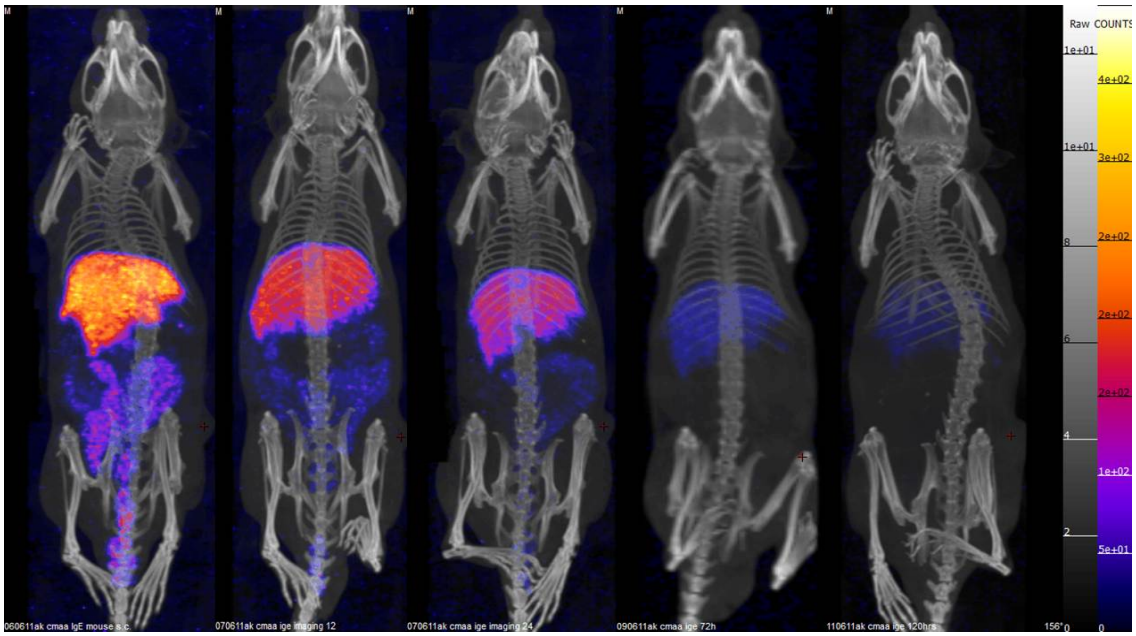

Figure 3.2: NanoSPECT/CT images of a NSG mouse with subcutaneous tumour located in the lower left side and engrafted human PBLCs after injection of In-111 labelled CSPG4-IgE. Mouse injected i.v. with 20 MBq of ^{111}In-anti-CSPG4-IgE (70μg). A-E: SPECT acquisitions at 4 h, 12 h, 24 h, 72 h and 120 h post-injection, overlaid with CT image acquired following the SPECT scan. Images normalised by image software processing to the same arbitrary threshold limits.

***Ex vivo* biodistribution of anti-CSPG4-IgE**

For each time point 3 mice were injected with anti-CSPG4-IgE (70μg, 3-5 MBq). As observed in the NanoSPECT/CT images, high uptake in the liver and intestines was confirmed in the dissections and determined via gamma counting. Additionally, moderate uptake in the spleen was evident (Figure 3.2 and Table 3.1). In line with SPECT/CT imaging, there was no significant uptake in the tumour. As seen in the NanoSPECT/CT images radioactivity remained mainly in liver and spleen and intestines.

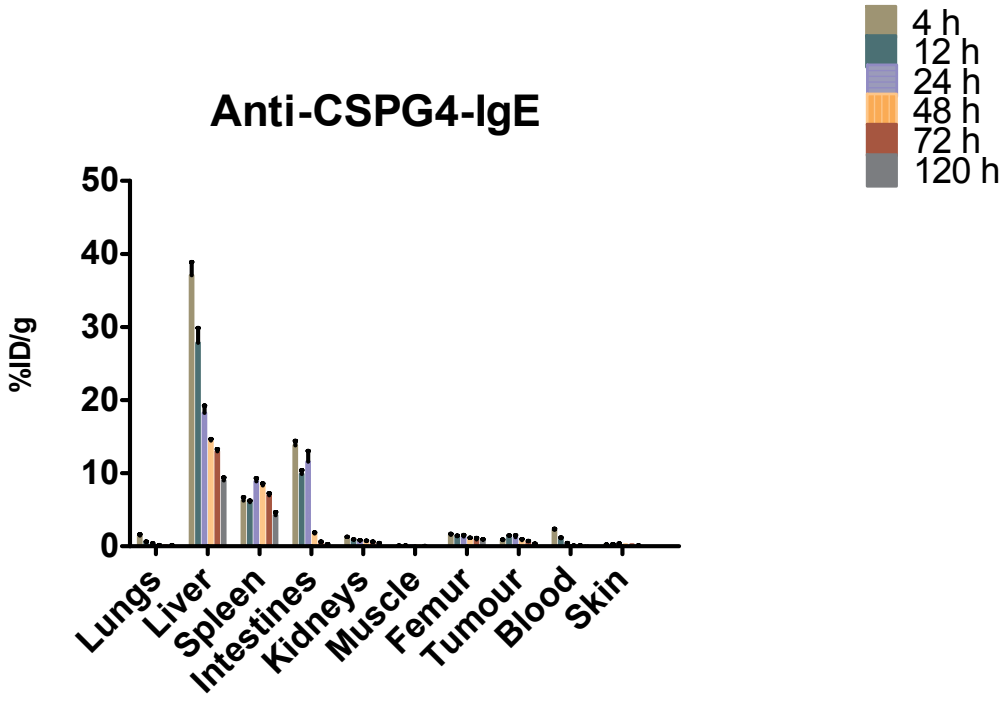

Figure 3.3: Biodistribution of ^{111}In labelled anti-CSPG4-IgE in an s.c. tumour xenograft NSG mouse model with splenic engrafted human PBMC's. Values in graph on linear y-axes in % injected dose per gram in relevant tissue (x-axis) at measured time points. 4h time point (olive); 12h (green); 24h (blue); 48h (orange); 72h (red); 120h (grey). Data plotted in Mean with SEM bars.

Accumulation of ^{111}In-anti-CSPG4-IgE was seen at 4 h post injection in the liver and spleen with 37 % ID/g and 6.2 % ID/g, respectively. The signal in the liver gradually decreased over the 120 h period from 37% ID/g at 4h to 18% ID/g at 24h and to 14% ID/g at 48h. After 120h radioactivity measured in the liver was at 9% ID/g. Signal in spleen increased from ∼6% at 4h and 12h to ∼9% ID/g at the 24 h time point before gradually decreasing to 4.2% ID/g over time. Blood levels dropped rapidly and were measured at 4h post injection with only 2% ID/g with further decline in blood levels of ∼1% ID/g at 12h and 0.36% at 24h. Blood levels measured between 48h and 120h post injections were <0.1% ID/g.

High accumulation of radioactive signal from ^{111}In-anti-CSPG4-IgE or its degraded radioactive products were observed in the intestines with values of 14% ID/g at the 4 h time point.

Accumulation at the tumour site was initially at 0.8% ID/g increasing to 1.44% ID/g at 12 h and 1.2% ID/g at 24 h. Values observed at 48 h show a decline to 0.85% ID/g, and at 72 h and 120 h to a level of 0.7% ID/g and 0.35% ID/g, respectively. Muscle tissue values measured around ∼0.1 %ID/g gradually declining to values of < 0.05% ID/g.

Table 3.1: Biodistribution over the time course of 120h of indium-111 labelled Anti-CSPG4-IgE injected NSG mice. Data of relevant tissue in %ID/g (n=3).

Tissue/Time point	4h	12h	24h	48h	72h	120h
Lungs	1.45	0.58	0.36	0.17	0.11	0.15
Liver	37.09	27.83	18.24	14.44	12.98	9.00
Spleen	6.23	6.02	8.89	8.32	6.97	4.23
Intestines	13.79	9.90	11.57	1.74	0.59	0.29
Kidneys	1.26	0.91	0.80	0.72	0.60	0.43
Muscle	0.09	0.11	0.08	0.05	0.03	0.02
Femur	1.56	1.38	1.33	1.13	0.91	0.92
Tumour	0.83	1.44	1.23	0.85	0.68	0.35
Blood	2.25	1.10	0.36	0.08	0.10	0.04
Skin	0.22	0.29	0.35	0.24	0.23	0.12

3.3.2 NanoSPECT/CT and biodistribution study of anti-CSPG4-IgG

NanoSPECT/CT imaging anti-CSPG4-IgG

The IgG study was carried out analogously to the IgE study with 70 μg of antibody (20 MBq indium-111) Figure 3.4 illustrates ^{111}In-anti-CSPG4-IgG tissue biodistribution and tumour accumulation 4, 12, 24, 72 and 120 hours after administration. Significant accumulation of the radiolabelled antibody in tumours was seen from 4 hours p.i. with degrease of background radioactivity by antibody clearance from blood over time. Antibody not yet cleared from circulation is particularly apparent in the heart. In addition accumulation was detected in the spleen. Circulating antibody signal was visualised in the blood over the whole imaging time of 120 hours. The imaging time course showed the tumour was clearly visible from the earliest imaged time point and throughout the imaging study (Figure 4).

The SPECT/CT imaging data of ^{111}In-anti-CSPG4-IgG was in line with other published biodistributions of IgG type antibodies. A prolonged half-life in the blood pool and a strong accumulation in the subcutaneous tumour over time were observed.

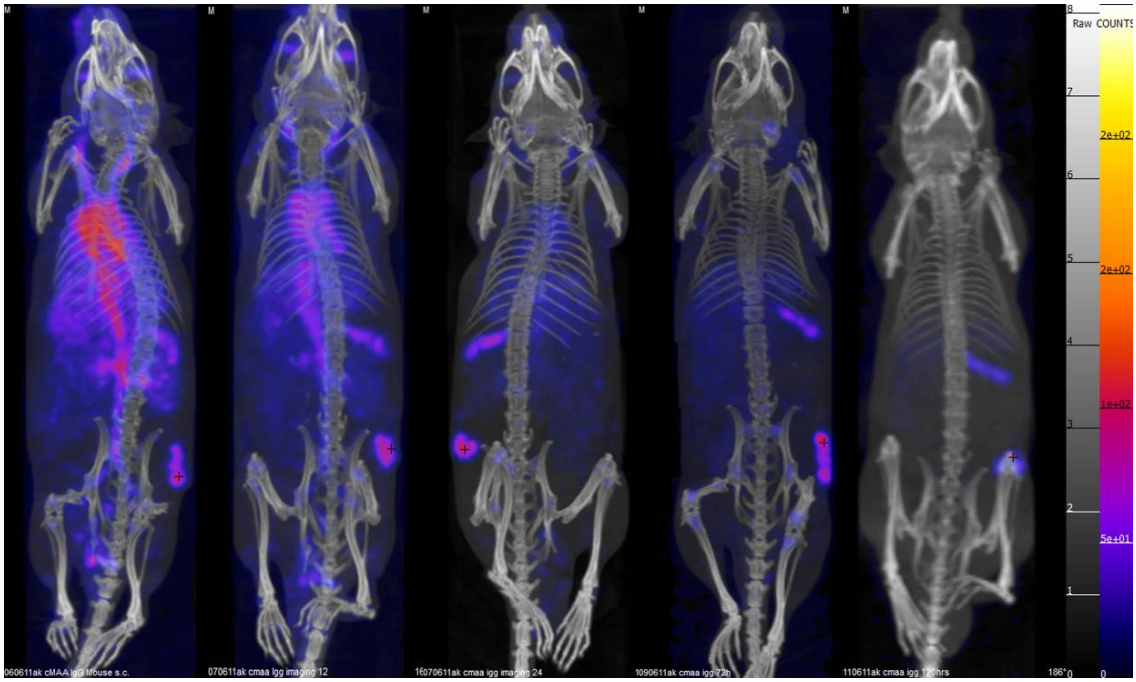

Figure 3.4: NanoSPECT/CT images of mice with subcutaneous tumour injected with In-111 labelled anti-CSPG4-IgG. Sequence of images of the same mouse over time of 120 h (from left to right: 4h, 12h, 24h, 72h and 120h after injection). 70μg of anti-CSPG4-IgG labelled with 20 MBq ^{111}In and injected i.v.. Arrows indicate the position of the tumour.

Ex vivo biodistribution of anti-CSPG4-IgG

Following the protocol described in section (Methods, Subcutaneous human melanoma xenograft model), three mice per time point were injected with 3-5 MBq of ^{111}In labelled anti-CSPG4-IgG and organs were dissected at planned time points. Observations were in line with the imaging data acquired and high uptake was found at the tumour site and in the spleen. A moderate to high uptake in the spleen was apparent (Figure 3.4). Activity seen in circulation was gradually decreasing over 120 hours resulting in an increased signal-to-background ratio in tumour and spleen. Blood levels were observed at 25% ID/mL at 4 h time point and around 13% ID/mL at 12 h post injection. Radioactivity measured in blood then slowly declined over time from 13% ID/mL at 12 h and 24 h, respectively, to 5.8% ID/mL at 48 h and ∼4% ID/mL at 72 h and 120 h post injection. High levels of ^{111}In-anti-CSPG4-IgG accumulated in the spleen over the time course of 120 h. High levels of radioactivity were measured with initially 24% ID/g at 4 h p.i. and 20% ID/g at 12 h p.i.. Further increases in values were observed at 24 h and 48 h with 25% ID/g and 46% ID/g, respectively. Activity observed in spleen reached a high at 72 h p.i. and 120 h p.i. with about 69% ID/g. Activity levels in the liver were above 10% ID/g throughout the time course of 120 h. Intestine levels of ^{111}In-signal were ∼5% ID/g at 48 h p.i. and increased to >8% ID/g at 72 h and 120 h, respectively. Accumulation levels at the tumour site were 13% ID/g at 4h, 18% ID/g at 12 h, 26% ID/g at 24 h and highest at 48 h with 27% ID/g. At 72 h and 120 h post injection radioactivity measured in the tumour stayed above 23% ID/g.

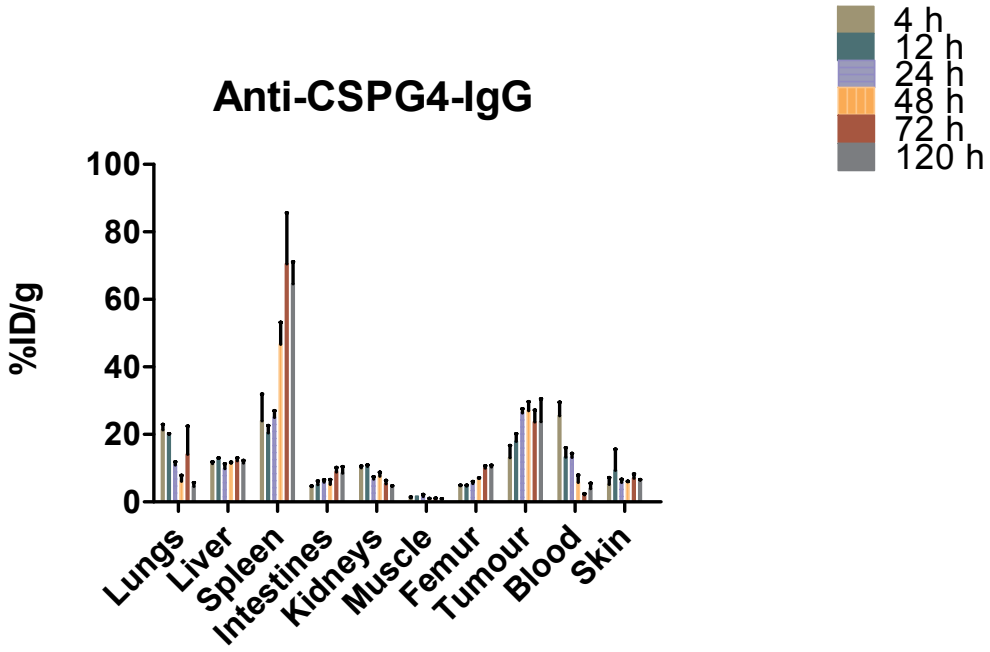

Figure 3.5: Biodistribution of of ^{111}In labelled anti-CSPG4-IgG. Biodistribution in an s.c. tumour xenograft NSG mouse model with splenic engrafted human PBMCs. Values on y-axis in % injected dose per gram in relevant tissue (x-axis) at measured time points. 4h time point (olive); 12h (green); 24h (blue); 48h (orange); 72h (red); 120h (grey). Data plotted are mean with SEM bars.

Table 3.2: Biodistribution over the time course of 120 h of indium-111 labelled anti-CSPG4-IgG injected NSG mice. Data of relevant tissue in %ID/g (n=3).

Tissue/Time point	4h	12h	24h	48h	72h	120h
Lungs	21.40	20.02	10.92	6.11	13.08	4.62
Liver	11.41	12.99	9.84	11.42	12.08	11.55
Spleen	24.05	20.47	25.01	46.71	69.19	64.60
Intestines	4.51	5.16	5.90	5.18	9.21	8.52
Kidneys	10.12	10.57	6.82	7.64	5.30	4.73
Muscle	1.18	1.73	1.66	0.99	1.04	0.78
Femur	4.77	4.68	5.47	6.93	10.03	10.35
Tumour	13.13	17.95	26.39	27.02	23.53	23.83
Blood	25.56	13.29	13.18	5.76	4.11	3.96
Skin	5.18	9.34	5.76	5.98	6.40	6.55

3.3.3 Imaging and biodistribution of an IgE class isotype control antibody (MOv18-IgE)

Unspecific IgE isotype control for the CSPG tumour model (MOv18-IgE)

A NanoSPECT/CT imaging study was performed in the same *in vivo* model using a non-specific IgE as isotype control in order to assess the influence of the targeting on the biodistribution of IgE. A similar biodistribution of the IgE isotype control antibody was observed compared to the specific anti-CSPG4-IgE. Results showed a very high accumulation of signal in the liver and spleen accompanied by a rapid drop in blood pool activity (Figure 3.6+3.7). Like for anti-CSPG4-IgE images, the IgE isotype control showed strong radioactive signal in the intestinal lumen concordant with excretion of antibody degradation products via liver and bile. At no time point a visual signal could be confirmed at the tumour site.

No underlying weaker signal in other organs could be detected when overlaying stronger signal of liver, spleen and intestines were removed by software post imaging processing.

Due to a technical defect in the software the image at 120 h was not saved in the usual data format. The picture was in a low quality format which did not allow the enlargement to a size appropriate for work and publication. The imaging at the 12 h time point was cancelled due to stress related ethical reasons for the animal.

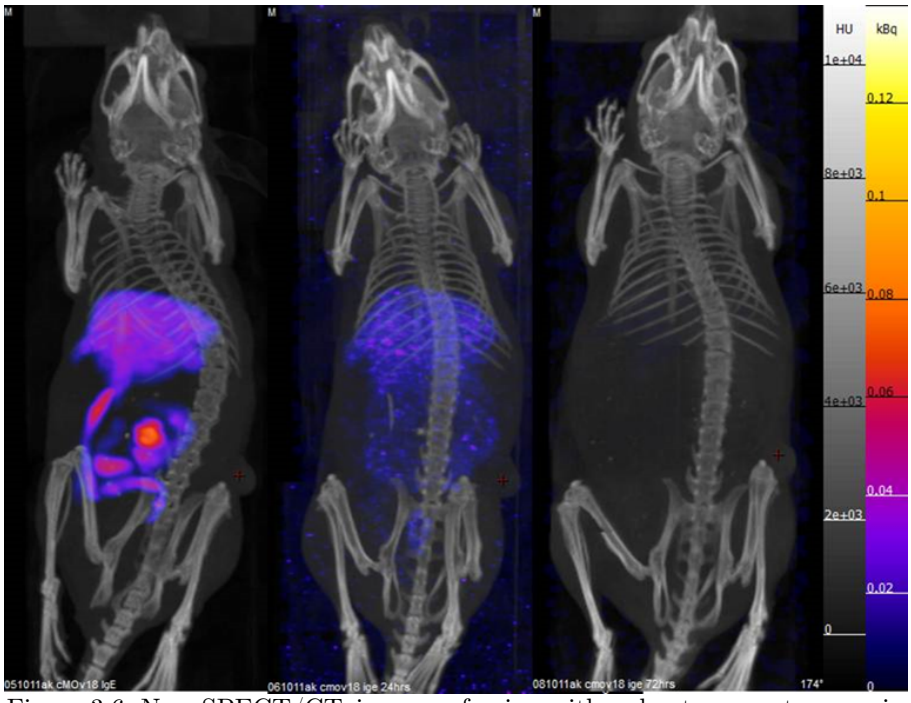

Figure 3.6: NanoSPECT/CT images of mice with subcutaneous tumour injected with indium-111 labelled IgE isotype control (MOv18-IgE). Sequence of images of the same mouse over time of 120 hours (from left to right: 4 h, 24 h and 72 h after injection). 70μg of IgE isotype control labelled with 20 MBq ^{111}In and injected i.v.. Arrows indicate the position of the tumour.

Biodistribution of unspecific IgE isotype control (MOv18-IgE)

The biodistribution measurements confirmed the high liver and spleen uptake seen in the SPECT/CT scans (Figure 3.6). Liver showed uptake values of more than 25% ID/g at 4 h. Further measurements showed a progressive decline in radioactivity with 20% ID/g at 12 h p.i. and 14% ID/g 24 h p.i.. Between 24 and 48 h values decreased further to 7% ID/g and ∼5% ID/g at 72 and 120 h. Spleen showed an uptake from 3.8% ID/g at 4 h and highest accumulation of activity was measured at 12 h with 6% ID/g. Signal decreased to 4.3% ID/g at 24 h and at 48, 72 and 120 hours p.i. consistent signal of around 3-4% ID/g was observed. The intestines showed high signal, as expected from the NanoSPECT/CT, from the first time point at 4 h post injection with an uptake value of more than 36% ID/g. The signal showed a strong decline and after the 24 h time point about 11% ID/g was observed before further decline to <3% ID/g at 48 h and below 1% ID/g in the remaining time points.

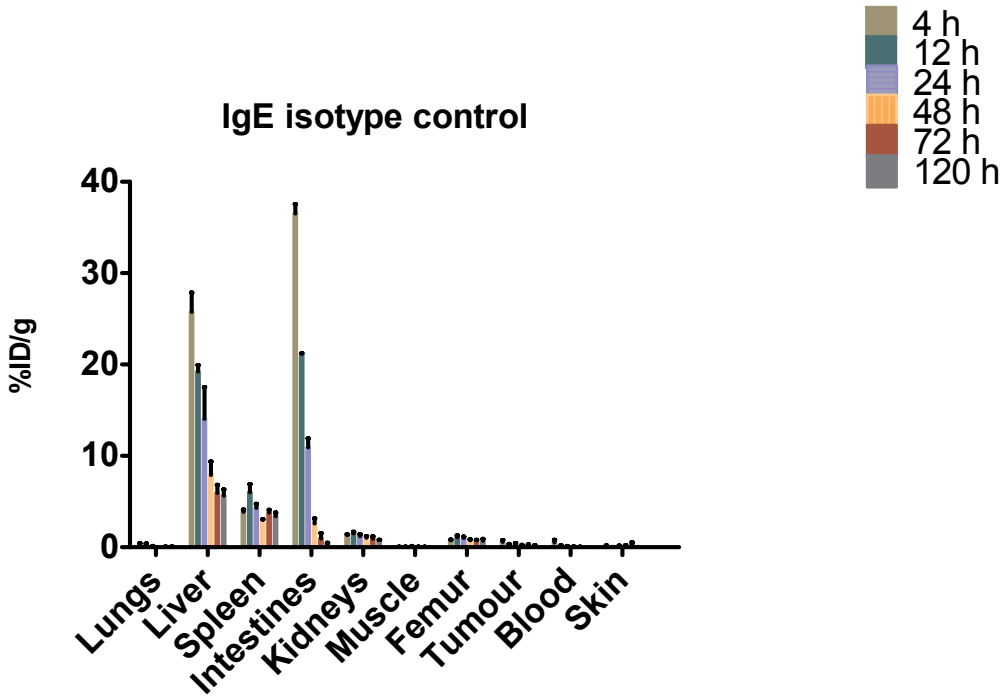

Figure 3.7: Biodistribution of ^{111}In labelled unspecific isotype control IgE in an s.c. tumour xenograft (CSPG) NOD/SCID mouse model with splenic engrafted humann PBMCs. Values are on linear y-axes in % injected dose per gram in relevant tissue (x-axis) at measured time points. 4h time point (red); 12h (blue); 24h (pink); 48h (green); 72h (yellow); 120h (orange). Data plotted are mean with SEM bars.

Blood levels observed initially were very low at 0.5% ID/g at 4 h with further decrease to <0.2% ID/g at 12 h post injection, and then progressively further decline to 0.03% ID/g at 120 h post injection.

Accumulation on the tumour site remained low during all time points but significantly higher than blood. Values observed were between 0.5% ID/g and 0.2% ID/g.

Table 3.3: Biodistribution over the time course of 120h of indium-111 labelled non-specific IgE isotype control injected in tumour bearing NSG mice. Data of relevant tissue in %ID/g (n=3).

Tissue/Time point	4h	12h	24h	48h	72h	120h
Lungs	0.42	0.34	0.13	0.09	0.07	0.07
Liver	25.75	19.22	14.05	7.92	5.96	5.66
Spleen	3.88	6.03	4.32	3.00	3.79	3.40
Intestines	36.52	21.18	10.94	2.59	0.98	0.45
Kidneys	1.35	1.53	1.22	1.05	0.95	0.81
Muscle	0.05	0.05	0.11	0.05	0.04	0.04
Femur	0.78	1.10	1.01	0.77	0.77	0.72
Tumour	0.58	0.29	0.38	0.24	0.21	0.20
Blood	0.55	0.17	0.12	0.07	0.04	0.03
Skin	0.19	0.11	0.17	0.19	0.33	0.11

3.3.4 Comparison of anti-CSPG4-IgE and -IgG

Figure 3.8 shows a comparison of the % ID/g observed for indium-111 labelled anti-CSPG4-IgE and -IgG and the unspecific IgE isotype control at 4 h, 48 h and 72 h post injection. Antibody data compared here originates from the biodistribution studies. The acquired data showed that most of the IgE was taken up by liver, intestines and spleen. Anti-CSPG4-IgG showed also a very high spleen uptake but did not show a high liver uptake. In contrast to anti-CSPG4-IgE the IgG variant showed a clear tumour targeting with elevated uptake. This was not seen with its specific IgE counterpart or the isotype control, although, the tbr of anti-CSPG4-IgE was still high. In addition, IgE antibodies showed a very strong and exclusive excretion via liver. Anti-CSPG4-IgG showed a long circulation time in blood while both IgE antibodies are cleared from blood within 24 h.

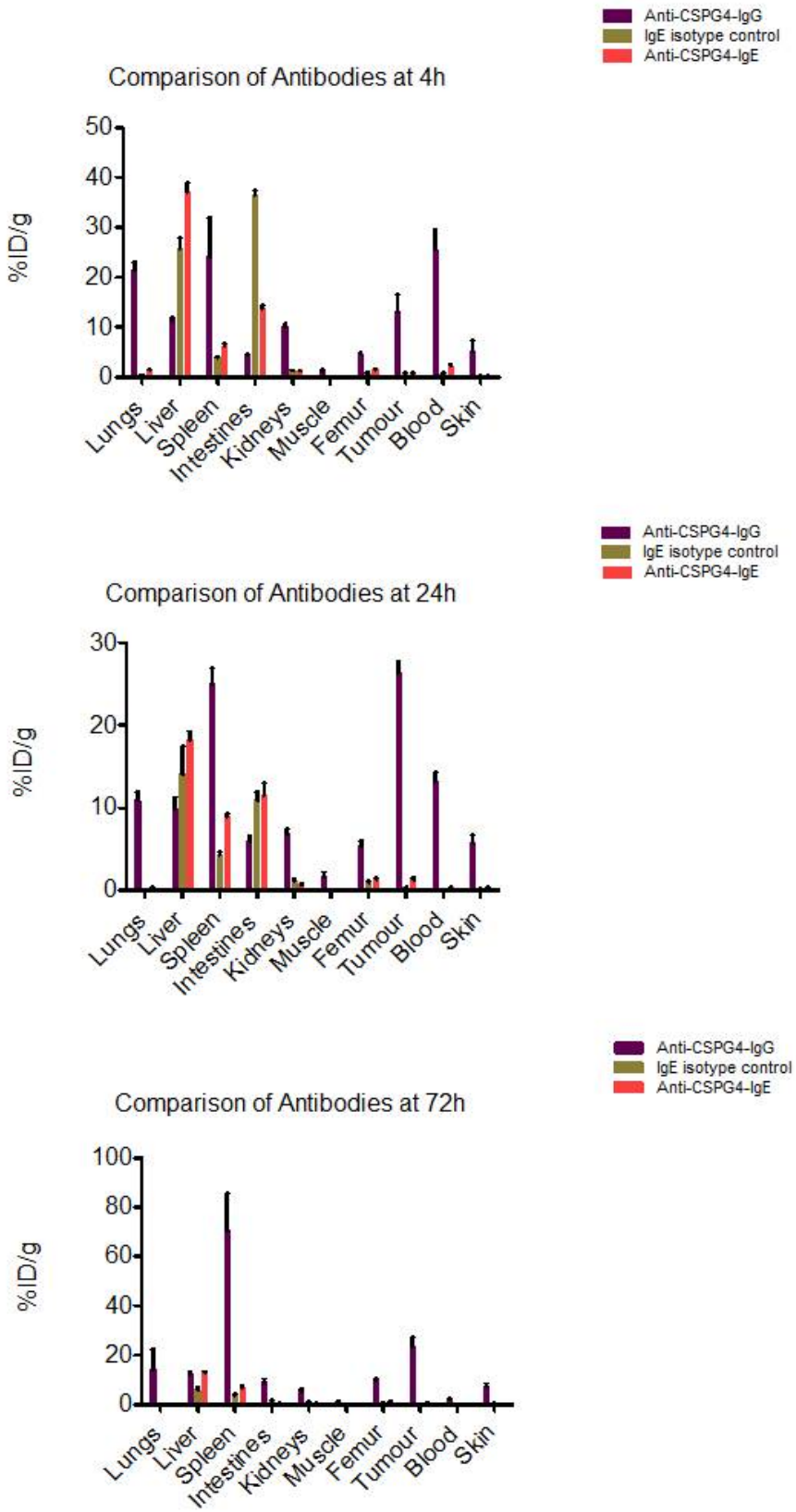

Figure 3.8: Comparison of the biodistribution of ^{111}In labelled anti-CSPG4-IgE and -IgG and an unspecific isotype control in an s.c. tumour xenograft NOD/SCID mouse models with splenic engrafted of hPBMC's at 48h post i.v. injection in % injected dose per gram of dissected tissue (lungs, liver, spleen, intestines, kidneys, muscle, femur, tumour, blood and skin). Data plotted are mean with SEM error bars.

3.3.5 Biodistribution of a deglycosylated anti-CSPG4-IgE after 48 hours

The results of the deglycosylated anti-CSPG4-IgE show distinct differences to the anti-CSPG4-IgE with native glycosylation (Figure 3.9, Table 3.4). The measured values of deglycosylated IgE originate from only one s.c. tumour bearing NSG mouse, which was engrafted with human PBMC's as described for all studies in this chapter. Biodistribution was performed after 48 h. Activity observed in liver showed a markedly lower uptake of 5.7% ID/g compared to the normal IgE (14% ID/g). Tumour uptake after 48 h was a 14.3% ID/g compared to 0.85% ID/g at 48 h in the normal anti-CSPG4-IgE.

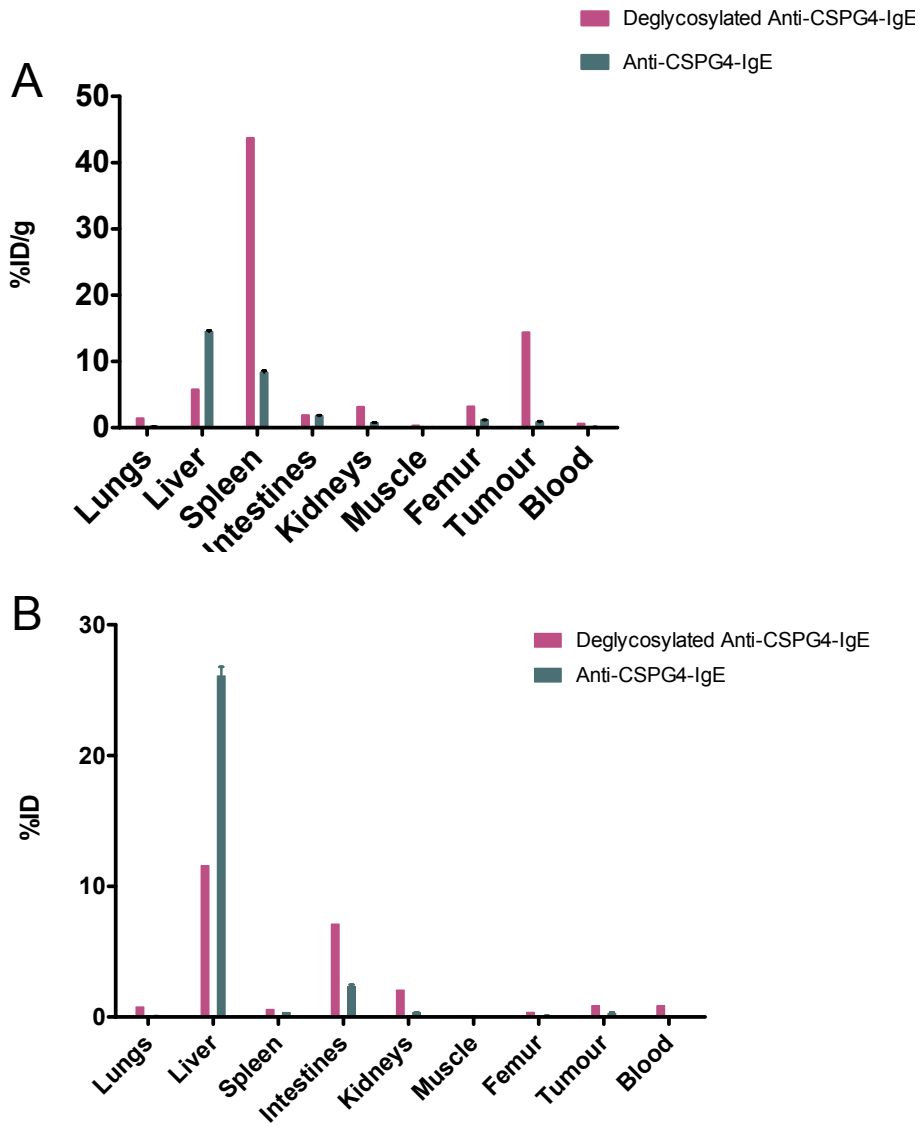

Figure 3.9: (A) shows a comparison of deglycosylated (violet) and native glycosylated anti-CSPG4-IgE 48 h post injection in %ID/g. (B) shows a comparison of the % ID of the same anti-CSPG4-IgE (deglycosylated and native) 48 h post injection. Anti-CSPG4-IgE was deglycosylated after labelling using PNGase F enzyme. Deglycosylated anti-CSPG4-IgE was injected in 1 mouse and *ex vivo* biodistribution was performed after 48 h. For native anti-CPSG4-IgE n = 3 and data plotted in mean including SEM error bars.

Table 3.4: Biodistribution of deglycosylated anti-CSPG4-IgE in %ID/g and %ID 48 h post injection (n = 1).

Tissue/Organs	%ID/g	%ID
Lungs	1.38	0.77
Liver	5.76	11.57
Spleen	43.70	2.62
Intestines	1.86	7.11
Kidneys	3.12	2.06
Muscle	0.30	0.05
Femur	3.19	0.35
Tumour	14.37	0.86
Blood	0.57	0.85

3.3.6 Tumour-to-Blood-Ratios

Tumour-to-Blood ratio (TBR) is commonly used to correct for the contribution of blood pool activity to the uptake observed in tumour tissue and shows how much more signal is in the tumour tissue than in blood. The TBR of ^{111}In-anti-CSPG4-IgE (Figure 3.10, red) was calculated at 4 h time point to be 0.4. Ratios increased further over 12 h and 24 h to 1.3 and 4.5 before reaching the highest ratio at 48 h of 11.4. While TBR usually accounts for the background of blood pool signal, in case of IgE the progression of increased TBR might originate at least in part from the strong decline of blood pool signal. ^{111}In-anti-CSPG4-IgG showed a similar starting point at the 4 h time point compared to IgE with a ratio of 0.5. ^{111}In-labelled IgE isotype control (Figure 3.10, , green and Table 3.5) showed a higer TBR starting point compared to anti-CSPG4-IgE and -IgG with 1.7 at 4h post injection.

Table 3.5: Tumour-to-Blood ratios of anti-CSPG4-IgE and -IgG and IgE isotype control over the time course of 120 h.

T/B ratio	4h	12h	24h	48h	72h	120h
Anti-CSPG4-IgG	0.53	1.37	2.02	6.30	11.26	6.37
IgE isotype control	1.69	1.73	3.37	3.53	5.46	6.43
Anti-CSPG4-IgE	0.37	1.34	4.54	11.45	8.32	8.76

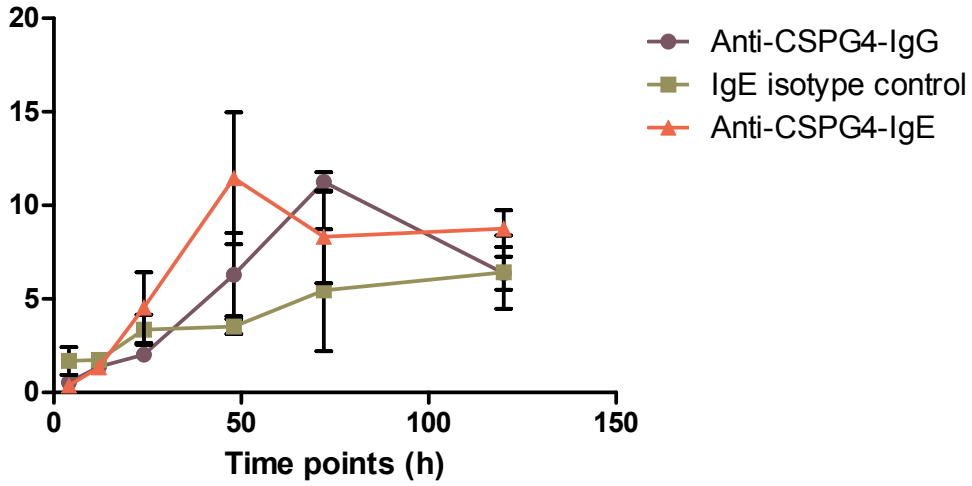

Figure 3.10: Tumour-to-Blood ratio. Data shown in this figure compares the tumour-to-blood ratios of the dissected tumour tissue and blood from the tumour bearing NSG mice injected with ^{111}In labelled anti-CSPG4-IgE (red) and ^{111}In labelled anti-CSPG4-IgG (violet) and IgE isotype control (green) Time points at 4, 12, 24, 48, 72 and 120 hours post injection. Data plotted ratio (y-axis) over time (h) (x-axis).

3.3.7 Tumour-to-Muscle-Ratio

Anti-CSPG4-IgE and -IgG antibody tumour-to-muscle (TMR) ratio compares the accumulation of antibody in the tumour tissue and unaffected tissue (here muscle). This ratio was compared between the antibodies. Together the tumour-to-blood ratio the tumour-to-muscle ratio can be an important marker to evaluate specific accumulation and help interpret the biodistribution data.

TMR showed a manifold higher accumulation of antibody in tumour tissue against non-tumour tissue for all antibodies. Here antibody accumulation and biodistribution patterns are shown both comparing anti-CSPG4-IgE and -IgG or anti-CSPG4-IgE against its isotype control (Figure 3.11).

^{111}In-anti-CSPG4-IgG TMR increased from 11.0 at the 4 h time point to 27.8 at 48 h and

Table 3.6: Tumour-to-Muscle ratios of Anti-CSPG4-IgE and -IgG and IgE isotype control over the time course of 120 h.

T/M ratio	4h	12h	24h	48h	72h	120h
Anti-CSPG4-IgG	11.00	10.36	18.44	27.84	25.28	30.49
IgE isotype control	10.54	5.57	4.70	4.78	5.95	4.67
Anti-CSPG4-IgE	9.12	14.62	15.90	18.79	21.11	14.21

remained at >25 till 120 h post injection. The TMR of In-111 labelled anti-CPSG4-IgE increases from 9.1 at 4 h p.i. to 21.1 TMR during the first 72 h. From 72 h post injection a decrease to 14.2 in TMR was observed at 120 h post injection.

TMR of the IgE isotype control antibody ^{111}In-MOv18-IgE showed a lower TMR compared to anti-CSPG4-IgE and -IgG (see Figure 3.11 and Table 3.6). Anti-CSPG4-IgE showed a progressive increase in ratio over time as described above.

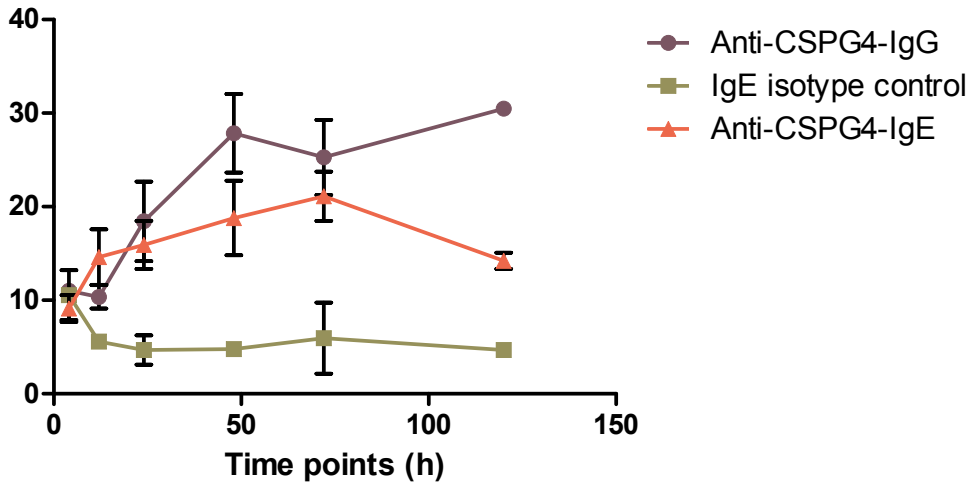

Figure 3.11: Comparison of the tumour-to-muscle ratio of s.c. tumour bearing NSG mice (n=3) injected with ^{111}In labelled anti-CSPG4-IgE and -IgG or IgE isotype control. Samples were dissected at 4, 12, 24, 48, 72 and 120 h post injection.

3.3.8 Blood clearance and excretion of anti-CSPG4-IgE

Blood clearance (Table 3.7, Figure 3.12) of anti-CSPG4-IgG at the first time point 4 hours post injection was 25% ID/mL. Activity levels remained at 12 h and 24 h around 13% before declining to 5% at 48 h. Anti-CSPG4-IgE at the 4 hour time point was 2.2% ID/mL with further strong decline in to 1% at 12 h p.i. and to <0.1% ID/mL after 48 h post injection. The IgE isotype

Table 3.7: Blood clearance of Anti-CSPG4-IgE and -IgG and IgE isotype control over 120 hours. Values are %ID/mL (n=3).

mAB/ time (h)	4h	12h	24h	48h	72h	120h
Anti-CSPG4-IgG	25.56	13.29	13.18	5.76	2.12	3.96
IgE isotype control	0.55	0.17	0.12	0.07	0.04	0.03
Anti-CSPG4-IgE	2.25	1.10	0.36	0.08	0.10	0.04

control showed even lower values, at 0.5% ID/mL at 4 h p.i.. Measurements taken at the 24 h time point and later remained at or below 0.1% ID/mL.

Biodistribution data collected in the *in vivo* experiments were used to research the elimination and metabolism of IgE (Figure 3.13; Table 3.8). The main way of elimination of anti-CSPG4-IgE was via liver and excretion via the intestinal way. At the 4 h time point almost 21% of the overall injected dose was already excreted. Levels of activity inside the mouse dropped to about 55% of the injected dose at 24 h. 120 hours post injection more than 80% of the injected dose were excreted.

99% of the injected dose of the unspecific isotype control was measured at 4hours p.i. dropping within 12 hours to 50% ID. Compared to anti-CSPG4-IgE elimination was very similar. Between the time points of 48 h and 120 h p.i. the values observed for the isotype control remained ~10% ID below the values measured for anti-CSPG4-IgE.

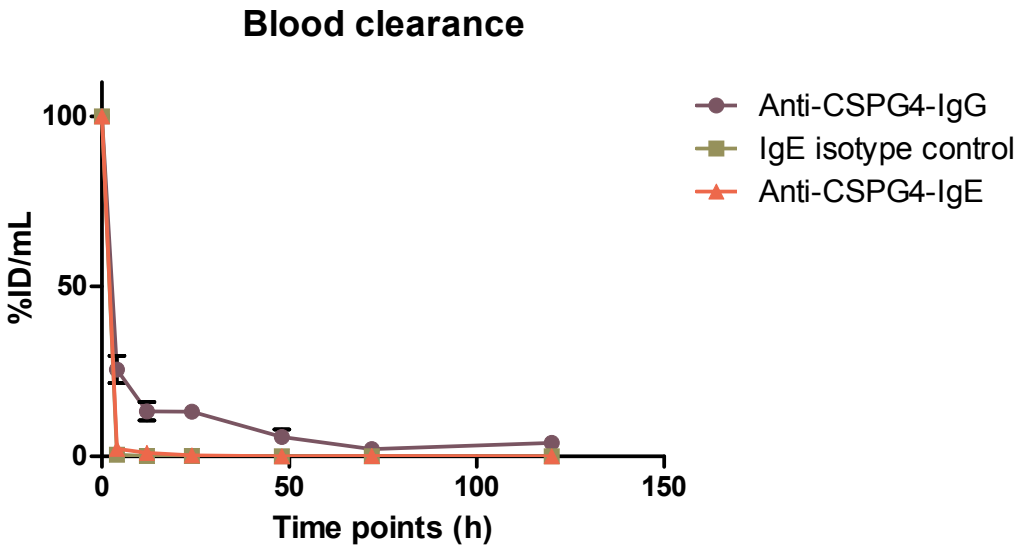

Figure 3.12: Blood clearance of Anti-CSPG4-IgE (red) and -IgG (violet) and IgE isotype control (green) over 120 hours.

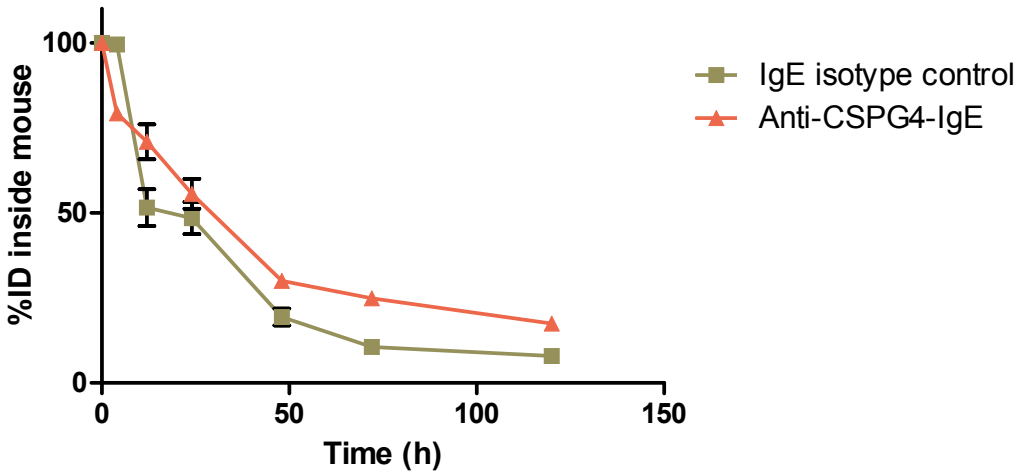

Figure 3.13: % ^{111}In-anti-CSPG4-IgE (red) and IgE isotype control (green) retained inside the mouse over the time of 120 h. Half-life of indium-111 inside the mouse was calculated $t_{1/2}$ = 24 hours for anti-CSPG4-IgE and $t_{1/2}$ = 17 hours for the IgE isotype control.

Table 3.8: Excretion of indium-111. Measured are %ID inside the mouse over a time course of 120 h (n=3).

mAB/ time (h)	4h	12h	24h	48h	72h	120h
IgE isotype control	99.49	51.55	48.49	19.39	10.63	7.94
Anti-CSPG4-IgE	79.26	70.91	55.60	30.01	24.92	17.49

3.4 Discussion

3.4.1 Efficacy results

The imaging and biodistribution studies were conducted to complement the positive results of a treatment study comparing anti-CSPG4-IgE with its IgG counterpart (PhD thesis of P. Karagiannis, Cutaneous Medicine and Immunotherapy Unit, St. John's Institute of Dermatology, Division of Genetics and Molecular Medicine, KCL). The results were of the treatment study (Figure 3.1, Introduction) compared anti-CSPG4-IgE to PBS, unspecific isotype controls for IgG and IgE and anti-CSPG4-IgG. Anti-CSPG4-IgE showed significantly better tumour growth inhibition at the same administered dose.

The anti-CSPG4-IgE antibody used in these studies and the presented imaging studies was a human/mouse chimeric IgE with a fully human Fc-region. Since human IgE does not bind to rodent FcεR [4], the results of the treatment study suggest that the observed anti-tumour activity of anti-CSPG4-IgE is mediated by the co-administered human PBMC. The treatment study was in

line with previous studies in other *in vivo* models looking into general IgE anti-tumour efficacy and reviewed in chapter 1 (Introduction) and chapter 3 (Introduction, *in vivo* models) [42, 35, 245].

3.4.2 The NSG mouse model with splenic engraftment of human PBMCs

In earlier studies, described in literature, various rodent models have been used with success to evaluate the *in vivo* therapeutic activity of several IgE antibodies. Here, a similar immunocompromised mouse model (NOD/SCID/Il2rg$^{-/-}$) bearing a human tumour (CSPG overexpression) was used. NSG mice were injected with PBMC prior to the injection of antibodies and splenic engraftment was validated by an ELISA assay (Data from PhD thesis of P. Karagiannis).

Disadvantages of the here used *in vivo* model were that cytokines secreted by human effector cells presumably did not interact with the murine system [246]. Furthermore, PBMC present only a partial cell population that express FcεRs and, in addition, based on the preparation method were restricted to certain cell types such as monocytes but excluding basophils and mast cells [247]. Therefore, biodistribution and targeting of antibodies tested in this model, such as the human/ mouse chimeric anti-CSPG4-IgE, could show differences in biodistribution and targeting when injected into humans and the anti-tumour effects could be even greater in humans without the drawbacks noted above and the source of FcεR-expressing effector cells is natural and constant.

With the human tumour xenograft in conjunction with human lymphocytes carrying FcR's for both IgE and IgG an environment was engineered that allowed a meaningful analysis of therapeutic IgE biodistribution and targeting and comparison to its IgG counterpart. In preparation for the *in vivo* experiments a tumour xenograft of A375 melanoma cells was subcutaneously injected into the lower left flank of each mouse.

3.4.3 Imaging and biodistribution of anti-CSPG4-IgE

The imaging data and biodistribution patterns were expected to be different from the biodistribution seen in general IgG biodistribution. Based on the knowledge of many other radiolabelled IgG antibodies anti-CSPG4-IgG was expected to circulate for a long time in blood and show targeting and accumulation rather quickly [248, 249]. For IgE, it was hypothesised by us, it would bind via its high affinity receptor FcεRI on the surface of human immune effector cells and 'patrol' pre-armed on the surface of these effector cells through tissues, slowly accumulating at the target side [41, 165].

Images were acquired from a mouse systemically injected with indium-111 labelled anti-CSPG4-IgE, anti-CSPG4-IgG or IgE isotype control antibody. Biodistribution data were obtained from dissected organs of mice injected with radiolabelled IgE, IgG or isotype IgE antibody from the same indium-111 labelled antibody stock prepared for imaging but with lower specific activity. Anti-CSPG4-IgE results showed a distribution with a very rapid blood clearance and accumulation

of radioactivity in the liver. Nearly all signal seemed trapped in the liver, with some signal in the spleen. Signals from the intestines indicated a fast excretion from the liver.

Biodistribution data confirmed the short serum half-life of IgE seen in the imaging study. The calculated biological half-life was 17 hours for IgE isotype control and 25 hours for anti-CSPG4-IgE. This half-life was calculated from excretion data of indium-111 and shows the half-life based on all tissues combined and is not to be confused with half-life calculated from blood clearance. From early IgE turnover studies by Waldmann et al., it is known that IgE has the lowest serum concentration compared to all other immunoglobulin classes and subclasses [250]. Intact IgE has a half-life in serum in healthy human adults of ∼2 days measured in blood samples [251]. Half-life of IgE in rodents is considerably shorter than in humans (5-12 h). For the half-life it has to be taken into account that anti-CSPG4-IgE is a chimeric mAb in a humanised mouse model and IgE half-life in rodents were measured by different serological quantification assays in different non-disease or tumour bearing mouse models.

In line with the publications by Haba et al. [46] of IgE half-life in rodents, an initial clearance phase of IgE could be seen in the biodistribution data presented in this chapter during the first hours. Haba et al. [46] determined the half-life of IgE in rodents at initially 1-2 hours with a progression of a relatively constant half-life of 5 to 8 hours after the first rapid blood clearance. Here, similar to observations by Haba et al,. after the first fast blood clearance phase a very small amount in the ng/mLregion seemed to remain in circulation with a longer half-life. This was calculated using the %ID in blood against the overall injected dose. Waldmann and colleagues [250] described a high catabolic rate for IgE and postulated two clearance mechanisms responsible, the intravascular and extravascular catabolic pathway. The intravascular pathway is the same to all immunoglobulins but later studies confirmed an extravascular pathway that is specific to IgE only [252]. Iio and colleagues [251] proposed the cellular catabolism of IgE may be related to the binding of IgE to basophils and mast cells through FcεRI. However, in those experiments, a rapid catabolic rate of ^{125}I- and ^{131}I-labelled IgE was demonstrated by their finding that a high proportion of free radiolabel was recovered from urine. This observation suggested that IgE antibody available to FcεRI-bearing cells were constantly being turned over rather than sequestered on FcεRI-bearing cells, where they would be unavailable for degradation. No further literature with strong evidence could be found and the full catabolic pathway of IgE remains not clearly identified today. The results in this chapter show that the extravascular pathway dominates and is based on liver uptake.

The blood clearance was in direct relation to the liver accumulation of anti-CSPG4-IgE. Several factors may be responsible for this accumulation in liver. The high mannose glycosylation of IgE and B cells residing in the liver that can bind IgE via the CD23 receptor.

In vivo data observed here suggests that IgE circulating free in serum could be cleared by several mechanisms. In earlier studies by Baenziger, Fridriksson and Arnold [201, 253, 200] IgE was identified to have high-mannose structures present, which included several terminal mannose

structures on its glycosylation sites located within the heavy chains [200]. It is known that terminal mannose or galactose groups, presented after antigen-antibody binding, lead to a rapid clearance of IgG and IgD immunoglobulins through the liver by lysosomal degradation [254]. These mannose sugar residues are otherwise not exposed on antibodies other than IgE. The terminal mannose sites, thus, might account for the IgE accumulation in the liver. Free IgE could also be bound in serum by mannose binding lectin (MBL) which is part of the innate immune system complement cascade. However, the complement system was not fully developed in the *in vivo* model used (NOD/ SCID/Il2rg$^{-/-}$ mice) and, therefore, the mechanism remains questionable as a reason for mediating the extensive liver binding of IgE.

An interesting experiment which points clearly at mannose glycosylation as main factor of the extensive liver binding was the injection of deglycosylated anti-CSPG4-IgE into one mouse and the biodistribution study at 48 h post injection. Although, the data is statistically not significant because only one animal was used and the experiment was crude, it showed clearly a reduction of liver uptake by two thirds and a higher 14% ID/g tumour uptake. By removing the mannose glycosylation of IgE the biodistribution characteristics resemble more the ones of IgG. However, this experiment has to be repeated for obvious reasons and more data is needed.

The comparison of imaging and *ex vivo* distribution data of IgE and IgG revealed a very different picture of the two mAbs. Anti-CSPG4-IgG share the same variable region (Fv) with anti-CSPG4-IgE, with the same affinity and epitope recognition [41, 4]. However, the Fc-region is isotype dependent. Anti-CSPG4-IgG followed in the NanoSPECT/CT scan and in the biodistribution a familiar distribution pattern seen in other publications looking into targeted full size IgG antibodies [255, 98, 248, 256, 242].

Accumulation in the spleen based on FcR interaction with lymphocytes residing in large numbers in the spleen is known from previous studies on IgG. Here, anti-CSPG4-IgG showed a very high signal uptake in spleen. This was based on the very small developed spleen in NSG mice and the engraftment of PBMCs in the spleen. The high spleen uptake was also observed for anti-CSPG4-IgE but less high than IgG. This may indicate FcR interaction of IgE and IgG antibodies to human PBMCs since the spleen was the main site of PBMC engraftment.

3.4.4 Tumour-to-blood ratio and tumour accumulation

Processing biodistribution data as tumour-to-blood ratios (tbr) for IgG is used to unmask contaminating blood signal effects. The perfusion effects of IgG circulation in blood can distort results to some extent. Thus, higher blood activity represented in target organs can account for signal originating from blood perfusion and an increased non-specific organ uptake. Significantly higher uptake of tumour specific IgE compared to unspecific IgE were observed. Uptake in tumour compared to blood levels of ^{111}In-anti-CSPG4-IgE was comparable to its IgG counterpart. This cannot

be explained by a contaminating effect of IgE circulation and tumour blood perfusion. In general, IgE did not show the extended half-life in serum and blood circulation like IgG [46, 257, 241]. However, IgE did show some specific targeting despite its fast clearance because the tbr was similar.

3.4.5 Tumour-to-muscle ratio

A different measurement of IgE activity is the tumour-to-muscle ratio (TMR). TMR is mostly used as an important marker for [^{18}F]FDG to confirm standard uptake values (SUV) and establish the anti-tumour activity of inhibitors [258]. IgE half-life in serum is very short (2-4 hours) but the half-life of IgE in tissues, presumably bound to FcεR receptors on the surface of immune effector cells, is estimated at approximately 2 weeks [44, 47]. To compare IgE in the tumour tissue to non-tumour tissue was of major interest as both tissues were expected to show signal originating from IgE bound to FcR receptors on the surface of immune effector cells located in tissues. It is not clear from the data, tbr or tmr on anti-CSPG4-IgE if the accumulation at the tumour site was from circulating IgE (even if it was only a very small amount) or an accumulation of IgE actively trafficked into the tumour site bound on the surface of immune effector cells. The hypothesis of IgE bound to the surface of FcεR expressing effector cells actively infiltrating the tumour cannot be answered with the imaging and biodistribution data gathered in this thesis.

3.4.6 Comparison with IgE isotype control (MOv18-IgE)

Chimeric MOv18-IgE was used as an unspecific IgE isotype control. The target of MOv18-IgE is the folate receptor alpha (FRα) which is expressed in normal tissues at the luminal surface of epithelial cells and inaccessible to the circulation [91, 259]. FR*alpha* was not overexpressed on A375 tumour cells. Comparison of the NanoSPECT/CT scans and biodistribution data showed overall a similar distribution pattern of the IgE antibodies, anti-CSPG4-IgE and MOv18-IgE. However, IgE isotype control signal accumulation in liver was ∼40% lower than anti-CSPG4-IgE at 48 hours, signal in spleen was 53% lower while signals from the intestines were 40% higher indicating a faster catabolic rate of unspecific IgE. Tumour uptake of anti-CSPG4-IgE was ∼80% higher compared to its isotype control. Therefore, a significant influence of the specificity of anti-CSPG4-IgE against the tumour receptor in biodistribution over time and treatment were observed. This was seen in the tmr as well.

4 *In vivo* comparison of an engineered rat MOv-18-IgE and -IgG in a immunocompetent disseminated tumour rat model

4.1 Introduction

4.1.1 Aim of the work on rat MOv18 IgE

The aim of the work presented in chapter 4 is the comparison of the *in vivo* fate and biodistribution of therapeutic antibodies rMOv18-IgE and rMOv18-IgG targeted against the human folate alpha receptor (FRα). Both antibodies were engineered to allow a comparison of IgG and IgE with identical variable domains (Fv) but different antibody class determining region (Fc). In a series of experiments rMOv18-IgE and -IgG antibodies were radiolabelled and biodistribution studies and NanoSPECT/CT scanning were employed to visualise and compare targeting, organ and tissue distribution and clearance of both antibodies. For the *in vivo* studies a new fully immunocompetent surrogate rat model system was introduced. Rat MOv18-IgE (rMOv18-IgE) and rat MOv18-IgG (rMOv18-IgG) antibodies were engineered as chimeric (rat/mouse) antibodies with rat constant domains and mouse variable domains specific to the human FRα. The antibodies were targeted against a human ovarian carcinoma antigen, the human folate receptor alpha (FRα), which is overexpressed and upregulated on a number of human tumours, including over 90% of ovarian carcinomas. For these studies an engineered rat cell line expressing FRα was used. Both antibodies were conjugated to CHX-A"-DTPA and radiolabelled with indium-111 using the method described in chapter 2.

To identify the potential role of therapeutic MOv18-IgE and effect in the tumour therapy, biodistribution studies and NanoSPECT/CT imaging of indium-111 labelled MOv18-IgE were performed. The methods of the imaging and biodistribution studies followed the description of imaging and biodistribution in chapter 3. The focus of the experiments in this chapter was on the deployed immunocompetent surrogate rat model described below and the comparison of rat

MOv18-IgE and -IgG in a native environment.

4.1.2 *In vivo* Model

The model used in chapter 3 whilst providing a comparison of IgE and IgG antibodies *in vivo*, does not provide a full picture of the biological behaviour of these two antibody classes in their normal biological setting because the antibody Fc-domains (human) and the host organism (mouse) are from different species. This is not fully resolved by grafting of human immune cells into the mouse. This leads to the following specific limitations:

- In contrast to human IgG which binds to murine Fc receptors, human IgE does not interact with rodent FcεRs. There is also a different cellular distribution of FcεRs in humans and rodents [260, 6]. Rodent models can, therefore, not readily be used to assess antibody efficacy that depends on FcεR mediated recruitment of effector cells. As described in more detail in chapter 3, this was one disadvantage of the NSG mouse model used for anti-CSPG4-IgG and -IgE.

- FcεRI receptor distribution and structure in mice and humans show significant differences. Murine FcεRI is expressed solely on mast cells and basophils but human FcεRI is expressed on mast cells, basophils, eosinophils, monocytes, Langerhans cells, and DC [6].

- human and rat FcεRI but not the murine FcεRI show structural similarities. While murine FcεRI is always found in a tetrameric configuration, functional human and rat FcεRI can exist either as an $\alpha\beta\gamma 2$ tetramer or as an $\alpha\gamma 2$ trimer [64, 6]. Importantly, the α chain of the human receptor is sufficient to bind human IgE [261].

- In addition, the expression level of human FcεRI is much higher on mast cells and basophils compared to the other human cell types [6]. These expression levels and the above described effector cell distribution are similar between human and rat but not mouse, with the exception of FcεRI expression on human Langerhans cells and DC cells which is not found in rats or mice.

- The low affinity receptor FcεRII shows differences in expression pattern in mouse and humans. In humans, CD23 is expressed on eosinophils, monocytes, lymphocytes, follicular DC, Langerhans cells, and platelets. In the mouse, CD23 is expressed mostly on B cells and a subset of T cells [260, 262].

- Another limitation referring to the NSG mouse model employed in chapter 3 is that the self-replenishing supply of human effector cells was only partly overcome by the injection and engraftment of PBMC in xenograft models of immunocompromised mice. Limitations remaining were that human cytokines secreted by human effector cells may have not interacted

with the murine immune system [246]. In addition, the type of effector cells that express FcεRs in the PBMC preparations is restricted [247]. Thus, the full spectrum of human effector cells (including basophils and mast cells) were not active in the model used in chapter 3.

Therefore, in this chapter we compare the behaviour of the two classes of antibody in which the constant domains and the host animal are the same species - i.e. the rat. This serves two purposes: it enables the study of the effect of the interactions of the constant domains of the antibodies with their host immune system; and it provides a model for the use in the clinical setting of IgE as a therapeutic antibody, in which biodistribution, tumour targeting and potential toxicities can be evaluated.

The immunocompetent rat lung metastases model was developed and validated in cooperation and under the lead of Debra Josephs (D.H. Josephs, Cutaneous Medicine and Immunotherapy Unit, St. John's Institute of Dermatology, Division of Genetics and Molecular Medicine & NIHR Biomedical Research Centre at Guy's and St. Thomas's Hospitals and King's College London, London, UK). Further investigations of efficacy, toxicology and pharmacodynamics of rMOv18-IgE were performed by Debra Josephs.

4.1.3 MOv18-IgG

The murine monoclonal antibody MOv18 IgG1, binding the FRα, originated from an immunisation experiment in mice using a surgical specimen of ovarian carcinoma [263]. Later, Buist et al. demonstrated localisation of chimeric MOv18-IgG antibody [264] in ovarian carcinoma tissue and was able to show a prolonged accumulation in the tumour relative to normal tissues. Several clinical studies presented the targeting of FRα with a chimeric MOv18-IgG as a safe and promising potential therapeutic for the treatment of ovarian carcinoma [109, 265].

For the work with the rat surrogate *in vivo* model the variable region was re-engineered based on the original chimeric MOv18-IgG. The rat MOv18-IgE and -IgG antibodies were designed as chimeric antibodies with rat constant domains and mouse variable domains specific for the human FRα. The heavy and light chains of each rat MOv18 antibody were cloned into a single mammalian expression vector containing a hygromycin resistance gene (pVITRO1) allowing the transfection, selection and antibody expression by HEK293-F cells (cloning performed by T. Dodev, Randall Division, King's College London). Rat IgG2b class corresponds to the human IgG1 class antibody in terms of effector function [266].

MOv18-IgE efficacy studies

Earlier studies showed a significant therapeutic efficacy advantage of MOv18-IgE over MOv18-IgG across different xenograft tumour models and different routes of injection, [41, 165, 13, 170, 35]. To further investigate the hypothesis that IgE antibodies may offer some advantages over IgG

in passive immunotherapy of cancer and to translate MOv18-IgE into clinical first-in-man studies, a rat MOv18-IgE, targeting the ovarian tumour associated antigen FRα was engineered and compared to MOv18-IgG. MOv18-IgE was evaluated in an immunocompromised mouse xenograft model of ovarian carcinoma. Results showed inhibition of tumour growth in treatment with MOv18-IgE and -IgG when co-injected with PBMCs. After 19 days no longer-lasting effect of IgG could be seen while MOv18-IgE continued to show significant growth inhibition to the end of the experiment at day 35 and 48 [41]. Karagiannis and colleagues confirmed anti-tumour efficacy of MOv18-IgE in a different nude mouse model using patient-derived human ovarian carcinoma xenografts. Results seen were similar to earlier experiments and in addition to the tumour growth inhibition the tumour infiltration of human monocytes could be shown. MOv18-IgE was again co-injected with human PBMC [165]. A later study published by Karagiannis et al. analysed the mechanisms of MOv18-IgE anti-tumour activities. The study highlighted that within the heterogeneous cell group of peripheral blood lymphocytes, monocytes were essential to mediate the enhanced anti-tumour capabilities of IgE [13].

4.2 Materials and Methods

4.2.1 Rat MOv18-IgE and -IgG Antibody Production and Purification

Transfected cells were grown in AppliFlex Single Use Bioreactors (Applikon Biotechnology) and antibody production was monitored in culture supernatants by ELISA. Pilot experiments determined that the optimum timeframe for supernatant harvest, at which point the maximum level of antibody was detected in the cultures, was between 7 - 10 days following transfection. Following rat IgE and IgG detection by ELISA, culture supernatants were collected. Volumes of less than 5 L were filtered using Vacuum Stericup® filter units (0.22 μm pore size; Millipore). Larger volumes were filtered using a pump-driven Sartoclean® MidiCap pre-filter unit (3 + 0.8 μm pore size; Sartorius Stedim Biotech) followed by a pump-driven Sartpore® 300 filter unit (0.45 + 0.2 μm pore size; Sartorius Stedim Biotech). After addition of sodium azide (0.1% final concentration) the supernatants were directly applied to the appropriate purification medium. Purification of rat MOv18-IgE and -IgG was investigated using different methods. FPLC-SEC was used for analysis and fractionation of the purified antibodies. Fractionation was performed to isolate pure monomeric antibodies from oligomers and aggregated materials according to size.

4.2.2 CC531tFR Cell Line

The adherent CC531 cell line is derived from a chemically-induced colon adenocarcinoma of a WAG rat model for hepatic colon cancer [267] and transfected with to express human FRα (Dr. S. Canevari, Prof M. Colnaghi, Instituto Nazionale Tumori, Milan, Italy) and provided as a gift.

Cells were maintained in RPMI 1640 with standard additives, additionally supplemented with 0.4 mg/mL G418 to maintain selection of the transfected human FRα plasmid. Cells were passaged at a ratio of 1:6.

4.2.3 WAG rats

As part of this work, an immunocompetent rat model bearing a syngeneic rat tumour expressing human FRα antigen was established in collaboration with Debra Josephs. This model was used to further evaluate the biodistribution and for NanoSPECT/CT imaging of rMOv18-IgE. The rat colon carcinoma cell line CC531tFR (where tFR stands for transfected with human FRα) was transfected to express the human FRα and was syngeneic with the WAG rat strain. CC531tFR grows as lung metastases when injected intravenously. To evaluate the optimal dose of i.v. CC531tFR tumour cell inoculation in the development of the lung metastasis model in WAG rats, rats were given CC531tFR tumour cells i.v. in 250 μL PBS at increasing concentrations. Lung tumour burden was determined by two different methods; the first calculated the mean number of surface-visible metastases counted in 3 separate demarcated 1 cm^2 areas (reported as number of metastases/cm^2) [268, 269]. For the second method, each lung was dissected into 3 sections and each section imaged using a Nikon SMZ1500 Stereo Microscope (Nikon UK Ltd.). Analysis was performed using NIS Elements Basic Research software (Nikon) in order to determine the total surface area (mm^2) occupied by the entire lung section and by the white tumours. After 20 days the rats were sacrificed and the lungs infused with 15 % Indian ink solution followed by destaining in Fekete solution for 24 hours. The number of lung metastases per cm^2 surface lung area was determined for each rat. Representative image of a rat lung 26 days after i.v. injection of syngeneic CC531tFR tumour cells is presented in figure 4.1. At a dose of $4x10^6$ CC531tFR injected cells an average of 8.5 $\pm$ 2.9 lung metastases/cm^2 was observed (n = 5 rats) and this dose was chosen as optimal for all following experiments (PhD thesis of Debra Josephs, 'Antibodies of the IgE Class: Preclinical Evaluations for Therapeutic Use in the Treatment of Solid Tumours'). WAG rat *in vivo* work was in line with approved guidelines for the humane treatment of animals (Home Office, 1995). Animal studies were carried out in accordance with UK Research Councils' and Medical Research Charities' guidelines on Responsibility in the Use of Animals in Bioscience Research, under UK Home Office Project and Personal licences.

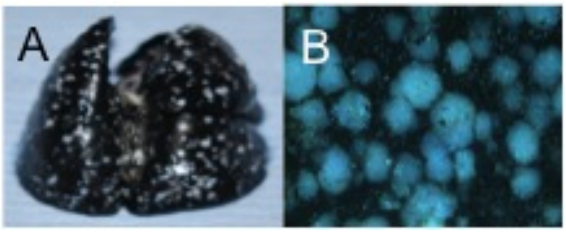

Figure 4.1: Rat lung 26 days after i.v. injection of syngeneic CC531tFR tumour cells. The lung was infused with 15 % Indian ink solution followed by destaining in Fekete solution for 24 hours. A. Overview of the whole lung, B. Close up

4.2.4 Conjugation and radiolabelling of rat MOv18-IgE and -IgG antibodies with Bi-functional chelator p-SCN-Bn-CHX-A"-DTPA

Methods describing the conjugation and radiolabelling of MOv18-IgE and -IgG are described in detail in chapter 2.

4.2.5 NanoSPECT/CT imaging of rat MOv18-IgE and -IgG in the lung metastasis tumour model

Imaging experiments were performed using a NanoSPECT/CT instrument/scanner (Bioscan, US). Generally, an intravenous tail vein injection was performed on WAG rats with ∼100-150μL of ∼10-20 MBq of 0.07 mg protein under anaesthesia (Isoflurane, VetOne, UK). WAG rats were injected intravenously on day 0 with tumour cells (CC531) and on day 28 a dose of ^{111}In-rMOv18-IgE or ^{111}In-rMOv18-IgG was injected via a tail vein. Following the injection, rats were scanned at 20 min, 24 h, 48 h, 72 h and 144 h using NanoSPECT/CT. Rats were transferred onto the NanoSPECT/CT heated (37°C) rat bed which supplied anaesthesia throughout the imaging experiment. A low resolution CT (topogram) of the whole animal was first acquired so that a scanning range could be set (parameters: tube voltage - 45 kVp, exposure time - 500ms, topogram direction - side view, rat position - prone and feet-first). Next a CT of the chosen range was performed (parameters: acquisition field; number of projections - 180, pitch - 1, number of scans - 1, frames field; frame resolution - standard, tube voltage -45kVp, exposure time - 500ms). Finally SPECT imaging was carried out using 1mm 9-pinhole Rat apertures and Pyramid collimators in helical scanning mode (parameters: detected energy range - 126-143 keV, number of projections - variable, time per projection ∼60 seconds). Scan times were approximately 5 min for topogram, 6 min for CT, and variable from minimum of 25 min to up to 60 min for SPECT acquisition. The scan time was variable, adjusted depending on injected dose and time lapsed after protein injection. Images were reconstructed using InVivoScope software (Bioscan).

4.2.6 *Ex vivo* Biodistribution Studies

Tumour-bearing rats were injected through the tail vein with ^{111}In labelled rMOv18-IgE or -IgG antibodies conjugated p-SCN-Bn-CHX-A"-DTPA chelator using the methods outlined in chapter 2. A group of male and female WAG rats bearing CC531tFR metastatic lung tumours were injected with one of the radiolabelled antibodies. Rats (three per group) were killed at 8 h, 24 h, 48 h and 144 h post injection of the radiolabelled antibody. Blood, tumour, and various organs were immediately collected and weighed on an analytical balance. Radioactivity in all organs was measured by gamma counting after the last biodistribution time point at 144 h together with standards prepared from the injected material. Percent injected dose (% ID) was calculated. The blood volume was estimated in mL based on 6% of the total body weight of the rat. Percent of injected dose/g (% ID/g) was calculated for each organ, as well as tumour-to-blood and tumour-to-muscle ratios.

4.3 Results

4.3.1 NanoSPECT/CT and biodistribution study

The aim of this study was to compare the rat MOv18-IgE and rat MOv18-IgG antibody in an immunocompetent syngeneic tumour model. This was performed using NanoSPECT/CT to visualise antibody targeting, clearance and organ and tissue distribution continuously over specific time points up to 144 hours post injection. The imaging study served as a ">rangefinder"< study to find the best time points for biodistribution and identify organs that needed sampling. For each indium-111 labelled rMOv18-IgE and -IgG antibody, a rat was injected with ∼100 μg of the radiolabelled (5 MBq) rMOv18-IgE antibody or with ∼100 μg the radiolabelled (5 MBq) rMOv18-IgG antibody. This was for the imaging study only. Imaging was performed at 20 min, 24 h, 48 h and 144 h post injection via NanoSPECT/CT.

In addition, *ex vivo* biodistribution studies were performed in order to quantify biodistribution. At each time point (8h, 24h, 48h, 144h post injection of radiolabelled rMOv18-IgE or -IgG) 3 rats were were culled for biodistribution, tumour targeting and clearance studies. For biodistribution studies, for each time point a number of rats (n=3) were systemically injected with ∼100 μg of ^{111}In labelled rMOv18-IgE antibody or rMOv18-IgG antibody, respectively, with ∼5 MBq at the beginning of the study. The biodistribution study included culling time points at 20 min, 24 h, 48 h, and 144 h post injection. Antibody radiolabelling results are discussed in chapter 2. Also, antibody production and purification results are described in the PhD thesis of Debra Josephs (PhD thesis of Debra Josephs, 'Antibodies of the IgE Class: Preclinical Evaluations for Therapeutic Use in the Treatment of Solid Tumours').

4.3.2 MOv18-IgE

NanoSPECT/CT

One WAG rat was injected intravenously on day 0 with tumour cells (CC531) expressing the human FRα and on day 28 a single dose of ^{111}In-rMOv18-IgE was injected via tail vein. The individual rat was scanned at 20 min, 24 h, 48 h, and 144 h using NanoSPECT/CT (Figure 4.2).

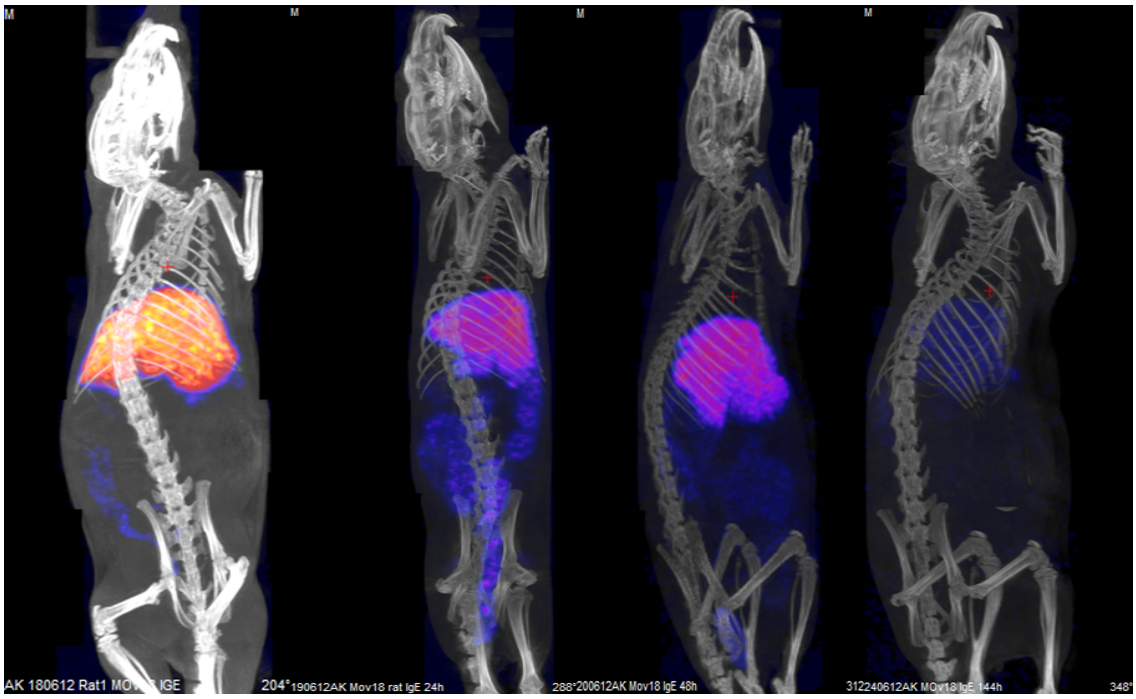

Figure 4.2: NanoSPECT-CT images of tumour bearing rat injected with In-111 labelled rMOv18-IgE. Sequence of images of an individual rat over the time course of 144 hours (from left to right: 20min, 24h, 48h and 144h after injection).

Whole body imaging showed rapid (20min p.i.) accumulation of ^{111}In-rMOv18-IgE in the liver (signal in spleen can be observed in 3D rotating images). Additional signal can be seen in the intestines at 20 min post injection. No signal was detected from the lungs were the tumour metastases were located. No signal was observed in blood or heart.

At 24 h post injection signal from the liver was decreased compared to 20 min post injection. Stronger signal from the intestines was visible. 48 h post injection of indium-111 labelled rMOv18-IgE the strongest signal was still visible in liver. Signal from the intestines was still apparent.

At the last scan at 144 h post injection signal has decreased overall. Low but distinct signal was observed from the liver. At no time point could a visual signal be confirmed at the tumour site (lung tissue with tumour metastases).

Biodistribution

For organ and tissue distribution studies (Figure 4.3, Table 4.1) of rat MOv18-IgE WAG rats were injected intravenously with human FRα expressing CC531tFR tumour cells. About 28 days post tumour cell injection ^{111}In-MOv18-IgE was injected i.v. via tail vein. 3 Rats were culled

per time point, at 8 h, 24 h, 48 h, and 144 h post injection and organs were collected to assess antibody biodistribution. Biodistribution of ^{111}In-MOv18-IgE showed high accumulation in the liver (13.7% ID/g) at the first time point, 8 h post injection). The second time point at 24 h showed a significant drop to 8% ID/g. Radioactivity in the liver declined further to 6% ID/g at 48 h and to 2.5% ID/g at 144 h.

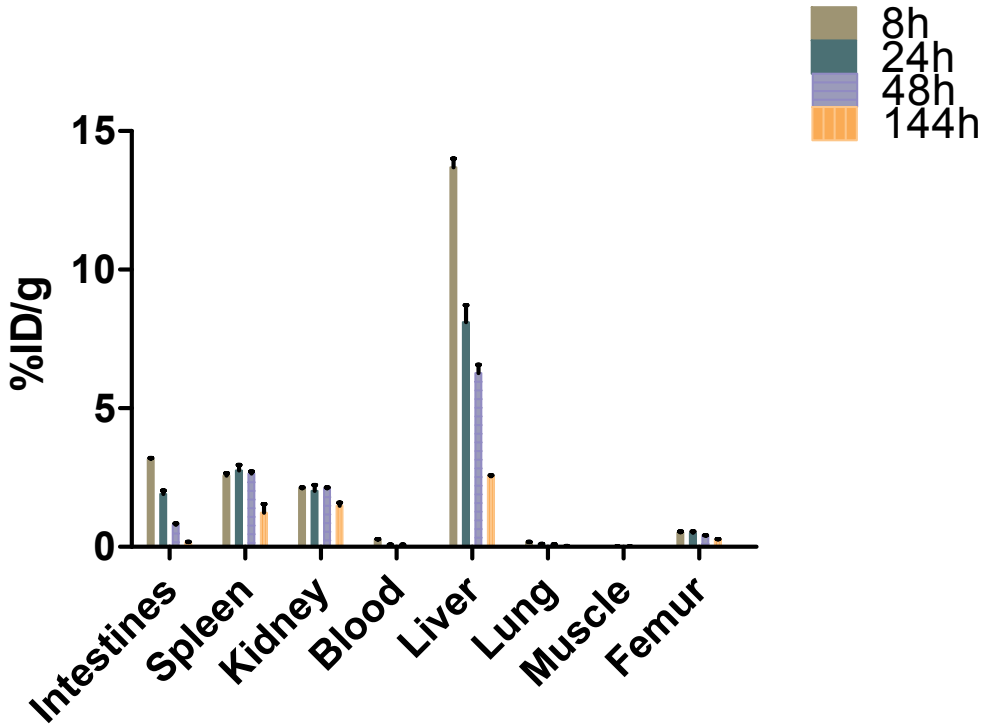

Figure 4.3: Biodistribution in a disseminated tumour bearing rat injected with radiolabelled rMOv18-IgE in % injected dose per gram of tissue at different time points. 8h time point (red); 24 h (blue); 48h (pink); 144 h (green). Data plotted including SEM error bars.

Activity measured in the blood pool was 0.25% ID/mL after 8 h post injection, progressively dropping to below 0.01% ID/mL at 144 h. In the spleen a moderate accumulation of radioactivity was measured over the first 48 h post injection. At 8 h 2.5% ID/g, at 24 h 2.7% ID/g and 2.6% ID/g at 48 h were observed. Signal from the spleen then decreased over the next time point at 144 h but remained at a higher level compared to other organs (other than liver) at 1.4% ID/g. Intestines showed a high signal at 8 h (3.1% ID/g) and the signal decreased steadily and fast to 1.9% ID/g at 24 h and 0.8% ID/g at 48 h to 0.17% ID/g over the next 144 h. An injected dose per gram of around 2.0% was observed in the kidneys over the first 48 hours before dropping to 1.5% ID/g. Lung tissue (including the tumour) showed only minimal uptake with 0.17% ID/g of ^{111}In-rMOv18-IgE measured at 8 h, 0.1% ID/g at 24 h and 0.05% ID/g and 0.02% ID/g, respectively, for 48 h and 144 h.

The biodistribution is shown as injected dose per organ for each time point in Figure 4.4. Data values are shown as mean with SEM (n = 3 rats) and showed distribution of gamma signal

Table 4.1: Biodistribution of rat Mov18-IgE in WAG rats over the time course of 144 hours. Data for selected organs and tissue at 8 h, 24 h, 48 h and 144 h post injection (n=3).

Tissue/Time point	8h	24h	48h	144h
Intestines	3.163	1.909	0.790	0.173
Spleen	2.574	2.755	2.646	1.235
Kidney	2.110	2.019	2.109	1.482
Blood	0.255	0.080	0.058	0.008
Liver	13.691	8.112	6.270	2.548
Lung	0.172	0.103	0.080	0.027
Muscle	0.016	0.011	0.012	0.009
Femur	0.519	0.506	0.417	0.267

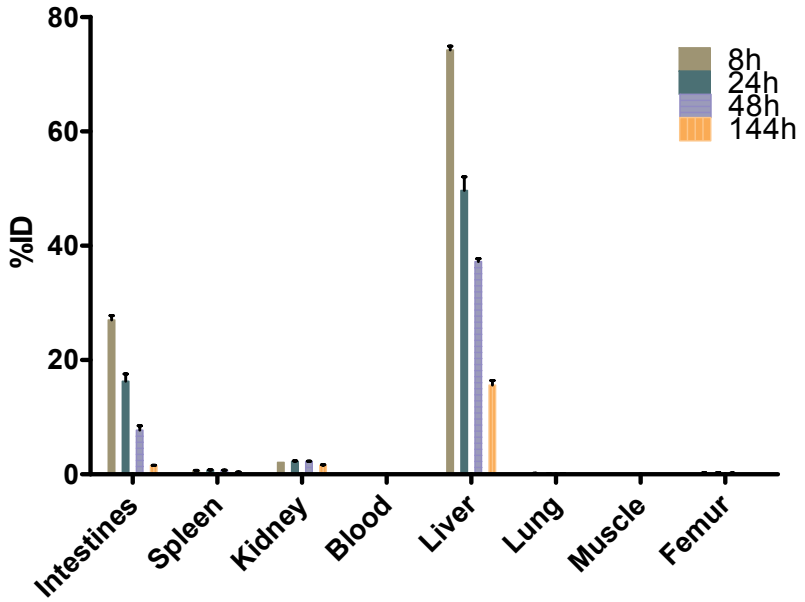

Figure 4.4: Biodistribution of rat Mov18-IgE in selected organs and tissue showing the calculated percentage of the injected dose. Values are mean with SEM (n=3 rats). 4 time points of biodistribution colour coded for time post injection in olive=8h, green=24h, blue=48h and orange=144h.

without the normalisation for weight. At 8 hours post injection about 75% of the injected dose was measured in the liver. Radioactivity in the liver then dropped to 50% ID at 24 hours and 37% ID at 48 hours, respectively. The last value observed in the liver at 144 h p.i. was 16% of the injected dose.

Signal in the spleen, although relatively high when normalised against its weight, was low when seen in % injected dose. 8 h post injection it was observed at 0.6% ID with an increase at 24h and 48 h to about 0.7% ID. The last value showed a declined to about 0.4% ID. The intestines showed the highest accumulation of radioactivity after liver with 27% of the injected dose at 8 hours post injection. Values decreased steadily to 16% ID and 7.7% ID at 24 h and 48 h post

injection, respectively. At 144 h the %ID was at 1.6.

Both kidneys were collected together and therefore account for a relatively high organ weight. The % of injected dose was very stable throughout the first 48 hours post injection. Values were at 2.9% at 8 h, 2.4% at 24 h and 2.2% at 48 h post injection. The value at 144 hours was at 1.6% of the injected dose.

At 8 hours post injection overall 1.8% of the injected dose were measured in the blood pool. Values declined to 0.6% at 24 h, 0.5% at 48 h and 0.05% after 144 hours. Blood pool was generally estimated with 6% of the rat's body weight.

Lung which included the metastatic tumour tissue accounted for about 0.18% of the injected dose at 8 hours post injection. The signal in lung declined to 0.08% at 24 h. At 48 h an increase of signal to 0.12% was observed before the signal declined to 0.04% of the injected dose at 144 h post injection.

4.3.3 MOv18-IgG

NanoSPECT/CT

Analogous to the rMOv18-IgE NanoSPECT/CT imaging described above rMOv18-IgG was radiolabelled with indium-111 under the same conditions and used for *in vivo* imaging studies. One WAG rat was injected intravenously on day 0 with tumour cells expressing the human FRα (CC531tFR). About 28 days after the initial tumour cell xenograft injection a single dose of ^{111}In-rMOv18-IgG was injected via tail vein. Following the injection, the individual rat was scanned at 20 min, 24 h, 48 h and 144 h using NanoSPECT/CT (Figure 4.5). NanoSPECT/CT showed the characteristic distribution in the blood pool known from IgG antibodies in general. Strong signal was originating from the heart 20 minutes post injection. This was in line with the signal from blood pool showing in the major arteries and veins. Whole body imaging showed a clear accumulation of ^{111}In-rMOv18-IgG within the lung tissue. The lung was also the metastatic tumour area.

The overexposed, bright signal of activity accumulation in the abdominal area of the rat at the 20 min scan was identified as an artefact. The signal did not show up at the 12 h and 48 h scans. It was not possible to locate the activity to the outside or to a subcutaneous location. Therefore, the area was dissect after the 144 h time point but did not show any activity or visual signs of unexpected tissue (e.g. tumour). This suggests that during the transfer of the rat to the scanning table or at the beginning of the scan a small amount of urine contaminated the abdominal area or the scanner bed.

At 24 h post injection with indium-111 labelled rMOv18-IgG signal was decreased overall. Signal was observed in the blood pool and subsequently in the heart. Significant signal was observed in the lung tissue which contained the metastasis of CC531tFR expressing human FRα. In addition, strong signal from the kidneys was determined.

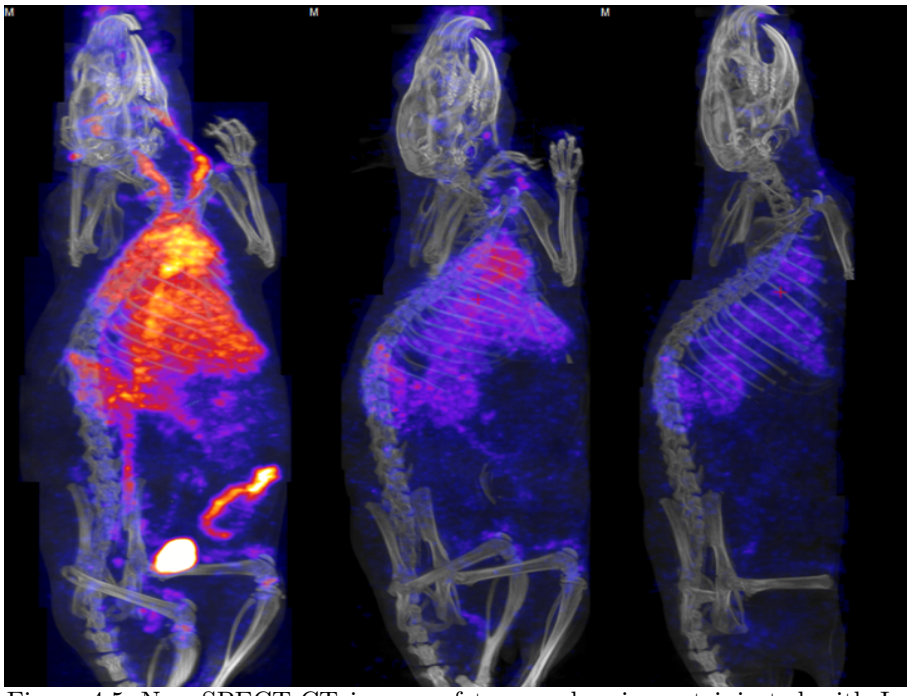

Figure 4.5: NanoSPECT-CT images of tumour bearing rat injected with In-111 labelled rMOv18-IgG. Sequence of images of an individual rat over time of 144 h (from left to right: 20 min, 24 h and 48 h after injection).

48 hours post injection of ^{111}In-rMOv18-IgG a similar NanoSPECT/CT image was taken compared to 24 h post injection. Signal and shapes from heart, lungs and kidneys were visible. General background signal originating from blood pool was seen.

Biodistribution

WAG rats were injected with indium-111 labelled rat MOv18-IgG. Rats for biodistribution were injected intravenously with CC531tFR tumour cells expressing the human FRα receptor. On day 28 ^{111}In-rMOv18-IgG was injected i.v. via tail vein and rats were culled for dissection at specific time points (8 h, 24 h, 48 h and 144 h) post injection. Tissues (intestines, stomach, spleen, kidney, blood, liver, thymus, heart, lung including tumour metastases, salivary glands, trachea, thyroid, muscle, femur and bladder) were collected and analysed (n=3/time point, full data set in the appendix).

Biodistribution (Figure 4.6, Table 4.2) of ^{111}In-labelled rat MOv18-IgG showed accordance with the NanoSPECT/CT images including high retention of activity in the blood pool at the first time point. 8 h post injection signals observed in blood were at 13% ID/mL. Signal from the blood pool dropped down to 5% ID/mL at 24 h post injection and remained at 5% ID/mL at 48 hours post injection. At 144 hours post injection activity from the blood pool showed 2% ID/mL. Signal from the spleen was measured initially at 8.4% ID/g at 8 h post injection and remained at roughly the same level between 48 h and 144 h post injection at 4.7% ID/g and 5.1% ID/g at 24 and 48 hours, respectively, and 4.8% ID/g at 144 h. Kidneys showed elevated uptake of radioactivity with

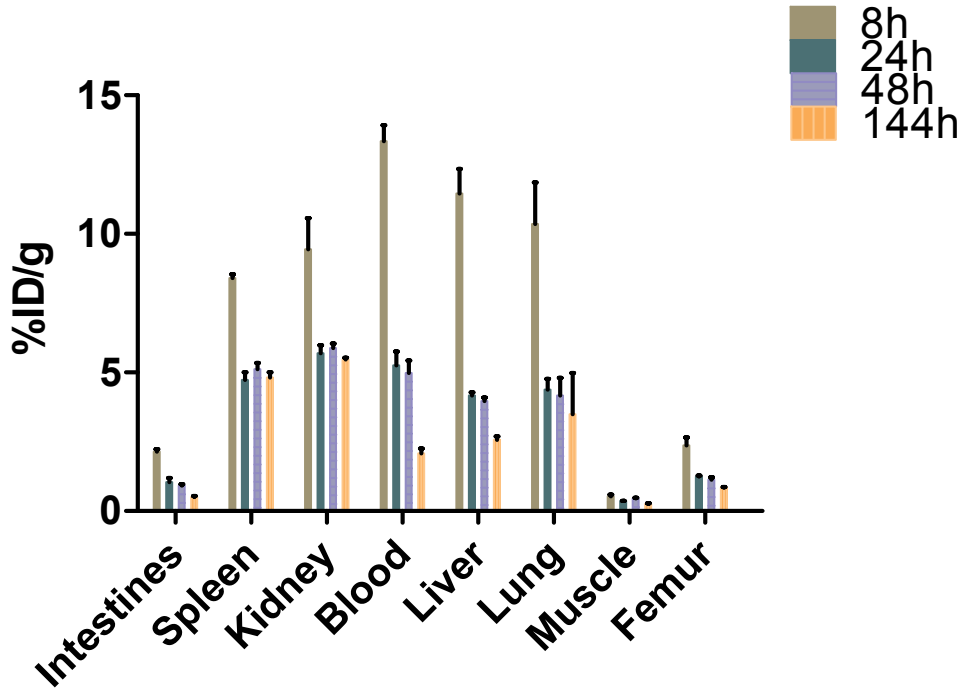

Figure 4.6: Biodistribution of tumour bearing rats (n=3) injected with radiolabelled rMOv18-IgG in % injected does per gram of tissue at different time points. 8h time point (olive); 24 h (green); 48 h (blue); 144 h (orange). Data plotted are mean with SEM error bars.

values measured at 9.4% at 8 h 5.6% ID/g at 24 h. At 48 h and 144 h post injection 5.8% ID/g and 5.4% ID/g were observed. Accumulation of ^{111}In-MOv18-IgG in liver was observed at the 8 h time point with 11.4% ID/g declining to 4.1% and 3.9% ID/g at 24 h and 48 h, respectively, before a further decline to 2.5% ID/g at 144 h. Metastatic tumour bearing lung tissue showed activity accumulation of 10.3% ID/g at the 8 h time point. Measurements showed progressive decline to 4.3% ID/g at 24 h and 4.1% ID/g at 48 h before dropping to 3.5% ID/g at 144 h. Muscle uptake of ^{111}In-rMOv18-IgG was at negligible levels of below 0.5% to 0.25% ID/g over the time course of 144 hours. Figure 4.7 shows the distribution of the injected dose in organs and tissues over a time course of 144 hours post injection of rat MOv18-IgG as % injected dose. Values were not corrected against the weight of the organ or tissue collected. Most activity was observed in blood circulation with about 95% of the injected dose. Activity levels in blood pool declined to about 40% at 24 h and 37% of the injected dose at 48 h, respectively. After 144 hours post injection 16% of the initially injected dose was still found in the blood pool in circulation. Liver showed the second highest accumulation of % injected dose after blood pool. 59% of the injected dose was found in liver at 8 h post injection. A substantial amount of the signal measured in the liver originated from blood perfusion. Metastatic tumour tissue was located within the lung tissue. Lung accounted for about 10% of the injected dose at 8 hours post injection. Signal values were observed at little under 5% ID at 24 and 48 hours before declining to about 3.5% of the injected dose at 144 hours post injection of indium-111 labelled rMOv18-IgG.

Table 4.2: Biodistribution of indium-111 labelled rat Mov18-IgG in a disseminated WAG rat model (n=3).

Tissue/Time point	8h	24h	48h	144h
Intestines	2.138	1.049	0.916	0.501
Spleen	8.405	4.729	5.125	4.822
Kidney	9.449	5.694	5.882	5.475
Blood	13.348	5.261	4.985	2.076
Liver	11.454	4.173	3.968	2.569
Lung	10.357	4.382	4.174	3.493
Muscle	0.529	0.368	0.455	0.259
Femur	2.361	1.245	1.132	0.845

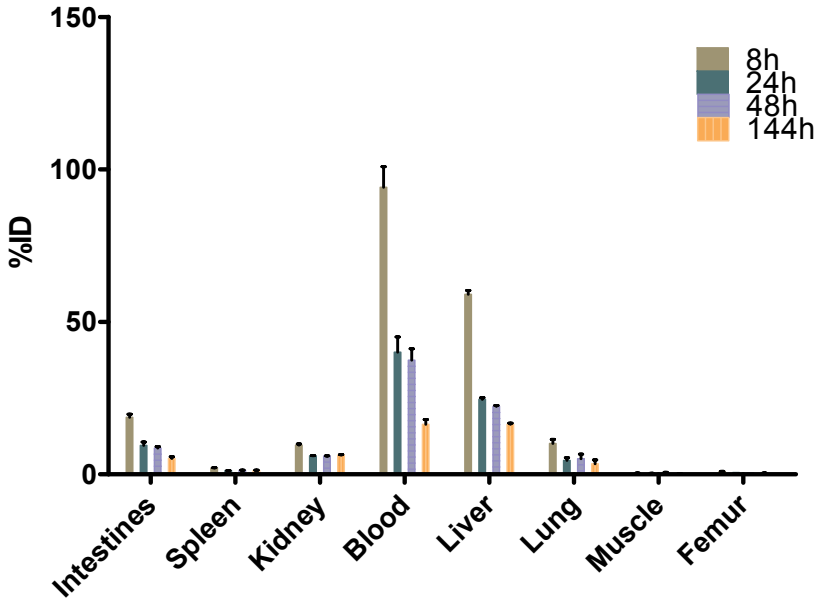

Figure 4.7: Biodistribution of lung tumour bearing immunocompetent rat injected with radiolabelled rat MOv18-IgG in % injected dose in selected organs and tissues at different time points. 8 h time point (olive); 24 h (green); 48 h (blue); 144 h (orange). Data plotted in mean (n=3) with SEM error bars.

4.3.4 Blood clearance of rat MOv18-IgE and rat MOv18-IgG

Blood clearance of MOv18-IgE and -IgG antibody was plotted as % injected dose found in blood over time in hours. Biodistribution data shows blood clearance at time points 8, 24, 48 and144 h post injection (Figure 4.8). At time point 0 h it was assumed that 100% of the dose was injected into the blood via tail vein (the time point 0 h was not measured in the biodistribution study). Figure 4.8 shows blood clearance of MOv18-IgE at 0.25% ID 8 h post injection with further decline to 0.08 and 0.05% ID at 24 and 48 hours, respectively. Signal observed at 144 h post injection was 0.008% ID.

In comparison, MOv18-IgG showed much slower clearance and higher signal in blood at all

time points. Starting at about 94% ID signal from blood pool showed almost no or very slow clearance over the first 8 hours post injection. Signal measurements subsequently declined to 40% ID at 24 h post injection and 37% ID at 48 h. Blood pool observed at 144 hours showed still 16% ID. Analysis of the blood clearance with a one phase exponential decay equation resulted in a half-life of 18.25 hours for MOv18-IgG and 0.9 h for MOv18-IgE in blood.

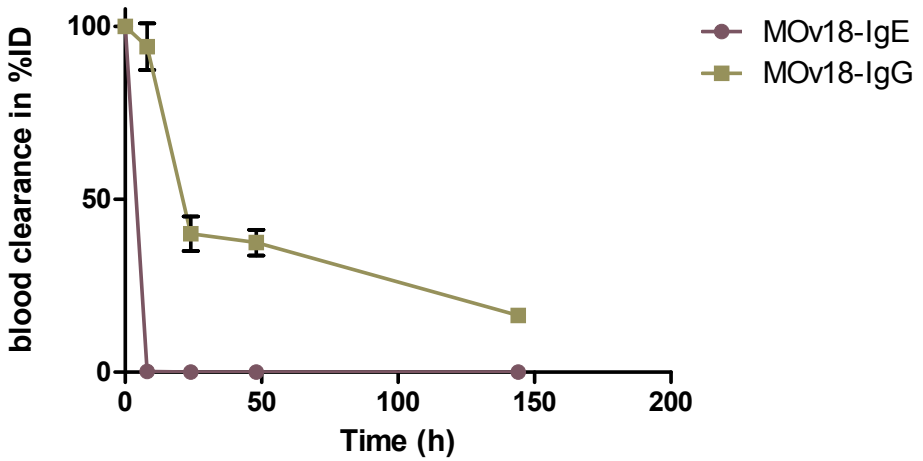

Figure 4.8: Blood clearance plotted in %ID over time in hours. Comparison of blood clearance of rat MOv18-IgE versus rat MOv18-IgG in a disseminated tumour rat model (n=3).

4.3.5 Excretion rate of rat MOv18-IgE

The excretion rate of rMOv18-IgE (Figure 4.9, Table 4.3) shows the total signal originating from indium-111 inside the whole rat plotted against time. The signal from inside the rat body was calculated for each time point by the addition of the activity measured in all dissected organs and tissues (excluding tail) against the injected dose.

The values were fitted into a single exponential equation to calculate the excretion of rat MOv18-IgE. The excretion rate constant of MOv18-IgE was 0.025 h^{-1}. The rate constant was then used to calculate the half-life of MOv18-IgE in an immunocompetent metastatic lung tumour bearing rat. Half-life using the single exponential equation was 27.7 hours. This half-life was measured summarising all radioactivity inside the rat and includes not only full functional free or bound MOv18-IgE but also degraded and metabolised IgE products. The calculation of excretion was only performed for MOv18-IgE but not possible for IgG. The excretion could only be calculated for IgE because of the blood clearance which avoids a 'double' measurement of blood and blood in organs in regards to the % ID.

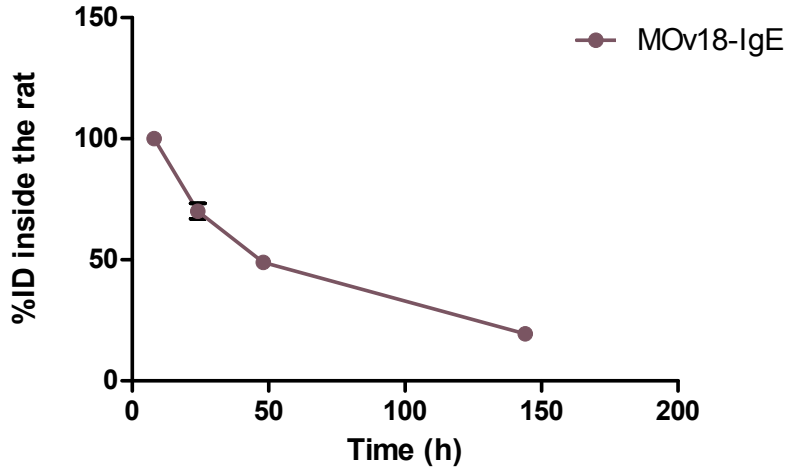

Figure 4.9: Graph plotting the % ID of signal from inside the rat injected with indium-111 labelled MOv18-IgE against time in hours. Single exponential equation fitted resulting in a constant rate of excretion of 0.025 h^{-1} (n=3).

Table 4.3: Excretion table showing ^{111}In-MOv18-IgE excretion rate over the time course of 144h post injection.

Rat ^{111}In-MOv18-IgE	8h	24h	48h	144h
%ID inside the rat	100.0	70.1	48.9	19.5
%ID excreted	0.0	29.9	51.1	80.5

4.3.6 Comparison of IgE excretion data between the mouse model and the rat model

The excretion rate constant of IgE was expected to be similar for the IgE antibodies compared over the two different animal models used (NSG mouse model-Anti-CSPG4-IgE and Rat-MOv18-IgE; Figure 4.10, Table 4.4). % ID from indium-111 measured inside the animal was added and subtracted from the initial % injected dose. Results were plotted against time in hours for each time point and a single exponential equation was used to calculate the rate constant of the excretion. Excretion rate constant for anti-CSPG4-IgE in NOD/SCID mice was 0.032 h^{-1}. The result was a half-life of 21.2 hours.

Table 4.4: Comparison of excretion rate constants from indium-111 labelled mice injected with anti-CSPG4-IgE and WAG rats injected with rat MOv18-IgE. Rate constant and half-life expressed with exponential decay equation.

System	rate constant	$t_{1/2}$
Mouse CSPG4-IgE	0.032 h^{-1}	21.2 hours
Rat MOv18-IgE	0.025 h^{-1}	27.7 hours

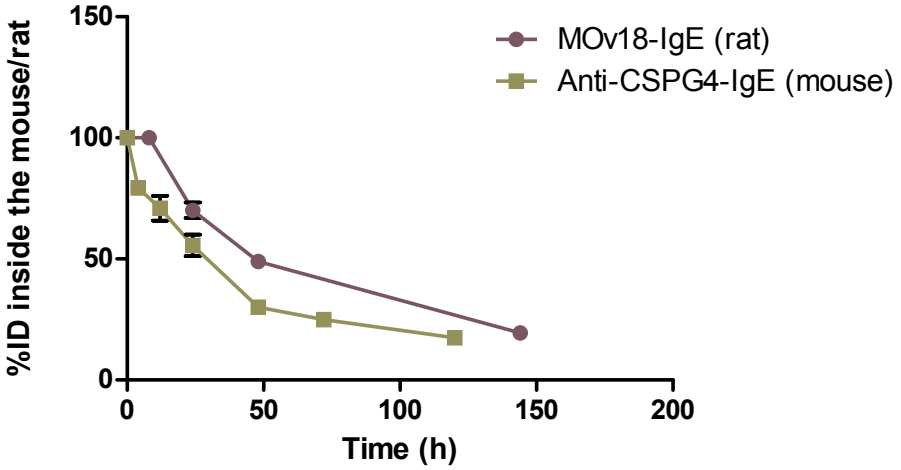

Figure 4.10: Excretion rate. Percentage of injected dose inside the NOD/SCID CSPG4 overexpressing s.c. tumour bearing mice with splenic engraftment of human PBLC (green) and the WAG rat human FRα overexpressing disseminated tumour model (violet) plotted against time in hours. Excretion rate constant and half-life were calculated with single exponential decay.

4.3.7 Comparison of rat MOv18-IgE and rat MOv18-IgG

Comparison of %-injected dose per gram at 48h of rat MOv18-IgE and -IgG

To better compare the differences in biodistribution between ^{111}In-MOv18-IgG and ^{111}In-MOv18-IgE the data of the two antibodies were compared at one specific time point in each graph (Figure 4.11). The biodistribution data showed that relative to IgG uptake IgE showed high accumulation of indium-111 only in liver. IgG showed a more even distribution of indium-111 signal.

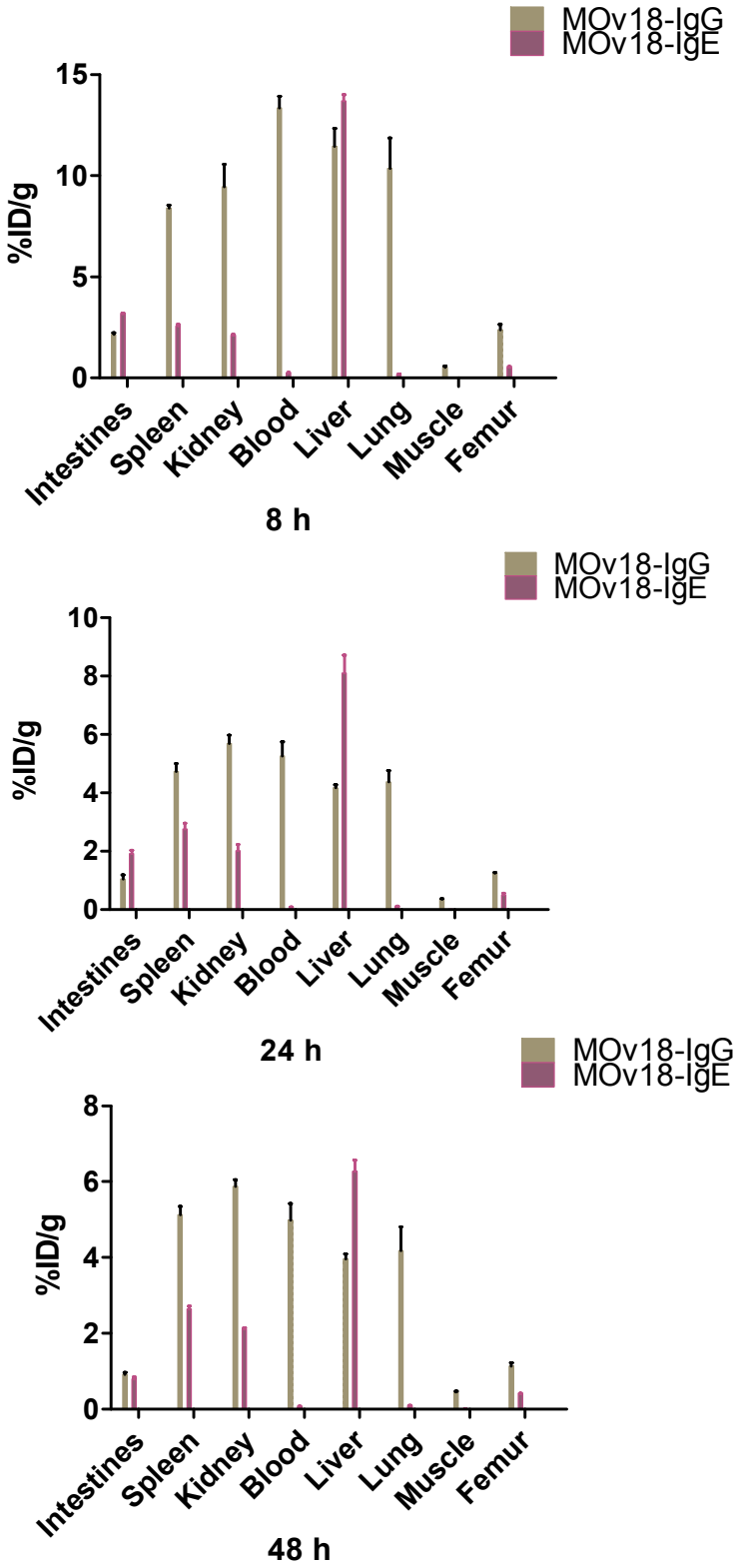

Figure 4.11: Biodistribution of disseminated lung tumour bearing rats at 8 h(A), 24 h (B) and 48 h (C) post injection of radiolabelled rat MOv18-IgE (violet) and rat MOv18-IgG (green), respectively, in % injected dose per gram of dissected tissue (Intestines, Spleen, Kidney, Blood, Liver, Lung, Muscle, Femur). Data plotted including SEM error bars (n=3).

Table 4.5: Tumour-to-blood ratio of MOv18-IgE and -IgG over the time course of 144 h.

T/B ratio	8h	24h	48h	144h
MOv18-IgE	0.69	1.47	1.64	3.48
MOv18-IgG	0.77	0.84	0.87	1.73

Tumour-to-Blood ratio comparison for ^{111}In-rMOv18-IgE and -IgG

Tumour-to-Blood ratios (tbr) were calculated (the lung tissue is holding the metastatic tumour tissue and was therefore accounted as tumour tissue). Tbr was used to correct for the influence of blood pool signal and show specific uptake of indium-111 signal in tumour tissue (Table 4.5, Figure 4.12). 8 h post injection of rat ^{111}In-MOv18-IgE the tbr ratio was at 0.7 times in tumour/lung tissue than in the blood pool. Data showed an increase of IgE in tumour/lung tissue over 24 h and 48 h post injection of IgE to 1.47 and 1.64, respectively, times higher accumulation compared to the activity measured in blood pool. Tumour-to-blood ratios progressively increased to 3.4 at 144 h post injection. ^{111}In-MOv18-IgG showed a similar picture at the 8 h time point compared to its IgE counterpart with a ratio of 0.77 before an increase was observed that progressively over 144 h increased to a tbr of 1.7 of higher accumulation of IgG in tumour tissue compared to blood. This is a 48% lower rise in tumour-to-blood ratio compared to ^{111}In-MOv18-IgE (ratio at 24 h: 0.8 ; 48 h: 0.86).

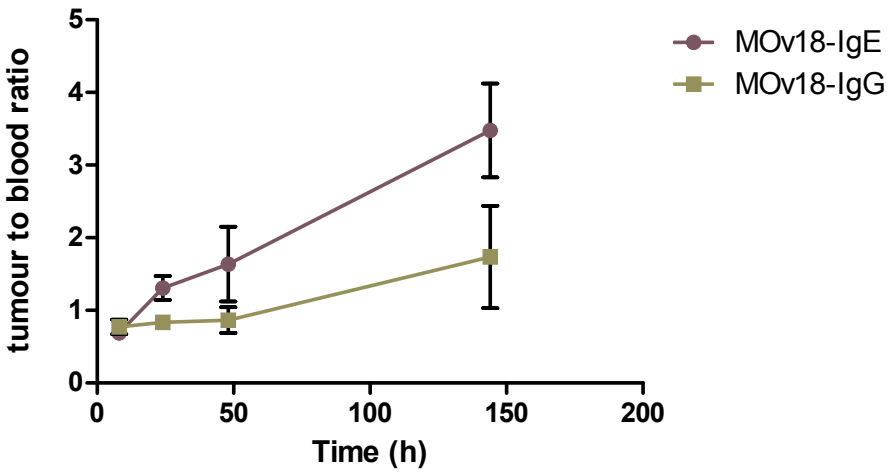

Figure 4.12: Comparison of the ratio between the tumour bearing tissue (lung) and blood in rats injected with rMOv18-IgE and -IgG over time (h) (n=3).

Table 4.6: Tumour-to-muscle ratio of MOv18-IgE and -IgG over the time course of 144 h.

T/M ratio	8 h	24 h	48 h	144 h
Mov-18-IgE	11.02	8.53	6.56	3.08
Mov-18-IgG	19.49	11.88	9.11	13.14

Rat antibody tumour- to-muscle ratio comparison between rat MOv18-IgG and -IgE

Tumour (lung)-to-Muscle ratios showed accumulation in tumour tissue against internal non-tumour muscle tissue (Figure 4.13, Table 4.6). Comparing the tmr of ^{111}In-MOv18-IgE to ^{111}In-MOv18-IgG over time shows significant differences. At 8 h the tmr was 11 for IgE but nearly 20 for IgG. Both ratios progressively decrease to a tumour-to-muscle ratio of 3 for IgE and 13 for IgG at 144 h.

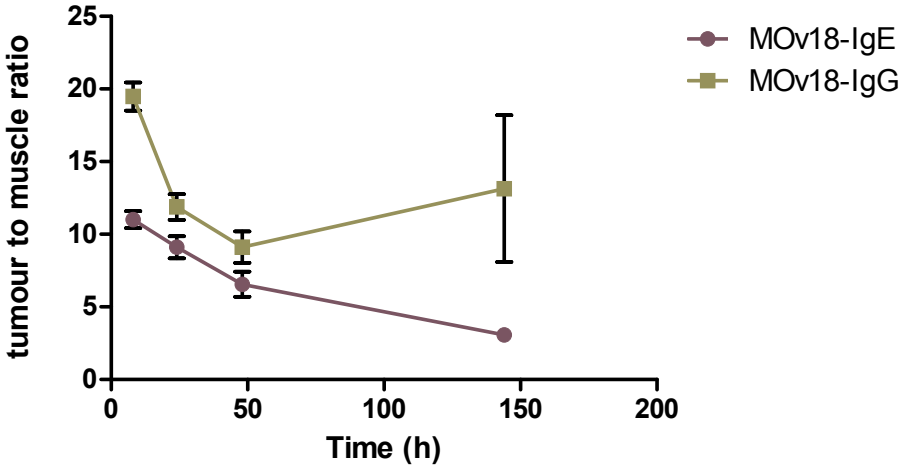

Figure 4.13: Comparison of the ratio between the tumour bearing tissue (lung) and muscle tissue in rats (n=3) injected with rat MOv18-IgE and -IgG over time (h).

4.4 Discussion

The antibodies in this chapter were investigated in regards to their biodistribution, targeting and clearance. MOv18-IgG showed a familiar pattern in distribution characterised by the long serum half-life. MOv18-IgE, like IgE observed in the previous chapter 3, showed a very strong clearance from serum and liver uptake. Although, efficacy results showed better outcome for IgE, no direct or indirect tumour targeting of IgE was measured.

4.4.1 *In vivo* model

On the basis of a immune effector cell reservoir and the FcR distribution comparable to the human reservoir and distribution, it was proposed that the use of a fully immunocompetent rat model with a syngeneic metastatic lung tumour would overcome limitations seen in *in vivo* models described in chapter 3 (NOD/SCID mouse model with splenic engraftment of human PBMC) and earlier studies looking into the anti-cancer therapeutic efficacy of IgE [41, 165, 13]. Here, employing a chimeric (rat/mouse) antibody, rat MOv18-IgE, in a rat model showed significant differences when compared to results in chapter 3 where a NOD/SCID mouse model with splenic engraftment of human PBMC was used. It was shown that signal originated from indium-111 and associated with the full antibodies or its degradation products was excreted much faster and in higher quantities in NOD/SCID mice compared to the rat MOv18-IgE in the rat model. This resulted in a higher excretion rate constant for the mouse model. One argument for this observation was the presence of a natural and constantly renewed pool of FcεR expressing cells in rats to which the rat MOv18-IgE antibody could bind and in the mouse model the cells available for binding to IgE via FcεR receptors in the NOD/SCID mouse model were available in much smaller quantities. However, the underlying catabolic processes and the way the majority of the injected anti-CSPG4- and rat MOv18-IgE were metabolised and must be the same [212].

4.4.2 Biodistribution and SPECT imaging Liver/Spleen/Intestines/Blood

Results observed in NanoSPECT/CT imaging and biodistributions from rat MOv18-IgE showed a massive accumulation of indium-111 signal ($\sim$75% ID at 8h) in the liver. Rat MOv18-IgG showed in contrast only $\sim$50% ID in the liver while $\sim$80% ID were found in blood circulation. This data is inconclusive in regards to IgG because the % injected dose measured in the organs almost always includes a fraction of blood that was measured. It was not possible to determine conclusively the origin of the signal (organ or blood). Both antibodies, rat MOv18-IgE and -IgG, were radiolabelled with the same method and targeted the same FRα epitope in the rat model. Since rat MOv18-IgE and -IgG differed only in the Fc-part the reason for the biodistribution patterns must be dependent on the Fc region of both antibodies [270, 60, 249]. It is now understood that the neonatal Fc receptor (FcRn) is in large part responsible for the long serum half-life of IgG. IgG binds to the neonatal

Fc receptor with high affinity at acidic pH, but with very low affinity at neutral (i.e., plasma, pH 4.5). This enables IgG to be bound by FcRn in the acidic environment of the sorting endosome (pH $\leq$ 6.0) in endothelial cells and to be recycled back into circulation where dissociation occurs under more alkaline (pH $>$ 7) conditions [249]. However, since IgE does not bind to FcRn, in the case of rat MOv18-IgE and IgE in general several other factors have been shown to influence the distribution [51, 52, 242]. IgE when produced naturally in the mucosa is thought to bind to its FcR receptor and circulates bound to the respective effector cell until this cell encounters a cognate antigen. The high affinity FcεRI receptor is thought to promote binding to FcεR receptor expressing cells [271]. This is hypothesised, with injected IgE as with the natively produced IgE, to happen potentially before the antigen binding site has bound to its target receptor and would alter the biodistribution compared to its rat MOv18-IgG counterpart in a way that FcεRI expressing cells would instantly bind the IgE [13, 170]. Rather than showing target specific accumulation at the tumour site, IgE signal would be observed further distributed in regards to the location of immune cells. The FcεRII (CD23) receptor, also known as low affinity receptor, can bind to several co-receptors like CD21 (complement protein) and different integrin (CD18/CD11b) among others. CD21 is expressed on B cells, follicular dendritic cells (FDCs), activated T cells and basophils. Adhesion pairing between these two molecules may have important consequences for, not only the immune reaction, but also biodistribution and clearance of IgE. Especially, many immune cells are not in free circulation in serum or tissue but concentrated in organs like liver and spleen [272, 55, 71]. IgE biodistribution based on its FcεRI and FcεRII Fc-receptors would show the location of FcεR receptor expression. That would explain not only the high accumulation of signal seen with rat MOv18-IgE in liver but also spleen since both organs are known to host a huge quantities of immune cell clusters. Another reason for the alternative biodistribution of rat MOv18-IgE compared to rat MOv18-IgG was the glycosylation of IgE. Glycosylation in IgG antibodies is known to be involved into the Fc-mediated effector cell binding; this is not known from IgE antibody. However, there is significant glycosylation found on IgE (as described in chapter 3), many with terminal mannose residues which can bind to mannose binding lectin (MBL) and complement proteins in circulation and in the liver [201, 253]. The function of IgE glycosylation is not understood today [44]. Accumulation of rat MOv18-IgE in the spleen was 2.75% ID/g highest with 0.73% ID at 24 h but did not show any significant reduction in signal over the time course of 144 hours. The spleen is part of the lymphatic system and contains a high quantity of FcεR expressing immune cells; it seems reasonable to assume that binding and accumulation seen in spleen did not decline because of rMOv18-IgE was bound via one of its FcεR receptors to the FcεR expressing immune cell fraction [273]. In contrast, most of the liver bound rat MOv18-IgE was presumably degraded [211, 212, 274]. Additionally, the decline of indium-111 signal in liver seemed to be associated with a rise in the signal from the intestines and, therefore, is thought to show hepatobilary excretion of indium-111 and its associated rat MOv18-IgE degradation products or

intact ^{111}In-rat MOv18-IgE. Interesting here was also that IgG excretion and no metabolism was not observed, although, IgG was found in liver.

4.4.3 Biodistribution blood and lung/tumour

The biodistribution analysis showed a rapid clearance of rat MOV18-IgE from blood pool. Since the first biodistribution time point was at 8 hours it was not possible to assess the circulating amounts of MOv18-IgE and their binding kinetics in the first 8 hours post injection. There are a number of possible fates for MOv18-IgE in blood pool. MOv18-IgE is unbound in circulation and could either bind over time to (a) free FcεR receptors on the surface of immune cells or (b) it could be bound by MBL or complement proteins or on receptors on e.g. macrophages via the free terminal mannose sugar residues in the blood pool or directly in liver. The third option (c) would be the binding of free rat MOv18-IgE, similar to rat MOv18-IgG, to the tumour target receptor FRα. To (a), FcεR expressing cells are not found in huge numbers in the blood pool but more in lymph nodes or organs like spleen and liver [270, 275, 59]. The signal accumulation in the spleen but also part of the liver binding of MOv18-IgE can be assumed to be a result of FcεR binding. The terminal mannose sugar residues mentioned under point (b) might account for a large part of the blood clearance, liver binding and subsequent hepatobilary excretion. Compared to rat MOv18-IgG, rat MOv18-IgE shows a $\sim$100 fold lower tumour accumulation. This does not exclude that the tumour accumulation observed with MOv18-IgE, although much lower than seen with IgG, is originating from free circulating MOv18-IgE binding the FRα receptor via the variable regions before binding to FcεR receptors on immune effector cells.

4.4.4 Biodistribution in kidneys

The biodistribution results showed a relatively high accumulation of rMOv18-IgE in the kidneys. Compared to rMOv18-IgG the values observed are twice as high in rMOv18-IgE. In both biodistribution studies MOv18-IgE and -IgG the observed kidney values are constant without any significant de- or increase. It was also standing out that anti-CSPG4-IgE in the NOD/SCID mouse model did not show any significant accumulation in the kidneys. In general, proteins and peptides lower in size than $\sim$50kDa are excreted via kidneys. Degradation products of ^{111}In-DTPA conjugated and labelled antibodies are known from literature and change over the process to different size degradation products. ^{111}In-DTPA and even more so ^{111}In-CHX-A"<-DTPA metabolites are very stable. The major metabolite known from literature from an IgG antibody labelled with indium-111 via DTPA was found in urine and kidneys was ^{111}In-DTPA-ε-lysine [212]. It is likely that all signals from kidneys come from either degraded rat MOv18-IgE antibody fragments below the size of $\sim$50 kDa or from MOv18-IgE bound to its target receptor FRα which is expressed lightly in kidneys. It could highlight the possibility that MOv18-IgE was released from liver after partial degradation

or that a significant amount of MOv18-IgE bound to immune cells via the FcεR receptors was cleared from the blood, internalised, and delivered to the lysosome for subsequent degradation and excretion via the kidneys. The difference in a complete lack of the immune system in the mouse model would be an explanation of low kidney measurements observed in the mouse model.

4.4.5 Conclusions

Overall, the experiments in rats might improve the translation of therapeutic IgE experiments and the data output compared to other *in vivo* models. Here, the lack of unspecific antibody isotype controls, the only small amount of rat antibody produced at the time and general time constraints, build up to a situation where it was difficult to find a concluding outcome. However, a consistent outcome for IgE is the high liver uptake and metabolism while the high blood retention was consistent for IgG. The disseminated rat model, though mirroring more closely the clinical set up, made it difficult to conclusively discuss tumour uptake. However, results in rats were in line with observations from the NSG mouse model. IgE clears quickly from the circulation and is metabolised by liver, whereas IgG stays in blood and slowly reaches tumour. The high liver uptake and fast metabolism of MOv18-IgE and general difference of biodistribution in comparison to the IgG counterpart are significant observations.

5 Final remarks and future work

IgE class antibodies have shown promising results in (early) pre-clinical anti-tumour efficacy studies [170, 35, 58]. In an attempt to better understand the mode of action of this novel type of anti-tumour immunotherapy, this thesis aimed at development of a method to radiolabel IgE class antibodies and for the first time deliver *in vivo* imaging data on biodistribution, targeting and clearance of IgE and compare these findings to IgG in a clinical relevant *in vivo* model.

To date, nearly all monoclonal antibodies used in tumour immunotherapy are of the IgG isotype class and have for long time and almost exclusively been used in the treatment of some cancers and improved prognosis for many patients [159]. Available antibodies for clinical applications are of the IgG class. The reason for IgG being the most prevalent antibody class is historically grown as IgG constitute the largest fraction of circulating antibodies found in human blood. Work in the late 1980s compared chimeric antibodies of the same specificity, each with Fc regions belonging to one of the antibody classes, IgG1-4, IgM, IgA1-2, IgD, and IgE [190]. Antibodies were evaluated for their ability to bind to complement factors and their potency to mediate haemolysis and cytotoxicity of antigen-expressing target cells in the presence of complement. IgG in combination with human peripheral blood mononuclear cells (PBMC) was the most effective antibody class in complement-dependent cell killing *in vitro*, while the IgA and IgE antibodies were completely inert. Since this pioneering work, antibody isotopes other than IgG have not been extensively considered and only recent research brought other antibody classes into the focus of applied drug development [276]. While over half of IgG antibody treatments available are approved for haematological malignancies where IgG class antibodies have the combined advantages of high specificity and affinity for their target antigen and a long serum half-life, efficacious antibodies for solid tumours are still urgently needed [27]. IgG antibodies showed only mediocre efficacy in tissue penetration and recruitment of ADCP/ADCC or recruitment of Th2 directed immune response.

In contrast to IgG which acts by recruiting complement and FcγR expressing cells like macrophages, neutrophils, eosinophils, dendritic cells, langerhans cells, B cells, mast cells, IgE interacts with the same set of immune effector cells more efficiently by binding to one of its two high affinity FcεR receptors. The high affinity and the different pathways triggered by two receptors enable IgE to promote differential methods of cell killing. The degranulation of mast cells and basophils with release of pro-inflammatory mediators and cytokines or ADCC, mediated by the release of mediators such as NO, enzymes and cytokines results in target cell lysis or ADCP,

mediated by the activation of macrophages and monocytes [170, 58, 50]. Native IgE antibodies reside in tissues, bound to cell surface FcεR receptors, with only very low levels circulating in blood. For this project it was hypothesised that these unique properties of IgE, i.e. effector cell bound and tissue-resident, can be employed to trigger powerful immune responses against solid tumours. It was further postulated that the properties of IgE commonly described in allergy and protection from parasitic infections, if redirected against cancer cells, may translate to effective targeting of solid tumours. In this context the aims of this thesis were:

- The development of an advanced conjugation and radiolabelling method. This method was required to protect not only the antigen binding site but also the IgE Fc-receptors. The method was needed to be the same for IgE and IgG class antibodies for the comparison of imaging and biodistribution outcomes. Further, the method was needed to be straight forward for the simple and reliant translation into later clinical application.
- A radiolabelled IgE was used in imaging studies as a powerful surveillance tool of targeting, clearance and biodistribution kinetics in a single tumour bearing animal over time.
- *Ex vivo* biodistribution data was collected to observe and compare distribution, targeting and clearance of IgE at specific time points.
- IgG radiolabelled by the same developed method and engineered as an IgE counterpart, was compared to IgE in imaging and biodistribution studies in the same *in vivo* models.
- Imaging and biodistribution data of IgE and IgG antibodies with different target receptors were collected in a humanised tumour xenograft model in NSG mice and a disseminated lung metastases model in immunocompetent rats. The data was used with the aim to to compare and assess, along with other research, the clinical relevance of the *in vivo* models in the progress of drug development.

Various radiolabelling methods are available. Here, a suitable method was selected and evaluated for this specific project. In chapter 2 a labelling strategy and method for IgE class antibodies was developed. The conjugation and radiolabelling method used is based on a published method of conjugation of chelating agents to antibodies and radiolabelling with trivalent metallic isotopes [197]. IgE was radiolabelled with high specific activity and without the loss of affinity or functionality. Further, the method allowed IgE and IgG class antibodies to be radiolabelled in the same way to allow comparative assessment of biodistribution.

Chapter 3 describes the comparison of IgE vs. IgG biodistribution in a subcutaneous tumour xenograft NSG mouse model with engrafted human PBMC's [247, 238]. While IgG showed a long serum half-life and good tumour targeting, IgE showed a greatly different distribution with rapid liver uptake, fast clearance from blood and very little uptake in the tumour. This results cannot directly support previous studies by Panos Karagiannis (NIHR Biomedical Research Centre at

Guy's and St. Thomas's Hospitals and King's College London, London, UK) that showed superior efficacy of IgE over IgG in the same NSG mouse model and IgE dependent tumour infiltration of monocytes and basophiles.

Imaging and biodistribution studies allowed assessing the differences between IgG and IgE. The massive liver uptake was not predicted and no reports were found in literature.

It is based on the imaging and biodistribution data and the current knowledge of therapeutic IgE difficult to explain antitumour effects only the very little tumour targeting seen. A possible mechanism could be that IgE bound on its effector cells infiltrate the tumour and introduce with high potency an immune response that is subsequently IgE independent [165, 37]. Another explanation could be differences in the setup of the imaging study vs. the therapy study. In the efficacy study of IgE a repeated dose of 10 mg/Kg antibody were used while a single dose of 3 mg/Kg were injected for the imaging and biodistribution studies. It is possible that the repeated and higher dosage offers explanations that could not have been followed with the experimental set up described in this thesis. IgE type antibodies are known to have high mannose type glycosylation. The deglycosylation with PNGase F changed the biodistribution of anti-CSPG4-IgE by lower liver uptake and higher tumour retention indicating that the biodistribution and clearance is mostly dependant on the high mannose glycosylation on IgE. There is no evidence for the glycosylation to interact with the binding of the FC receptors or interaction with the antigen binding [201, 253, 200, 45]. The function of the high mannose glycosylation is unknown but results about the influence of the mannose glycosylation on biodistribution in this thesis could suggest that IgE antibodies are mannose glycosylated to filter any IgE out of serum. The IgE produced for the efficacy and imaging/biodistribution studies resembled the high mannose glycosylation found in native IgE antibodies. Naturally produced IgE, however, is not released into the blood circulation in higher amounts but is released directly into tissues [44].

In addition to the mouse model described in chapter 3, IgE vs IgG biodistribution was analysed in chapter 4 in a completely immune competent disseminated lung tumour rat model. Use of the two different models gives a broader picture and allows drawing more general conclusions on IgE biodistribution. The biodistribution seen in the rat model resembled the distribution pattern of the mouse model. This was expected after the assessment of the mouse model because of the high mannose glycosylation of IgE and its by then postulated impact on the biodistribution of IgE in general.

The biodistribution and imaging studies were part of the pre-clinical analyses in an attempt to translate the folate receptor alpha specific MOv18-IgE into a phase 0 or first-in-man study [151]. High radiation signal was observed in the liver, spleen, kidney and intestines and therefore these organs in particular, were closely evaluated during the IHC toxicity study. Further studies have shown that rat MOv18-IgE induced an anti-tumour effect in the tumour microenvironment (TME), and indicated that the macrophages/monocytes activated in MOv18-IgE-treated animals may be

involved in the observed antibody-mediated responses. Analysis of lung tumours demonstrated that CD68+ macrophages infiltrated tumours, injected with rat MOv18-IgG or rat MOv18-IgE, but the quantity of macrophages that penetrated deep into the tumour mass were significantly higher in IgE treated animals. In addition, the IgE-treated cohort showed the population of macrophages in necrotic areas where tumours were once present (Debra Josephs, unpublished).

The infiltration of macrophages, monocytes and other effector cells shown by Debra Josephs in rats and in mice shown Panos Karagiannis (Data from the PhD thesis of Debra Josephs and Panos Karagiannis, respectively) may explain the positive results for IgE in the efficacy studies. Also, the analysis showed an infiltration of effector cells and IgE. This does not necessarily translate into a high fraction of effector cells bound via FcεR to IgE being responsible for the whole extend of the immune response. The high recruitment of effector cells could have been triggered by a smaller fraction of IgE mediating a degranulation of effector cells that established a further IgE independent recruitment of effector cells. However, the here presented imaging and biodistribution studies did show only little infiltration of IgE.

5.1 Future work

One of the most promising additional research into IgE would be to follow up on the indication that mannose glycosylation of IgE has a strong influence in IgE biodistribution. The process of deglycosylation of IgE has to be standardised and stability and radiolabelling of the deglycosylated IgE would need to be assessed. Alternatively, IgE without any sugar residues could be engineered by mutating the IgE amino sequence at the location of glycosylation. This would avoid complex enzymatic deglycosylation with further need of purification. A study to combine therapy and imaging would allow investigating the effects of higher and/or repeated dosing into IgE biodistribution. The SPECT/CT and PET/CT small animal scanner are by now set up to enable the quantification of detected signal from the image. This would allow reducing or excluding the *ex vivo* biodistribution study and relying on *in vivo* models being assessed over time non-invasively by the small animal imaging.

Other research could be performed to look further into the mode of action of IgE. For example, in the NSG mouse model human PBMC's could be incubated with therapeutic radiolabelled IgE and co-injected. IgE would be bound on the surface of effector cells and biodistribution, splenic engraftment and targeting over time could be compared to biodistribution data from chapter 3.

The comparison of rat MOV18-IgE and -IgG in an immunocompetent rat model with disseminated lung tumour were difficult to interpret because of the lack of non-specific IgG and IgE controls. These control experiments have to be included in future work. This requires also more research into the stability issues of the rat MOv18 antibodies. So far, rat MOv18-IgE and -IgG had to be re-purified the day before used for injection in the treatment studies or before conjugation

and radiolabelling because of their instability under storage conditions.

Bibliography

[1] Kenneth Todar. Todar's Online Textbook of Bacteriology, 2014. Available online at 'textbookofbacteriology.net'.

[2] Jagadeesh Bayry, Sébastien Lacroix-Desmazes, Michel D Kazatchkine, and Srini V Kaveri. Monoclonal antibody and intravenous immunoglobulin therapy for rheumatic diseases: rationale and mechanisms of action. *Nature clinical practice. Rheumatology*, 3(5):262–72, May 2007.

[3] Jenny M Woof. A route to improved antibody reagents. Insights from Fc receptor biology. (June):291–293, 2012.

[4] JV Ravetch and Silvia Bolland. Igg fc receptors. *Annual review of immunology*, 2001.

[5] H Metzger. Transmembrane signaling: the joy of aggregation. *Journal of immunology (Baltimore, Md. : 1950)*, 149(5):1477–87, September 1992.

[6] J P Kinet. The high-affinity IgE receptor (Fc epsilon RI): from physiology to pathology. *Annual review of immunology*, 17:931–972, 1999.

[7] Donald MacGlashan. Ige and fcεri regulation. *Annals of the New York Academy of Sciences*, 1050(1):73–88, 2005.

[8] BJ Sutton and HJ Gould. The human ige network. 1993.

[9] Fredrik Carlsson, Fredrik Hjelm, Daniel H Conrad, and Birgitta Heyman. Ige enhances specific antibody and t-cell responses in mice overexpressing cd23. *Scandinavian journal of immunology*, 66(2-3):261–270, 2007.

[10] Sophia N Karagiannis, John K Warrack, Kevin H Jennings, Paul R Murdock, Gary Christie, Kevin Moulder, Brian J Sutton, and Hannah J Gould. Endocytosis and recycling of the complex between cd23 and hla-dr in human b cells. *Immunology*, 103(3):319–331, 2001.

[11] Geert C Mudde, Roy Bheekha, and Carla AFM Bruijnzeel-Koomen. Consequences of ige/cd23-mediated antigen presentation in allergy. *Immunology today*, 16(8):380–383, 1995.

[12] David Dombrowicz and Monique Capron. Eosinophils, allergy and parasites. *Current opinion in immunology*, 13(6):716–720, 2001.

[13] Sophia N Karagiannis, Marguerite G Bracher, James Hunt, Natalie McCloskey, Rebecca L Beavil, Andrew J Beavil, David J Fear, Richard G Thompson, Nicholas East, Frances Burke, Robert J Moore, David D Dombrowicz, Frances R Balkwill, and Hannah J Gould. IgE-antibody-dependent immunotherapy of solid tumors: cytotoxic and phagocytic mechanisms of eradication of ovarian cancer cells. *Journal of immunology (Baltimore, Md. : 1950)*, 179(5):2832–43, September 2007.

[14] J I Clark, R K Alpaugh, M von Mehren, J Schultz, J R Gralow, M A Cheever, D B Ring, and L M Weiner. Induction of multiple anti-c-erbB-2 specificities accompanies a classical idiotypic cascade following 2B1 bispecific monoclonal antibody treatment. *Cancer immunology, immunotherapy : CII*, 44(5):265–72, July 1997.

[15] Louis M Weiner, Madhav V Dhodapkar, and Soldano Ferrone. Monoclonal antibodies for cancer immunotherapy. *Lancet*, 373(9668):1033–40, March 2009.

[16] Isobel S Okoye and Mark S Wilson. CD4+ T helper 2 cells–microbial triggers, differentiation requirements and effector functions. *Immunology*, 134(4):368–77, December 2011.

[17] William R Heath and Francis R Carbone. CROSS-PRESENTATION,DENDRITIC CELLS,TOLERANCE AND I MMUNITY. *Annual review of immunology*, 19:47–64, 2001.

[18] Garland Science - Book: Janeway's Immunobiology + 8.

[19] G Köhler and C Milstein. Continuous cultures of fused cells secreting antibody of predefined specificity. 1975. *Journal of immunology (Baltimore, Md. : 1950)*, 174:2453–2455, 1975.

[20] Louis M Weiner. antibody therapy for cancer. 2007.

[21] A F LoBuglio, R H Wheeler, J Trang, A Haynes, K Rogers, E B Harvey, L Sun, J Ghrayeb, and M B Khazaeli. Mouse/human chimeric monoclonal antibody in man: kinetics and immune response. *Proceedings of the National Academy of Sciences of the United States of America*, 86(11):4220–4, June 1989.

[22] G L Boulianne, N Hozumi, and M J Shulman. Production of functional chimaeric mouse/human antibody. *Nature*, 312(5995):643–6.

[23] S L Morrison, M J Johnson, L A Herzenberg, and V T Oi. Chimeric human antibody molecules: mouse antigen-binding domains with human constant region domains. *Proceedings of the National Academy of Sciences of the United States of America*, 81(21):6851–5, November 1984.

[24] L Riechmann, M Clark, H Waldmann, and G Winter. Reshaping human antibodies for therapy. *Nature*, 332(6162):323–7, March 1988.

[25] William N Hait and Trevor W Hambley. Targeted cancer therapeutics. *Cancer research*, 69(4):1263–7; discussion 1267, February 2009.

[26] David M Goldenberg and Robert M Sharkey. Using antibodies to target cancer therapeutics. *Expert opinion on biological therapy*, 12(9):1173–90, September 2012.

[27] Andrew M Scott, Jedd D Wolchok, and Lloyd J Old. Antibody therapy of cancer. *Nature reviews. Cancer*, 12(4):278–87, April 2012.

[28] Peter J. Delves Ivan M. Roitt. Encyclopedia of Immunology, Four-Volume Set, Second Edition: Ivan M. Roitt, Peter J. Delves.

[29] Bethan Hughes. Antibody-drug conjugates for cancer: poised to deliver? *Nature reviews. Drug discovery*, 9(9):665–7, September 2010.

[30] Andrew M Scott, Fook-Thean Lee, Niall Tebbutt, Rebecca Herbertson, Sanjeev S Gill, Zhanqi Liu, Effie Skrinos, Carmel Murone, Timothy H Saunder, Bridget Chappell, Anthony T Papenfuss, Aurora M T Poon, Wendie Hopkins, Fiona E Smyth, Duncan MacGregor, Lawrence M Cher, Achim A Jungbluth, Gerd Ritter, Martin W Brechbiel, Roger Murphy, Antony W Burgess, Eric W Hoffman, Terrance G Johns, and Lloyd J Old. A phase I clinical trial with monoclonal antibody ch806 targeting transitional state and mutant epidermal growth factor receptors. *Proceedings of the National Academy of Sciences of the United States of America*, 104(10):4071–6, March 2007.

[31] Louis M Weiner, Rishi Surana, and Shangzi Wang. Monoclonal antibodies: versatile platforms for cancer immunotherapy. *Nature reviews. Immunology*, 10(5):317–27, May 2010.

[32] Clare Taylor, Dawn Hershman, Nina Shah, Nicole Suciu-Foca, Dan P Petrylak, Robert Taub, Linda Vahdat, Bin Cheng, Mark Pegram, Keith L Knutson, and Raphael Clynes. Augmented HER-2 specific immunity during treatment with trastuzumab and chemotherapy. *Clinical cancer research : an official journal of the American Association for Cancer Research*, 13(17):5133–43, September 2007.

[33] E O Long. Regulation of immune responses through inhibitory receptors. *Annual review of immunology*, 17:875–904, 1999.

[34] J V Ravetch and J P Kinet. Fc receptors. *Annu Rev Immunol*, 9:457–492, 1991.

[35] Sophia N Karagiannis, Debra H Josephs, Panagiotis Karagiannis, Amy E Gilbert, Louise Saul, Sarah M Rudman, Tihomir Dodev, Alexander Koers, Philip J Blower, Christopher Corrigan, Andrew J Beavil, James F Spicer, Frank O Nestle, and Hannah J Gould. Recombinant IgE antibodies for passive immunotherapy of solid tumours: from concept towards

clinical application. *Cancer immunology, immunotherapy : CII*, 61(9):1547–64, September 2012.

[36] Claire E Lewis and Jeffrey W Pollard. Distinct role of macrophages in different tumor microenvironments. *Cancer research*, 66(2):605–12, January 2006.

[37] E Y Lin and J W Pollard. Role of infiltrated leucocytes in tumour growth and spread. *British journal of cancer*, 90:2053–2058, 2004.

[38] Frédéric Bibeau, Evelyne Lopez-Crapez, Frédéric Di Fiore, Simon Thezenas, Marc Ychou, France Blanchard, Aude Lamy, Frédérique Penault-Llorca, Thierry Frébourg, Pierre Michel, Jean-Christophe Sabourin, and Florence Boissière-Michot. Impact of Fc{gamma}RIIa-Fc{gamma}RIIIa polymorphisms and KRAS mutations on the clinical outcome of patients with metastatic colorectal cancer treated with cetuximab plus irinotecan. *Journal of clinical oncology : official journal of the American Society of Clinical Oncology*, 27(7):1122–9, March 2009.

[39] Antonino Musolino, Nadia Naldi, Beatrice Bortesi, Debora Pezzuolo, Marzia Capelletti, Gabriele Missale, Diletta Laccabue, Alessandro Zerbini, Roberta Camisa, Giancarlo Bisagni, Tauro Maria Neri, and Andrea Ardizzoni. Immunoglobulin G fragment C receptor polymorphisms and clinical efficacy of trastuzumab-based therapy in patients with HER-2/neu-positive metastatic breast cancer. *Journal of clinical oncology : official journal of the American Society of Clinical Oncology*, 26(11):1789–96, April 2008.

[40] Wen-Kai Weng and Ronald Levy. Two immunoglobulin G fragment C receptor polymorphisms independently predict response to rituximab in patients with follicular lymphoma. *Journal of clinical oncology : official journal of the American Society of Clinical Oncology*, 21(21):3940–7, November 2003.

[41] H J Gould, G a Mackay, S N Karagiannis, C M O'Toole, P J Marsh, B E Daniel, L R Coney, V R Zurawski, M Joseph, M Capron, M Gilbert, G F Murphy, and R Korngold. Comparison of IgE and IgG antibody-dependent cytotoxicity in vitro and in a SCID mouse xenograft model of ovarian carcinoma. *European journal of immunology*, 29(11):3527–37, November 1999.

[42] Panagiotis Karagiannis, Josef Singer, James Hunt, Samuel K E Gan, Sarah M Rudman, Diana Mechtcheriakova, Regina Knittelfelder, Tracy R Daniels, Philip S Hobson, Andrew J Beavil, James Spicer, Frank O Nestle, Manuel L Penichet, Hannah J Gould, Erika Jensen-Jarolim, and Sophia N Karagiannis. Characterisation of an engineered trastuzumab IgE antibody and effector cell mechanisms targeting HER2/neu-positive tumour cells. *Cancer immunology, immunotherapy : CII*, 58(6):915–30, June 2009.

[43] Robert L Ferris, Elizabeth M Jaffee, and Soldano Ferrone. Tumor antigen-targeted, monoclonal antibody-based immunotherapy: clinical response, cellular immunity, and immunoescape. *Journal of clinical oncology : official journal of the American Society of Clinical Oncology*, 28(28):4390–9, October 2010.

[44] Hannah J Gould and Brian J Sutton. IgE in allergy and asthma today. *Nature reviews. Immunology*, 8:205–217, 2008.

[45] Hannah J Gould, Brian J Sutton, Andrew J Beavil, Rebecca L Beavil, Natalie McCloskey, Heather A Coker, David Fear, and Lyn Smurthwaite. The biology of IGE and the basis of allergic disease. *Annual review of immunology*, 21:579–628, 2003.

[46] S Haba, Z Ovary, and a Nisonoff. Clearance of IgE from serum of normal and hybridoma-bearing mice. *Journal of immunology (Baltimore, Md. : 1950)*, 134(5):3291–7, May 1985.

[47] Lars Hellman. Regulation of IgE homeostasis, and the identification of potential targets for therapeutic intervention. *Biomedicine & pharmacotherapy = Biomedecine & pharmacotherapie*, 61:34–49, 2007.

[48] T. Tada, K. Okumura, B. Platteau, A. Beckers, and H. Bazin. Half-Lives of Two Types of Rat Homocytotropic Antibodies in Circulation and in the Skin. *International Archives of Allergy and Immunology*, 48(1):116–131, 1975.

[49] Tommy Wan, Rebecca L Beavil, Stella M Fabiane, Andrew J Beavil, Maninder K Sohi, Maura Keown, Robert J Young, Alistair J Henry, Ray J Owens, Hannah J Gould, and Brian J Sutton. The crystal structure of IgE Fc reveals an asymmetrically bent conformation. *Nature immunology*, 3(7):681–6, July 2002.

[50] E. Sally Ward, Jinchun Zhou, Victor Ghetie, and Raimund J. Ober. Evidence to support the cellular mechanism involved in serum IgG homeostasis in humans. *International Immunology*, 15:187–195, 2003.

[51] M Firan, R Bawdon, C Radu, R J Ober, D Eaken, F Antohe, V Ghetie, and E S Ward. The MHC class I-related receptor, FcRn, plays an essential role in the maternofetal transfer of gamma-globulin in humans. *International immunology*, 13:993–1002, 2001.

[52] Raimund J Ober, Cruz Martinez, Carlos Vaccaro, Jinchun Zhou, and E Sally Ward. Visualizing the site and dynamics of IgG salvage by the MHC class I-related receptor, FcRn. *Journal of immunology (Baltimore, Md. : 1950)*, 172:2021–2029, 2004.

[53] Adam D Kennedy, Paul V Beum, Michael D Solga, David J DiLillo, Margaret A Lindorfer, Charles E Hess, John J Densmore, Michael E Williams, and Ronald P Taylor. Rituximab

infusion promotes rapid complement depletion and acute CD20 loss in chronic lymphocytic leukemia. *Journal of immunology (Baltimore, Md. : 1950)*, 172:3280–3288, 2004.

[54] Dominique Levêque, Sandra Wisniewski, and François Jehl. Pharmacokinetics of therapeutic monoclonal antibodies used in oncology. *Anticancer research*, 25(3c):2327–43, 2005.

[55] Richard G Hibbert, Peter Teriete, Gabrielle J Grundy, Rebecca L Beavil, Rajko Reljic, V Michael Holers, Jonathan P Hannan, Brian J Sutton, Hannah J Gould, and James M McDonnell. The structure of human CD23 and its interactions with IgE and CD21. *The Journal of experimental medicine*, 202:751–760, 2005.

[56] Derry C Roopenian, Gregory J Christianson, Thomas J Sproule, Aaron C Brown, Shreeram Akilesh, Nadja Jung, Stefka Petkova, Lia Avanessian, Eun Young Choi, Daniel J Shaffer, Peter A Eden, and Clark L Anderson. The MHC class I-like IgG receptor controls perinatal IgG transport, IgG homeostasis, and fate of IgG-Fc-coupled drugs. *Journal of immunology (Baltimore, Md. : 1950)*, 170:3528–3533, 2003.

[57] M H Kershaw, P K Darcy, J A Trapani, and M J Smyth. The use of chimeric human Fc(epsilon) receptor I to redirect cytotoxic T lymphocytes to tumors. *Journal of leukocyte biology*, 60:721–728, 1996.

[58] E Reali, J W Greiner, a Corti, H J Gould, F Bottazzoli, G Paganelli, J Schlom, and a G Siccardi. IgEs targeted on tumor cells: therapeutic activity and potential in the design of tumor vaccines. *Cancer research*, 61(14):5517–22, July 2001.

[59] D Maurer, E Fiebiger, B Reininger, B Wolff-Winiski, M H Jouvin, O Kilgus, J P Kinet, and G Stingl. Expression of functional high affinity immunoglobulin E receptors (Fc epsilon RI) on monocytes of atopic individuals. *The Journal of experimental medicine*, 179(2):745–50, February 1994.

[60] D Maurer, C Ebner, B Reininger, E Fiebiger, D Kraft, J P Kinet, and G Stingl. The high affinity IgE receptor (Fc epsilon RI) mediates IgE-dependent allergen presentation. *Journal of immunology (Baltimore, Md. : 1950)*, 154:6285–6290, 1995.

[61] D Maurer, S Fiebiger, C Ebner, B Reininger, G F Fischer, S Wichlas, M H Jouvin, M Schmitt-Egenolf, D Kraft, J P Kinet, and G Stingl. Peripheral blood dendritic cells express Fc epsilon RI as a complex composed of Fc epsilon RI alpha- and Fc epsilon RI gamma-chains and can use this receptor for IgE-mediated allergen presentation. *Journal of immunology (Baltimore, Md. : 1950)*, 157(2):607–16, jul 1996.

[62] H Matsuda, N Watanabe, Y Kiso, S Hirota, H Ushio, Y Kannan, M Azuma, H Koyama, and Y Kitamura. Necessity of IgE antibodies and mast cells for manifestation of resistance

against larval Haemaphysalis longicornis ticks in mice. *Journal of immunology (Baltimore, Md. : 1950)*, 144:259–262, 1990.

[63] Michele W L Teng, Michael H Kershaw, Jacob T Jackson, Mark J Smyth, and Phillip K Darcy. Adoptive transfer of chimeric FcepsilonRI gene-modified human T cells for cancer immunotherapy. *Human gene therapy*, 17:1134–1143, 2006.

[64] D Dombrowicz, B Quatannens, J P Papin, A Capron, and M Capron. Expression of a functional Fc epsilon RI on rat eosinophils and macrophages. *Journal of immunology (Baltimore, Md. : 1950)*, 165:1266–1271, 2000.

[65] M D Mossalayi, M Arock, D Mazier, P Vincendeau, and I Vouldoukis. The human immune response during cutaneous leishmaniasis: NO problem. *Parasitol Today*, 15:342–345, 1999.

[66] I Vouldoukis, V Riveros-Moreno, B Dugas, F Ouaaz, P Bécherel, P Debré, S Moncada, and M D Mossalayi. The killing of Leishmania major by human macrophages is mediated by nitric oxide induced after ligation of the Fc epsilon RII/CD23 surface antigen. *Proceedings of the National Academy of Sciences of the United States of America*, 92:7804–7808, 1995.

[67] R de Waal Malefyt, C G Figdor, R Huijbens, S Mohan-Peterson, B Bennett, J Culpepper, W Dang, G Zurawski, and J E de Vries. Effects of IL-13 on phenotype, cytokine production, and cytotoxic function of human monocytes. Comparison with IL-4 and modulation by IFN-gamma or IL-10. *Journal of immunology (Baltimore, Md. : 1950)*, 151:6370–6381, 1993.

[68] J. Punnonen, G. Aversa, B. G. Cocks, A. N. J. McKenzie, S. Menon, G. Zurawski, R. D. Malefyt, and J. E. De Vries. Interleukin-13 induces Interleukin-4 independent IgG4 and IgE synthesis and CD23 expression by human B cells. *Proceedings Of the National Academy Of Sciences Of the United States Of America*, 90:3730–3734, 1993.

[69] A Spittler, C Schiller, M Willheim, C Tempfer, S Winkler, and G Boltz-Nitulescu. IL-10 augments CD23 expression on U937 cells and down-regulates IL-4-driven CD23 expression on cultured human blood monocytes: effects of IL-10 and other cytokines on cell phenotype and phagocytosis. *Immunology*, 85:311–317, 1995.

[70] A Spittler, R Oehler, P Goetzinger, S Holzer, C M Reissner, F Leutmezer, V Rath, F Wrba, R Fuegger, G Boltz-Nitulescu, and E Roth. Low glutamine concentrations induce phenotypical and functional differentiation of U937 myelomonocytic cells. *The Journal of nutrition*, 127:2151–2157, 1997.

[71] A Vecchiarelli, A Siracusa, C Monari, D Pietrella, C Retini, and C Severini. Cytokine regulation of low-affinity IgE receptor (CD23) on monocytes from asthmatic subjects. *Clinical and experimental immunology*, 97:248–253, 1994.

[72] Akira Yokota, Hitoshi Kikutani, Tetsuji Tanaka, Ryoichi Sato, Edward L Barsumian, Masaki Suemura, and Tadamitsu Kishimoto. Two species of human Fc-epsilon receptor II (Fc-epsilonRII/CD23): Tissue-specific and IL-4-specific regulation of gene expression. *Cell*, 55:611–618, 1988.

[73] Michael R Campoli, Chien-Chung Chang, Toshiro Kageshita, Xinhui Wang, James B McCarthy, and Soldano Ferrone. Human high molecular weight-melanoma-associated antigen (HMW-MAA): a melanoma cell surface chondroitin sulfate proteoglycan (MSCP) with biological and clinical significance. *Critical reviews in immunology*, 24(4):267–296, January 2004.

[74] Matthew a Price, Leah E Colvin Wanshura, Jianbo Yang, Jennifer Carlson, Bo Xiang, Guiyuan Li, Soldano Ferrone, Arkadiusz Z Dudek, Eva a Turley, and James B McCarthy. CSPG4, a potential therapeutic target, facilitates malignant progression of melanoma. *Pigment cell & melanoma research*, 24(6):1148–57, December 2011.

[75] B S Wilson, K Imai, P G Natali, and S Ferrone. Distribution and molecular characterization of a cell-surface and a cytoplasmic antigen detectable in human melanoma cells with monoclonal antibodies. *International journal of cancer. Journal international du cancer*, 28:293–300, 1981.

[76] Chien-Chung Chang, Michael Campoli, Wei Luo, Wanzhou Zhao, Kurt S Zaenker, and Soldano Ferrone. Immunotherapy of melanoma targeting human high molecular weight melanoma-associated antigen: potential role of nonimmunological mechanisms. *Annals of the New York Academy of Sciences*, 1028:340–350, 2004.

[77] Peter Baluk, Hiroya Hashizume, and Donald M. M. Cellular abnormalities of blood vessels as targets in cancer, 2005.

[78] Paulo Cesar Maciag, Matthew Seavey, Zhen-kun Pan, and Soldano Ferrone. NIH Public Access. 68(19):8066–8075, 2010.

[79] Zeyana Rivera, Soldano Ferrone, Xinhui Wang, Sandro Jube, Haining Yang, Harvey I Pass, Shreya Kanodia, Giovanni Gaudino, and Michele Carbone. CSPG4 as a target of antibody-based immunotherapy for malignant mesothelioma. *Clinical cancer research : an official journal of the American Association for Cancer Research*, 18(19):5352–63, October 2012.

[80] Desiree Von Tell, Annika Armulik, and Christer Betsholtz. Pericytes and vascular stability, 2006.

[81] Michael Campoli, Robert Ferris, Soldano Ferrone, and Xinhui Wang. Immunotherapy of malignant disease with tumor antigen-specific monoclonal antibodies. *Clinical cancer research : an official journal of the American Association for Cancer Research*, 16:11–20, 2010.

[82] M A Burg, E Tillet, R Timpl, and W B Stallcup. Binding of the NG2 proteoglycan to type VI collagen and other extracellular matrix molecules. *The Journal of biological chemistry*, 271:26110–26116, 1996.

[83] J E de Vries, G D Keizer, A A te Velde, A Voordouw, D Ruiter, P Rümke, H Spits, and C G Figdor. Characterization of melanoma-associated surface antigens involved in the adhesion and motility of human melanoma cells. *International journal of cancer. Journal international du cancer*, 38:465–473, 1986.

[84] A C Antony. Folate receptors. *Annual review of nutrition*, 16:501–521, 1996.

[85] J Sudimack and R J Lee. Targeted drug delivery via the folate receptor. *Advanced drug delivery reviews*, 41(2):147–62, March 2000.

[86] Chun-Yen Ke, Carla J. Mathias, and Mark a. Green. The folate receptor as a molecular target for tumor-selective radionuclide delivery. *Nuclear Medicine and Biology*, 30(8):811–817, November 2003.

[87] R. G Anderson, B. A Kamen, K. G Rothberg, and S. W Lacey. Potocytosis: sequestration and transport of small molecules by caveolae. *Science*, 255(5043):410–1, January 1992.

[88] M Forgac. Structure and function of vacuolar class of ATP-driven proton pumps. *Physiological reviews*, 69(3):765–96, July 1989.

[89] K G Rothberg, Y S Ying, J F Kolhouse, B A Kamen, and R G Anderson. The glycophospholipid-linked folate receptor internalizes folate without entering the clathrin-coated pit endocytic pathway. *The Journal of cell biology*, 110(3):637–49, March 1990.

[90] M C Willingham and I Pastan. Endocytosis and exocytosis: current concepts of vesicle traffic in animal cells. *International review of cytology*, 92:51–92, January 1984.

[91] C P Leamon and P S Low. Delivery of macromolecules into living cells: a method that exploits folate receptor endocytosis. *Proceedings of the National Academy of Sciences of the United States of America*, 88(13):5572–6, July 1991.

[92] C P Leamon and P S Low. Cytotoxicity of momordin-folate conjugates in cultured human cells. *The Journal of biological chemistry*, 267(35):24966–71, December 1992.

[93] G B Henderson, J M Tsuji, and H P Kumar. Mediated uptake of folate by a high-affinity binding protein in sublines of L1210 cells adapted to nanomolar concentrations of folate. *The Journal of membrane biology*, 101(3):247–58, March 1988.

[94] M J Spinella, K E Brigle, E E Sierra, and I D Goldman. Distinguishing between folate receptor-alpha-mediated transport and reduced folate carrier-mediated transport in L1210 leukemia cells. *The Journal of biological chemistry*, 270(14):7842–9, April 1995.

[95] G R Westerhof, J H Schornagel, I Kathmann, A L Jackman, A Rosowsky, R A Forsch, J B Hynes, F T Boyle, G J Peters, and H M Pinedo. Carrier- and receptor-mediated transport of folate antagonists targeting folate-dependent enzymes: correlates of molecular-structure and biological activity. *Molecular pharmacology*, 48(3):459–71, September 1995.

[96] *Antifolate Drugs in Cancer Therapy*. Humana Press, 1999.

[97] M Bagnoli, S Canevari, M Figini, D Mezzanzanica, F Raspagliesi, A Tomassetti, and S Miotti. A step further in understanding the biology of the folate receptor in ovarian carcinoma. *Gynecologic oncology*, 88(1 Pt 2):S140–4, January 2003.

[98] M R Buist, P Kenemans, W den Hollander, J B Vermorken, C J Molthoff, C W Burger, T J Helmerhorst, J P Baak, and J C Roos. Kinetics and tissue distribution of the radiolabeled chimeric monoclonal antibody MOv18 IgG and F(ab')2 fragments in ovarian carcinoma patients. *Cancer research*, 53:5413–5418, 1993.

[99] G Toffoli, C Cernigoi, A Russo, A Gallo, M Bagnoli, and M Boiocchi. Overexpression of folate binding protein in ovarian cancers. *International journal of cancer. Journal international du cancer*, 74:193–198, 1997.

[100] S D Weitman, R H Lark, L R Coney, D W Fort, V Frasca, V R Zurawski, and B A Kamen. Distribution of the folate receptor GP38 in normal and malignant cell lines and tissues. *Cancer research*, 52:3396–3401, 1992.

[101] M Wu, W Gunning, and M Ratnam. Expression of folate receptor type alpha in relation to cell type, malignancy, and differentiation in ovary, uterus, and cervix. *Cancer epidemiology, biomarkers & prevention : a publication of the American Association for Cancer Research, cosponsored by the American Society of Preventive Oncology*, 8(9):775–82, September 1999.

[102] P Garin-Chesa, I Campbell, P E Saigo, J L Lewis, L J Old, and W J Rettig. Trophoblast and ovarian cancer antigen LK26. Sensitivity and specificity in immunopathology and molecular identification as a folate-binding protein. *The American journal of pathology*, 142:557–567, 1993.

[103] J F Ross, P K Chaudhuri, and M Ratnam. Differential regulation of folate receptor isoforms in normal and malignant tissues in vivo and in established cell lines. Physiologic and clinical implications. *Cancer*, 73:2432–2443, 1994.

[104] A C Antony, M A Kane, R M Portillo, P C Elwood, and J F Kolhouse. Studies of the role of a particulate folate-binding protein in the uptake of 5-methyltetrahydrofolate by cultured human KB cells. *The Journal of biological chemistry*, 260(28):14911–7, December 1985.

[105] O C Boerman, C C van Niekerk, K Makkink, T G Hanselaar, P Kenemans, and L G Poels. Comparative immunohistochemical study of four monoclonal antibodies directed against ovarian carcinoma-associated antigens. *International journal of gynecological pathology : official journal of the International Society of Gynecological Pathologists*, 10:15–25, 1991.

[106] M J Mattes, P P Major, D M Goldenberg, A S Dion, R V Hutter, and K M Klein. Patterns of antigen distribution in human carcinomas. *Cancer research*, 50:880s–884s, 1990.

[107] I G Campbell, T A Jones, W D Foulkes, and J Trowsdale. Folate-binding protein is a marker for ovarian cancer. *Cancer research*, 51:5329–5338, 1991.

[108] P Y Li, S Del Vecchio, R Fonti, M V Carriero, M I Potena, G Botti, S Miotti, S Lastoria, S Menard, M I Colnaghi, and M Salvatore. Local concentration of folate binding protein GP38 in sections of human ovarian carcinoma by in vitro quantitative autoradiography. *Journal of nuclear medicine : official publication, Society of Nuclear Medicine*, 37:665–672, 1996.

[109] F Crippa, G L Buraggi, E Di Re, M Gasparini, E Seregni, S Canevari, M Gadina, M Presti, A Marini, and E Seccamani. Radioimmunoscintigraphy of ovarian cancer with the MOv18 monoclonal antibody. *European journal of cancer*, 27:724–729, 1991.

[110] F Crippa, G Bolis, E Seregni, N Gavoni, G Scarfone, C Ferraris, G L Buraggi, and E Bombardieri. Single-dose intraperitoneal radioimmunotherapy with the murine monoclonal antibody I-131 MOv18: clinical results in patients with minimal residual disease of ovarian cancer. *European journal of cancer*, 31A:686–690, 1995.

[111] H P Kalofonos, M V Karamouzis, and A A Epenetos. Radioimmunoscintigraphy in patients with ovarian cancer. *Acta oncologica (Stockholm, Sweden)*, 40:549–557, 2001.

[112] I van Zanten-Przybysz, C F Molthoff, J C Roos, M A Plaizier, G W Visser, R Pijpers, P Kenemans, and R H Verheijen. Radioimmunotherapy with intravenously administered 131I-labeled chimeric monoclonal antibody MOv18 in patients with ovarian cancer. *Journal of nuclear medicine : official publication, Society of Nuclear Medicine*, 41:1168–1176, 2000.

[113] I van Zanten-Przybysz, C F Molthoff, J C Roos, R H Verheijen, A van Hof, M R Buist, H M Prinssen, W den Hollander, and P Kenemans. Influence of the route of administration on targeting of ovarian cancer with the chimeric monoclonal antibody MOv18: i.v. vs. i.p. *International journal of cancer. Journal international du cancer*, 92(1):106–14, April 2001.

[114] Michelle L James and Sanjiv S Gambhir. A molecular imaging primer: modalities, imaging agents, and applications. *Physiological reviews*, 92(2):897–965, April 2012.

[115] Freek J Beekman, David P McElroy, Frank Berger, Sanjiv S Gambhir, Edward J Hoffman, and Simon R Cherry. Towards in vivo nuclear microscopy: iodine-125 imaging in mice using

micro-pinholes. *European journal of nuclear medicine and molecular imaging*, 29:933–938, 2002.

[116] Freek J Beekman, Frans van der Have, Brendan Vastenhouw, Annemarie J A van der Linden, Peter P van Rijk, J Peter H Burbach, and Marten P Smidt. U-SPECT-I: a novel system for submillimeter-resolution tomography with radiolabeled molecules in mice. *Journal of nuclear medicine : official publication, Society of Nuclear Medicine*, 46:1194–1200, 2005.

[117] Tobias Schaeffter. Imaging modalities: principles and information content. *Progress in drug research. Fortschritte der Arzneimittelforschung. Progrès des recherches pharmaceutiques*, 62:15–81, January 2005.

[118] Arion F. Chatziioannou. Instrumentation for Molecular Imaging in Preclinical Research. 2(PROCEEDINGS OF THE AMERICAN THORACIC SOCIETY):533–536, 2005.

[119] Harald Becher, Klaus Tiemann, Thomas Schlosser, Christoph Pohl, Navin C. Nanda, Michalakis a. Averkiou, Jeff Powers, and Berndt Lüderitz. Improvement in Endocardial Border Delineation Using Tissue Harmonic Imaging. *Echocardiography*, 15:511–518, 1998.

[120] H O ANGER. A multiple scintillation counter in vivo scanner. *The American journal of roentgenology, radium therapy, and nuclear medicine*, 70(4):605–12, October 1953.

[121] L Farde, C Halldin, L Müller, T Suhara, P Karlsson, and H Hall. PET study of [11C]beta-CIT binding to monoamine transporters in the monkey and human brain. *Synapse (New York, N.Y.)*, 16:93–103, 1994.

[122] C Halldin, B Gulyás, O Langer, and L Farde. Brain radioligands - State of the art and new trends. *Quarterly Journal Of Nuclear Medicine*, 45:139–152, 2001.

[123] M E Phelps. Inaugural article: positron emission tomography provides molecular imaging of biological processes. *Proceedings of the National Academy of Sciences U.S.A.*, 97:9226–9233, 2000.

[124] Michael E Phelps. MOLECULAR IMAGING WITH POSITRON EMISSION TOMOGRAPHY. *Annual Review of Nuclear and Particle Science*, 52:303–338, 2002.

[125] Jennifer R Stickel and Simon R Cherry. High-resolution PET detector design: modelling components of intrinsic spatial resolution. *Physics in medicine and biology*, 50:179–195, 2005.

[126] Stephen E. Derenzo. Mathematical Removal of Positron Range Blurring in High Resolution Tomography. *IEEE Transactions on Nuclear Science*, 33, 1986.

[127] S.F. Haber, S.E. Derenzo, and D. Uber. Application of mathematical removal of positron range blurring in positron emission tomography. *IEEE Transactions on Nuclear Science*, 37, 1990.

[128] M.N. Wernick, G. Wang, C.-M. Kao, J.T. Yap, J. Mukherjee, M. Cooper, and C.-T. Chen. An image reconstruction method for dynamic PET. *1995 IEEE Nuclear Science Symposium and Medical Imaging Conference Record*, 3, 1995.

[129] Miles N. Wernick and John N. Aarsvold. *Emission Tomography: The Fundamentals of PET and SPECT*. Academic Press, 2004.

[130] Simon R Cherry and Arion F Chatziioannou. Small animal PET systems. *Emission Tomography First Edition*, pages 213–228, 2004.

[131] Steven R Meikle, Peter Kench, Michael Kassiou, and Richard B Banati. Small animal SPECT and its place in the matrix of molecular imaging technologies. *Physics in medicine and biology*, 50:R45–R61, 2005.

[132] D J Rowland, J S Lewis, and M J Welch. Molecular imaging: The application of small animal positron emission tomography. *J Cell Biochem Suppl*, 39:110–115, 2002.

[133] Bernd J Pichler, Martin S Judenhofer, and Christina Pfannenberg. Multimodal imaging approaches: PET/CT and PET/MRI. *Handbook of experimental pharmacology*, pages 109–132, 2008.

[134] H Wehrl, M Judenhofer, P Martirosian, F Maier, G Reischl, F Schick, and B Pichler. Multifunctional PET/MR imaging in small animal models. In *Proceedings 17th Scientific Meeting, International Society for Magnetic Resonance in Medicine, Honolulu*, page 3086, 2009.

[135] AM Blamire. The technology of mri - the next 10 years? *British Journal of Radiology*, 81:601–617, 2008.

[136] W Faulkner. Basic principles of mri, 1996.

[137] TF Massoud and SS Gambhir. Molecular imaging in living subjects: seeing fundamental biological processes in a new light. *Genes Dev*, 17:545–580, 2003.

[138] ML James and SS Gambhir. A molecular imaging primer: modalities, imaging agents, and applications. *Physiological reviews*, 92:897–965, 2012.

[139] Liang F and Chen B. A review on biomedical applications of single-walled carbon nano-tubes. *British Journal of Radiology*, 17:10–24, 2010.

[140] Debbage P and Jaschke W. Molecular imaging with nano-particles: giant roles for dwarf actors. *Histochem Cell Biology*, 130:845–875, 2008.

[141] P Blake, B Johnson, and J W VanMeter. Positron Emission Tomography (PET) and Single Photon Emission Computed Tomography (SPECT): Clinical Applications. *J Neuroophthalmol*, 23:34–41, 2003.

[142] Gairin Dancey, Richard H Begent, and Tim Meyer. Imaging in targeted delivery of therapy to cancer. *Targeted oncology*, 4(3):201–17, September 2009.

[143] Misara Hamoudeh, Muhammad Anas Kamleh, Roudayna Diab, and Hatem Fessi. Radionuclides delivery systems for nuclear imaging and radiotherapy of cancer. *Advanced drug delivery reviews*, 60:1329–1346, 2008.

[144] PD Acton. Small animal imaging with high resolution single photon emission tomography. *Nuclear medicine and biology*, 30:889–895, 2003.

[145] Benjamin L Franc, Paul D Acton, Carina Mari, and Bruce H Hasegawa. Small-animal SPECT and SPECT/CT: important tools for preclinical investigation. *Journal of nuclear medicine : official publication, Society of Nuclear Medicine*, 49:1651–1663, 2008.

[146] Célia M Gomes, Antero J Abrunhosa, Pedro Ramos, and Ernest K J Pauwels. Molecular imaging with SPECT as a tool for drug development. *Advanced drug delivery reviews*, October 2010.

[147] Rachel Goodwin, Giuseppe Giaccone, Hilary Calvert, Marinus Lobbezoo, and Elizabeth a Eisenhauer. Targeted agents: how to select the winners in preclinical and early clinical studies? *European journal of cancer (Oxford, England : 1990)*, 48(2):170–8, January 2012.

[148] B Liedert, S Bassus, C K Schneider, U Kalinke, and J Löwer. Safety of phase I clinical trials with monoclonal antibodies in Germany–the regulatory requirements viewed in the aftermath of the TGN1412 disaster. *International journal of clinical pharmacology and therapeutics*, 45:1–9, 2007.

[149] M J H Kenter and A F Cohen. Establishing risk of human experimentation with drugs: lessons from TGN1412. *Lancet*, 368:1387–1391, 2006.

[150] Ganesh Suntharalingam, Meghan R Perry, Stephen Ward, Stephen J Brett, Andrew Castello-Cortes, Michael D Brunner, and Nicki Panoskaltsis. Cytokine storm in a phase 1 trial of the anti-CD28 monoclonal antibody TGN1412. Technical report, 2006.

[151] Giovanna Damia and Maurizio D'Incalci. Contemporary pre-clinical development of anticancer agents–what are the optimal preclinical models? *European journal of cancer*, 45:2768–2781, 2009.

[152] Paul Workman. How much gets there and what does it do?: The need for better pharmacokinetic and pharmacodynamic endpoints in contemporary drug discovery and development. *Current pharmaceutical design*, 9:891–902, 2003.

[153] Timothy A Yap, Shahneen K Sandhu, Paul Workman, and Johann S de Bono. Envisioning the future of early anticancer drug development. *Nature reviews. Cancer*, 10:514–523, 2010.

[154] Pharmaceutical Press - Sampson's Textbook of Radiopharmacy Fourth edition.

[155] Anders Holmberg and Lennart Meurling. Preparation of sulfhydrylborane-dextran conjugates for boron neutron capture therapy. *Bioconjugate Chemistry*, 4(6):570–573, November 1993.

[156] G N Ranadive, H S Rosenzweig, M W Epperly, T Seskey, and W D Bloomer. A new method of technetium-99m labeling of monoclonal antibodies through sugar residues. A study with TAG-72 specific CC-49 antibody. *Nuclear medicine and biology*, 20(6):719–26, August 1993.

[157] Author D J Hnatowich, W W Layne, R L Childs, D Lanteigne, M A Davis, and P W Doherty. Radioactive Labeling of Antibody : A Simple and Efficient Method Published by : American Association for the Advancement of Science Stable URL : http://www.jstor.org/stable/1690030 Radioactive Labeling of Antibody : A Simple and Efficient Method. *Advancement Of Science*, 220(4597):613–615, 2009.

[158] D J Hnatowich. Antibody radiolabeling, problems and promises. *International journal of radiation applications and instrumentation. Part B, Nuclear medicine and biology*, 17(1):49–55, January 1990.

[159] S E Order. Monoclonal antibodies: potential role in radiation therapy and oncology. *International journal of radiation oncology, biology, physics*, 8(7):1193–201, July 1982.

[160] *Protein Pharmacokinetics and Metabolism (Google eBook)*, volume 1992. Springer, 1992.

[161] D J Hnatowich. Recent developments in the radiolabeling of antibodies with iodine, indium, and technetium. *Seminars in nuclear medicine*, 20:80–91, 1990.

[162] S. Frytak, E. T. Creagan, M. L. Brown, Darrell Salk, and W. Nelp. A Technetium-Labeled Monoclonal Antibody for Imaging Metastatic Melanoma. *American Journal of Clinical Oncology*, 14(2):156–161, April 1991.

[163] S Kasina, T N Rao, A Srinivasan, J A Sanderson, J N Fitzner, J M Reno, P L Beaumier, and A R Fritzberg. Development and biologic evaluation of a kit for preformed chelate technetium-99m radiolabeling of an antibody Fab fragment using a diamide dimercaptide chelating agent. *Journal of nuclear medicine : official publication, Society of Nuclear Medicine*, 32(7):1445–51, July 1991.

[164] Tracy R Daniels, Richard K Leuchter, Rafaela Quintero, Gustavo Helguera, José a Rodríguez, Otoniel Martínez-Maza, Birgit C Schultes, Christopher F Nicodemus, and Manuel L Penichet. Targeting HER2/neu with a fully human IgE to harness the allergic reaction against cancer cells. *Cancer immunology, immunotherapy : CII*, 61(7):991–1003, July 2012.

[165] Sophia N Karagiannis, Qin Wang, Nick East, Frances Burke, Stephane Riffard, Marguerite G Bracher, Richard G Thompson, Stephen R Durham, Lawrence B Schwartz, Frances R Balkwill, and Hannah J Gould. Activity of human monocytes in IgE antibody-dependent surveillance and killing of ovarian tumor cells. *European journal of immunology*, 33:1030–1040, 2003.

[166] Mieke Van Hemelrijck, Hans Garmo, Elisa Binda, Adrian Hayday, Sophia N Karagiannis, Niklas Hammar, Göran Walldius, Mats Lambe, Ingmar Jungner, and Lars Holmberg. Immunoglobulin E and cancer: a meta-analysis and a large Swedish cohort study. *Cancer causes & control : CCC*, 21(10):1657–67, October 2010.

[167] Elisa a Nigro, Elisa Soprana, Anna T Brini, Alessandro Ambrosi, Vijay a Yenagi, David Dombrowicz, Antonio G Siccardi, and Luca Vangelista. An antitumor cellular vaccine based on a mini-membrane IgE. *Journal of immunology (Baltimore, Md. : 1950)*, 188(1):103–10, January 2012.

[168] D H Josephs, J F Spicer, C J Corrigan, H J Gould, and S N Karagiannis. Epidemiological associations of allergy, IgE and cancer. *Clinical and experimental allergy : journal of the British Society for Allergy and Clinical Immunology*, 43(10):1110–23, October 2013.

[169] M a Pysz, S S Gambhir, and J K Willmann. Molecular imaging: current status and emerging strategies. *Clinical radiology*, 65(7):500–16, July 2010.

[170] Sophia N Karagiannis, Marguerite G Bracher, Rebecca L Beavil, Andrew J Beavil, James Hunt, Natalie McCloskey, Richard G Thompson, Nicholas East, Frances Burke, Brian J Sutton, David Dombrowicz, Frances R Balkwill, and Hannah J Gould. Role of IgE receptors in IgE antibody-dependent cytotoxicity and phagocytosis of ovarian tumor cells by human monocytic cells. *Cancer immunology, immunotherapy : CII*, 57(2):247–63, February 2008.

[171] Donald J Hnatowich. Preparation and quality control of gallium-68 radiopharmaceuticals. *Journal of Nuclear Medicine*, 16:764–768, 1975.

[172] Irfan Kayani, Jamshed B. Bomanji, Ashley Groves, Gerard Conway, Sveto Gacinovic, Thida Win, John Dickson, Martyn Caplin, and Peter Joseph Ell. Functional imaging of neuroendocrine tumors with combined PET/CT using 68Ga-DOTATATE (Dota-DPhe1, Tyr3-octreotate) and 18F-FDG. *Cancer*, 112:2447–2455, 2008.

[173] M U Khan, S Khan, S El-Refaie, Z Win, D Rubello, and A Al-Nahhas. Clinical indications for Gallium-68 positron emission tomography imaging. *European journal of surgical oncology : the journal of the European Society of Surgical Oncology and the British Association of Surgical Oncology*, 35:561–567, 2009.

[174] Denis R Beckford Vera, Sebastian Eigner, Katerina Eigner Henke, and Rene Leyva Montan. *Theranostics, Gallium-68, and Other Radionuclides*, volume 194. 2013.

[175] Jaya Shukla and Br Mittal. Ga-68: A Versatile PET Imaging Radionuclide. *Journal of Postgraduate Medicine Education and Research*, 47:74–76, January 2013.

[176] Maggie S Cooper, Michelle T Ma, Kavitha Sunassee, Karen P Shaw, Jennifer D Williams, Rowena L Paul, Paul S Donnelly, and Philip J Blower. Comparison of (64)Cu-Complexing Bifunctional Chelators for Radioimmunoconjugation: Labeling Efficiency, Specific Activity, and in Vitro/in Vivo Stability. *Bioconjugate chemistry*, April 2012.

[177] K A Krohn, L C Knight, J F Harwig, and M J Welch. Differences in the sites of iodination of proteins following four methods of radioiodination. *Biochimica et biophysica acta*, 490:497–505, 1977.

[178] J M Esteban, J Schlom, O a Gansow, R W Atcher, M W Brechbiel, D E Simpson, and D Colcher. New method for the chelation of indium-111 to monoclonal antibodies: biodistribution and imaging of athymic mice bearing human colon carcinoma xenografts. *Journal of nuclear medicine : official publication, Society of Nuclear Medicine*, 28(5):861–70, May 1987.

[179] D J Hnatowich, W W Layne, R L Childs, D Lanteigne, M A Davis, T W Griffin, and P W Doherty. Radioactive labeling of antibody: a simple and efficient method. *Science (New York, N.Y.)*, 220:613–615, 1983.

[180] Gary E. Krejcarek and Karen L. Tucker. Covalent attachment of chelating groups to macromolecules. *Biochemical and Biophysical Research Communications*, 77(2):581–585, July 1977.

[181] S E Halpern, P L Hagan, P R Garver, J a Koziol, a W Chen, J M Frincke, R M Bartholomew, G S David, and T H Adams. Stability, characterization, and kinetics of 111In-labeled monoclonal antitumor antibodies in normal animals and nude mouse-human tumor models. *Cancer research*, 43(11):5347–55, November 1983.

[182] J A Carrasquillo, J L Mulshine, P A Bunn, J C Reynolds, K A Foon, R W Schroff, P Perentesis, R G Steis, A M Keenan, and M Horowitz. Indium-111 T101 monoclonal antibody is superior to iodine-131 T101 in imaging of cutaneous T-cell lymphoma. *Journal of nuclear medicine : official publication, Society of Nuclear Medicine*, 28(3):281–7, March 1987.

[183] S E Halpern, R O Dillman, K F Witztum, J F Shega, P L Hagan, W M Burrows, J B Dillman, M L Clutter, R E Sobol, and J M Frincke. Radioimmunodetection of melanoma utilizing In-111 96.5 monoclonal antibody: a preliminary report., May 1985.

[184] C J Anderson and M J Welch. Radiometal-labeled agents (non-technetium) for diagnostic imaging. *Chemical reviews*, 99(9):2219–34, September 1999.

[185] Stephen J Mather. Design of radiolabelled ligands for the imaging and treatment of cancer. *Molecular bioSystems*, 3:30–35, 2007.

[186] C F Meares, M J McCall, D T Reardan, D a Goodwin, C I Diamanti, and M McTigue. Conjugation of antibodies with bifunctional chelating agents: isothiocyanate and bromoacetamide reagents, methods of analysis, and subsequent addition of metal ions. *Analytical biochemistry*, 142(1):68–78, October 1984.

[187] M De Jong, W H Bakker, W A Breeman, B F Bernard, L J Hofland, T J Visser, A Srinivasan, M Schmidt, M Béhé, H R Mäcke, and E P Krenning. Pre-clinical comparison of [DTPA0] octreotide, [DTPA0,Tyr3] octreotide and [DOTA0,Tyr3] octreotide as carriers for somatostatin receptor-targeted scintigraphy and radionuclide therapy. *International journal of cancer. Journal international du cancer*, 75:406–411, 1998.

[188] S. W. Schwarz, C. J. Mathias, J. Y. Sun, W. G. Dilley, S. A. Wells, A. E. Martell, and M. J. Welch. Evaluation of two new bifunctional chelates for radiolabeling a parathyroid-specific monoclonal antibody with In-111. *Nuclear Medicine and Biology*, 18:477–481, 1991.

[189] Thaddeus J Wadas, Edward H Wong, Gary R Weisman, and Carolyn J Anderson. Coordinating radiometals of copper, gallium, indium, yttrium, and zirconium for PET and SPECT imaging of disease. *Chemical reviews*, 110(5):2858–902, may 2010.

[190] M Brüggemann, G T Williams, C I Bindon, M R Clark, M R Walker, R Jefferis, H Waldmann, and M S Neuberger. Comparison of the effector functions of human immunoglobulins using a matched set of chimeric antibodies. *The Journal of experimental medicine*, 166:1351–1361, 1987.

[191] Paul-Pierre Pastoret, Philip Griebel, Hervé Bazin, and André Govaerts. *Handbook of vertebrate immunology*. Academic Press, 1998.

[192] Egisto Boschetti. Antibody separation by hydrophobic charge induction chromatography. *TRENDS in Biotechnology*, 20(8):333–337, 2002.

[193] Jerome Pezzini, Gilles Joucla, René Gantier, Magali Toueille, Anne-Marie Lomenech, Caroline Le Sénéchal, Bertrand Garbay, Xavier Santarelli, and Charlotte Cabanne. Antibody

capture by mixed-mode chromatography: A comprehensive study from determination of optimal purification conditions to identification of contaminating host cell proteins. *Journal of Chromatography A*, 1218(45):8197–8208, 2011.

[194] Anant K Menon, David Holowka, and Barbara Baird. Small oligomers of immunoglobulin e (ige) cause large-scale clustering of ige receptors on the surface of rat basophilic leukemia cells. *The Journal of cell biology*, 98(2):577–583, 1984.

[195] B Akerström, Th Brodin, K Reis, and L Björck. Protein g: a powerful tool for binding and detection of monoclonal and polyclonal antibodies. *The Journal of immunology*, 135(4):2589–2592, 1985.

[196] Yves Durocher, Sylvie Perret, and Amine Kamen. High-level and high-throughput recombinant protein production by transient transfection of suspension-growing human 293-ebna1 cells. *Nucleic acids research*, 30(2):e9–e9, 2002.

[197] Maggie S Cooper, Emmanuelle Sabbah, and Stephen J Mather. Conjugation of chelating agents to proteins and radiolabeling with trivalent metallic isotopes. *Nature protocols*, 1:314–317, 2006.

[198] Marguerite Bracher, Hannah J Gould, Brian J Sutton, David Dombrowicz, and Sophia N Karagiannis. Three-colour flow cytometric method to measure antibody-dependent tumour cell killing by cytotoxicity and phagocytosis. *Journal of immunological methods*, 323(2):160–71, June 2007.

[199] Jonathan H Langford, Margaret S Cooper, and Kim H Orchard. Development and validation of the 57Co assay for determining the ligand to antibody ratio in bifunctional chelate/antibody conjugates for use in radioimmunotherapy. *Nuclear medicine and biology*, 38(8):1103–10, November 2011.

[200] Einar K Fridriksson, Andrew Beavil, David Holowka, Hannah J Gould, Barbara Baird, and Fred W Mclafferty. Heterogeneous Glycosylation of Immunoglobulin E Constructs Characterized by. *biochemistry*, 39(12):3369–3376, 2000.

[201] J. N. Arnold, C. M. Radcliffe, M. R. Wormald, L. Royle, D. J. Harvey, M. Crispin, R. a. Dwek, R. B. Sim, and P. M. Rudd. The Glycosylation of Human Serum IgD and IgE and the Accessibility of Identified Oligomannose Structures for Interaction with Mannan-Binding Lectin. *The Journal of Immunology*, 173(11):6831–6840, November 2004.

[202] L W Bergman, E Harris, and W M Kuehl. Glycosylation causes an apparent block in translation of immunoglobulin heavy chain. *The Journal of biological chemistry*, 256(2):701–6, January 1981.

[203] Stefan Schlatter, Scott H Stansfield, Diane M Dinnis, Andrew J Racher, John R Birch, and David C James. On the optimal ratio of heavy to light chain genes for efficient recombinant antibody production by CHO cells. *Biotechnology progress*, 21(1):122–33, 2005.

[204] Sharon X Lu, Edward J Takach, Marjorie Solomon, Qing Zhu, Say-Jong Law, and Frank Y Hsieh. Mass spectral analyses of labile DOTA-NHS and heterogeneity determination of DOTA or DM1 conjugated anti-PSMA antibody for prostate cancer therapy. *Journal of pharmaceutical sciences*, 94(4):788–97, April 2005.

[205] Fares Al-Ejeh, Jocelyn M. Darby, Benjamin Thierry, and Michael P. Brown. A simplified suite of methods to evaluate chelator conjugation of antibodies: effects on hydrodynamic radius and biodistribution. *Nuclear Medicine and Biology*, 36:395–402, 2009.

[206] Erik D. Brady, Hyun Soon Chong, Diane E. Milenic, and Martin W. Brechbiel. Development of a spectroscopic assay for bifunctional ligand-protein conjugates based on copper. *Nuclear Medicine and Biology*, 31:795–802, 2004.

[207] Martin W Brechbiel, Otto A Gansow, Robert W Atcher, Jeffrey Schlom, Jose Esteban, Diane E Simpson, and David Colcher. Synthesis of 1-(p-isothiocyanatobenzyl) derivatives of DTPA and EDTA. Antibody labeling and tumor-imaging studies. *Inorganic Chemistry*, 25:2772–2781, 1986.

[208] M R Lewis, J Y Kao, a L Anderson, J E Shively, and a Raubitschek. An improved method for conjugating monoclonal antibodies with N-hydroxysulfosuccinimidyl DOTA. *Bioconjugate chemistry*, 12(2):320–4, 2001.

[209] T. K. Nikula, M. J. Curcio, M. W. Brechbiel, O. A. Gansow, R. D. Finn, and A. Scheinberg. A rapid, single vessel method for preparation of clinical grade ligand conjugated monoclonal antibodies. *Nuclear Medicine and Biology*, 22:387–390, 1995.

[210] Clinical kit preparations for Octreoscan. Octreoscan. 2014.

[211] Peter L Jones, Beverly A Brown, and Howard Sands. Uptake and Metabolism of n ' In-labeled Monoclonal Antibody B6 . 2 by the Rat Liver1. pages 852–856, 1990.

[212] BE Rogers, FN Franano, and JR Duncan. Identification of metabolites of 111In-diethylenetriaminepentaacetic acid-monoclonal antibodies and antibody fragments in vivo. *Cancer research*, 1995, 1995.

[213] Ian Sayers, Jonathan E M Housden, Alan C Spivey, and Birgit a Helm. The importance of Lys-352 of human immunoglobulin E in FcepsilonRII/CD23 recognition. *The Journal of biological chemistry*, 279(34):35320–5, August 2004.

[214] RA Clynes, TL Towers, LG Presta, and JV Ravetch. Inhibitory Fc receptors modulate in vivo cytoxicity against tumor targets. *Nature medicine*, (14):443–446, 2000.

[215] Nicola Hardwick and Benjamin Chain. Epitope spreading contributes to effective immunotherapy in metastatic melanoma patients. *Immunotherapy*, 3:731–733, 2011.

[216] Tracy R Daniels-Wells, Gustavo Helguera, Richard K Leuchter, Rafaela Quintero, Maggie Kozman, José a Rodríguez, Elizabeth Ortiz-Sánchez, Otoniel Martínez-Maza, Birgit C Schultes, Christopher F Nicodemus, and Manuel L Penichet. A novel IgE antibody targeting the prostate-specific antigen as a potential prostate cancer therapy. *BMC cancer*, 13:195, January 2013.

[217] X Wang, Y Wang, L Yu, K Sakakura, C Visus, J H Schwab, C R Ferrone, E Favoino, Y Koya, M R Campoli, J B McCarthy, A B DeLeo, and S Ferrone. CSPG4 in cancer: multiple roles. *Current molecular medicine*, 10:419–429, 2010.

[218] Xinhui Wang, Takuya Osada, Yangyang Wang, Ling Yu, Koichi Sakakura, Akihiro Katayama, James B McCarthy, Adam Brufsky, Mamatha Chivukula, Thaer Khoury, David S Hsu, William T Barry, H Kim Lyerly, Timothy M Clay, and Soldano Ferrone. CSPG4 protein as a new target for the antibody-based immunotherapy of triple-negative breast cancer. *Journal of the National Cancer Institute*, 102:1496–1512, 2010.

[219] William B Stallcup. The NG2 proteoglycan: past insights and future prospects. *Journal of neurocytology*, 31(6-7):423–35.

[220] R O Schlingemann, F J Rietveld, R M de Waal, S Ferrone, and D J Ruiter. Expression of the high molecular weight melanoma-associated antigen by pericytes during angiogenesis in tumors and in healing wounds. *The American journal of pathology*, 136:1393–1405, 1990.

[221] Feng-Ju Huang, Weon-Kyoo You, Paolo Bonaldo, Thomas N Seyfried, Elena B Pasquale, and William B Stallcup. Pericyte deficiencies lead to aberrant tumor vascularizaton in the brain of the NG2 null mouse. *Developmental biology*, 344:1035–1046, 2010.

[222] James Legg, Uffe B Jensen, Simon Broad, Irene Leigh, and Fiona M Watt. Role of melanoma chondroitin sulphate proteoglycan in patterning stem cells in human interfollicular epidermis. *Development (Cambridge, England)*, 130(24):6049–63, December 2003.

[223] Lucy Ghali, Soon-Tee Wong, Nick Tidman, Anthony Quinn, Michael P Philpott, and Irene M Leigh. Epidermal and hair follicle progenitor cells express melanoma-associated chondroitin sulfate proteoglycan core protein. *The Journal of investigative dermatology*, 122:433–442, 2004.

[224] Yasufumi Goto, Soldano Ferrone, Takaaki Arigami, Minoru Kitago, Atsushi Tanemura, Eiji Sunami, Sandy L Nguyen, Roderick R Turner, Donald L Morton, and S B Dave. NIH Public Access. 14(11):3401–3407, 2009.

[225] K S Midwood and D M Salter. Expression of NG2/human melanoma proteoglycan in human adult articular chondrocytes. *Osteoarthritis and cartilage / OARS, Osteoarthritis Research Society*, 6:297–305, 1998.

[226] Ilknur Kozanoglu, Can Boga, Hakan Ozdogu, Oktay Sozer, Erkan Maytalman, Ayse Canan Yazici, and Feride Iffet Sahin. Human bone marrow mesenchymal cells express NG2: possible increase in discriminative ability of flow cytometry during mesenchymal stromal cell identification. *Cytotherapy*, 11(5):527–33, January 2009.

[227] K A Grako and W B Stallcup. Participation of the NG2 proteoglycan in rat aortic smooth muscle cell responses to platelet-derived growth factor. *Experimental cell research*, 221(1):231–40, November 1995.

[228] K A Grako, T Ochiya, D Barritt, A Nishiyama, and W B Stallcup. PDGF (alpha)-receptor is unresponsive to PDGF-AA in aortic smooth muscle cells from the NG2 knockout mouse. *Journal of cell science*, 112 (Pt 6:905–15, March 1999.

[229] M Tsujisaki, M Igarashi, K Sakaguchi, M Eisinger, M Herlyn, and S Ferrone. Immunochemical and functional analysis of HLA class II antigens induced by recombinant immune interferon on normal epidermal melanocytes. *Journal of immunology (Baltimore, Md. : 1950)*, 138(4):1310–6, February 1987.

[230] CM Paulos, JA Reddy, and CP Leamon. Ligand binding and kinetics of folate receptor recycling in vivo: impact on receptor-mediated drug delivery. *Molecular ...*, 66(6):1406–1414, 2004.

[231] Sandra Medic, Helen Rizos, and Mel Ziman. Differential PAX3 functions in normal skin melanocytes and melanoma cells. *Biochemical and biophysical research communications*, 411(4):832–7, aug 2011.

[232] Jianbo Yang, Matthew A Price, Cheryl L Neudauer, Christopher Wilson, Soldano Ferrone, Hong Xia, Joji Iida, Melanie A Simpson, and James B McCarthy. Melanoma chondroitin sulfate proteoglycan enhances FAK and ERK activation by distinct mechanisms. *The Journal of cell biology*, 165:881–891, 2004.

[233] Elisa a Nigro, Anna T Brini, Elisa Soprana, Alessandro Ambrosi, David Dombrowicz, Antonio G Siccardi, and Luca Vangelista. Antitumor IgE adjuvanticity: key role of Fc epsilon RI. *Journal of immunology (Baltimore, Md. : 1950)*, 183(7):4530–6, October 2009.

[234] M H Kershaw, P K Darcy, J A Trapani, D MacGregor, and M J Smyth. Tumor-specific IgE-mediated inhibition of human colorectal carcinoma xenograft growth. *Oncology research*, 10:133–142, 1998.

[235] L D Shultz, P a Schweitzer, S W Christianson, B Gott, I B Schweitzer, B Tennent, S McKenna, L Mobraaten, T V Rajan, and D L Greiner. Multiple defects in innate and adaptive immunologic function in NOD/LtSz-scid mice. *Journal of immunology (Baltimore, Md. : 1950)*, 154(1):180–91, January 1995.

[236] L. D. Shultz, B. L. Lyons, L. M. Burzenski, B. Gott, X. Chen, S. Chaleff, M. Kotb, S. D. Gillies, M. King, J. Mangada, D. L. Greiner, and R. Handgretinger. Human Lymphoid and Myeloid Cell Development in NOD/LtSz-scid IL2R null Mice Engrafted with Mobilized Human Hemopoietic Stem Cells. *The Journal of Immunology*, 174(10):6477–6489, May 2005.

[237] Leonard D Shultz, Fumihiko Ishikawa, and Dale L Greiner. Humanized mice in translational biomedical research. *Nature reviews. Immunology*, 7:118–130, 2007.

[238] Stefani Spranger, Bernhard Frankenberger, and Dolores J Schendel. NOD/scid IL-2Rg(null) mice: a preclinical model system to evaluate human dendritic cell-based vaccine strategies in vivo. *Journal of translational medicine*, 10(1):30, January 2012.

[239] L T Baxter and R K Jain. Transport of fluid and macromolecules in tumors. III. Role of binding and metabolism. *Microvascular research*, 41:5–23, 1991.

[240] R De Bree, J C Roos, J J Quak, De Bree, C Roos, J Quak, J Wilhelm, Van Lingen, B Snow, and Guus A M S Van Dongen. Biodistribution of radiolabeled monoclonal antibody E48 IgG and F (ab ') 2 in patients with head and neck cancer . in Patients of Radiolabeled. pages 277–286, 1995.

[241] a Morell, W D Terry, and T a Waldmann. Metabolic properties of IgG subclasses in man. *The Journal of clinical investigation*, 49(4):673–80, April 1970.

[242] David Ternant and Gilles Paintaud. Pharmacokinetics and concentration-effect relationships of therapeutic monoclonal antibodies and fusion proteins. *Expert opinion on biological therapy*, 5 Suppl 1:S37–47, September 2005.

[243] Amy E Gilbert, Panagiotis Karagiannis, Tihomir Dodev, Alexander Koers, Katie Lacy, Debra H Josephs, Pooja Takhar, Jenny L C Geh, Ciaran Healy, Mark Harries, Katharine M Acland, Sarah M Rudman, Rebecca L Beavil, Philip J Blower, Andrew J Beavil, Hannah J Gould, James Spicer, Frank O Nestle, and Sophia N Karagiannis. Monitoring the systemic human memory B cell compartment of melanoma patients for anti-tumor IgG antibodies. *PloS one*, 6(4):e19330, January 2011.

[244] Réjean Lapointe, Angélique Bellemare-Pelletier, Franck Housseau, Jacques Thibodeau, and Patrick Hwu. CD40-stimulated B lymphocytes pulsed with tumor antigens are effective antigen-presenting cells that can generate specific T cells. *Cancer research*, 63:2836–2843, 2003.

[245] Pearline Zhaoying Teo, Paul J Utz, and Joseph a Mollick. Using the allergic immune system to target cancer: activity of IgE antibodies specific for human CD20 and MUC1. *Cancer immunology, immunotherapy : CII*, 61(12):2295–309, December 2012.

[246] Qingfeng Chen, Maroun Khoury, and Jianzhu Chen. Expression of human cytokines dramatically improves reconstitution of specific human-blood lineage cells in humanized mice. *Proceedings of the National Academy of Sciences of the United States of America*, 106:21783–21788, 2009.

[247] Ivan J Fuss, Marjorie E Kanof, Phillip D Smith, and Heddy Zola. Isolation of whole mononuclear cells from peripheral blood and cord blood. *Current protocols in immunology / edited by John E. Coligan ... [et al.]*, Chapter 7:Unit7.1, 2009.

[248] Douglas W Schneider, Tara Heitner, Bruno Alicke, David R Light, Kirk McLean, Noboru Satozawa, Gordon Parry, Jeongsoo Yoo, Jason S Lewis, and Renate Parry. In vivo biodistribution, PET imaging, and tumor accumulation of 86Y- and 111In-antimindin/RG-1, engineered antibody fragments in LNCaP tumor-bearing nude mice. *Journal of nuclear medicine : official publication, Society of Nuclear Medicine*, 50(3):435–43, March 2009.

[249] Victor Yip, Enzo Palma, Devin B Tesar, Eduardo E Mundo, Daniela Bumbaca, Elizabeth K Torres, Noe a Reyes, Ben Q Shen, Paul J Fielder, Saileta Prabhu, Leslie a Khawli, and C Andrew Boswell. Quantitative cumulative biodistribution of antibodies in mice: Effect of modulating binding affinity to the neonatal Fc receptor. *mAbs*, 6(3):689–96, 2014.

[250] Thomas A Waldmann, Atsushi Iio, Makio Ogawa, and O Ross Mcintyre. The metabolism IgE Studies in normal indiviuials and in a patient with IgE myeloma. *The Journal of Immunology*, 117(4), 1976.

[251] Atsushi Iio, TA Waldmann, and Warren Strober. Metabolic study of human IgE: evidence for an extravascular catabolic pathway. *The Journal of Immunology*, 1978.

[252] S C Dreskin, P K Goldsmith, W Strober, L a Zech, and J I Gallin. Metabolism of immunoglobulin E in patients with markedly elevated serum immunoglobulin E levels. *The Journal of clinical investigation*, 79(6):1764–72, June 1987.

[253] Jacques Baenziger, S. Kornfeld, and S. Kochwa. Structure of the carbohydrate units of IgE immunoglobulin. I. Over-all composition, glycopeptide isolation, and structure of the high mannose oligosaccharide unit. *The Journal of biological chemistry*, 249(6):1889, 1974.

[254] D K Meijer, H B Scholtens, and M J Hardonk. The role of the liver in clearance of glycoproteins from the general circulation, with special reference to intestinal alkaline phosphatase. *Pharmaceutisch weekblad. Scientific edition*, 4:57–70, 1982.

[255] Surinder K Batra, Maneesh Jain, Uwe A Wittel, Subhash C Chauhan, and David Colcher. Pharmacokinetics and biodistribution of genetically engineered antibodies. *Current opinion in biotechnology*, 13(6):603–8, December 2002.

[256] R M Sharkey, C Motta-Hennessy, D Pawlyk, J A Siegel, and D M Goldenberg. Biodistribution and radiation dose estimates for yttrium- and iodine-labeled monoclonal antibody IgG and fragments in nude mice bearing human colonic tumor xenografts. *Cancer research*, 50:2330–2336, 1990.

[257] Elke O Luger, Verena Fokuhl, Michael Wegmann, Melanie Abram, Kati Tillack, Gernot Achatz, Rudolf a Manz, Margitta Worm, Andreas Radbruch, and Harald Renz. Induction of long-lived allergen-specific plasma cells by mucosal allergen challenge. *The Journal of allergy and clinical immunology*, 124(4):819–26.e4, October 2009.

[258] Karen E Pollok, Michael Lahn, Nathan Enas, Ann McNulty, Jeremy Graff, Shanbao Cai, Jennifer R Hartwell, Aaron Ernstberger, Donald Thornton, Les Brail, and Gary Hutchins. In Vivo Measurements of Tumor Metabolism and Growth after Administration of Enzastaurin Using Small Animal FDG Positron Emission Tomography. *Journal of oncology*, 2009:596560, January 2009.

[259] Philip S Low, Walter A Henne, and Derek D Doorneweerd. Discovery and Development of Folic-Acid-Based Receptor Targeting for Imaging and Therapy of Cancer and Inflammatory Diseases. *Accounts of Chemical Research*, 41(1):120–129, 2008.

[260] H Conrad, John R Wingard, Teruko Ishizaka, The Johns, Samaritan Hosprtal, and Loch Raven. The interaction of human and rodent Ige with the human receptor. 130(1), 1983.

[261] John Hakimi, Cary Seals, and Jo Ann Kondass. The CY Subunit of the Human IgE Receptor (FcERI) Is Sufficient. 265(38):22079–22081, 1990.

[262] G Delespesse, M Sarfati, CY Wu, S Fournier, and M Letellier. The low-affinity receptor for ige. *Immunological reviews*, 125(1):77–97, 1992.

[263] S Miotti, S Canevari, S Menard, D Mezzanzanica, G Porro, SM Pupa, M Regazzoni, E Tagliabue, and MI Colnaghi. Characterization of human ovarian carcinoma-associated antigens defined by novel monoclonal antibodies with tumor-restricted specificity. *International journal of cancer*, 39(3):297–303, 1987.

[264] Leslie R Coney, Delia Mezzanzanica, David Sanborn, Patrizia Casalini, Maria I Colnaghi, and Vincent R Zurawski. Chimeric murine-human antibodies directed against folate binding receptor are efficient mediators of ovarian carcinoma cell killing. *Cancer research*, 54(9):2448–2455, 1994.

[265] Carla FM Moltoff, Helma M Prinssen, Peter Kenemans, Arjan C van Hof, Wim den Hollander, and René HM Verheijen. Escalating protein doses of chimeric monoclonal antibody mov18 immunoglobulin g in ovarian carcinoma patients: a phase i study. *Cancer*, 80(S12):2712–2720, 1997.

[266] H Bazin, A Beckers, and P Querinjean. Three classes and four (sub)classes of rat immunoglobulins: IgM, IgA, IgE and IgG1, IgG2a, IgG2b, IgG2c. *European journal of immunology*, 4(1):44–8, January 1974.

[267] C Thomas, A M Nijenhuis, W Timens, P J Kuppen, T Daemen, and G L Scherphof. Liver metastasis model of colon cancer in the rat: immunohistochemical characterization. *Invasion & metastasis*, 13:102–112, 1993.

[268] M K Demetrikopoulos, R H Goldfarb, Z B Zhang, and J M Weiss. Blood level of B and CD4+ lymphocytes measured before induction of an experimental tumor in rats predicts tumor progression and survival. *Cancer epidemiology, biomarkers & prevention : a publication of the American Association for Cancer Research, cosponsored by the American Society of Preventive Oncology*, 9(6):609–17, June 2000.

[269] N Quan, Z Zhang, M K Demetrikopoulos, R P Kitson, W H Chambers, R H Goldfarb, and J M Weiss. Evidence for involvement of B lymphocytes in the surveillance of lung metastasis in the rat. *Cancer research*, 59(5):1080–9, March 1999.

[270] S Bournazos, J M Woof, S P Hart, and I Dransfield. Functional and clinical consequences of Fc receptor polymorphic and copy number variants. *Clinical and experimental immunology*, 157(2):244–54, August 2009.

[271] G Alber, U M Kent, and H Metzger. Functional comparison of Fc epsilon RI, Fc gamma RII, and Fc gamma RIII in mast cells. *Journal of immunology (Baltimore, Md. : 1950)*, 149(7):2428–36, October 1992.

[272] Andrew Getahun, Fredrik Hjelm, and Birgitta Heyman. IgE enhances antibody and T cell responses in vivo via CD23+ B cells. *Journal of immunology (Baltimore, Md. : 1950)*, 175(3):1473–82, August 2005.

[273] Reina E Mebius and Georg Kraal. Structure and function of the spleen. *Nature reviews. Immunology*, 5:606–616, 2005.

[274] Rhona Stein, David M Goldenberg, Gaik Lin Ong, Suzanne R Thorpe, and M Julles Mattes. Manipulation of blood clearance to optimize delivery of residualizing label-antibody conjugates to tumor cells in vivo. *Journal of nuclear medicine: official publication, Society of Nuclear Medicine*, 38(9):1392–1400, 1997.

[275] A L Gavin, J Snider, M D Hulett, I F Mckenzie, and P M Hogarth. Expression of recombinant soluble Fc epsilon RI: function and tissue distribution studies. *Immunology*, 86(3):392–8, November 1995.

[276] Caroline Staff, Carl G M Magnusson, Mohammad Hojjat-Farsangi, Szilvia Mosolits, Maria Liljefors, Jan-Erik Frödin, Britta Wahrén, Hå kan Mellstedt, and Gustav J Ullenhag. Induction of IgM, IgA and IgE antibodies in colorectal cancer patients vaccinated with a recombinant CEA protein. *Journal of clinical immunology*, 32(4):855–65, August 2012.

6 Appendices

Anti-CSPG4-IgE full list of organs biodistribution in % ID/g

MAA IgE	4h	12h	24h	48h	72h	120h
Trachea	0.6274	0.7801	0.3987	0.3864	0.4269	0.0983
Thyroid	0.5951	0.3458	0.2977	0.1747	0.1495	0.0866
heart	0.6553	0.6678	0.4667	0.3293	0.3854	0.1511
Lungs	1.4533	0.5845	0.3556	0.1658	0.1145	0.1515
Liver	37.0854	27.8283	18.2411	14.4441	12.9757	8.9998
Spleen	6.2346	6.0178	8.8939	8.3226	6.9692	4.2303
Stomach	0.2632	0.2054	2.8512	0.2715	0.0896	0.0715
lrg intes	7.7384	7.8196	9.1332	1.4030	0.4423	0.2071
sml intes	6.0525	2.0755	2.4389	0.3382	0.1456	0.0823
Pancreas	0.2287	0.1904	0.1478	0.0944	0.0859	0.0476
Kidneys	1.2627	0.9090	0.8013	0.7189	0.5977	0.4288
REP	0.1976	0.2439	0.2222	0.1352	0.1195	0.0735
Muscle	0.0932	0.1055	0.0762	0.0459	0.0325	0.0250
Femur	1.5561	1.3784	1.3338	1.1317	0.9150	0.9199
Salivary glands	0.2332	0.1823	0.2288	0.1422	0.1356	0.0946
Tumour	0.8316	1.4383	1.2292	0.8452	0.6762	0.3511
bladder	0.8574	1.8144	1.6094	0.8116	0.4949	0.1791
blood	2.2457	1.0958	0.3588	0.0819	0.1015	0.0408
skin	0.2196	0.2894	0.3544	0.2376	0.2284	0.1192

Anti-CSPG4-IgG full list of organs biodistribution in % ID/g

MAA IgG	4hr	12hr	24h	48h	72h	120h
Trachea	22.0046	27.1502	8.6682	5.4977	4.3851	2.9612
Thyroid	8.5743	7.4895	4.8848	2.7733	2.9931	2.0615
heart	8.2242	10.8789	4.6041	3.2137	8.2655	2.0316
Lungs	21.3979	20.0201	10.9182	6.1149	14.0926	4.6209
Liver	11.4068	12.9918	9.8384	11.4178	12.1732	11.5501
Spleen	24.0497	20.4702	25.0051	46.7053	70.5806	64.6027
Stomach	1.8382	1.9415	1.9974	1.5630	2.0328	1.9209
lrg intes	1.4624	1.8650	1.6531	1.8479	2.6517	2.1947
sml intes	3.0502	3.2944	4.2499	3.3336	6.2526	6.3282
Pancreas	2.4320	4.3817	3.2151	2.0266	2.7430	2.0251
Kidneys	10.1230	10.5742	6.8240	7.6396	5.3887	4.7264
REP	7.4570	11.0618	3.7474	12.0822	8.0244	11.4349
Muscle	1.1760	1.7315	1.6585	0.9891	0.9695	0.7778
Femur	4.7732	4.6760	5.4676	6.9285	10.0223	10.3495
Salivary glands	4.5753	8.9425	6.4388	8.1649	6.6827	6.6611
Tumour	13.1341	17.9528	26.3937	27.0239	23.7488	23.8255
bladder	4.2424	4.0814	4.7817	5.5791	4.9030	3.9456
blood	25.5559	13.2879	13.1837	5.7633	2.1203	3.9622
skin	5.1769	9.3394	5.7630	5.9811	7.0278	6.5539

IgE isotype control full list of organs biodistribution in % ID/g

MOV18 IgE	4h	12h	24h	48h	72h	120h
Trachea	0.9140	0.2834	0.2809	0.1985	0.4279	0.1148
Thyroid	0.3696	0.3538	0.2065	0.1321	0.3062	0.7025
heart	0.2539	0.3273	0.1949	0.1183	0.1402	0.1195
Lungs	0.4194	0.3445	0.1298	0.0855	0.0737	0.0719
Liver	25.7456	19.2242	14.0537	7.9158	5.9647	5.6606
Spleen	3.8793	6.0317	4.3225	2.9970	3.7863	3.3959
Stomach	0.8204	0.3350	2.2016	0.2611	0.1028	0.1052
lrg intes	29.1134	19.2587	9.3411	2.3095	0.8090	0.3449
sml intes	7.4033	1.9249	1.6024	0.2769	0.1675	0.1041
Pancreas	0.4249	0.1105	0.0948	0.0528	0.0661	0.0498
Kidneys	1.3500	1.5264	1.2224	1.0484	0.9521	0.8060
REP	0.1154	0.1591	0.1844	0.1422	0.1592	0.1181
Muscle	0.0537	0.0512	0.1054	0.0513	0.0438	0.0421
Femur	0.7757	1.1013	1.0083	0.7681	0.7666	0.7186
Salivary glands	0.1434	0.1046	0.1369	0.1059	0.1628	0.0757
Tumour	0.5814	0.2900	0.3755	0.2400	0.2069	0.1989
bladder	2.0739	0.8284	0.3311	0.1325	0.3129	0.1517
blood	0.5499	0.1657	0.1152	0.0709	0.0444	0.0317
skin	0.1894	0.1108	0.1686	0.1925	0.3339	0.1118

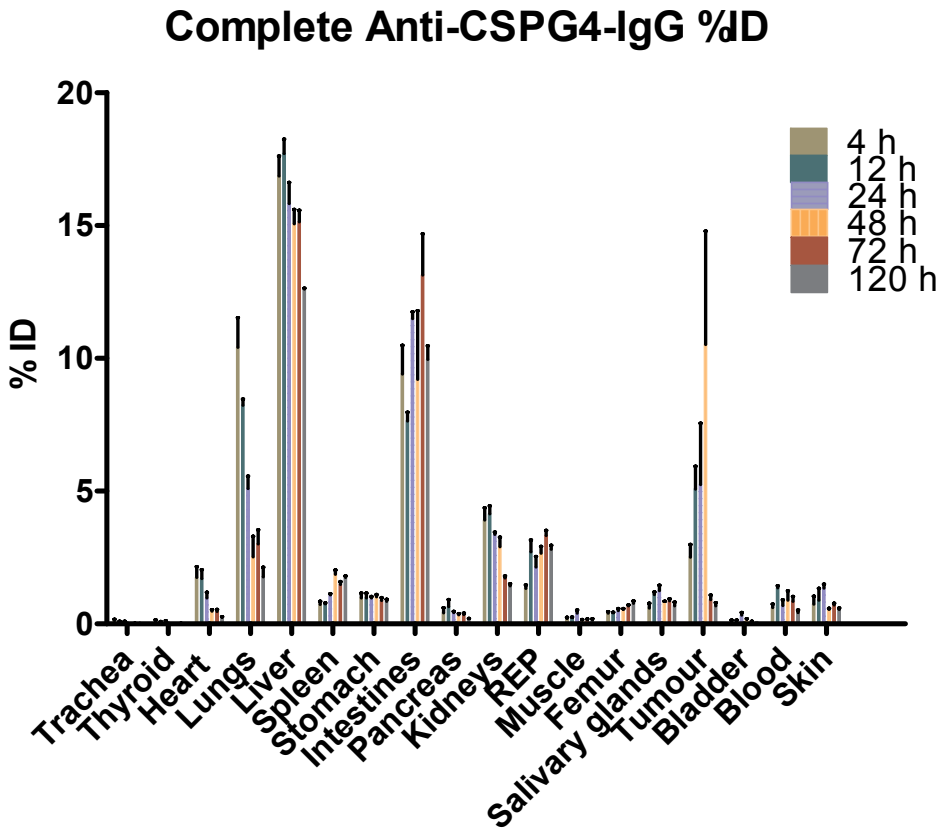

Biodistribution of anti-CSPG4-IgG in % ID of all organs harvested. Data plotted including SEM error bars (n=3).

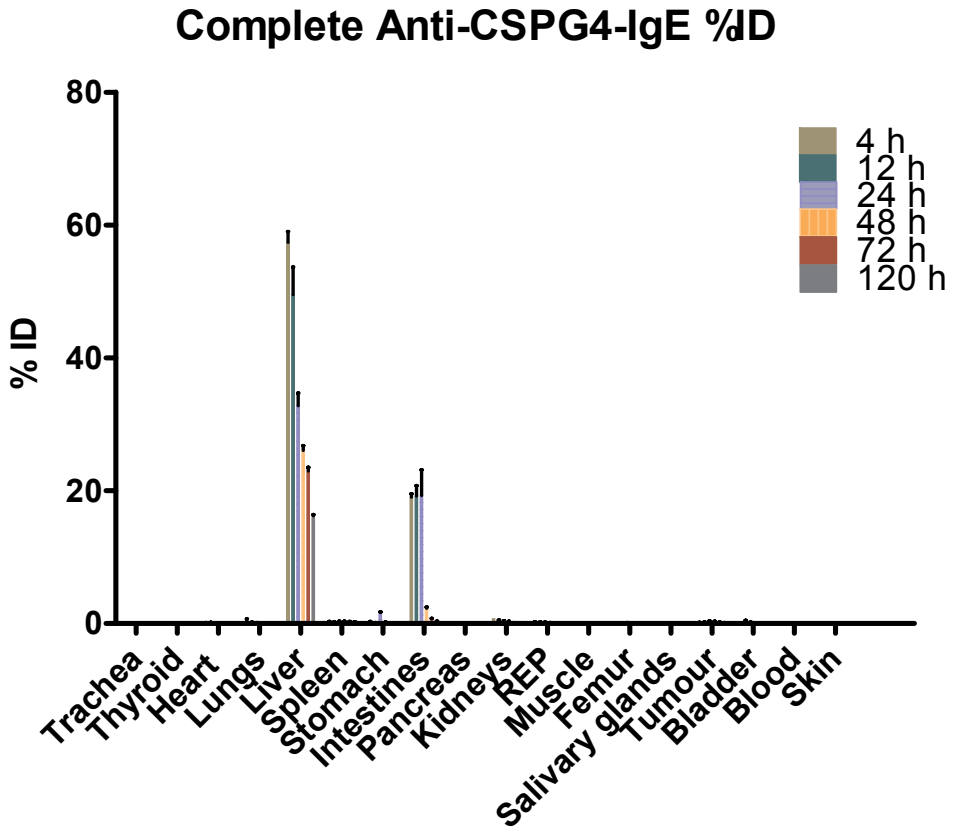

Biodistribution of anti-CSPG4-IgE in % ID of all organs harvested. Data plotted including SEM error bars (n=3).

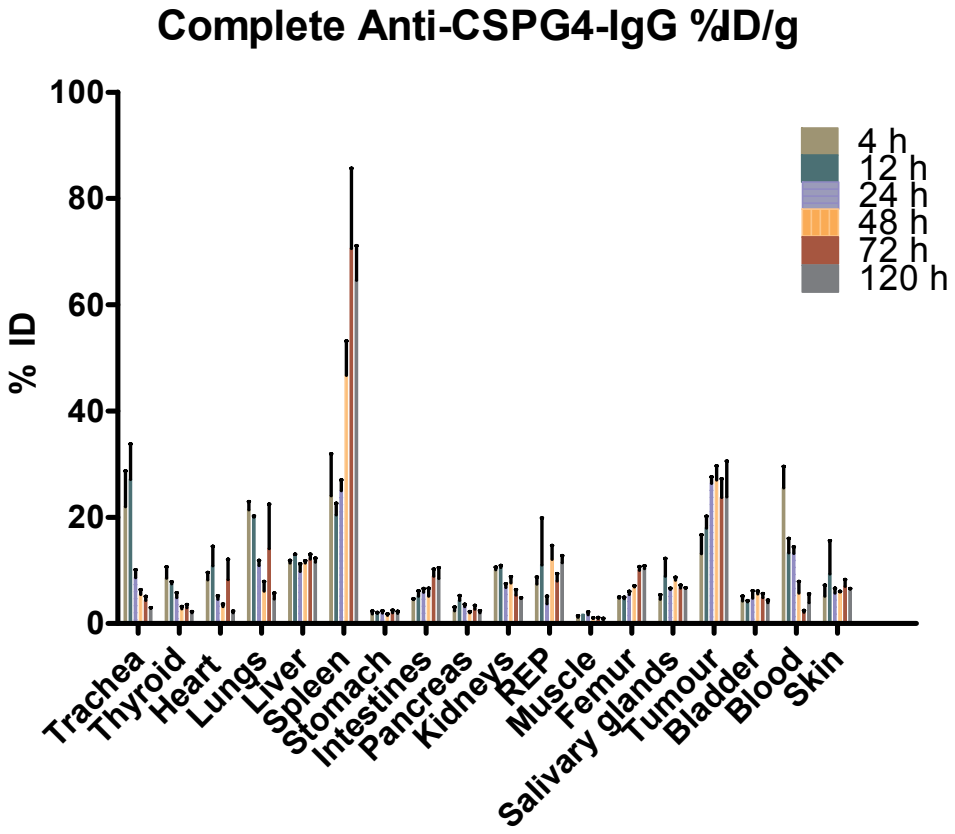

Biodistribution of anti-CSPG4-IgG in % ID/g of all organs harvested. Data plotted including SEM error bars (n=3).

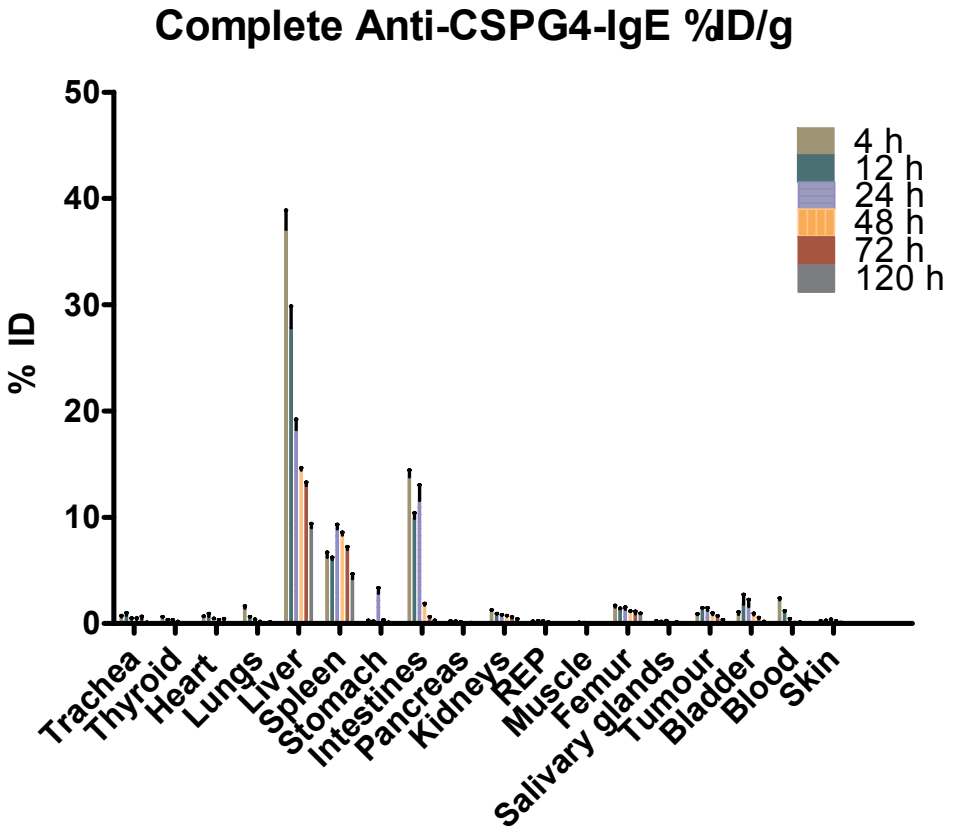

Biodistribution of anti-CSPG4-IgE in % ID/g of all organs harvested. Data plotted including SEM error bars (n=3).

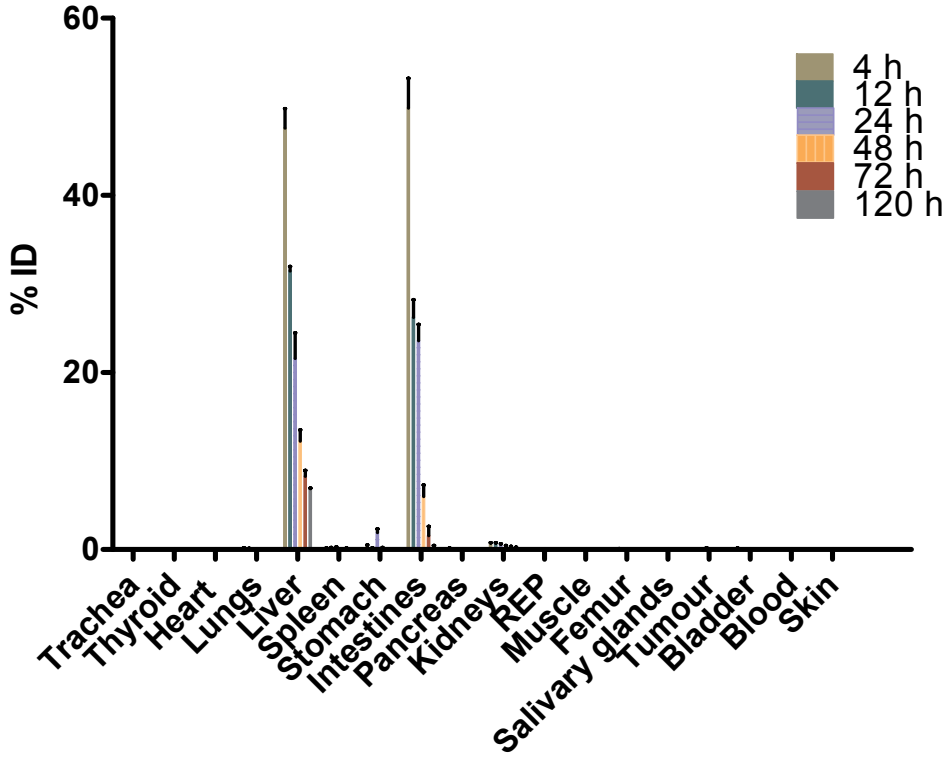

Biodistribution of IgE isotype control in % ID of all organs harvested. Data plotted including SEM error bars (n=3).

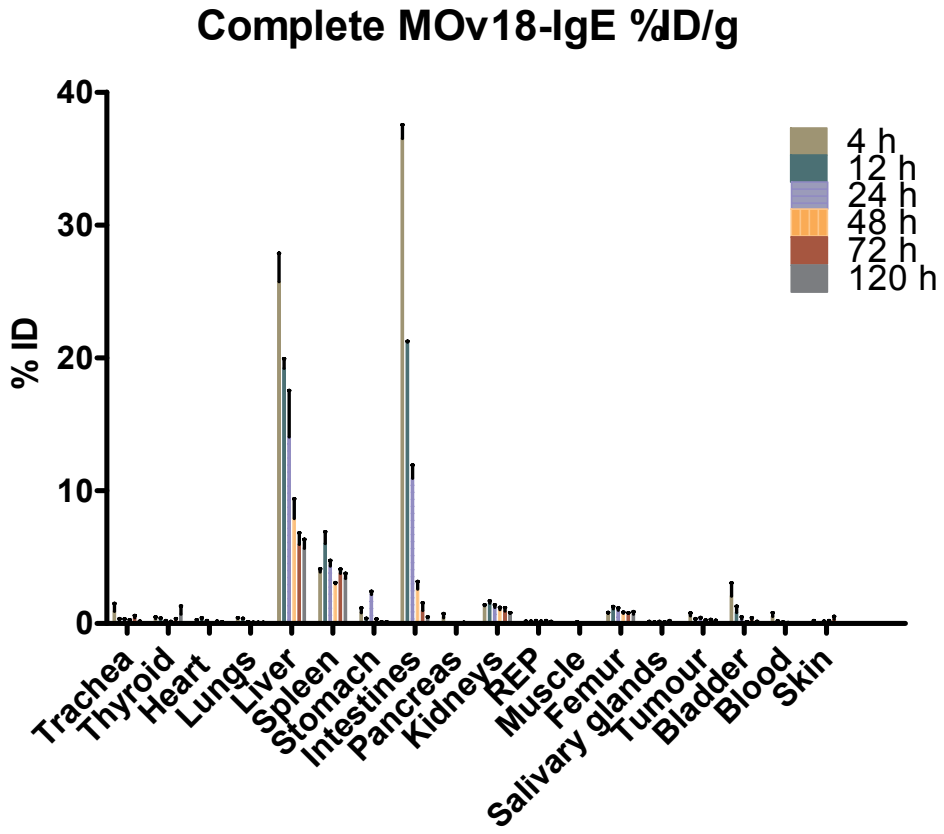

Biodistribution of IgE isotype control in % ID/g of all organs harvested. Data plotted including SEM error bars (n=3).

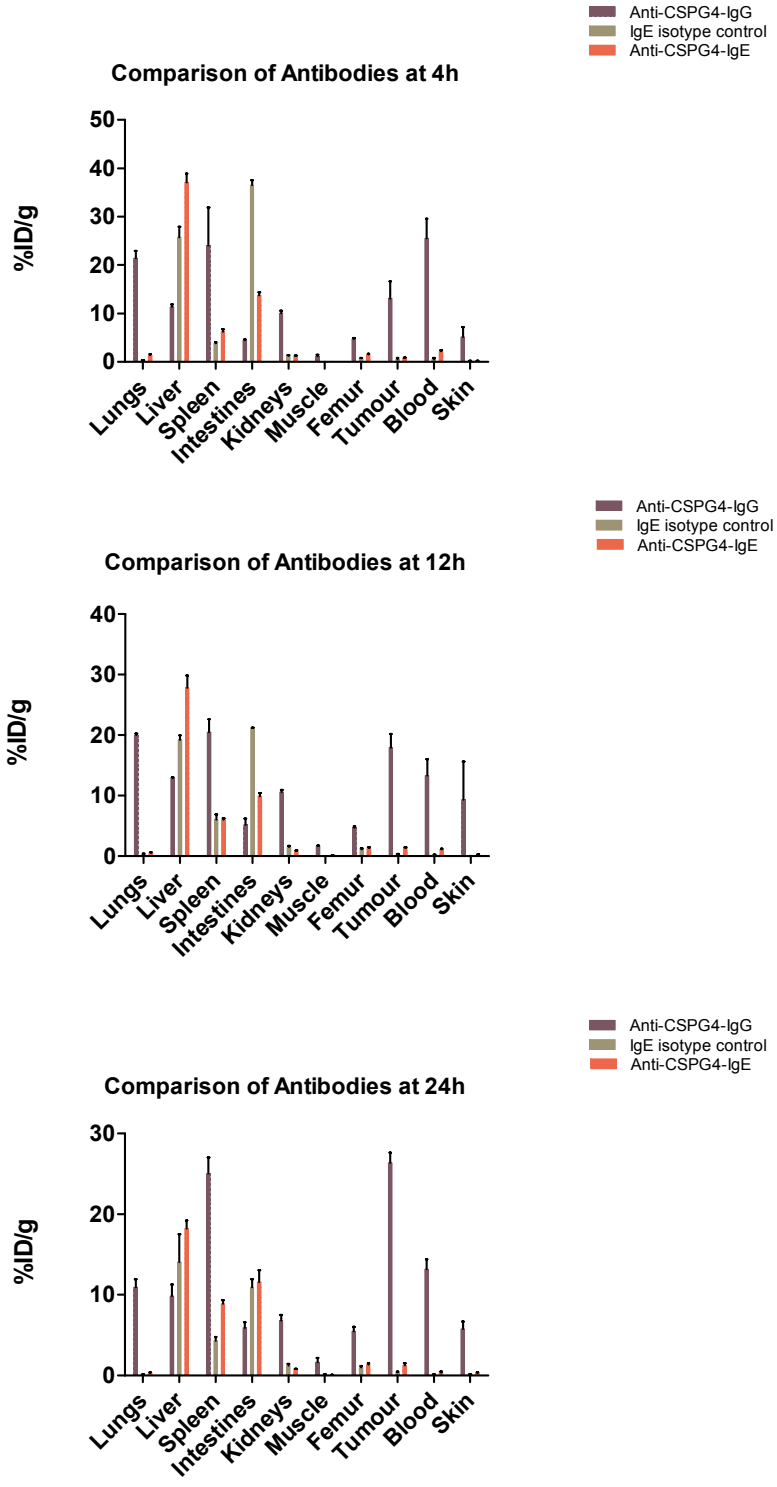

Comparison of biodistribution of anti-CSPG4-IgE, anti-CSPG4-IgG and IgE isotype control in % ID/g at specific time points. Data plotted including SEM error bars (n=3).

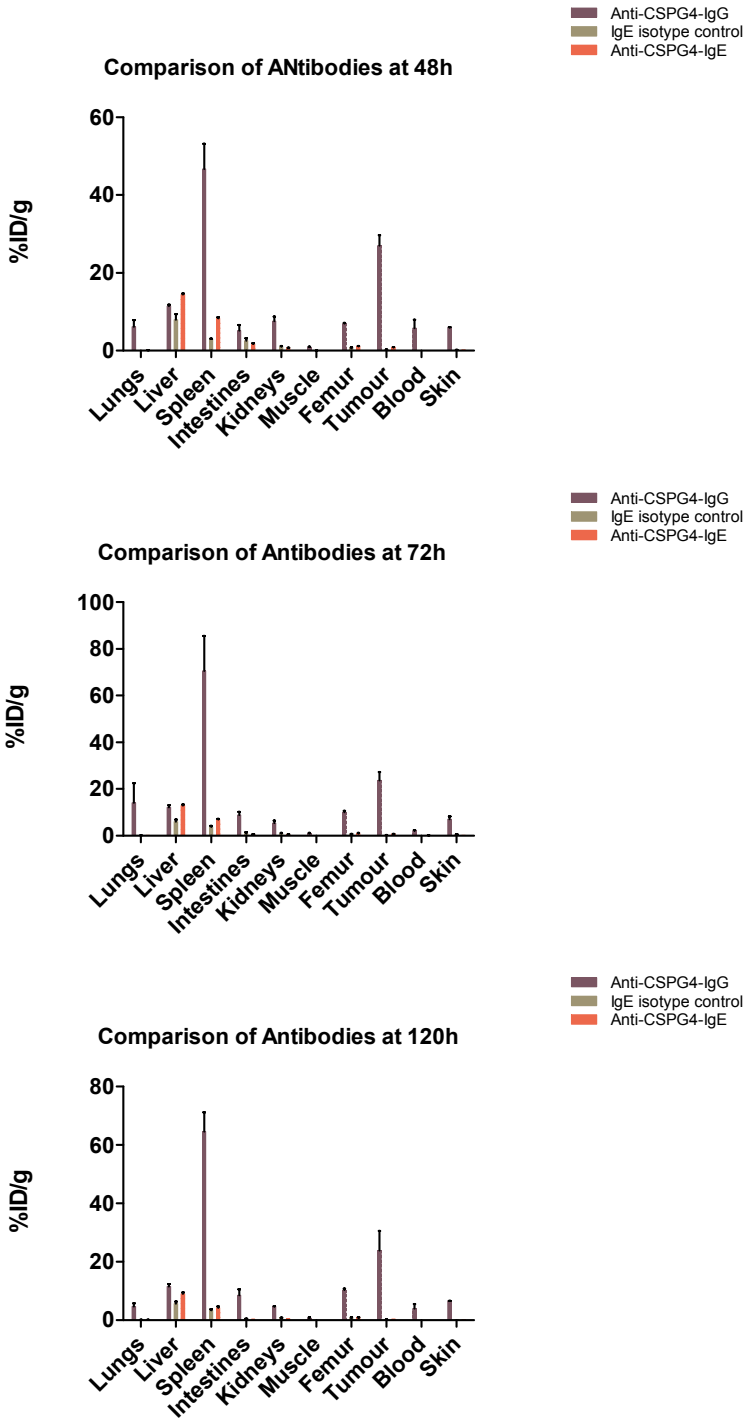

Comparison of biodistribution of anti-CSPG4-IgE, anti-CSPG4-IgG and IgE isotype control in % ID/g at specific time points. Data plotted including SEM error bars (n=3).

Rat MOv18-IgE full list of organs biodistribution in % ID/g

MOV18 IgE	8h	24h	48h	144h
Bladder	0.1639	0.1246	0.2202	0.0304
Intestines	3.1635	1.9088	0.7899	0.1735
Stomach	0.0835	0.0531	0.0395	0.0243
Spleen	2.5743	2.7555	2.6462	1.2348
Kidney	2.1103	2.0192	2.1088	1.4820
Blood	0.2547	0.0799	0.0576	0.0082
Liver	13.6910	8.1117	6.2696	2.5483
Thymus	0.0505	0.0395	0.0603	0.0207
Heart	0.1052	0.0813	0.0714	0.0426
Lung	0.1722	0.1025	0.0802	0.0271
Salavery Glands	0.1750	0.0801	0.0671	0.0476
Trachea	0.1942	0.1032	0.0973	0.0690
Thyroid	0.1062	0.0635	0.0640	0.0347
Muscle	0.0157	0.0115	0.0121	0.0088
Femur	0.5193	0.5064	0.4172	0.2671

Rat MOv18-IgG full list of organs biodistribution in % ID/g

MOV18 IgG	8h	24h	48h	144h
Bladder	2.3725	1.6351	1.9772	1.3341
Intestines	2.1378	1.0489	0.9161	0.5008
Stomach	1.2857	0.6215	0.3208	0.2756
Spleen	8.4053	4.7293	5.1247	4.8224
Kidney	9.4486	5.6938	5.8815	5.4754
Blood	13.3483	5.2610	4.9850	2.0757
Liver	11.4543	4.1727	3.9677	2.5688
Thymus	1.8873	1.0355	0.9334	0.7617
Heart	4.3649	1.6232	1.3972	0.8624
Lung	10.3574	4.3820	4.1743	3.4935
Salavery Glands	2.0870	1.3880	1.3048	0.9690
Trachea	6.0379	2.7771	2.8801	1.0397
Thyroid	2.4854	1.3443	1.1224	0.6586
Muscle	0.5287	0.3683	0.4555	0.2593
Femur	2.3606	1.2453	1.1319	0.8454

Rat MOv18-IgG full list of organs biodistribution data at 8h for each individual rat

A2	CPM	uL/organ	%ID/organ	organ weight	%ID/g
Tail	80219	4.278574857	3.077637028	2.855	
Bladder	2394	0.12768681	0.091846857	0.033	2.783238
Intestines 1	505154	26.94298363	19.3804542	9.374	2.067469
Stomach	38948	2.077337458	1.494257058	2.458	0.607916
Spleen	54876	2.9268761	2.105341746	0.246	8.5583
Kidney	269618	14.38039362	10.34401252	1.04	9.946166
Blood	37103	1.97893221	1.423472826	0.1	14.23473
Liver 1	1603131	85.50488026	61.50482213	5.553	11.07596
Thymus	11628	0.620193077	0.446113307	0.289	1.543645
Heart	49030	2.615072804	1.881057399	0.538	3.496389
Lung	257287	13.72270521	9.87092831	0.9863	10.00804
Salavery Glands	18713	0.998079898	0.717932431	0.372	1.929926
Trachea	4605	0.245613099	0.17667284	0.034	5.19626
Thyroid	6140	0.327484132	0.235563786	0.084	2.804331
Muscle	8207	0.437730012	0.314865145	0.653	0.482182
Femur	28060	1.496613153	1.076534175	0.49	2.197009
A3	CPM	uL/organ	%ID/organ	organ weight	%ID/g
Tail	77332	4.124593312	2.925753795	2.838	
Bladder	2438	0.130033602	0.092238501	0.056	1.647116
Intestines 1	528018	28.162462	19.97686168	9.856	2.026873
Stomach	56283	3.001920102	2.129392759	1.246	1.708983
Spleen	58747	3.133340445	2.222614936	0.273	8.141447
Kidney	245735	13.10656568	9.297058254	1.272	7.309008
Blood	48694	2.597151848	1.842272996	0.15	12.28182
Liver 1	1512785	80.68616993	57.23421682	5.64	10.14791
Thymus	16170	0.862445997	0.611770533	0.29	2.109554
Heart	56283	3.001920102	2.129392759	0.529	4.025317
Lung	208691	11.13078031	7.895547578	0.9909	7.968057
Salavery Glands	18329	0.977598805	0.693453439	0.367	1.889519
Trachea	2057	0.109712518	0.077823871	0.016	4.863992
Thyroid	5884	0.313830071	0.222613347	0.122	1.8247
Muscle	11030	0.588298043	0.417305441	0.921	0.4531
Femur	22799	1.216011521	0.862569968	0.443	1.947111

Rat MOv18-IgG full list of organs biodistribution data at 8h for each individual rat

A4	CPM	uL/organ	%ID/organ	organ weight	%ID/g
Tail	98672	5.262787349		2.31	
Bladder	4293	0.228972212	0.166601321	0.062	2.687118
Intestines 1	432519	23.06891034	16.78505399	7.238	2.319018
Stomach	46510	2.480665636	1.804944664	1.172	1.540055
Spleen	51570	2.750546696	2.001311466	0.235	8.516219
Kidney	234341	12.49885327	9.094227852	0.82	11.09052
Blood	17430	0.929649581	0.676417663	0.05	13.52835
Liver 1	1505961	80.32220385	58.44283531	4.448	13.13913
Thymus	14338	0.764734119	0.556424351	0.277	2.008752
Heart	62613	3.339538109	2.42986455	0.436	5.573084
Lung	323626	17.26097392	12.55917054	0.959	13.09611
Salavery Glands	21832	1.164435437	0.847249019	0.347	2.44164
Trachea	4358	0.232439063	0.169123819	0.021	8.053515
Thyroid	5391	0.287535335	0.209212141	0.074	2.827191
Muscle	9760	0.520561097	0.378762845	0.582	0.650795
Femur	22256	1.187049976	0.863703471	0.294	2.937767

Rat MOv18-IgG full list of organs biodistribution data at 24h for each individual rat

C4	CPM	uL/organ	%ID/organ	organ weight	%ID/g
Tail	248507	3.832086848	2.80394041	2.758	
Bladder	6939	0.107002421	0.07829374	0.04	1.957344
Intestines 1	896724	13.82787707	10.1178665	8.488	1.19202
Stomach	100211	1.545297537	1.1306952	1.472	0.768135
Spleen	111910	1.725701244	1.26269671	0.263	4.801128
Kidney	522299	8.054079477	5.89317514	1.124	5.243038
Blood	132430	2.042128637	1.49422684	0.35	4.26922
Liver 1	2113522	32.59143549	23.8471743	5.786	4.12153
Thymus	21934	0.338231893	0.24748449	0.24	1.031185
Heart	63346	0.976823081	0.71474208	0.428	1.669958
Lung	245883	3.791623618	2.77433344	0.7481	3.708506
Salavery Glands	47023	0.725115268	0.53056731	0.374	1.418629
Trachea	2710	0.041789388	0.03057732	0.01	3.057732
Thyroid	7954	0.122654166	0.08974613	0.069	1.300669
Muscle	26292	0.405434162	0.29665644	0.813	0.364891
Femur	56532	0.871748215	0.63785873	0.5	1.275717

Rat MOv18-IgG full list of organs biodistribution data at 24h for each individual rat

C5	CPM	uL/organ	%ID/organ	organ weight	%ID/g
Tail	221695	3.418634058	2.65460304	3.229	
Bladder	8030	0.123826119	0.0961522	0.079	1.217116
Intestines 1	921044	14.20290213	11.0286935	9.189	1.200206
Stomach	68289	1.053046308	0.81770084	1.332	0.61389
Spleen	107037	1.650557449	1.28167413	0.248	5.168041
Kidney	497634	7.673734368	5.95873037	0.957	6.226469
Blood	91730	1.414516801	1.09838624	0.192	5.720762
Liver 1	2025217	31.22973369	24.250196	5.548	4.37098
Thymus	22124	0.341161776	0.26491548	0.26	1.018906
Heart	60242	0.928958041	0.72134508	0.439	1.643155
Lung	484521	7.471526161	5.80171371	1.154	5.027482
Salavery Glands	51351	0.791854925	0.61488315	0.443	1.387998
Trachea	3792	0.058474302	0.04540587	0.016	2.837867
Thyroid	9306	0.143502598	0.11143118	0.081	1.375694
Muscle	28427	0.438356798	0.34038837	0.888	0.38332
Femur	52453	0.808848247	0.62807864	0.493	1.273993

Rat MOv18-IgG full list of organs biodistribution data at 24h for each individual rat

C6	CPM	uL/organ	%ID/organ	organ weight	%ID/g
Tail	199678	3.079122269		3.316	
Bladder	5638	0.086940431	0.06057685	0.035	1.730767
Intestines 1	679370	10.47618313	7.29941406	9.674	0.754539
Stomach	75904	1.170472945	0.81554194	1.69	0.482569
Spleen	99339	1.531850915	1.06733664	0.253	4.218722
Kidney	588656	9.077333498	6.32474776	1.127	5.612021
Blood	83571	1.288701445	0.89791915	0.155	5.793027
Liver 1	2391887	36.88394578	25.6993591	6.384	4.025589
Thymus	23501	0.362395719	0.25250383	0.239	1.056501
Heart	73597	1.134897994	0.79075464	0.508	1.556604
Lung	465871	7.183934987	5.00549823	1.135	4.410131
Salavery Glands	58112	0.896112508	0.62437781	0.46	1.357343
Trachea	3627	0.05592993	0.03896989	0.016	2.435618
Thyroid	9721	0.14990208	0.10444618	0.077	1.356444
Muscle	35551	0.548212	0.3819737	1.071	0.356651
Femur	52778	0.81385989	0.56706725	0.478	1.186333

Rat MOv18-IgG full list of organs biodistribution data at 48h for each individual rat

D6	CPM	uL/organ	%ID/organ	organ weight	%ID/g
Tail	185189	3.406463836	2.39228825	3.1785	
Bladder	7952	0.146273269	0.10272466	0.0457	2.247804
Intestines 1	684727	12.59522846	8.84536532	9.495	0.931581
Stomach	69623	1.280682069	0.89939621	2.615	0.343937
Spleen	104143	1.915661099	1.34532869	0.243	5.536332
Kidney	457015	8.406574204	5.9037611	1.0005	5.900811
Blood	41583	0.764899566	0.53717295	0.092	5.838836
Liver 1	1772264	32.59995585	22.8942666	5.7639	3.97201
Thymus	20453	0.376223236	0.2642137	0.3076	0.858952
Heart	49607	0.912497241	0.64082771	0.466	1.375167
Lung	256630	4.720587153	3.31516955	1.0929	3.03337
Salavery Glands	32261	0.593425796	0.41675052	0.332	1.255273
Trachea	2085	0.038352586	0.02693422	0.0118	2.282561
Thyroid	5846	0.107534398	0.07551916	0.068	1.110576
Muscle	39834	0.73272754	0.51457921	1.1788	0.436528
Femur	43747	0.80470532	0.5651277	0.478	1.182276

Rat MOv18-IgG full list of organs biodistribution data at 48h for each individual rat

D7	CPM	uL/organ	%ID/organ	organ weight	%ID/g
Tail	167129	3.074258701	2.16001594	2.783	
Bladder	10266	0.188838202	0.13268029	0.109	1.21725
Intestines 1	716818	13.18552719	9.26433059	9.281	0.998204
Stomach	72602	1.335479361	0.93832595	3.283	0.285814
Spleen	104968	1.930836583	1.35663202	0.27	5.024563
Kidney	480685	8.841972629	6.21249013	1.0078	6.164408
Blood	112161	2.063148407	1.44959611	0.3309	4.380768
Liver 1	1721837	31.6723751	22.2534412	5.3121	4.189198
Thymus	22452	0.412993893	0.29017512	0.289	1.004066
Heart	50965	0.937477007	0.65868409	0.461	1.428816
Lung	307946	5.664520639	3.97996918	0.934	4.261209
Salavery Glands	36610	0.673423589	0.47315657	0.376	1.258395
Trachea	2776	0.051063204	0.0358777	0.018	1.993206
Thyroid	6235	0.114689868	0.08058266	0.071	1.134967
Muscle	27721	0.509914649	0.35827296	0.839	0.427024
Femur	41184	0.75756015	0.53227206	0.426	1.249465

Rat MOv18-IgG full list of organs biodistribution data at 48h for each individual rat

D8	CPM	uL/organ	%ID/organ	organ weight	%ID/g
Tail	168313	3.096037819		3.247	
Bladder	5549	0.102071224	0.07152655	0.029	2.466433
Intestines 1	602089	11.07514164	7.76092091	9.483	0.818404
Stomach	45144	0.830402472	0.58190569	1.749	0.332708
Spleen	95963	1.765193878	1.23696207	0.257	4.813082
Kidney	451892	8.312339048	5.82488315	1.044	5.57939
Blood	83393	1.533974689	1.0749349	0.227	4.735396
Liver 1	1681718	30.93440512	21.6773274	5.793	3.741986
Thymus	19047	0.350360533	0.24551563	0.262	0.937083
Heart	51563	0.948476933	0.66464653	0.479	1.387571
Lung	625868	11.51254507	8.06743197	1.543	5.228407
Salavery Glands	45312	0.833492753	0.58407121	0.417	1.40065
Trachea	1456	0.02678243	0.01876782	0.0043	4.36461
Thyroid	5830	0.107240085	0.07514864	0.067	1.121621
Muscle	60787	1.118148039	0.78354379	1.558	0.502916
Femur	44159	0.680951133	0.47717745	0.495	0.963995

Rat MOv18-IgG full list of organs biodistribution data at 144h for each individual rat

A5	CPM	uL/organ	%ID/organ	organ weight	%ID/g
Tail	107641	2.072091322	1.44167639	3.145	
Bladder	6043	0.116327866	0.08093617	0.0699	1.157885
Intestines 1	444648	8.559482559	5.95533786	10.1712	0.58551
Stomach	38422	0.73962424	0.51460029	1.5745	0.326834
Spleen	89967	1.731866482	1.20496186	0.2606	4.623798
Kidney	489190	9.416916917	6.55190561	1.1796	5.554345
Blood	34632	0.666666667	0.4638394	0.2675	1.733979
Liver 1	1189455	22.89703165	15.9308181	6.2247	2.559291
Thymus	13950	0.268537769	0.1868376	0.2753	0.678669
Heart	25805	0.496746747	0.34561607	0.4808	0.718835
Lung	221812	4.26988527	2.97081152	0.904	3.286296
Salavery Glands	26266	0.505621006	0.35179041	0.3778	0.931155
Trachea	1016	0.01955802	0.01360767	0.0151	0.90117
Thyroid	4297	0.082717333	0.05755134	0.0954	0.603263
Muscle	15090	0.29048279	0.20210604	0.8496	0.237884
Femur	33026	0.635751136	0.44232964	0.5342	0.828023

Rat MOv18-IgG full list of organs biodistribution data at 144h for each individual rat

D9	CPM	uL/organ	%ID/organ	organ weight	%ID/g
Tail	97191	1.870928621	1.31821381	3.4456	
Bladder	4545	0.087491337	0.06164441	0.0407	1.514605
Intestines 1	410777	7.907465157	5.57142034	11.6763	0.477156
Stomach	40254	0.774890275	0.54597009	3.2622	0.167363
Spleen	106815	2.056190806	1.44874534	0.279	5.192636
Kidney	462310	8.899476399	6.27036893	1.1714	5.352885
Blood	23152	0.445676446	0.3140135	0.1462	2.147835
Liver 1	1191552	22.93739894	16.1611703	6.8227	2.368735
Thymus	18208	0.350504351	0.2469574	0.2963	0.833471
Heart	35134	0.676330176	0.47652688	0.5364	0.88838
Lung	433736	8.349426349	5.88281616	0.955	6.160017
Salavery Glands	25636	0.493493493	0.34770431	0.3555	0.978071
Trachea	1261	0.024274274	0.0171031	0.0128	1.33618
Thyroid	3494	0.067259567	0.04738956	0.0656	0.722402
Muscle	21272	0.409486409	0.28851482	1.0087	0.286026
Femur	27561	0.530549781	0.37381332	0.4609	0.811051

Rat MOv18-IgG full list of organs biodistribution data at 144h for each individual rat

D10	CPM	uL/organ	%ID/organ	organ weight	%ID/g
Tail	117909	2.26975052	1.5650187	3.052	
Bladder	5500	0.105875106	0.07300208	0.0549	1.329728
Intestines 1	315664	6.076538077	4.18984184	9.5311	0.439597
Stomach	49613	0.955051205	0.65851863	1.9794	0.332686
Spleen	85003	1.636309386	1.12825386	0.2426	4.650675
Kidney	456852	8.794409794	6.06384518	1.0987	5.519109
Blood	26875	0.517344267	0.35671473	0.1521	2.345265
Liver 1	1295474	24.93789944	17.1949642	6.189	2.778311
Thymus	14386	0.276930777	0.19094691	0.247	0.773064
Heart	35458	0.682567183	0.4706378	0.4803	0.979883
Lung	122578	2.35962886	1.62699083	1.5733	1.034126
Salavery Glands	35063	0.674963425	0.46539493	0.4665	0.997631
Trachea	1395	0.026853777	0.01851598	0.021	0.881713
Thyroid	4099	0.078905829	0.05440646	0.0837	0.650017
Muscle	15881	0.305709556	0.2107902	0.8299	0.253995
Femur	31934	0.614730115	0.42386338	0.4725	0.897065

Rat MOv18-IgE full list of organs biodistribution data at 8h for each individual rat

A2	CPM	uL/organ	%ID/organ	organ weight	%ID/g
Tail	5351	0.166076971	0.11635424		
Bladder	1172	0.036374922	0.025484427	0.077	0.33096658
Intestines 1	1311084	40.69162011	28.50872396	9.213	3.09440182
Stomach	5484	0.170204842	0.119246244	1.651	0.07222668
Spleen	30120	0.934823091	0.654941076	0.268	2.44380998
Kidney	95003	2.948572315	2.065782438	0.98	2.10794126
Blood	1399	0.043420236	0.030420404	0.1	0.30420404
Liver 1	3363713	104.398293	73.14189281	5.594	13.0750613
Thymus	840	0.026070764	0.018265289	0.327	0.05585715
Heart	2285	0.070918684	0.049685935	0.462	0.10754531
Lung	8048	0.249782744	0.174998864	1.001	0.17482404
Salavery Glands	770	0.0238982	0.016743182	0.188	0.08905948
Trachea	220	0.006828057	0.004783766	0.055	0.08697757
Thyroid	343	0.010645562	0.007458326	0.085	0.08774502
Muscle	524	0.016263191	0.011394061	0.648	0.01758343
Femur	11900	0.369335816	0.25875826	0.52	0.49761204

Rat MOv18-IgE full list of organs biodistribution data at 8h for each individual rat

A3	CPM	uL/organ	%ID/organ	organ weight	%ID/g
Tail	9971	0.309466	0.218719		
Bladder	422	0.013097	0.009257	0.101	0.091651
Intestines 1	1183996	36.74724	25.97152	7.973	3.257433
Stomach	5263	0.163346	0.115446	2.322	0.049719
Spleen	27153	0.842737	0.595614	0.232	2.567302
Kidney	95386	2.960459	2.092337	0.964	2.170474
Blood	549	0.017039	0.012043	0.0491	0.245266
Liver 1	3379886	104.9002	74.13941	5.345	13.8708
Thymus	620	0.019243	0.0136	0.258	0.052713
Heart	2149	0.066698	0.047139	0.477	0.098825
Lung	6968	0.216263	0.152846	0.93	0.164351
Salavery Glands	1558	0.048355	0.034175	0.383	0.089231
Trachea	372	0.011546	0.00816	0.022	0.370909
Thyroid	489	0.015177	0.010726	0.069	0.155456
Muscle	462	0.014339	0.010134	0.688	0.01473
Femur	10643	0.330323	0.233459	0.506	0.461382

Rat MOv18-IgE full list of organs biodistribution data at 8h for each individual rat

A4	CPM	uL/organ	%ID/organ	organ weight	%ID/g
Tail	11516	0.357418		2.798	
Bladder	144	0.004469	0.00345	0.05	0.069001
Intestines 1	1107878	34.38479	26.54324	8.457	3.138611
Stomach	7751	0.240565	0.185703	1.445	0.128514
Spleen	31466	0.976598	0.753882	0.278	2.711806
Kidney	88492	2.746493	2.120147	1.033	2.052417
Blood	448	0.013904	0.010733	0.05	0.214669
Liver 1	3148127	97.70723	75.4248	5.339	14.12714
Thymus	547	0.016977	0.013105	0.306	0.042828
Heart	2119	0.065767	0.050768	0.465	0.109179
Lung	8512	0.264184	0.203936	1.149	0.17749
Salavery Glands	5950	0.184668	0.142554	0.411	0.346846
Trachea	99	0.003073	0.002372	0.019	0.124837
Thyroid	299	0.00928	0.007164	0.095	0.075407
Muscle	576	0.017877	0.0138	0.929	0.014855
Femur	12400	0.384854	0.297087	0.496	0.598966

Rat MOv18-IgE full list of organs biodistribution data at 24h for each individual rat

C4	CPM	uL/organ	%ID/organ	organ weight	%ID/g
Tail	17654	0.272232417	0.191405955	3.018	
Bladder	418	0.006445743	0.004531986	0.046	0.09852145
Intestines 1	1386344	21.37803204	15.03084272	9.054	1.66013284
Stomach	5382	0.082992799	0.058352036	2.53	0.02306405
Spleen	64270	0.991071566	0.696820025	0.281	2.47978657
Kidney	197618	3.047356166	2.142588763	1.238	1.73068559
Blood	1420	0.021897022	0.015395744	0.227	0.06782266
Liver 1	4155882	64.08552175	45.05837562	6.33	7.1182268
Thymus	850	0.013107373	0.009215762	0.236	0.03904984
Heart	3285	0.05065614	0.035616209	0.528	0.06745494
Lung	8128	0.125337322	0.088124369	0.84	0.10490996
Salavery Glands	2078	0.032043671	0.022529827	0.354	0.06364358
Trachea	152	0.002343907	0.001647995	0.015	0.10986634
Thyroid	472	0.007278447	0.005117458	0.0802	0.06380871
Muscle	1308	0.020169933	0.014181431	1.0386	0.01365437
Femur	21470	0.331076809	0.232779305	0.541	0.43027598

Rat MOv18-IgE full list of organs biodistribution data at 24h for each individual rat

C5	CPM	uL/organ	%ID/organ	organ weight	%ID/g
Tail	137827	2.125353	1.482377	2.6723	
Bladder	392	0.006045	0.004216	0.0509	0.082831
Intestines 1	1391385	21.45577	14.96483	7.392	2.024462
Stomach	16221	0.250135	0.174462	1.9477	0.089574
Spleen	75731	1.167805	0.814513	0.258	3.157027
Kidney	208152	3.209795	2.238747	0.924	2.422886
Blood	1075	0.016577	0.011562	0.14	0.082586
Liver 1	4912349	75.75057	52.83401	5.732	9.217378
Thymus	1063	0.016392	0.011433	0.272	0.042033
Heart	4579	0.07061	0.049249	0.449	0.109685
Lung	6862	0.105815	0.073803	0.646	0.114246
Salavery Glands	2990	0.046107	0.032158	0.3869	0.083118
Trachea	250	0.003855	0.002689	0.024	0.112035
Thyroid	472	0.007278	0.005077	0.0712	0.071299
Muscle	907	0.013986	0.009755	0.8	0.012194
Femur	29661	0.457386	0.319014	0.538	0.592963

Rat MOv18-IgE full list of organs biodistribution data at 24h for each individual rat

C6	CPM	uL/organ	%ID/organ	organ weight	%ID/g
Tail	19987	0.308208		3.2962	
Bladder	932	0.014372	0.009871	0.0513	0.192424
Intestines 1	1775169	27.37388	18.8018	9.209	2.041677
Stomach	8548	0.131814	0.090537	1.935	0.046789
Spleen	65296	1.006893	0.691586	0.263	2.629606
Kidney	226343	3.490308	2.397325	1.259	1.90415
Blood	1391	0.02145	0.014733	0.165	0.08929
Liver 1	4826378	74.42486	51.11886	6.3903	7.999446
Thymus	987	0.01522	0.010454	0.2794	0.037415
Heart	3365	0.05189	0.035641	0.533	0.066868
Lung	7744	0.119416	0.082021	0.927	0.08848
Salavery Glands	3686	0.05684	0.03904	0.417	0.093622
Trachea	168	0.002591	0.001779	0.0203	0.087654
Thyroid	471	0.007263	0.004989	0.0902	0.055306
Muscle	867	0.01337	0.009183	1.065	0.008622
Femur	25190	0.388441	0.266801	0.538	0.495913

Rat MOv18-IgE full list of organs biodistribution data at 48h for each individual rat

D6	CPM	uL/organ	%ID/organ	organ weight	%ID/g
Tail	25867	0.475811199	0.336919052	3.011	
Bladder	1491	0.027426238	0.019420354	0.056	0.34679204
Intestines 1	532349	9.792307409	6.933874071	9.928	0.698416
Stomach	3941	0.072492826	0.051331735	2.638	0.01945858
Spleen	52402	0.96390994	0.68253884	0.2703	2.52511595
Kidney	175934	3.2362225	2.291549718	1.111	2.06260101
Blood	910	0.016739018	0.011852798	0.127	0.09332912
Liver 1	2927608	53.85196086	38.13225009	5.568	6.84846446
Thymus	1186	0.021815908	0.015447713	0.123	0.12559116
Heart	2575	0.047365904	0.033539512	0.466	0.0719732
Lung	7721	0.142024134	0.100566436	1.383	0.07271615
Salavery Glands	1723	0.031693768	0.022442167	0.3176	0.07066173
Trachea	122	0.002244132	0.001589056	0.011	0.14445968
Thyroid	334	0.006143772	0.004350368	0.057	0.07632224
Muscle	1500	0.027591789	0.01953758	1.476	0.01323684
Femur	16580	0.304981238	0.215955383	0.528	0.40900641

Rat MOv18-IgE full list of organs biodistribution data at 48h for each individual rat

D7	CPM	uL/organ	%ID/organ	organ weight	%ID/g
Tail	167270	3.076852	2.167971	3.628	
Bladder	653	0.012012	0.008463	0.037	0.228742
Intestines 1	715325	13.15806	9.27126	10.504	0.882641
Stomach	7118	0.130932	0.092256	1.406	0.065616
Spleen	56733	1.043577	0.735311	0.278	2.645004
Kidney	175668	3.23133	2.276816	1.049	2.170464
Blood	968	0.017806	0.012546	0.349	0.035949
Liver 1	2807681	51.64596	36.39009	6.232	5.839231
Thymus	750	0.013796	0.009721	0.312	0.031156
Heart	2789	0.051302	0.036148	0.535	0.067566
Lung	8601	0.158211	0.111477	1.9723	0.056521
Salavery Glands	2802	0.051541	0.036316	0.465	0.0781
Trachea	163	0.002998	0.002113	0.0618	0.034185
Thyroid	426	0.007836	0.005521	0.121	0.045631
Muscle	616	0.011331	0.007984	0.835	0.009562
Femur	18712	0.344198	0.242524	0.564	0.430008

Rat MOv18-IgE full list of organs biodistribution data at 48h for each individual rat

D8	CPM	uL/organ	%ID/organ	organ weight	%ID/g
Tail	24401	0.448845		2.133	
Bladder	254	0.004672	0.003228	0.038	0.084941
Intestines 1	546854	10.05912	6.94925	8.811	0.788702
Stomach	4176	0.076816	0.053067	1.5903	0.033369
Spleen	56646	1.041976	0.71984	0.26	2.768614
Kidney	179395	3.299886	2.279696	1.089	2.093385
Blood	826	0.015194	0.010497	0.241	0.043554
Liver 1	2922977	53.76678	37.14428	6.0681	6.121237
Thymus	559	0.010283	0.007104	0.294	0.024162
Heart	2688	0.049444	0.034158	0.457	0.074745
Lung	11335	0.208502	0.144042	1.292	0.111487
Salavery Glands	1580	0.029063	0.020078	0.382	0.052561
Trachea	98	0.001803	0.001245	0.011	0.113214
Thyroid	397	0.007303	0.005045	0.072	0.070069
Muscle	1546	0.028438	0.019646	1.457	0.013484
Femur	18695	0.288285	0.199159	0.4827	0.412594

Rat MOv18-IgE full list of organs biodistribution data at 144h for each individual rat

A5	CPM	uL/organ	%ID/organ	organ weight	%ID/g
Tail	10562	0.203318703	0.1436915	3.1005	
Bladder	187	0.003599754	0.002544055	0.0335	0.07594194
Intestines 1	121250	2.334064834	1.649554472	9.001	0.18326347
Stomach	1783	0.034322784	0.024256954	1.6754	0.01447831
Spleen	24920	0.47971048	0.339025958	0.2381	1.42388055
Kidney	102752	1.977977978	1.397897081	0.9125	1.53194201
Blood	74	0.001424501	0.001006738	0.1683	0.00598181
Liver 1	1035033	19.92440517	14.08118197	5.6039	2.51274683
Thymus	403	0.007757758	0.005482643	0.2603	0.02106278
Heart	1437	0.027662278	0.019549771	0.4278	0.04569839
Lung	3187	0.061349811	0.043357774	1.5464	0.02803788
Salavery Glands	1069	0.020578271	0.014543288	0.318	0.04573361
Trachea	89	0.001713252	0.001210807	0.019	0.06372668
Thyroid	145	0.002791253	0.001972663	0.0629	0.03136189
Muscle	883	0.016997767	0.012012838	1.1998	0.01001237
Femur	10047	0.193404943	0.136685145	0.4525	0.30206662

Rat MOv18-IgE full list of organs biodistribution data at 144h for each individual rat

D9	CPM	uL/organ	%ID/organ	organ weight	%ID/g
Tail	43238	0.832332	0.577336	2.9853	
Bladder	201	0.003869	0.002684	0.3235	0.008296
Intestines 1	115972	2.232463	1.548519	9.064	0.170843
Stomach	2129	0.040983	0.028428	1.1532	0.024651
Spleen	28967	0.557615	0.386782	0.234	1.652917
Kidney	125136	2.40887	1.670881	1.0151	1.646026
Blood	101	0.001944	0.001349	0.1435	0.009398
Liver 1	1212926	23.34885	16.19562	6.184	2.618956
Thymus	446	0.008586	0.005955	0.2706	0.022007
Heart	1462	0.028144	0.019521	0.4518	0.043208
Lung	2946	0.056711	0.039337	1.279	0.030756
Salavery Glands	1305	0.025121	0.017425	0.341	0.0511
Trachea	67	0.00129	0.000895	0.0126	0.071002
Thyroid	203	0.003908	0.002711	0.0692	0.03917
Muscle	920	0.01771	0.012284	1.3686	0.008976
Femur	9990	0.192308	0.133392	0.5016	0.265932

Rat MOv18-IgE full list of organs biodistribution data at 144h for each individual rat

D10	CPM	uL/organ	%ID/organ	organ weight	%ID/g
Tail	16414	0.31597	0.218085	3.1347	
Bladder	188	0.003619	0.002498	0.365	0.006843
Intestines 1	112002	2.156041	1.488115	8.9484	0.1663
Stomach	4247	0.081755	0.056428	1.6761	0.033666
Spleen	31156	0.599754	0.413954	0.6597	0.627489
Kidney	125004	2.406329	1.660866	1.3097	1.268127
Blood	155	0.002984	0.002059	0.2269	0.009076
Liver 1	1247093	24.00656	16.5695	6.5932	2.51312
Thymus	438	0.008432	0.005819	0.3051	0.019074
Heart	1526	0.029376	0.020275	0.5207	0.038938
Lung	2923	0.056268	0.038836	1.7311	0.022435
Salavery Glands	1461	0.028124	0.019412	0.422	0.045999
Trachea	93	0.00179	0.001236	0.0171	0.07226
Thyroid	233	0.004485	0.003096	0.092	0.03365
Muscle	416	0.008008	0.005527	0.739	0.007479
Femur	9924	0.191037	0.131855	0.5655	0.233166

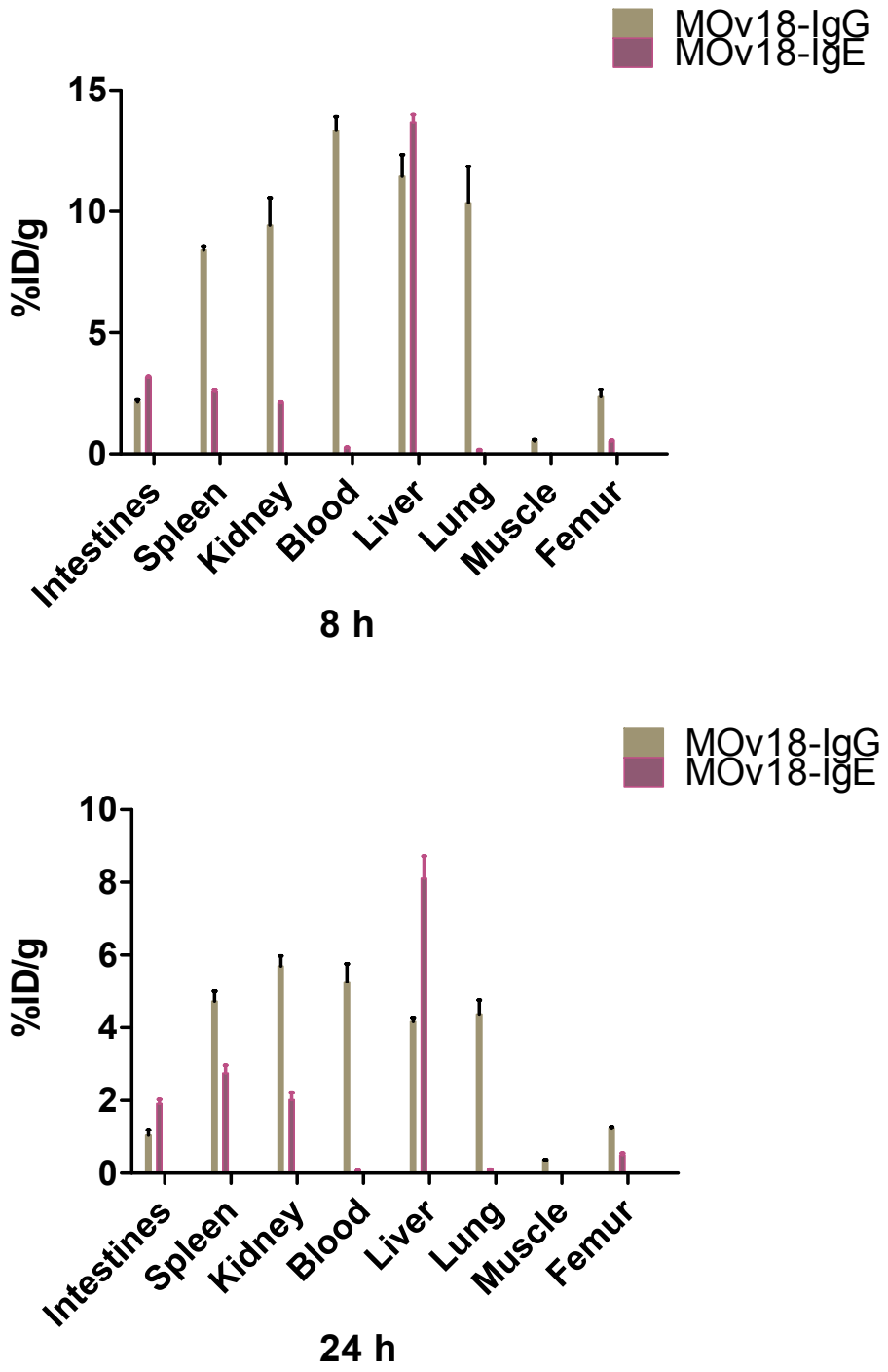

Comparison of biodistribution of rat MOv18-IgE and rat MOv18-IgG in % ID/g at specific time points. Data plotted including SEM error bars (n=3).

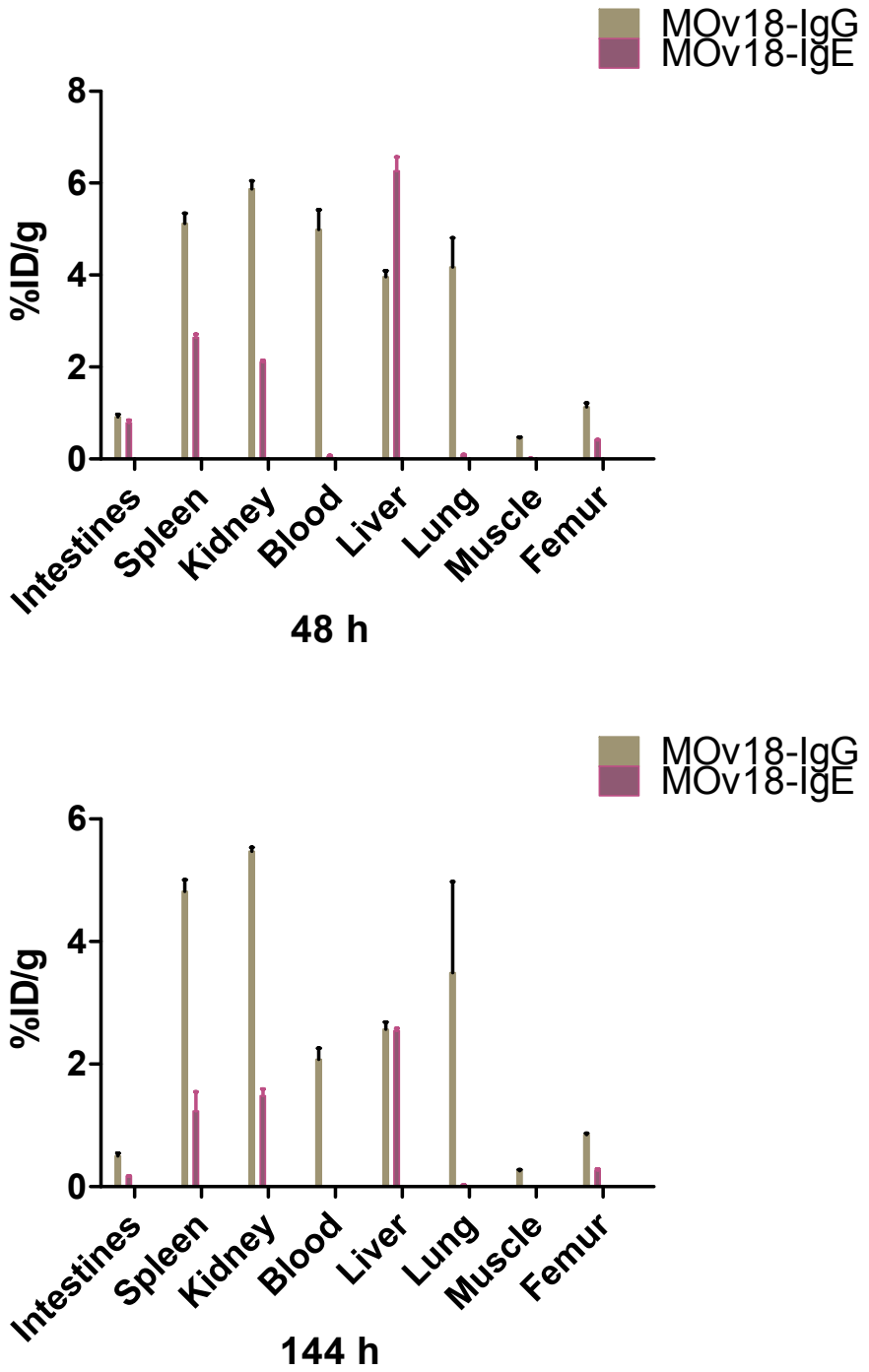

Comparison of biodistribution of rat MOv18-IgE and rat MOv18-IgG in % ID/g at specific time points. Data plotted including SEM error bars (n=3).